APPLIED COMPUTATIONAL ELECTROMAGNETICS SOCIETY JOURNAL

December 2015
Vol. 30 No. 12
ISSN 1054-4887

The ACES Journal is abstracted in INSPEC, in Engineering Index, DTIC, Science Citation Index Expanded, the Research Alert, and to Current Contents/Engineering, Computing & Technology.

The illustrations on the front cover have been obtained from the research groups at the Department of Electrical Engineering, The University of Mississippi.

EMERITUS EDITORIAL ASSISTANTS

DECEMBER 2015 REVIEWERS

THE APPLIED COMPUTATIONAL ELECTROMAGNETICS SOCIETY

JOURNAL

Vol. 30 No. 12 December 2015

TABLE OF CONTENTS

Efficient, Accurate and Scalable Reflectarray Phase-Only Synthesis Based on the Levenberg-Marquardt Algorithm

Daniel R. Prado, Jana Álvarez, Manuel Arrebola, Marcos R. Pino, Rafael G. Ayestarán, and Fernando Las-Heras

Department of Electrical Engineering
University of Oviedo, Gijón, Asturias, 33203, Spain
{drprado, jalvarez, arrebola, mpino, rayestaran, flasheras}@tsc.uniovi.es

Abstract ─ The Levenberg-Marquardt algorithm is used to perform an efficient phase-only synthesis for shaped-beam reflectarray antennas. A thorough analysis of the problem and algorithm allows to improve greatly its performance and its results with regard to those in the literature. Specifically, several optimizations in the Jacobian matrix computation are detailed, including its fully parallelization thanks to the fact that each column of the Jacobian can be independently computed. A Cholesky factorization based solver is used to obtain the updating vector at each iteration of the algorithm, which is the fastest exact solver for linear equation systems. Finally, some guidelines to choose proper values for the algorithm parameters are presented. Due to the high dimensionality of the problem, a good control in the algorithm evolution is important to guarantee good convergence and avoid non-desired local minima. The synthesis of a LMDS shaped beam for a dual-polarized reflectarray is proposed to test the developed algorithm and the results are compared with others in the literature, showing improvements in accuracy and time efficiency. The framework established for the phase-only synthesis can be used in a broader problem to directly optimize the geometry of the reflectarray through full wave analysis of the unit cell.

Index Terms ─ Levenberg-Marquardt algorithm, local multipoint distribution system, parallelization, phase-only synthesis, reflectarray antennas.

I. INTRODUCTION

Shaped-beam antennas are demanded in many applications that require non-canonical beams, such as direct broadcast satellite (DBS) missions, local multipoint distribution service (LMDS) technology or multibeam antennas [1]. Traditionally, parabolic reflectors and phased arrays have been used for these applications, although in recent years reflectarray antennas have proven to be a feasible solution while providing other benefits such as low cost, low weight and reduced physical dimensions [1]. As parabolic reflectors, they can be used in single configurations as well as dual-reflector setups [2]. However, reflectarrays present limitations mainly in the bandwidth [1,3], which can be overcome by choosing an appropriate element topology [1,4,5].

In order to achieve the required specifications, a number of algorithms has been used to synthesize the radiation patterns, for instance, analytical [6], steepest descent [7], conjugate gradient [8], intersection approach [9], Levenberg-Marquardt (LMA) [10], genetic algorithms [11] or particle swarm optimization [12], among others. However, the analytical approach has limitations when applied to complex shaped patterns, although they can be used to generate a starting point for a more powerful synthesis algorithm [13]. The steepest descent has a very slow convergence rate [14,15], which makes it impractical to synthesize arrays with a moderate number of elements. Conjugate gradient methods can be adapted to solve non-linear optimization problems and are faster than the steepest descent [14], but they tend to be both less efficient and less robust than quasi-Newton methods [15]. The intersection approach is very efficient when using only the fast Fourier transform (FFT), but suffers from the problem of traps, due to the non-convexity of the sets dealt with [16]. One manner of dealing with the trap problem is working with the far field squared amplitude instead of just the amplitude [16,17]. However, this approach causes that one of the projectors of the intersection approach cannot be implemented with FFT (the projector which recovers the reflected field on the reflectarray surface), and a minimization algorithm based on optimization techniques has to be used, reducing greatly the efficiency of the intersection approach algorithm (in [17], the Broyden-Fletcher-Goldfarb-Shanno (BFGS) algorithm is used, although other algorithms are also suitable, such as LMA). All these algorithms are local optimizers and depend

Submitted On: June 30, 2015
Accepted On: November 8, 2015

strongly on the starting point to converge with success.

Genetic algorithms (GA) and particle swarm optimization (PSO) are global search algorithms, which in contrast with the previous local search algorithms, do not depend on the starting point. These algorithms are potentially able to find the global maximum at the expense of taking many iterations. However, as the number of variables increase, the search space size grows exponentially, making it harder for these algorithms to find a suitable solution. Another aspect of evolutionary algorithms is that due to their non-deterministic approach, two instances using the same parameters will yield different results, in contrast with the deterministic approach of the local optimizers mentioned above. GA and PSO have been demonstrated capable of synthesizing phased arrays, although at the cost of several thousand iterations [18]. Each iteration involves several evaluations of the cost function, one for each member of the population, thus making their computing times very sensitive to the time cost of the cost function (also known as fitness in evolutionary algorithm terms). Both algorithms seem to have similar performance with small arrays, although PSO is easier to implement [18]. Recently, the PSO has been used to synthesize several reflectarray radiation patterns [12,19]. In [12], a single-fed reflectarray of 848 elements with asymmetric multiple beams was synthesized, taking more than 70000 iterations to converge and 44 hours. In [19], a reflectarray of 900 elements was synthesized, taking 5500 iterations to converge. Increasing the size of the antenna would dramatically increase computing times to achieve convergence with these algorithms because of their global search approach, unless a suitable starting point was used and the PSO was set up to prioritize local search.

Regarding memory usage, the LMA presents a disadvantage with regard to other synthesis algorithms. The LMA needs to store a Jacobian matrix, which is generally bigger than the Hessian matrix (or its approximation) used by Newton and quasi-Newton methods. Additionally, the LMA also needs to store the approximation of the Hessian. In contrast, the conjugate gradient only needs to store a smaller matrix (same size as the Hessian) and a few vectors, while the steepest descent only stores vectors. The intersection approach uses one to four small matrices with dimension the number of samples of the radiation pattern. (When an optimization algorithm is introduced in the intersection approach, the storage needs would be the same as the ones of the optimization algorithm plus the needs of the intersection approach.) Evolutionary algorithms, such as GA or PSO, store one solution per member of the population. In the phase-only synthesis case, the solution is a vector or matrix with the number of elements equal to the number of unknowns. Exact storage needs for the mentioned algorithms will vary according to their implementations, although they have been roughly laid out for the main data structures. The LMA trades more memory usage for a more robust algorithm for non-linear optimization when compared with other gradient methods, and a more flexible framework when compared with the intersection approach. It is also simpler and easier to implement than other quasi-Newton methods, and is faster than evolutionary algorithms due to its local search nature.

As an example, a reflectarray of $M \times N$ elements (which correspond to the unknowns of the problem) is considered, computing the radiation pattern only for one polarization in a grid with $U \times V$ points. The evolutionary algorithms are considered to have L members in their population. Note that, in general, $M \cdot N \leq U \cdot V$. In this case, the size of the Jacobian matrix is $M \cdot N \cdot U \cdot V$, the size of the Hessian or its approximation is $M^2 \cdot N^2$ and the size of a solution is $M \cdot N$. Then, the memory usage is $O(M \cdot N \cdot U \cdot V + M^2 \cdot N^2)$ for the LMA, corresponding to the Jacobian and approximation of the Hessian; $O(M^2 \cdot N^2)$ for quasi-Newton methods and the conjugate gradient, corresponding to the Hessian; $O(U \cdot V + M \cdot N)$ for the intersection approach, corresponding to a solution and the computed far field; and $O(L \cdot U \cdot V + L \cdot M \cdot N)$ for the GA and PSO, corresponding to one solution and one computed far field per member of the population. Auxiliary vectors and matrices might be used depending on the implementation, but the main data structures shown above take up most of the memory used by the algorithm.

In this work, an optimization framework based on the LMA described in [10], is presented with a number of improvements derived from a deeper insight into the problem and the algorithm itself that allows to improve both the performance and results, yielding a faster and more robust method for the synthesis of shaped radiation patterns. Specifically, the proposed improvements focus on accelerating the computing times by parallelizing different operations, which makes the algorithm scale well with the number of available processors, taking advantage of farm servers and new desktop computers to perform faster synthesis for a given problem size, or to increase the size for the same computing times. Also, a faster method for solving the equation system is used, taking advantage of the nature of the problem. The algorithm accuracy and convergence is improved yielding better results in less iterations, which also leads to further reduction in computing times. Finally, a general phase-only framework based on the LMA is established, which can be further extended to include direct optimization of the geometry through full wave analysis of the unit cell. This last feature can dramatically increase the computing times of the cost function, which makes it impractical to implement in evolutionary algorithms such as GA or PSO. Some of the improvements in the implementation of the LMA for

reflectarray synthesis can be used in other optimization algorithms, such as BFGS. The resulting framework based on the LMA is able to further optimize previous synthesis performed by other algorithms, or to carry out new ones in a more efficient way, provided a suitable starting point.

This paper is organized as follows. Section II describes how the reflectarray is analyzed to obtain the radiation pattern from the optimization variables, and also presents the approximations considered in the phase-only synthesis case along with their justification. Section III details the algorithm and all the optimizations implemented as well as a description of its parameters and implementation. Section IV shows some results for different synthesis. Finally, Section V has the conclusions.

II. ANALYSIS OF THE REFLECTARRAY

A. Computing co-polar far fields for phase-only synthesis

The scheme of an offset printed reflectarray is shown in Fig. 1. The reflectarray is illuminated by a feed which generates an incident electric field, $\vec{E}_{\text{inc}}$, on the surface of the reflectarray. This field can be expressed for both polarizations as:

$$\vec{E}_{\text{inc}}^{X/Y}(x,y) = E_{\text{inc},x}^{X/Y}(x,y)\hat{x} + E_{\text{inc},y}^{X/Y}(x,y)\hat{y}, \qquad (1)$$

where the superscripts indicate the polarization of the feed and the subscripts the component of the field with regard to the reflectarray coordinate system (E_x^X would be the $\hat{x}$ component of the projected field over the reflectarray surface when the feed radiates in X-polarization). Note that each polarization has, in general, two components of incident field, the desired and the cross-polar, due to the feed not being ideal and the projection of the field over the reflectarray surface. In a similar way, the field reflected on the reflectarray surface can be written as:

$$\vec{E}_{\text{ref}}^{X/Y}(x,y) = E_{\text{ref},x}^{X/Y}(x,y)\hat{x} + E_{\text{ref},y}^{X/Y}(x,y)\hat{y}. \qquad (2)$$

The relation between the incident and reflected fields at each element (m,n) of the reflectarray is given by a matrix of reflection coefficients that characterize that element:

$$\vec{E}_{\text{ref}}^{X/Y}(x_m,y_n) = R^{mn} \cdot \vec{E}_{\text{inc}}^{X/Y}(x_m,y_n), \qquad (3)$$

where

$$R^{mn} = \begin{pmatrix} \rho_{xx}^{mn} & \rho_{xy}^{mn} \\ \rho_{yx}^{mn} & \rho_{yy}^{mn} \end{pmatrix}, \qquad (4)$$

and (x_m,y_n) are the coordinates of the (m,n)th element.

The components of R^{mn} are complex numbers and fully characterize the behaviour of the element. This method of analysis takes into account three sources of cross-polarization: the feed, the projection of the incident field over the reflectarray surface and the reflectarray elements through the use of R^{mn}. However, considering lossless ideal phase shifters instead of real elements, the cross-polarization generated by them is not taken into account and the amplitude of ρ_{xx}^{mn} and ρ_{yy}^{mn} is set to one. Therefore, the synthesis is defined as a phase-only array synthesis where only the co-polar patterns are considered [20]. In this case, the reflected field in the aperture can be expressed as [13]:

$$\begin{aligned} E_{\text{ref},x}^{X}(x_m,y_n) &\approx \rho_{xx}^{mn} \cdot E_{\text{inc},x}^{X}(x_m,y_n), \\ E_{\text{ref},y}^{Y}(x_m,y_n) &\approx \rho_{yy}^{mn} \cdot E_{\text{inc},y}^{Y}(x_m,y_n). \end{aligned} \qquad (5)$$

Once the tangential electric field has been obtained using (5), the co-polar far field can be efficiently computed using the FFT [1], obtaining $\vec{E}_{cp}^{X/Y}(u,v)$, with:

$$u = \sin\theta\cos\varphi \quad ; \quad v = \sin\theta\sin\varphi. \qquad (6)$$

The far field pattern specifications can be given in form of masks with upper and lower bounds [1,9,10], $M_U(u,v)$ and $M_L(u,v)$, which can be defined in the whole UV grid or in the area of interest.

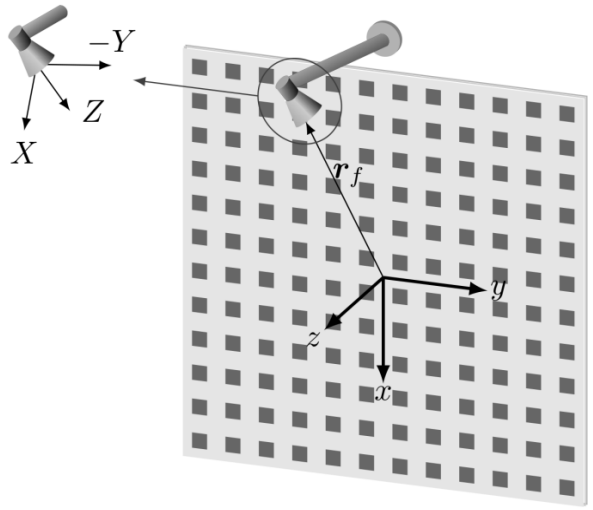

Fig. 1. Geometry of an offset printed reflectarray.

B. Phase-only synthesis considerations

When performing phase-only synthesis, the only variables to be optimized are the phases of the reflection coefficients ρ_{xx}^{mn} and ρ_{yy}^{mn}. The approximations made to obtain the co-polar far field patterns using the tangential field of (5) have proven to be valid in the case of reflectarray antennas [20], providing a co-polar pattern which is very close to the exact one.

Usually, the reflectarray is placed at far field distance of the feed, in which case can be modelled as a $cos^q\,\theta$ function [21], with very accurate results [22,23]. This feed model can also be used in the preliminary steps of the synthesis process and later use full wave simulations of the feed in order to accurately predict the far field [24-26]. However, the co-polar far fields obtained using both methods are very similar between each other. In any case, the algorithm described in the present work allows to use the real incident field from the feed, either by full wave simulations or near field

measurements. The incident field is fixed throughout the synthesis process and only the phase shift that the reflectarray elements have to introduce is optimized in order to obtain the required co-polar pattern.

Due to the simplifications made on the R^{mn} matrix, the cross-polar pattern that could be computed using (5) would not take into account the cross-polarization introduced by the reflectarray elements, which in practise is an important contribution to the cross-polar pattern. As it is explained in detail in [13,20], the co-polar pattern obtained with the simplifications made on the R^{mn} matrix is still accurate. However, the cross-polar pattern is not [13], hence a phase-only synthesis only deals with co-polar requirements.

Once the synthesis is finished and the phases of ρ_{xx}^{mn} and ρ_{yy}^{mn} are obtained, a design can be carried out that takes into account the real element behaviour. By using full wave simulations based on local periodicity [27-29], the full R^{mn} is computed, taking into account mutual coupling between elements. During this step, a zero finding routine is used that calls iteratively a full wave simulator to adjust the required phase shift for each element. Because the synthesized phases are accurately adjusted using this procedure, the resulting phase distribution will have a small error with regard to those obtained after the phase-only synthesis, and hence the co-polar pattern will be very close to the one synthesized.

III. IMPROVED SYNTHESIS BASED ON LMA

A. Cost function definition

In order to use the LMA, a proper cost function to be minimized has to be defined. The same cost function as in [10] will be used, where the residuals are defined as:

$$\begin{aligned} F_t^{X/Y} = C(\vec{r}_t)\Big[&\Big(M_U^2(\vec{r}_t) - \left|E_{\text{cp}}^{X/Y}(\vec{r}_t)\right|^2\Big) \\ &\cdot \Big(M_L^2(\vec{r}_t) - \left|E_{\text{cp}}^{X/Y}(\vec{r}_t)\right|^2\Big) \\ &+ \left|M_U^2(\vec{r}_t) - \left|E_{\text{cp}}^{X/Y}(\vec{r}_t)\right|^2\right| \\ &\cdot \left|M_L^2(\vec{r}_t) - \left|E_{\text{cp}}^{X/Y}(\vec{r}_t)\right|^2\right|\Big], \end{aligned} \tag{7}$$

and thus, the cost function is:

$$F^{X/Y} = \sum_{t=1}^{T} \left(F_t^{X/Y}\right)^2. \tag{8}$$

In (7) and (8), each $t = 1, \dots, T$ describes a $\vec{r}_t = (u, v)_t$ point in which the UV grid is discretized; $C(\vec{r}_t)$ is a weight function; $E_{\text{cp}}^{X/Y}(\vec{r}_t)$ can be either of both co-polar far fields, which are synthesized independently; and $F^{X/Y}$ is the total error, contributed by all the far field samples that lay outside the specified masks. This cost function penalizes the samples that lie outside the specified bounds (upper and lower) while it sets the error to zero when the samples are within bounds. It represents a non-convex search space [30] due to the non-convexity of the lower bound [31] and multiple solutions are possible. There are potentially a large number of solutions with minimum error. If the lower and upper bounds are too confined, the specifications might be too stringent and the algorithm might not find a solution, either because it does not exist or because the starting point is too far off from the solution. In that case, the specifications should be relaxed and/or the antenna optics redefined.

In order to alleviate the notation, from here on a generic F_t will be used, avoiding the superscripts and knowing that it can represent the residual of either of both polarizations (F_t^X or F_t^Y).

B. Jacobian matrix calculation

The LMA requires the calculation of a Jacobian matrix, which is a $T \times P$ matrix, where P is the number of variables to be optimized. Any element (t, p) of the Jacobian is calculated as:

$$J(t,p) = \frac{\partial F_t(\alpha)}{\partial \alpha_t}, \tag{9}$$

where $\alpha = [\alpha_1, \dots, \alpha_P]$ is an array with the optimization variables. Now, Equation (9) can be evaluated analytically, as in [10], as long as the analytical expression of the far field as a function of the optimization variables is provided. In [10], the partial derivatives are obtained deriving the cost function with respect to the tangent of the phases. However, in this work derivation is done with respect to the phases themselves, improving the performance of the algorithm greatly by making it converge faster, as it will be shown later.

In the case where the analytical expressions cannot be used, the derivative can be calculated using finite differences of the form [14]:

$$\frac{\partial F_t(\alpha)}{\partial \alpha_p} \approx \frac{F_t(\alpha + he_p) - F_t(\alpha - he_p)}{2h}, \tag{10}$$

where h is a small positive scalar and e_p is the pth unit vector. Because the evaluation of the cost function (8) can be computationally expensive, a one-sided-difference can be used instead of the central difference of (10) in order to reduce by half the number of evaluations required. Also, a proper choice of h can minimize the error of the evaluation of the derivative in (10). For the central difference the optimum choice of h [14] is:

$$h = \sqrt[3]{u_r}, \tag{11}$$

with u_r being the unit roundoff, whose value will depend on the precision of the real numbers used in the implementation of the algorithm. The optimum choice for a lateral difference would be the value $h = \sqrt{u_r}$. Note that, for the central difference there is an error of $O(h^2)$, while for the lateral one, the error is $O(h)$. Since $h \in (0, 1)$, the error will be lower for the central difference, although the evaluation of the derivative will be twice as

expensive, in time consuming terms.

An important point to consider when computing the Jacobian matrix is the fact that the columns of J are independent from each other because the derivatives are calculated with respect to one variable. Hence, the evaluation of the Jacobian can be fully parallelized by means of OpenMP [32], computing one column per available thread. Furthermore, each column can be obtained by just two calls to the cost function when the central difference is used (one call for the lateral difference). Also, the far field is computed efficiently by means of the FFT, and only one FFT is needed per cost function call. This way, one of the most time-consuming operations of the algorithm is performed efficiently and will scale well with the number of available processors, allowing the optimization of large problems.

C. Solving the matrix equation

Once the Jacobian matrix is calculated, the LMA can be applied iteratively as:

$$[J_i^T \cdot J_i + \mu_i \cdot \mathrm{diag}(J_i^T \cdot J_i)] \cdot \delta_i = -J_i^T \cdot F_{t,i}, \qquad (12)$$

which can be compactly written as:

$$A_i \cdot \delta_i = b_i. \qquad (13)$$

In (12), the subindex i represents the current iteration, $\mathrm{diag}(\cdot)$ is the diagonal matrix, δ_i is the updating vector which satisfies the equality and μ_i is a real positive number. The choice of $\mathrm{diag}(J_i^T \cdot J_i)$ instead of any other positive diagonal matrix, such as the identity, is to reduce the effects of poor scaling in the optimization variables by using an ellipsoidal trust region. This way, the algorithm is invariant under diagonal scaling of the components of α [14].

The matrix multiplication $J_i^T \cdot J_i$ and other matrix-vector operations can be computationally very expensive if the dimension is large. Nevertheless, these operations can be performed by routines from libraries such as OpenBLAS [33] or MKL [34], which take advantage of highly optimized and fully parallelized algorithms and low-level hardware operations in order to improve their performance and computing times. Also, since the resulting matrix is symmetric, only the upper or lower triangular part of it can be computed, further reducing computing times.

In [10], (13) is solved by forming its normal equation applying the Conjugate Gradient Squared (CGS) method. This is unnecessary because (13) is already a square matrix system, and the CGS additionally solves another system of normal equations, thus squaring the condition number of matrix A_i, which can lead to poor convergence of the CGS depending on the initial Jacobian matrix.

Nevertheless, because A_i is at least positive semi-definite, a Cholesky factorization based solver can be used [35], which is the fastest exact solver for this type of problems [36] since it takes advantage of the symmetric nature of the matrix. Compared with other methods, the Cholesky factorization involves $P^3/3$ floating-point operations, while LU takes $2P^3/3$ and SVD $12P^3$ [36]. Although SVD is more robust, in this case the Cholesky factorization is enough, being 26 times faster than SVD and twice as fast as LU.

After the matrix system is solved, the solution is updated as:

$$\alpha_{i+1} = \alpha_i + \delta_i. \qquad (14)$$

D. Choice of μ_0

The parameter μ in (12) is used to control the convergence of the algorithm. It controls the behaviour of the algorithm ranging from the steepest descent when $\mu \to \infty$ and the Gauss-Newton method when $\mu = 0$ [15]. A small value of μ when the current solution is not near the minimum may cause the algorithm to diverge. Hence, it is recommended to start with a high value of μ and decrease it as the error diminishes. Conversely, if the error increases, it could be necessary to increase the value of μ to control the algorithm and prevent it from diverging to non-desired solutions. A new real parameter $\beta > 1$ is defined to control μ. If the last k_d iterations have decreased the error, μ is updated as $\mu_{i+1} = \mu_i/\beta$. On the other hand, if the last k_i iterations have increased the error, μ is updated as $\mu_{i+1} = \mu_i\beta$. If neither of both conditions are fulfilled, μ remains the same.

Parameters β, k_d and k_i are artificially introduced in the algorithm in order to control μ. On the one hand, β controls how fast μ is decreased when the error diminishes and vice versa. A high value of β causes μ to decrease initially very fast, and could lead the algorithm to diverge, hence rapidly increasing the value of μ. These swings in μ can cause the algorithm to either diverge or converge to non-desired local minima. A low value of β (close to 1) causes the algorithm to converge slowly, specially when μ is high. It has been found that values of β between 1.05 and 1.5 provide a good trade-off for a good rate of convergence while keeping the algorithm from diverging. On the other hand, k_d and k_i control how tolerant the algorithm is to changes in μ when the error oscillates. When the algorithm reaches a flat valley in the search space, the error might behave irregularly due to the low gradient of the hypersurface around the current position. In order to control μ in this situation, k_d and k_i come into play, having complementary roles. If the error starts decreasing, k_d prevents μ from decreasing too much if previously the error had increased. This tries to prevent the algorithm from diverging because it ensures that μ remains constant until the error decreases k_d consecutive iterations. Conversely, the error has to increase during k_i consecutive iterations in order to increase μ. This prevents μ from increasing too much making the converge slower once the error begins to decrease again. Some reasonable values for these two parameters are within the range from 2 to 5.

However, the problem of choosing μ_0 remains. Nevertheless, there is a suitable strategy to choose it. The optimization variables are the reflection coefficient phases. Hence, in order to have a reliable design, the phase distribution should be as smooth as possible, because that way, the physical dimensions of the elements of the reflectarray would vary smoothly from one element to the next (which is necessary because the reflectarray analysis is based on a full-wave analysis assuming local periodicity [1,26-29]). Following this, μ_0 should be high enough to allow the phase at the initial iterations to vary smoothly and not to make jumps to valleys of the search space with noisy phase distributions. Due to the dimensionality of the problem being P (usually of the order of hundreds or thousands of optimization variables, at least one per element of the reflectarray), it is very easy to make false steps into non-desired solutions during the first iterations of the algorithm from which it will be virtually impossible to escape. For that reason a high value of μ_0, about the same order of magnitude of P (for instance, between $0.5P$ and $5P$), is a good choice.

E. Starting point

Another important issue is the starting point for the optimization process, which has been widely discussed in the literature [9,20]. As the LMA is a local optimizer, the starting point is of the utmost importance, since it will determine if the achieved solution is good enough. It has been determined [20] that a good initial point is that of a pencil beam pattern properly focused. Also, a pencil beam pattern can provide a smooth enough initial phase distribution in the center of the reflectarray, where the field amplitude is higher [1], depending on the placing of the feed antenna.

F. Seeking the correct solution

In the previous sections, different aspects of the algorithm have been discussed that can prevent it from converging to a solution. First, the specifications should be reasonable; i.e., not too stringent, to allow the algorithm to converge from the first iteration. Also, the starting point should be good enough and μ_0 high to ensure a soft descend towards the solution. In practise, the final solution should not only have a low error, but also a smooth phase distribution. With regard to having a low error, it means that the co-polar pattern is close to meet the specifications, which is the main goal of the synthesis. However, a smooth phase distribution is also needed for a real reliable design. Due to the local periodicity assumption when analysing the reflectarray unit cell [1], the design will perform better when the physical size of the reflectarray elements will vary smoothly across the surface of the antenna. The smoothness of the phase distribution is more critical in the centre of the reflectarray were the illumination level is higher.

G. Numerical implementation

A homemade version of the algorithm including all the described optimizations has been implemented in Fortran using the Intel Fortran Compiler and MKL library [34]. Double precision is used for real numbers, which implies a unit roundoff of:

$$u_r = 2.22\ldots \cdot 10^{-16}. \tag{15}$$

This means that the error for the lateral difference would be of the order of $O(10^{-8})$, while for the central difference would be $O(10^{-11})$. The difference between both errors is not as impressive due to the optimum choice of h to minimize the error in the derivative taking into account errors produced in floating-point arithmetic [14]. Since the rest of the operations are performed in double precision, the error in the evaluation of the Jacobian will propagate and will be the limiting factor in the minimum achievable error. However, since a phase-only synthesis is done, the evaluation of the cost function is fast, and the central difference is used in the optimization.

IV. VALIDATION

A. Antenna specifications

An outline of the reflectarray is shown in Fig. 1. It consists of a planar rectangular reflectarray with dual linear polarization formed by 900 elements (30×30) and a feed horn modelled as a $\cos^{\mathrm{q}}\theta$ function with a q-factor of 37, which produces an illumination taper of -19.5 dB on the surface of the reflectarray. The feed horn points to the centre of the reflectarray and its phase centre is placed at $\vec{r}_f = (-94, 0, 214)$ mm with regard to the centre of the reflectarray. The working frequency is 25.5 GHz and the periodicity of the elements is $5.84\ \text{mm} \times 5.84\ \text{mm}$, which is approximately half a wavelength [37]. Also, the far fields are discretized in a 128×128 UV grid, being $T = 16384$. Note that, according to Fig. 1, the X-polarization corresponds to the vertical polarization (V) because the electric field in $\hat{x}$-direction is vertical, while Y-polarization corresponds to the horizontal polarization (H).

The chosen pattern is a LMDS, which presents a 30º-sector beam in azimuth and a square cosecant beam in elevation [13]. Templates in the main cuts will be presented along with the results of the optimization in the next section.

B. Optimization of previous synthesis

In order to test the described procedure, a synthesis for a LMDS pattern was carried out. The first example uses as a starting point the final result of [13] for both polarizations. This constitutes an excellent initial radiation pattern since it is very close to the final specification. The geometry of the antenna is the same as in [37], with

the LMA parameters set to $\mu_0 = 1800, \beta = 1.05, k_d = 3$, $k_i = 2$ and $C(\vec{r}_t) = 1$. The initial error is 2.99 and 2.95 for vertical and horizontal polarizations, according to (8). The convergence is very similar for both polarizations. In the case of vertical polarization, after 500 iterations of the LMA, the error was 7.8×10^{-10}. The algorithm was left to complete 999 iterations. However, after iteration 500, approximately, it stagnates. The lowest error was 5.57×10^{-10} at iteration 990. For the horizontal polarization, the lowest error was 3.78×10^{-10} at iteration 995, stagnating around iteration 650.

The simulated radiation pattern for vertical polarization is shown in Fig. 2. The main cuts for horizontal polarization are shown in Fig. 3 along with the results of [13]. With a global error of the order of 10^{-10}, the radiated fields fit very well to the masks, improving back lobes and the coverage zone with regard to [13] while maintaining a similar shape of the synthesized phases, which are shown in Fig. 4.

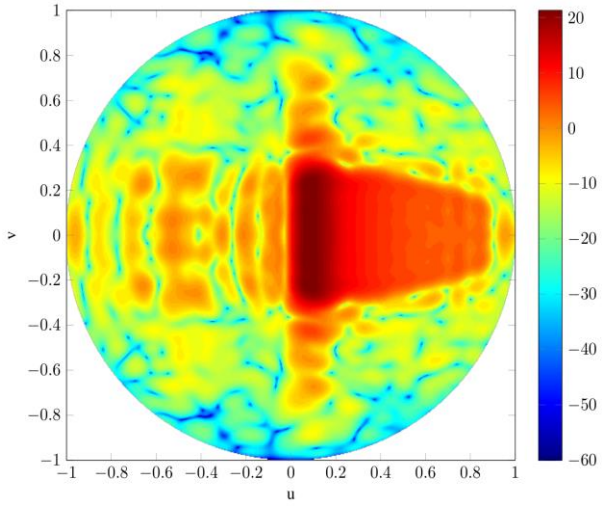

Fig. 2. Three dimensional synthesized radiation pattern in directivity (dB) for vertical polarization.

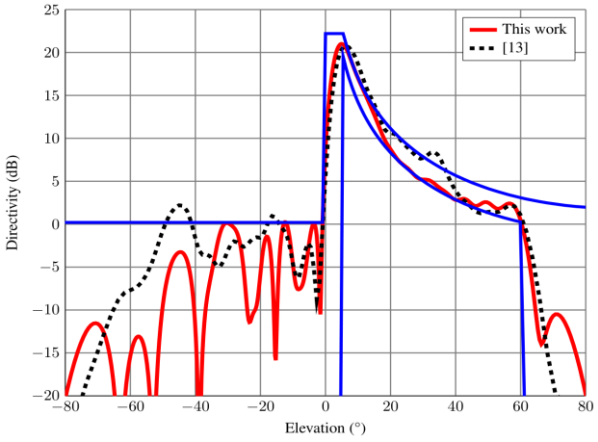

(a)

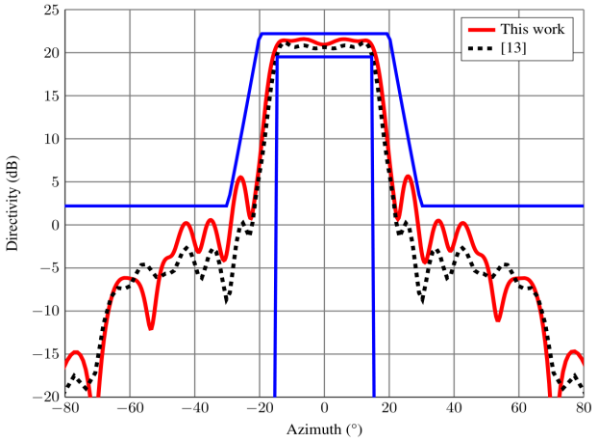

(b)

Fig. 3. Radiation pattern of the synthesized reflectarray considering an ideal model of the feed horn in dual polarization. Main cuts for horizontal polarization in (a) elevation and (b) azimuth.

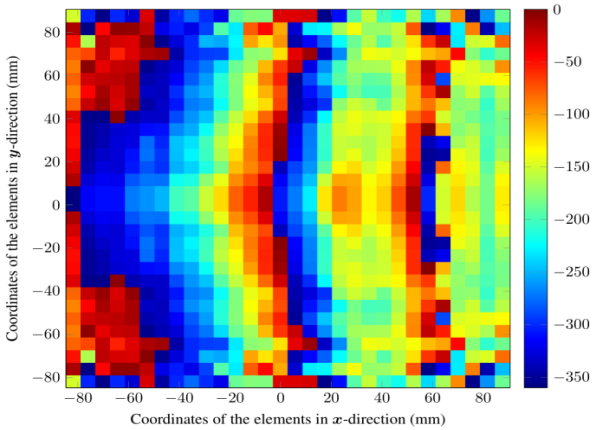

Fig. 4. Synthesized phase distribution of the reflection coefficient for the vertical polarization (degrees).

C. Synthesis with a pencil beam as starting point

In order to compare more faithfully the results with [10], a new synthesis was carried out employing the same initial point; i.e., the phases of a pencil beam pattern pointing to $(\theta, \varphi) = (5.4°, 0.0°)$, which corresponds to the area of maximum directivity in the masks. The LMA parameters for this case were $\mu_0 = 500, \beta = 1.1, k_d = 3$, $k_i = 2$ and $C(\vec{r}_t) = 1$. First, the H-polarization was synthesized from the phase distribution of the pencil beam. The initial error was 53.00 and after the iteration 450 (where the error was 5.05×10^{-7}) it stagnates. The lowest error achieved was 3.87×10^{-7} at iteration 998, out of 999. After the synthesis of the H-polarization, the V-polarization was synthesized starting with the synthesized phases of the H-polarization. This resulted in an initial error of 7.03×10^{-3} because the pattern is closer to the masks than the pencil beam, although higher

than the final error for the H-polarization because the incident field is different for both polarizations. The lowest error achieved was 2.97×10^{-9} at iteration 471. As comparison, the final error in [10] is 5.60×10^{-3}, which is several orders of magnitude higher than the error obtained in this work.

Figure 5 shows the main cuts for the horizontal polarization of the new synthesized radiation pattern. Because the starting point is not as good as in the previous case, the final pattern obtained now is slightly worse, although it greatly improves the results of [10]. In particular, the back lobes are reduced by about 6 dB and the coverage zone improves for large angles. Also, the results were obtained in less iterations (less than 500 vs. 3900, for each polarization) and with a final error several orders of magnitude lower, which accounts for the better results in the radiation patterns. Finally, Fig. 6 shows the synthesized phase distribution when using a pencil beam pattern as starting point.

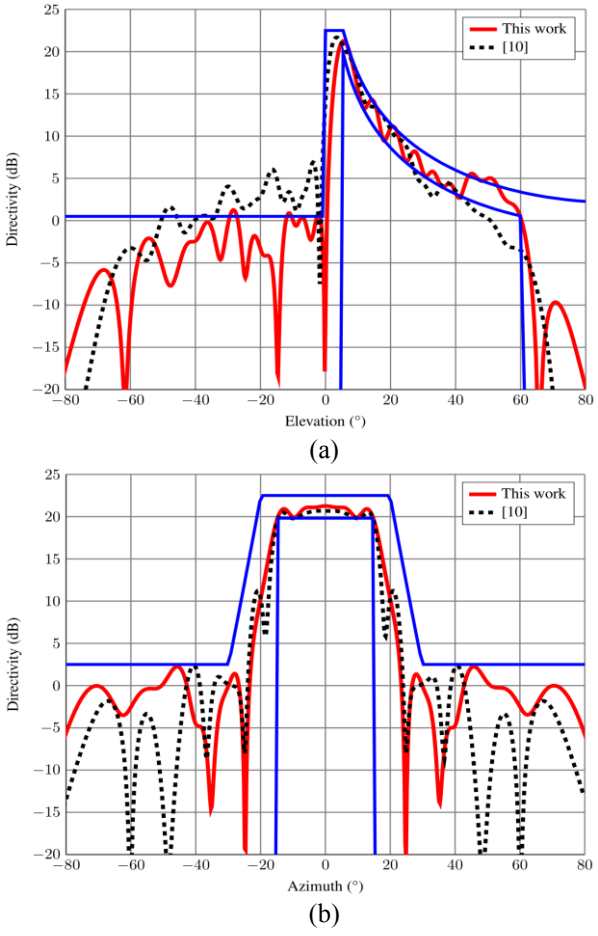

Fig. 5. Radiation pattern of the synthesized reflectarray considering an ideal model of the feed horn in dual polarization with starting point a pencil beam pattern. Main cuts for horizontal polarization in (a) elevation and (b) azimuth.

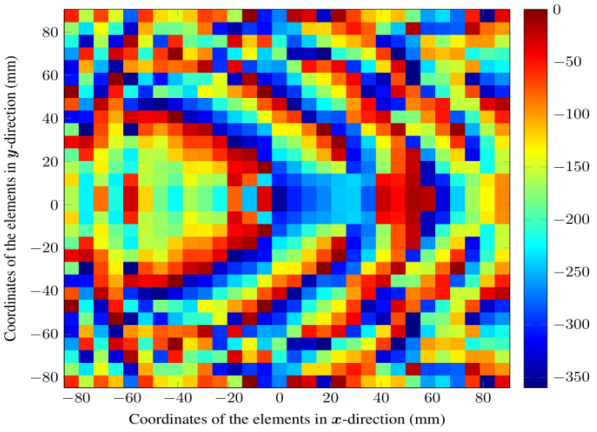

Fig. 6. Synthesized phase distribution of the reflection coefficient for the vertical polarization using a pencil beam as starting point (degrees).

D. Improvements in computing times

With the optimizations detailed in previous sections, the computing times were greatly reduced. In [10], it is reported that each iteration takes less than a minute. Here, each iteration takes about 5.7 seconds using the same computer (Intel Core 2 Duo with a 2.4 GHz processor), which along with the improved convergence of the LMA, reduces significantly the computing times of the synthesis process. The time for each iteration is reduced approximately by a factor of 10. Moreover, taking into account that the synthesis process took less than 500 iterations for each polarization (about eight times faster), the overall improvement in computing times is by a factor of 80.

V. CONCLUSION

An improved phase-only synthesis for reflectarrays based on the Levenberg-Marquardt algorithm with an ellipsoidal trust region has been developed, improving the accuracy and efficiency with regard to other works in the literature. By optimizing each building block of the algorithm, a great computational efficiency is achieved that will allow for more powerful synthesis techniques implemented with the same algorithm. For instance, it will be possible to implement a direct optimization of the geometry of the reflectarray through full wave analysis of the reflectarray unit cell [27-29] within reasonable computing times.

In particular, the Jacobian matrix is obtained through finite differences which allows to avoid using the analytical expressions for complex problems. By choosing the appropriate value of the increment in the finite difference equation, the error evaluating the derivative is minimized. Also, the columns of the Jacobian can be computed independently from each other, which allows to fully parallelize its evaluation. By deriving with respect to the reflection coefficient phases instead

of the tangent of the phases, the convergence of the algorithm is improved.

Further improvements were made regarding the choice of the solver for the equation system, where a Cholesky factorization based solver was selected to take advantage of the symmetry of the resulting matrix. Also, computationally expensive operations such as matrix and matrix-vector multiplications were performed using highly optimized and parallelized routines. Since the result of the matrix multiplication is symmetric, only the lower or upper triangular part needs to be computed.

In addition, due to the intrinsic high dimensionality of the problem, a few guidelines have been laid out in order to control the evolution of the synthesis, which allows for a better control of the obtained solution. In particular, it has been shown how the initial point of the synthesis is a key factor in a local search optimizer such as the LMA. Also, a suitable choice of the parameters of the LMA is important in order to control the speed of convergence as well as the initial evolution of the algorithm, which can determine the path to a good or bad solution.

Finally, two test cases of a LMDS pattern were shown to validate the proposed solution. The performance of the algorithm has proven to be better than others in the literature. The results are more accurate, reducing back lobes and better controlling the coverage zone, while reducing the computing times by a factor of 80.

ACKNOWLEDGMENT

This work was supported in part by the European Space Agency (ESA) under contract ESTEC/AO/1-7064/12/NL/MH; by the Ministerio de Economía y Competitividad, under project TEC2014-54005-P (MIRIIEM); by the Gobierno del Principado de Asturias/FEDER under project GRUPIN14-114 and under grant BP12-063; and contract FUO-EM-151-09.

REFERENCES

[1] J. Huang and J. A. Encinar, *Reflectarray Antennas*, John Wiley & Sons, 2008.

[2] M. Arrebola, E. Carrasco, and J. A. Encinar, "Beam scanning antenna using a reflectarray as sub-reflector," *Appl. Comp. Electro. Society (ACES) Journal*, vol. 26, no. 6, pp. 473-483, Jun. 2011.

[3] B. Devireddy, A. Yu, F. Yang, and A. Z. Elsherbeni, "Gain and bandwidth limitations of reflectarrays," *Appl. Comp. Electro. Society (ACES) Journal*, vol. 26, no. 2, pp. 170-178, Feb. 2011.

[4] J. A. Encinar and J. A. Zornoza, "Broadband design of three-layer printed reflectarrays," *IEEE Trans. Antennas Propag.*, vol. 51, no. 7, pp. 1662-1664, Jul. 2003.

[5] S. H. Yusop, N. Misran, M. T. Islam, and M. Y. Ismail, "Design of high performance dual frequency concentric split ring square element for broadband reflectarray antenna," *Appl. Comp. Electro. Society (ACES) Journal*, vol. 27, no. 4, pp. 334-339, Apr. 2012.

[6] P. M. Woodward, "A method of calculating the field over a plane aperture required to produce a given polar diagram," *J. Inst. Elec. Eng.*, vol. 93, pt. III, no. 10, pp. 1554-1558, 1946.

[7] J. Perini and M. Idselis, "Note on antenna patterns synthesis using numerical iterative methods," *IEEE Trans. Antennas Propag.*, vol. 19, no. 2, pp. 284-286, Mar. 1971.

[8] T. S. Fong and R. A. Birgenheier, "Method of conjugate gradients for antenna pattern synthesis," *Radio Sci.*, vol. 6, no. 12, pp. 1123-1130, Dec. 1971.

[9] O. M. Bucci, G. Franceschetti, G. Mazzarella, and G. Panariello, "Intersection approach to array pattern synthesis," *IEE Proc. Microw. Antennas Propag.*, vol. 137, no. 6, pp. 349-357, Dec. 1990.

[10] J. Álvarez, M. Arrebola, R. G. Ayestarán, and F. Las-Heras, "Systematic framework for reflectarray synthesis based on phase optimization," *Int. J. Antennas Propag.*, vol. 2012, pp. 1-9, Jun. 2012.

[11] J. M. Johnson and Y. Rahmat-Samii, "Genetic algorithm optimization and its application to antenna design," in *Antennas and Propagation Society International Symposium, 1994. AP-S. Digest*, vol. 1, pp. 326-329, Jun. 1994.

[12] P. Nayeri, F. Yang, and A. Z. Elsherbeni, "Design of single-feed reflectarray antennas with asymmetric multiple beams using the particle swarm optimization method," *IEEE Trans. Antennas Propag.*, vol. 61, no. 9, pp. 4598-4605, Sep. 2013.

[13] M. Arrebola, J. A. Encinar, and M. Barba, "Multifed printed reflectarray with three simultaneous shaped beams for LMDS central station antenna," *IEEE Trans. Antennas Propag.*, vol. 56, no. 6, pp. 1518-1527, Jun. 2008.

[14] J. Nocedal and S. J. Wright, *Numerical Optimization*, 2nd ed., Springer, 2006.

[15] G. A. F. Seber and C. J. Wild, *Nonlinear Regression*, John Wiley & Sons, 2003.

[16] O. M. Bucci, G. D'Elia, G. Mazzarella, and G. Panariello, "Antenna pattern synthesis: a new general approach," *Proc. IEEE*, vol. 82, no. 3, pp. 358-371, Mar. 1994.

[17] O. M. Bucci, G. D'Elia, and G. Romito, "Power synthesis of conformal arrays by a generalized projection method," *IEE Proc. Microw. Antennas Propag.*, vol. 142, no. 6, pp. 467-471, Dec. 1995.

[18] D. W. Boeringer and D. H. Werner, "Particle swarm optimization versus genetic algorithms for phased arrays synthesis," *IEEE Trans. Antennas Propag.*, vol. 52, no. 3, pp. 771-779, Mar. 2004.

[19] I. Lopez, J. R. Pérez, and J. Basterrechea, "An approach for the design of reflectarrays using CG-FFT and PSO," in *Proceedings of the Fourth*

European Conference on Antennas and Propagation (EuCAP), Barcelona, Spain, pp. 1-5, Apr. 12-16, 2010.

[20] J. A. Zornoza and J. A. Encinar, "Efficient phase-only synthesis of contoured-beam patterns for very large reflectarrays," *Int. J. RF Microw. Comput. Eng.*, vol. 14, no. 5, pp. 415-423, Sep. 2004.

[21] Y.-T. Lo and S.-W. Lee, Eds., *Antenna Handbook Vol. 1*, Van Nostrand Reinhold, 1993.

[22] J. A. Encinar, L. S. Datashvili, J. A. Zornoza, M. Arrebola, M. Sierra-Castaner, J. L. Besada-Sanmartin, H. Baier, and H. Legay, "Dual-polarization dual-coverage reflectarray for space applications," *IEEE Trans. Antennas Propag.*, vol. 54, no. 10, pp. 2827-2837, Oct. 2006.

[23] J. A. Encinar and M. Barba, "Design, manufacture and test of a Ka-band reflectarray antenna for transmitting and receiving in orthogonal polarization," in *14th International Symposium on Antenna Technology and Applied Electromagnetics (ANTEM) and the American Electromagnetics Conference (AMEREM)*, Ottawa, Canada, pp. 1-4, Jul. 5-8, 2010.

[24] J. A. Encinar, M. Arrebola, L. F. de la Fuente, and G. Toso, "A transmit-receive reflectarray antenna for direct broadcast satellite applications," *IEEE Trans. Antennas Propag.*, vol. 59, no. 9, pp. 3255-3264, Sep. 2011.

[25] R. Florencio, J. Encinar, R. R. Boix, and G. Perez-Palomino, "Dual-polarisation reflectarray made of cells with two ortogonal sets of parallel dipoles for bandwidth and cross-polarisation improvement," *IET Microw. Antennas Propag.*, pp. 1-9, Aug. 2014.

[26] P. Nayeri, A. Z. Elsherbeni, and F. Yang, "Design, full-wave analysis, and near-field diagnostics of reflectarray antennas," *Appl. Comp. Electro. Society (ACES) Journal*, vol. 28, no. 4, pp. 284-292, Apr. 2013.

[27] C. Wan and J. A. Encinar, "Efficient computation of generalized scattering matrix for analyzing multilayered periodic structures," *IEEE Trans. Antennas Propag.*, vol. 43, no. 11, pp. 1233-1242, Nov. 1995.

[28] R. Florencio, R. R. Boix, and J. A. Encinar, "Enhanced MoM analysis of the scattering by periodic strip gratings in multilayered substrates," *IEEE Trans. Antennas Propag.*, vol. 61, no. 10, pp. 5088-5099, Oct. 2013.

[29] D. M. Pozar and T. A. Metzler, "Analysis of a reflectarray antenna using microstrip patches of variable size," *Electron. Lett.*, vol. 29, no. 8, pp. 657-658, Apr. 1993.

[30] J. Álvarez, R. G. Ayestarán, G. León, L. F. Herrán, A. Arboleya, J. A. López-Fernández, and F. Las-Heras, "Near field multifocusing on antenna arrays via non-convex optimisation," *IET Microw. Antennas Propag.*, vol. 8, no. 10, pp. 754-764, Jul. 2014.

[31] S. E. Nai, W. Ser, Z.-L. Yu, and H. Chen, "Beampattern synthesis for linear and planar arrays with antenna selection by convex optimization," *IEEE Trans. Antennas Propag.*, vol. 58, no. 12, pp. 3923-3930, Dec. 2010.

[32] M. Sato, "OpenMP: parallel programming API for shared memory multiprocessors and on-chip multi-processors," in *15th International Symposium on System Synthesis*, Kyoto, Japan, pp. 109-111, Oct. 2-4, 2002.

[33] Z. Xianyi, W. Qian, and Z. Yunquan, "Model-driven level 3 BLAS performance optimization on Loongson 3a processor," in *IEEE 18th International Conference on Parallel and Distributed Systems (ICPADS)*, Singapore, pp. 684-691, Dec. 17-19, 2012.

[34] *Intel® Math Kernel Library Reference Manual*, Intel Corporation, Aug. 2008.

[35] R. A. Horn and C. R. Johnson, *Matrix Analysis*, 2nd ed., Cambridge University Press, 2013.

[36] G. H. Golub and C. F. V. Loan, *Matrix Computations*, 4th ed., The Johns Hopkins University Press 2013.

[37] M. Arrebola, Y. Álvarez, J. A. Encinar, and F. Las-Heras, "Accurate analysis of printed reflectarrays considering the near field of the primary feed," *IET Microw. Antennas Propag.*, vol. 3, no. 2, pp. 187-194, Mar. 2009.

Modeling of Anisotropic Magnetic Objects by Volume Integral Equation Methods

Lin E. Sun [1] and Weng C. Chew [2]

[1] Department of Electrical and Computer Engineering
Youngstown State University, Youngstown, OH 44512, USA
lsun@ysu.edu

[2] Department of Electrical and Computer Engineering
University of Illinois at Urbana-Champaign, Urbana, IL 61801, USA
w-chew@uiuc.edu

Abstract ─ This paper presents the modeling of electromagnetic scattering from objects with magnetic anisotropy. We study the solutions of both the volume integral equation (VIE) method and augmented volume integral equation (A-VIE) method. For the VIE method, it is built from the 3D vector wave equation for electric field only. For the A-VIE method, it is built from 3D vector wave equation for both electric and magnetic fields. Numerical results show that the A-VIE method has better accuracy and convergence for magnetic objects compared to the VIE method.

Index Terms ─ Anisotropic magnetics, augmented volume integral equation (A-VIE), method of moments, volume integral equation (VIE).

I. INTRODUCTION

The solution of electromagnetic wave scattering and propagation problems from penetrable objects has always been an active research area. In early years, approximate methods such as the geometrical theory of diffraction were used [1]. The extended boundary condition method was also investigated as a possible approach to solve such problems [2]. More recently, numerical methods have been adopted to tackle it such as finite difference method [3], finite element method [4], generalized multipole method [5] and method of moments [6-7]. Among them, method of moments equipped with modern computing power and fast algorithms provides an accurate and efficient numerical method for solving the scattering problems. There are two main categories of moment methods for penetrable objects. One is the surface integral equation based method, in which the unknown parameters are defined on the surfaces of the objects [8-9] and it is efficient in solving problems with piecewise homogenous properties. The other is the volume integral equation based method [10-12], which can solve the scattering problems from highly inhomogeneous scatterers.

Early research in analyzing wave scattering and propagation from penetrable objects mainly focuses on objects with isotropic material properties. With the revolution and development of new materials and technologies, modeling of 3D objects with generalized anisotropy has become of great interest in research. The applications of anisotropic materials cover a wide range from electromagnetic and optical design to geophysical exploration. In oil and gas exploration, with the development of highly deviated and horizontal drilling technology, formation anisotropy has become an important concern. Without consideration of the anisotropy effect in the modeling and inverse algorithms, it is difficult to interpret the measurements from modern logging tools. On the other hand, the incorporation of metamaterials and artificial materials in the electromagnetic and optical device design, induces a great need for the accurate and efficient electromagnetic solvers to model generalized anisotropic materials. In recent years, various volume integral equation methods have been proposed to solve scattering problems for anisotropic materials [13-18]. Analytical solutions for simple structures such as anisotropic spheres or spherical shells have been investigated in [20-21]. Most of these methods mainly focus on modeling of uniaxially anisotropic objects and the investigations mainly focus on dielectrics. Investigations for generalized anisotropic materials, especially anisotropic magnetics are still limited.

In this paper, the VIE method and A-VIE method with curl-conforming bases are applied to model the scattered fields of magnetic objects. The contributions of this work are twofold: i) convergence studies of the VIE method and A-VIE method for magnetic objects are presented; ii) it is demonstrated that the A-VIE method has better convergence and accuracy for magnetic objects.

Submitted On: August 1, 2014
Accepted On: September 20, 2015

II. VIE AND A-VIE METHODS

Consider a 3D inhomogeneous and anisotropic object in free space with relative permittivity and permeability $\bar{\epsilon}_r(\mathbf{r})$ and $\bar{\mu}_r(\mathbf{r})$. The volume of the anisotropic object is denoted as V and it is enclosed by the surface S. We assume that the object is excited by an incident plane wave characterized by ($\mathbf{E}^{inc}(\mathbf{r})$, $\mathbf{H}^{inc}(\mathbf{r})$).

To solve the scattered field of the anisotropic object, a VIE method built from the 3D vector wave equation has been introduced in [16]. It is derived from the 3D vector wave equation for the electric field given by:

$$\nabla\times\bar{\mu}_r^{-1}\cdot\nabla\times\mathbf{E}(\mathbf{r})-\omega^2\bar{\epsilon}_r(\mathbf{r})\cdot\mu_0\epsilon_0\mathbf{E}(\mathbf{r})=i\omega\mu_0\mathbf{J}(\mathbf{r}). \quad (1)$$

Here, $\mathbf{J}(\mathbf{r})$ is the current that produces the incident field, $\mathbf{E}(\mathbf{r})$ is the total electric field, $\bar{\epsilon}_r(\mathbf{r})$ and $\bar{\mu}_r(\mathbf{r})$ are the relative permittivity and permeability tensors, ϵ_0 and μ_0 are the permittivity and permeability of free space.

From the equation above and the definition for dyadic Green's function, we can get the volume integral equation:

$$\begin{aligned}\mathbf{E}(\mathbf{r})&=\mathbf{E}^{inc}(\mathbf{r})\\&+\nabla\times\int_{V+}g(\mathbf{r},\mathbf{r}')\left[\bar{\mathbf{I}}-\bar{\mu}_r^{-1}(\mathbf{r}')\right]\cdot\nabla'\times\mathbf{E}(\mathbf{r}')d\mathbf{r}' \quad (2)\\&-k_0^2\int_{V+}\bar{\mathrm{G}}(\mathbf{r},\mathbf{r}')\cdot\left[\bar{\mathbf{I}}-\bar{\epsilon}_r(\mathbf{r}')\right]\cdot\mathbf{E}(\mathbf{r}')d\mathbf{r}'.\end{aligned}$$

Here, V^+ represents the volume that is slightly larger than the volume of the object V, $\bar{\mathrm{G}}(\mathbf{r},\mathbf{r}')$ is the dyadic Green's function for the unbounded and homogeneous media. It is a 3 by 3 matrix given by:

$$\bar{\mathrm{G}}(\mathbf{r},\mathbf{r}')=\left(\bar{\mathbf{I}}+\frac{\nabla\nabla}{k_0^2}\right)g(\mathbf{r},\mathbf{r}'), \quad (3)$$

or

$$\bar{\mathrm{G}}(\mathbf{r},\mathbf{r}')=\frac{1}{k_0^2}\left[\nabla\times\nabla\times\bar{\mathbf{I}}g(\mathbf{r},\mathbf{r}')-\bar{\mathbf{I}}\delta(\mathbf{r},\mathbf{r}')\right], \quad (4)$$

where $g(\mathbf{r},\mathbf{r}')$ is the scalar Green's function, k_0 is the wave number in free space.

By substituting the definitions of the dyadic Green's function into (2), we can get two sets of volume integral equations [16]. Then by discretizing the volume object using a sum of tetrahedra and expanding the total electric field $\mathbf{E}(\mathbf{r})$ using the edge basis on each edge of the tetrahedron, the volume integral equation can be converted into the discrete form. Using the Galerkin's method, we can convert the discretized volume integral equation to a linear matrix equation. By solving this equation using the iterative method, the total electric field in the whole solution domain can be obtained.

The VIE method presented in [16] serves as an efficient method to model the scattering problem of generalized anisotropic materials. However, further study shows that due to the curl operator acting on the electric field in (2), the permeability term is not represented as well as the permittivity term. In order to overcome this, we use the similar idea for the augmented EFIE (A-EFIE) method [19] and apply it to the VIE method. In A-VIE, the magnetic field unknowns are added to the original VIE method that is based on the electric field. Hence, the permeability term are better represented compared to the original VIE method. Next, the A-VIE formulations are introduced [17]. First, by substituting Faraday's law into (2), we get:

$$\begin{aligned}-\mathbf{E}^{inc}(\mathbf{r})&=-\mathbf{E}(\mathbf{r})\\&+ik_0\nabla\times\int_{V+}g(\mathbf{r},\mathbf{r}')\left[\bar{\mu}_r(\mathbf{r}')-\bar{\mathbf{I}}\right]\cdot\mathbf{H}(\mathbf{r}')d\mathbf{r}' \quad (5)\\&-k_0^2\int_{V+}\bar{\mathrm{G}}(\mathbf{r},\mathbf{r}')\cdot\left[\bar{\mathbf{I}}-\bar{\epsilon}_r(\mathbf{r}')\right]\cdot\mathbf{E}(\mathbf{r}')d\mathbf{r}'.\end{aligned}$$

And using the duality principle, we get a dual equation for (5):

$$\begin{aligned}-\eta_0\mathbf{H}^{inc}(\mathbf{r})&=-\eta_0\mathbf{H}(\mathbf{r})\\&-ik_0\nabla\times\int_{V+}g(\mathbf{r},\mathbf{r}')\left[\bar{\epsilon}_r(\mathbf{r}')-\bar{\mathbf{I}}\right]\cdot\mathbf{E}(\mathbf{r}')d\mathbf{r}' \quad (6)\\&-k_0^2\int_{V+}\bar{\mathrm{G}}(\mathbf{r},\mathbf{r}')\cdot\left[\bar{\mathbf{I}}-\bar{\mu}_r(\mathbf{r}')\right]\cdot\eta_0\mathbf{H}(\mathbf{r}')d\mathbf{r}'.\end{aligned}$$

We see that in (5) and (6), the curl operator acting on the electric field is removed and replaced by the magnetic field in the solution domain. Here, η_0 is used as a normalization factor for the magnetic field, it is the intrinsic impedance of free space.

To solve the A-VIE in (5) and (6) by the moment method, we need to convert it into a set of linear algebraic equations. First we expand the electric field $\mathbf{E}(\mathbf{r})$ and magnetic field $\mathbf{H}(\mathbf{r})$ into discretized forms using the edge bases:

$$\mathbf{E}(\mathbf{r})=\sum_{i=1}^{Ne}I_i\mathbf{N}_i(\mathbf{r}),\mathbf{r}\in V, \quad (7)$$

$$\mathbf{H}(\mathbf{r})=\frac{1}{\eta_0}\sum_{i=1}^{Ne}J_i\mathbf{N}_i(\mathbf{r}),\mathbf{r}\in V. \quad (8)$$

Here, $\mathbf{N}_i(\mathbf{r})$ is the basis function on the i-th edge, I_i and J_i are the expansion coefficients for the electric and magnetic field respectively. N_e is the total number of the edge bases. V is the support of the object. The summation in the above includes an assembly process as in the FEM. That is using the fact that tangential $\mathbf{E}$ and $\mathbf{H}$ are continuous from element to element, I_i and J_i from contiguous elements are the same.

Next by inserting (7) and (8) into (5) and (6), testing them with $\mathbf{N}_j(\mathbf{r})$ and integrating over the tetrahedral element that $\mathbf{N}_j$ is defined on, we can get the matrix representation of the augmented volume integral equation:

$$\begin{bmatrix}\boldsymbol{e}^{inc}\\\boldsymbol{h}^{inc}\end{bmatrix}=\begin{bmatrix}\bar{\mathbf{Z}}_{EE}&\bar{\mathbf{Z}}_{EH}\\\bar{\mathbf{Z}}_{HE}&\bar{\mathbf{Z}}_{HH}\end{bmatrix}\cdot\begin{bmatrix}\mathbf{I}\\\mathbf{J}\end{bmatrix}, \quad (9)$$

where the matrix element in each block is given by:

$$(\bar{\mathbf{Z}}_{EE})_{ji} = (\bar{\mathbf{Z}}^{i}_{EE})_{ii} + (\bar{\mathbf{Z}}^{\epsilon}_{EE})_{ji} = -\left\langle \mathbf{N}_j(\mathbf{r}), \mathbf{N}_i(\mathbf{r}) \right\rangle - k_0^2 \left\langle \mathbf{N}_j(\mathbf{r}), \bar{\mathrm{G}}(\mathbf{r},\mathbf{r}') \cdot \left[\bar{\mathbf{I}} - \bar{\epsilon}_r(\mathbf{r}') \right], \mathbf{N}_i(\mathbf{r}') \right\rangle, \quad (10)$$

$$(\bar{\mathbf{Z}}_{EH})_{ji} = (\bar{\mathbf{Z}}^{\mu}_{EH})_{ji} = ik_0 \left\langle \mathbf{N}_j(\mathbf{r}), \nabla \times g(\mathbf{r},\mathbf{r}') \left[\bar{\mu}_r(\mathbf{r}') - \bar{\mathbf{I}} \right], \mathbf{N}_i(\mathbf{r}') \right\rangle, \quad (11)$$

$$(\bar{\mathbf{Z}}_{HE})_{ji} = (\bar{\mathbf{Z}}^{\epsilon}_{HE})_{ji} = -ik_0 \left\langle \mathbf{N}_j(\mathbf{r}), \nabla \times g(\mathbf{r},\mathbf{r}') \left[\bar{\epsilon}_r(\mathbf{r}') - \bar{\mathbf{I}} \right], \mathbf{N}_i(\mathbf{r}') \right\rangle, \quad (12)$$

$$(\bar{\mathbf{Z}}_{HH})_{ji} = (\bar{\mathbf{Z}}^{i}_{HH})_{ii} + (\bar{\mathbf{Z}}^{\mu}_{HH})_{ji} = -\left\langle \mathbf{N}_j(\mathbf{r}), \mathbf{N}_i(\mathbf{r}) \right\rangle - k_0^2 \left\langle \mathbf{N}_j(\mathbf{r}), \bar{\mathrm{G}}(\mathbf{r},\mathbf{r}') \cdot \left[\bar{\mathbf{I}} - \bar{\mu}_r(\mathbf{r}') \right], \mathbf{N}_i(\mathbf{r}') \right\rangle, \quad (13)$$

and the j-th elements of the incident vectors $\mathbf{e}^{inc}$ and $\mathbf{h}^{inc}$ are written as:

$$e_j^{inc} = -\left\langle \mathbf{N}_j(\mathbf{r}), \mathbf{E}^{inc}(\mathbf{r}) \right\rangle, \quad (14)$$

$$h_j^{inc} = -\left\langle \mathbf{N}_j(\mathbf{r}), \mathbf{H}^{inc}(\mathbf{r}) \right\rangle. \quad (15)$$

In the above, $i = 1, ..., N_e$, $j = 1, ..., N_e$, $\mathbf{I}$ and $\mathbf{J}$ are the vectors of length N_e for the expansion coefficients I_i and J_i respectively.

III. NUMERICAL EXAMPLES

The first example is used to show the convergence performance of the original VIE method for the permittivity term. We calculate the RCS of a sphere with radius of 0.2λ and material properties of $\epsilon_r = 2.2$, $\mu_r = 1.0$ using different mesh densities. The sphere is placed in free space and illuminated by a θ-polarized plane wave. The observation points are at $\theta = [0°, 180°]$ and $\phi = 0°$. The iterative method GMRES (generalized minimum residue method) is applied to solve the final matrix equation. Figure 1 (a) shows the RCS plots with different mesh densities compared to the Mie analytical result. It is seen that the RCS converges to the analytical result as the mesh density increases. Figure 1 (b) shows the convergence of the RCS error. As the mesh density increases, the error of RCS decreases fast. Hence, the original VIE method has good convergence performance for the ϵ_r term.

The second example is to show the convergence performance of the original VIE method for the permeability term. We calculate the RCS for a sphere with material properties of $\mu_r = 2.2$ and $\epsilon_r = 1.0$. The radius of the sphere is 0.15λ. It is excited by a ϕ-polarized plane wave in free space. We calculate the RCS results using the same mesh densities as those in the first case. Figure 2 shows the RCS and convergence results. We can see that the RCS result converges to the analytical value slowly as the mesh density increases compared to the first example. Next, we show the convergence performance of the A-VIE method for the permeability term. We calculate the RCS results by the A-VIE method using different meshes for the same sphere as in the second example. It is shown in Fig. 3 that the RCS results by the A-VIE method have better accuracy and convergence performance than those by the VIE method.

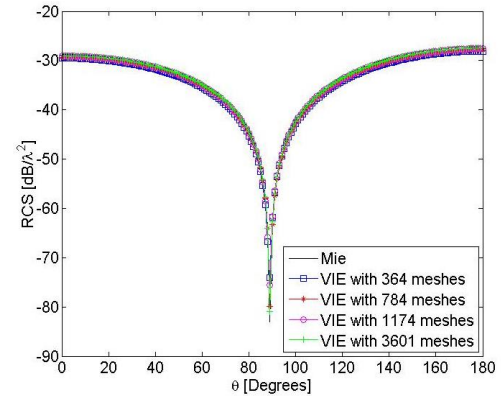

(a) RCS

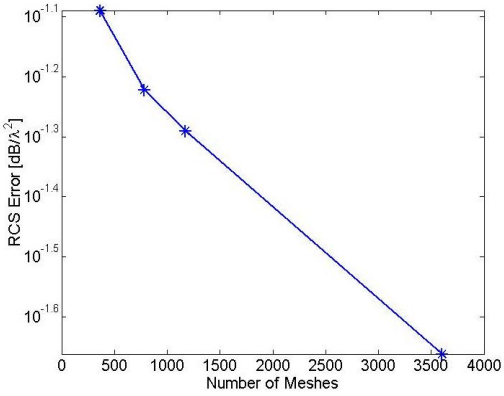

(b) Error of RCS

Fig. 1. Convergence of RCS for different mesh densities for the sphere of $\epsilon_r = 2.2$, $\mu_r = 1.0$ and $r = 0.2\lambda$ by original VIE method.

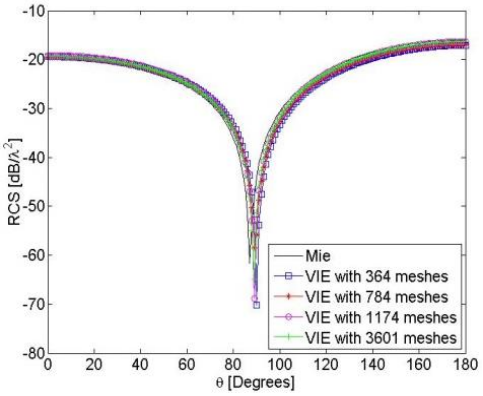

(a) RCS

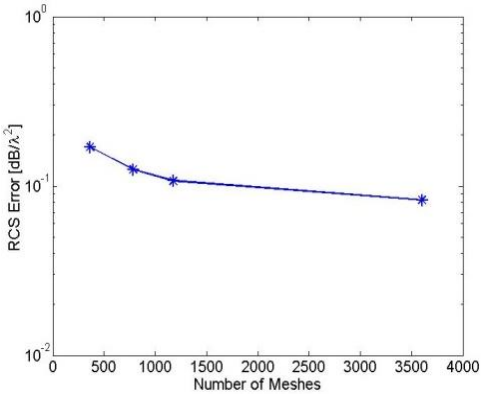

(b) Error of RCS

Fig. 2. Convergence of RCS for different mesh densities for the sphere of μ_r= 2.2, ϵ_r= 1.0 and r = 0.15λ by original VIE method.

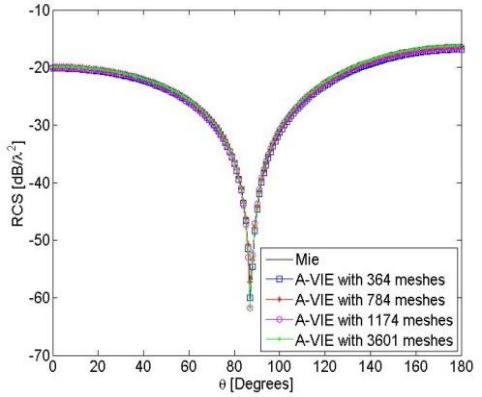

(a) RCS

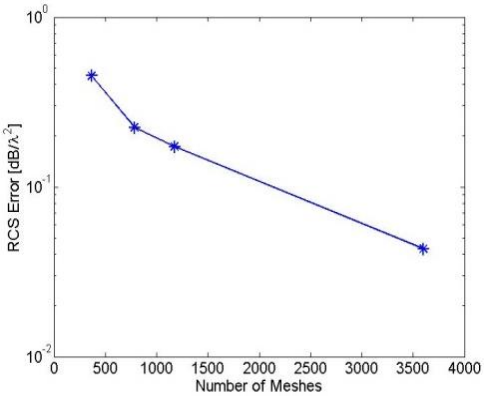

(b) Error of RCS

Fig. 3. Convergence of RCS for different mesh densities for the sphere of μ_r= 2.2, ϵ_r= 1.0 and r = 0.15λ by the A-VIE method.

The third example is the scattered problem of an anisotropic spherical shell using the A-VIE method. The electric dimension of the inner and outer spherical surfaces are k_0a_1 = 0.6π and k_0a_2 = 1.2π, where k_0 is the wave number in the free space, a_1 is the inner radius of the spherical shell and a_2 is the outer radius of the spherical shell. It is placed in the free space and the incident **E**-field is $\hat{x}$ polarized propagating in $+\hat{z}$ direction. In order to test the accuracy of the μ_r term for the general anisotropic case, we consider the permeability of the sphere as a 3 by 3 matrix:

$$\bar{\mu}_r = \begin{pmatrix} 2.5 & -i & 0 \\ i & 2.5 & 0 \\ 0 & 0 & 1.5 \end{pmatrix},$$

ϵ_r is an identity. The mesh includes 3,354 tetrahedra and 4,824 edge elements. Figure 4 shows the RCS result of the spherical shell in the H-plane. We can see that it agrees well with the result of the duality case shown in Ref. [21] by the analytical method. Figure 5 shows the error convergence of GMRES method. We see that the matrix solution takes 24 steps to converge to 10^{-3} by GMRES method.

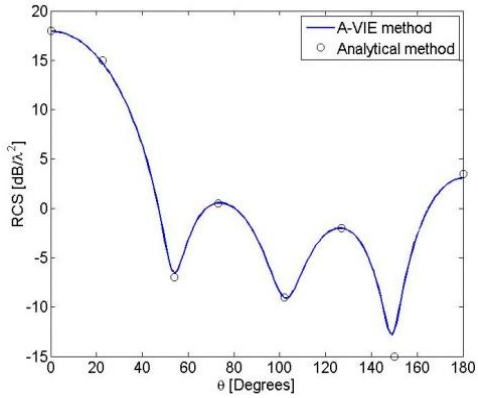

Fig. 4. RCS of the A-VIE method for the gyrotropic spherical shell with electrical radii of 1.2π and 0.6π $\mu_{r,xx} = \mu_{r,yy}$ = 2.5, $\mu_{r,yx} = -\mu_{r,xy} = i$, $\mu_{r,zz}$ = 1.5, $\epsilon_r = I$ in H-plane and RCS of its duality case in E-plane in Ref. [21].

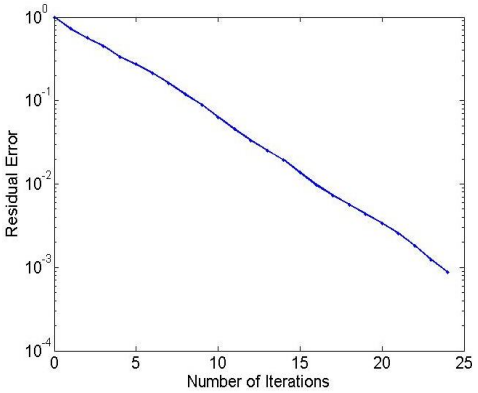

Fig. 5. Residual error converges to 10^{-3} in 24 iterative steps for GMRES method.

Finally, we show an example for a coated magnetic sphere using the A-VIE method. The dimensions of the inner and outer spheres are 0.9 m and 1 m as in Fig. 6. It is placed in the free space and the incident wave is ϕ-polarized. The frequency of incident plane wave is 0.02 GHz. We consider the permeability of the inner and outer sphere are 3.0 and 10.0 respectively. The mesh includes 2,283 tetrahedrons and 3,798 edges. Figure 7 shows the RCS result compared to Mie series result. It can be seen the result from the A-VIE method agrees well with that of Mie series.

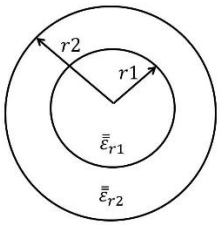

Fig. 6. Coated sphere.

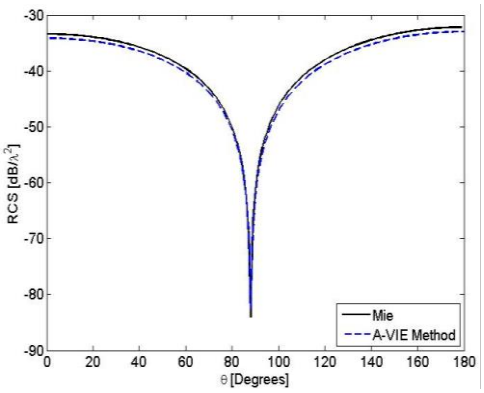

Fig. 7. RCS of the A-VIE method for the coated magnetic sphere with inner and outer radii of r_1 = 0.9 m and r_2 = 1.0 m, μ_{r1} = 3.0 and μ_{r2} = 10.

IV. CONCLUSION

A convergence study for magnetic objects by the VIE and A-VIE methods is discussed. The VIE method originally proposed in [16] is based on vector wave equation for electric field, and the A-VIE method is based on vector wave equations for both electric and magnetic fields. Compared to the VIE method, the A-VIE method has improved accuracy and convergence for the permeability term by removing the differential operations of the electric field in the original formulation. Numerical results show the accuracy of the RCS results for anisotropic magnetics illuminated by the plane waves.

REFERENCES

[1] R. C. Hansen, ed., *Geometrical Theory of Diffraction*, IEEE Press, New York, 1981.

[2] P. C. Waterman, "Scattering by dielectric obstacles," *Alta Freq*., vol. 38, pp. 348-352, 1969.

[3] A. Taflove and K. R. Umashankar, "Review of FDTD numerical modeling of electromagnetic wave scattering and radar cross-section," *Proc. IEEE*, vol. 77, pp. 682-699, 1989.

[4] J. M. Jin, *The Finite Element Method in Electromagnetics*, Wiley, New York, 1993.

[5] A. C. Ludwig, "The generalized multipole method," *Comput. Phys. Commun.*, vol. 68, pp. 306-314, 1991.

[6] R. F. Harrington, *Field Computation by Moment Methods*, Malabar, FL: Krieger, 1968.

[7] W. C. Chew, *Waves and Fields in Inhomogeneous Media*, IEEE Press, 1995.

[8] A. J. Poggio and E. K. Miller, "Integral equation solutions of three-dimensional scattering problems," in *Computer Techniques for Electromagnetics*, R. Mittra, ed., 2nd ed., pp. 159-264, (Hemisphere, New York, 1987).

[9] L. N. Medgyesi-Mitschang, J. M. Putnam, and M. B. Gedera, "Generalized method of moments for three-dimensional penetrable scatterers," *J. Opt. Soc. Amer. A*, vol. 11, pp. 1383-1398, Apr. 1994.

[10] D. H. Schaubert, D. R. Wilton, and A. W. Glisson, "A tetrahedral modeling method for electromagnetic scattering by arbitrarily shaped inhomogeneous dielectric bodies," *IEEE Trans. Antennas Propagat.*, vol. AP-32, pp. 77-85, Jan. 1984.

[11] H. Gan and W. C. Chew, "A discrete BCG-FFT algorithm for solving 3D inhomogeneous scatterer problems," *J. Electromagn. Waves Appl.*, vol. 9, no. 10, pp. 1339-1357, 1995.

[12] A. F. Peterson, "Efficient solenoidal discretization of the volume EFIE for electromagnetic scattering from dielectric objects," *IEEE Trans. Antennas Propagat.*, vol. 62, no. 3, pp. 1475-1478, 2014.

[13] G. Kobidze and B. Shanker, "Fast computational scheme for analyzing scattering from inhomogeneous anisotropic bodies," *IEEE Trans. Antennas Propagat.*, vol. 52, pp. 2650-2658, 2004.

[14] M. I. Sancer, K. Sertel, J. L. Volakis, and P. Van Alstine, "On volume integral equations," *IEEE Trans. Antennas Propag.*, vol. 54, no. 5, pp. 1488-1495, May 2006.

[15] N. A. Ozdemir and J.-F. Lee, "A nonconformal volume integral equation for electromagnetic scattering from penetrable objects," *IEEE Trans. Magn.*, vol. 43, no. 4, pp. 1369-1372, Apr. 2007

[16] L. E. Sun and W. C. Chew, "A novel formulation of the volume integral equation for electromagnetic scattering," *Waves in Random and Complex Media*, vol. 19, no. 1, pp. 162-180, Feb. 2009.

[17] L. E. Sun and W. C. Chew, "An augmented volume integral equation method for electromagnetic scattering of generalized anisotropic media," *The 30th International Review of Progress in Applied*

Computational Electromagnetics, Jacksonville, Florida, Mar. 23-17, 2014.

[18] J. Markkanen, C.-C. Lu, X. Cao, and P. Yla-Oijala, "Analysis of volume integral equation formulations for scattering by high-contrast penetrable objects," *IEEE Trans. Antennas Propag*., vol. 60, no. 5, pp. 2367-2374, May 2012.

[19] Z.-G. Qian and W. C. Chew, "Fast full-wave surface integral equation solver for multiscale structure modeling," *IEEE Trans. Antennas Propag.*, vol. 57, no. 11, pp. 3594-3601, Nov. 2009.

[20] Y.-L. Geng, X.-B. Wu, L.-W. Li, and B.-R. Guan, "Mie scattering by a uniaxial anisotropic sphere," *Physical Review E*, vol. 70, 056609, 2004.

[21] Y.-L. Geng, X.-B. Wu, and L. W. Li, "Characterization of electromagnetic scattering by a plasma anisotropic spherical shell," *IEEE Antennas and Wireless Propagation Letters*, vol. 3, pp. 100-103, 2004.

Lin E. Sun received the B.S. and M.S. degrees in Electrical Engineering from Tsinghua University, Beijing, China, in 2001 and 2004, and the Ph.D. degree in Electrical and Computer Engineering from University of Illinois at Urbana-Champaign in 2010.

From 2010 to 2013, she worked at Schlumberger-Doll Research as the Post-doctoral Research Scientist, where her work focused on electromagnetic forward and inverse algorithms for characterizing complex subsurface structures. In summers 2007 and 2008, she worked with IBM T. J. Watson Research Center and Mentor Graphics on signal integrity analysis of inhomogeneous packaging structures as summer interns. Since 2013, she has been working at Youngstown State University, where she is the Assistant Professor at the Department of Electrical and Computer Engineering. Her research interests include waves in inhomogeneous and anisotropic media, modeling and inversion of subsurface problems, integral equation based method, fast algorithms and inverse algorithms.

Weng C. Chew received the B.S. degree in 1976, both the M.S. and Engineer's degrees in 1978, and the Ph.D. degree in 1980, all in Electrical Engineering from the Massachusetts Institute of Technology, Cambridge, MA. He has been with the University of Illinois since 1985.

He served as the Dean of Engineering at The University of Hong Kong (2007-2011). Previously, he was the Director of the Center for Computational Electromagnetics and the Electromagnetics Laboratory at the University of Illinois (1995-2007). Before joining the University of Illinois, he was a Department Manager and a Program Leader at Schlumberger-Doll Research (1981-1985). He served on the IEEE Adcom for Antennas and Propagation Society as well as Geoscience and Remote Sensing Society. He has been active with various journals and societies.

His research interests are in the areas of wave physics and mathematics in inhomogeneous media for various sensing applications, integrated circuits, microstrip antenna applications, and fast algorithms for solving wave scattering and radiation problems. He is the originator of several fast algorithms for solving electromagnetics scattering and inverse problems. He led a research group that developed computer algorithms and codes that solved dense matrix systems with tens of millions of unknowns for the first time for integral equations of scattering. Recently, he has been interested in multiphysics phenomena in complex technologies involving nanoeletronics and N/MEMS.

He has authored a book entitled Waves and Fields in Inhomogeneous Media, co-authored two books entitled Fast and Efficient Methods in Computational Electromagnetics, and Integral Equation Methods for Electromagnetic and Elastic Waves, authored and co-authored over 350 journal publications, over 400 conference publications and over ten book chapters.

He is a Fellow of IEEE, OSA, IOP, Electromagnetics Academy, Hong Kong Institute of Engineers (HKIE), and was an NSF Presidential Young Investigator (USA). He received the Schelkunoff Best Paper Award for AP Transaction, the IEEE Graduate Teaching Award, UIUC Campus Wide Teaching Award, IBM Faculty Awards. He was a Founder Professor of the College of Engineering (2000-2005), and the First Y. T. Lo Endowed Chair Professor (2005-2009). He has served as an IEEE Distinguished Lecturer (2005-2007), the Cheng Tsang Man Visiting Professor at Nanyang Technological University in Singapore (2006). In 2002, ISI Citation elected him to the category of Most Highly Cited Authors (top 0.01%). He was elected by IEEE AP Society to receive the Chen-To Tai Distinguished Educator Award (2008). He was on the Board of Directors of Applied Science Technology Research Institute, Hong Kong. He is currently the Editor-in-Chief of PIER Journals, and the Chair of the IEEE Joint Chapter on Antennas and Propagation Society, Geoscience and Remote Sensing Society, and Photonic Society, of which he heads a seminar series. Recently, he has been elected to the US National Academy of Engineering.

The Computational Performance and Power Consumption of the Parallel FDTD on a Smartphone Platform

Robert G. Ilgner and David B. Davidson

Department of Electrical and Electronic Engineering
University of Stellenbosch, Matieland, Private Bag X1, Western Cape, South Africa
bobilgner@gmail.com, davidson@sun.ac.za

Abstract ─ The use of the FDTD in Android applications heralds the use of mobile phone platforms for performing electromagnetic modeling tasks. The Samsung S4 and Alpha smartphones computations are powered by a pair of multi-core Advanced RISC Machines (ARM) processors, supported by the Android operating system, which comprises a self-contained platform, which can be exploited for numerical simulation applications. In this paper, the parallelized two dimensional FDTD is implemented on the Samsung Smartphone using threading and SIMD techniques. The computational efficiency and power consumption of the parallelized FDTD on this platform are compared to that for other systems, such as Intel's i5 processor, and Nvidia's GTX 480 GPU. A comparison is made of the power consumption of the different techniques that can be used to parallelize the FDTD on a conventional multicore processor. In addition to parallelizing the FDTD using threading, the feasibility of accelerating the FDTD with the SIMD registers inherent in the phone's ARM processor is also examined.

Index Terms ─ ARM, EXYNOS, FDTD, NEON.

I. INTRODUCTION

The viability of using Smartphones for High Performance Computing (HPC) is currently being examined for a variety of scientific disciplines [1], [2]. The Smartphone is commonly described as being a low power processing device and the work described in this article will quantify this assertion in the context of electromagnetic modeling using the FDTD method.

The finite difference time domain technique has been used for the modelling of electromagnetic scenarios since the late 1960s and is a popular choice for parallelization in HPC owing to its simple deployment on a wide variety of hardware architectures [3].

Power consumption of processors is a topic of interest owing to the cost implications of supplying electricity to HPC processing centers [4]. Koomey's law [5] states that the power being consumed by modern processors is halved every 18 months for an equivalent computational output. Here, the two dimensional parallel FDTD implemented on the Samsung S4's ARM based platform will be used to gauge how the Samsung S4 compares to the power consumption of the FDTD on other HPC platforms. The power consumption of different parallelization techniques will be compared to a contemporary multi-core processor, Intel's i5-4440k.

This paper is structured into three main sections. The first section describes the parallelization of the two dimensional finite differences time domain (FDTD) method on the Samsung S4 and Alpha smartphones using generic threading. The second section presents measurements of computational performance and power consumption of the parallel FDTD on the Samsung S4. Comparison is made with different implementations of the parallel FDTD on an Intel i5 multi core processor. In the third section, the computational/power performance ratio of the parallel FDTD is also compared to the parallel FDTD implemented on other contemporary computing platforms. Several practical real world scenarios that can be computed on the Samsung S4 and Alpha are given as examples, including computing the RFI screening of a large soil berm; results are compared with computations on the Intel i5-4440k processor.

The main contributions of this paper are firstly, a description of parallelizing the FDTD algorithm onto an Android platform, and secondly, an evaluation of the power efficiency of the Android based parallel FDTD implementation compared to the parallel FDTD implemented on a number of other more conventional computing-platforms.

II. PROCESSING THE FDTD ON THE SAMSUNG S4

A. Maxwell's equations and the parallel FDTD method

The FDTD is a numerical approximation to Maxwell's equations [6] and is based on the finite differences formulation of the scalar computations as originally proposed by Yee [7]. For most of the work in this article the peripheral boundaries of the computational

Submitted On: July 2, 2015
Accepted On: November 3, 2015

space are defined using the split field perfectly matched layers (PML). A computational stencil, incorporating some values of adjacent cells, is applied to every field value in the calculation space and repeated in an iterative leap-frog manner [6], [7]. The implications of this stencil processing are two-fold:

i) The vector processing of data has to accommodate non-consecutive array reads [8] for two and three dimensional data.

ii) Threads must communicate fringe data between adjacent data chunks as the values contributing to the computational stencil may be contributed by different data chunks. This inter-chunk communication results in the parallelization of the FDTD being more sophisticated than for an embarrassingly parallel algorithm.

Parallelisation technologies such as MPI, OpenMP and generic threading are generally used to speed up the FDTD in parallel form on multi-core microprocessors [9], [10]. The openMP and generic threading method for the parallelization of the FDTD requires a shared memory architecture, such as a multi-core microprocessor, as the representative sections of the FDTD code are divided amongst several threads and these are each computed on dedicated cores. The FDTD was parallelised for the ARM processors using generic threading, as neither the openMP or the MPI facilities were readily available for the Android platform.

Results for the acceleration of the FDTD on the GPU were attained using the techniques described by [11]. Further acceleration of the parallel FDTD for the Intel processors using SIMD engines such as the SSE and AVX were implemented according to the descriptions by [12].

B. Hardware architecture of the ARM platform

The ARM platform used for the processing of the results shown in this article is part of Exynos System [13] on a Chip (SoC) processors. The Exynos 5410 or Exynos 5430 processor provides the processing power of the Samsung S4 phone. The Exynos 5410 and the 5430 SoCs shown in Figs. 1 and 2, both have an embedded ARM 7 and an ARM 15 processor, a GPU, and embedded storage, albeit in different configurations. The Exynos 5410 resident ARM cores are configured such that low power tasks are processed on the cores of the ARM 7 processor and more computationally intensive tasks are processed on the ARM 15 cores. Although there are eight cores available in total, the tasks are managed between corresponding ARM 7 and ARM 15 cores, as shown in Fig. 1, in a power saving strategy that ARM refers to as a "big.Little" configuration. The switching of the tasks between the ARM 7 and ARM 15 cores is controlled by the firmware and is not available to the programmer.

The Exynos 5430 SoC on the other hand, uses a more conventional arrangement of the ARM 7 and the ARM 15 cores, where the scheduler has direct access to both the ARM 15 and ARM 7 cores. This configuration will allow the processing of eight tasks simultaneously, but the ARM 7 processor cores will run at a lower operating frequency than the ARM 15 cores. Although the availability of the larger number of cores is appealing at first impression, one has to note that the speed of processing of equal sized computational loads will be limited by the capacity of the slowest core. It is not programmatically trivial to assign computational threads to specific cores in the Exynos 5430 SoC.

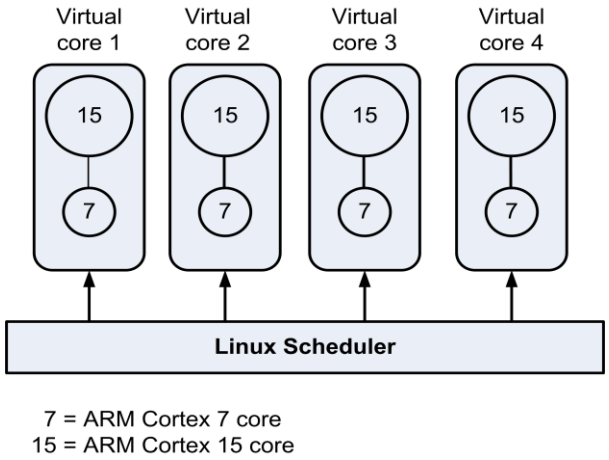

Fig. 1. Schematic arrangement of ARM cores in the Exynos 5410 SoC.

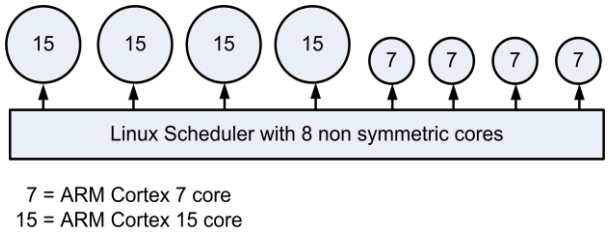

Fig. 2. Schematic arrangement of ARM 7 and ARM 15 cores in the Exynos 5430 SoC.

The 5430 SoC has better computational performance than the 5410 SoC but will consume more power, as is described in the subsequent discussion.

C. Programming on the Exynos System on a Chip

The serial form of the FDTD was parallelised on the Samsung S4's Android v4.4.2 platform using generic threading techniques. The program was built on the phone using the Android-specific gcc compiler. The editing of the program code itself was performed on a

desktop computer and the code was transferred to the phone using local area wireless technology (WiFi). Timing markers were embedded in the code to provide profiling and performance statistics. All computational performance and power consumption measurements for this work were made with programs written in single floating point precision. Graphical results were written to the phone's storage in the VTK [14] format and transferred to the desktop computer for visualisation using Paraview [15].

Android v4.4.2 uses the Dalvik runtime system for the interpretation of the FDTD code. The newer Android Run Time (ART) system is claimed to process Android application code quicker and more power efficiently. The ART was not available for the development platforms used for this work and will be superseded by the Dalvik runtime system in subsequent versions of the Android generations.

For the purpose of comparison with the ARM platform, the two dimensional serial FDTD was also parallelised for the i5-4440k processor using the openMP, MPI, generic threading and various SIMD techniques.

D. The parallel FDTD on multicore platforms using generic threading

The serial form of the FDTD was parallelised using the generic threading for the Exynos 5410 SoC, Exynos 5430 SoC, and the Intel i5-4440k processor.

The computational throughput of the serial FDTD and the parallel FDTD on the four core i5-4440k is shown in Fig. 3. The performance of the serial FDTD on the i5-4440k is shown as a performance reference. The computational throughput of the parallel FDTD on the i5 results shown in Fig. 3 was achieved by using four threads, so that each core is occupied by one thread. The results shown in Fig. 3 do not include the optimisation using the SIMD registers in the i5 processor, although these throughput results are used in Table 1 and shown in Fig. 4.

The computational throughput of the 2D parallel FDTD on the 5410 and 5430 Exynos SoCs is also shown in Fig. 3. The computational throughput was achieved using four threads on the Exynos 5410, although eight cores are made available when one combines the number of ARM 7 and ARM 15 cores, as shown in Fig. 1. The Exynos 5410 did not achieve greater throughput by doubling the number of threads owing to the exclusive core scheduling strategy of the Exynos 5410, as described in section II.B. The computational performance of the 2D FDTD implemented on the Exynos 5430 was not improved either when using more than four threads, very probable because the smaller processing capacity of the ARM 7 core is a limiting factor.

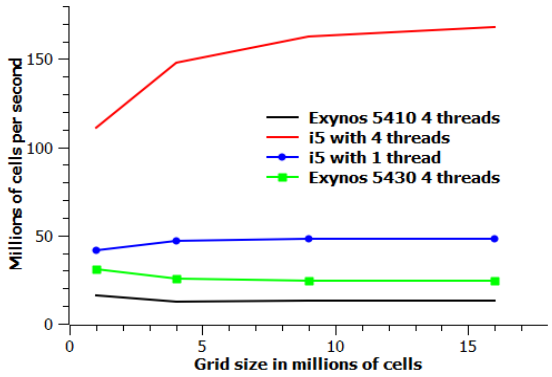

Fig. 3. The processing throughput of the two dimensional FDTD with an increase in grid size.

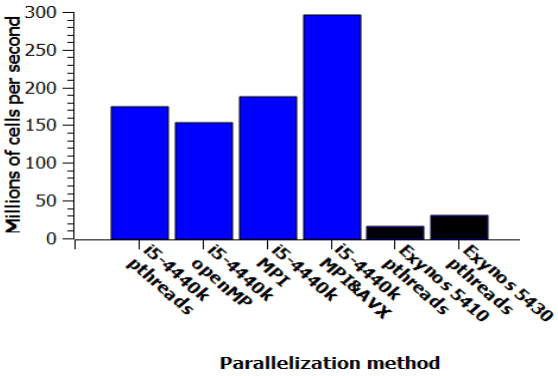

Fig. 4. The performance of the parallel FDTD on the Exynos SoC and the Intel i5-4440k processor. Peak throughput for a grid of 16 million cells.

E. Further parallelisation using the NEON SIMD registers on the Exynos processor

The ARM 7 and ARM 15 processors both have an inherently SIMD engine called NEON. The width of the NEON registers is 128 bits and the NEON operations are capable of handling four floating point operations simultaneously. FDTD implementations making use of the SIMD engines on other processors have shown acceleration of two to three times that of the serial versions.

The implementation of the serial FDTD when using the NEON compiler intrinsics in the Exynos processor did not provide any improvement in computational performance over the serial FDTD. As a test, the FDTD array data was substituted with constant data values, which did indeed provide a marked speedup of the SIMD based acceleration. Whilst the computed results in this case are clearly of no value from a modelling perspective, it showed that the NEON registers are indeed processing the data values effectively, but moving the FDTD data to the NEON registers from the data array to the SIMD engine is

inefficient. Attempts to improve the performance of the array data movement to the SIMD engine by explicitly prefetching the FDTD array data into the cache memory did not enhance the efficiency of the FDTD program when making use of the NEON functionality.

It can also be noted that making use of the automated implementation of the NEON functionality provided by the gcc compiler did not provide any further acceleration of the FDTD either.

By contrast with the lack of acceleration improvement obtained using the SIMD facility for the ARM processors on the Exynos SoCs, further acceleration of the FDTD by using the SIMD facilities inherent in Intel processors provided very good speedups. The speedup in the computational throughput of the two dimensional FDTD on the i5-4440k is shown in Fig. 5. The FDTD was implemented using compiler intrinsic and single precision floating point arithmetic for the AVX registers. The computational performance of the i5-4440k processor is limited when supplying data using only one channel to the physical memory chip, a situation which is alleviated when using two memory channels to the physical memory chips. The use of the auto-vectorisation options on different compilers resulted in a small improvement in computational performance of the FDTD on one core only. Auto-vectorization did not accelerate the parallel FDTD when implemented for more than one core.

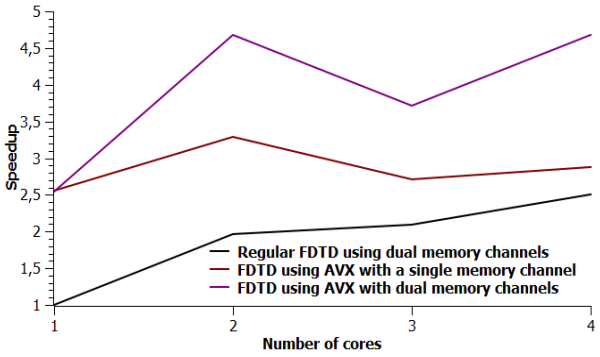

Fig. 5. The data bottleneck effect of using the SIMD registers on the Intel i5-4440k.

III. FDTD COMPUTATIONAL PERFORMANCE/POWER COMPARISON

A. A note on the use of power consumption values on different processors and systems

Although power consumption values are readily given by manufacturers, it is often unclear what these values refer to or how to apply this data to calculate the power consumed by a specific program or process. The peak power consumed for different processes performing at the their maximum capacity is varied [4] and even relatively minor variations within one algorithm can affect the power consumption, as is shown by the results of the parallel FDTD on the i5-4440k, shown in Fig. 6.

The power consumption measurements made for the Intel i5 processor results used in this article were made using a dedicated power meter between the desktop computer and the mains power supply. The baseline power consumption of the desktop computer was measured before the testing and readings were taken while the program was running. The difference in these two power values was used to identify the amount of power consumed by the FDTD itself. Readings were also taken to determine what the effect of the AVX is on the power consumption of the parallel FDTD, as is shown in Fig. 6.

The power consumed by the FDTD on the Samsung phone was determined by calculating the drop of the battery capacity and relating that to the Watt Hour rating of the phone's battery. As it was not possible to exclude the functioning of the myriad of other devices operating in the phone, such as the screen, this power consumption calculation should be assumed to be the worst case scenario for the FDTD. WiFi, Bluetooth, and other unrequired phone features, were switched off during the performance testing.

Another variable affecting the power consumption comparison is the effect of the release age of the processor. According to Koomey's law, new generations of processors are becoming twice as efficient every 18 months. It is therefore implied that newer processors will be more power efficient than older processors. When comparing performance across platforms, programming implementation can also impact on performance evaluation; however, other than the data obtained from Simon [9], all implementations were done by the present authors using very similar code. The power measurements to be presented later on in the article are taken from manufacturers' specification sheets.

B. The performance/power ratio of different parallel algorithms

When comparing the power consumption of the parallelized FDTD for different platforms, it has to be noted that the FDTD may have been parallelized using a different technique to the method with generic threading, and that these techniques all consume power at different rates. This can be demonstrated by examining the techniques used to parallelize the FDTD on the Intel i5-4440k four core processor, where each technique consumes different amounts of power, as shown in Fig. 6. The technique consuming the least amount of power on the Intel four core i5-4440k platform is the FDTD implemented with generic threads, and this has been implemented on the Exynos 5410 SoC, as is shown in Fig. 6. As expected, the FDTD implementation using the SIMD capability of

the i5-4440k also consumes more power than the non-vectorized version. The relative throughput of the parallelized 2D FDTD shown in Fig. 4, measured in millions of cells per second, is as one would expect. The throughput from the Intel i5 four core processor far outstrips the eight cores on the Exynos processor. To achieve this computational throughput advantage though, the i5-4440k processor consumes much more power.

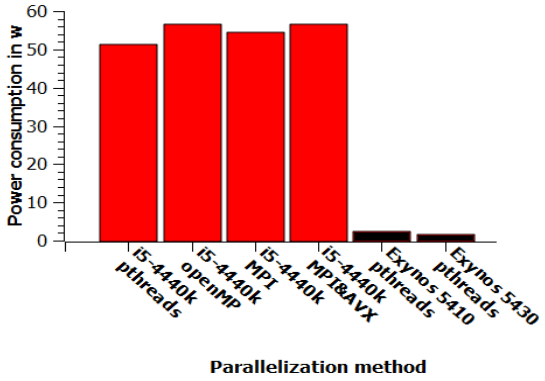

Fig. 6. Power consumption of the parallel FDTD on the Exynos and Intel i5-4440k processors.

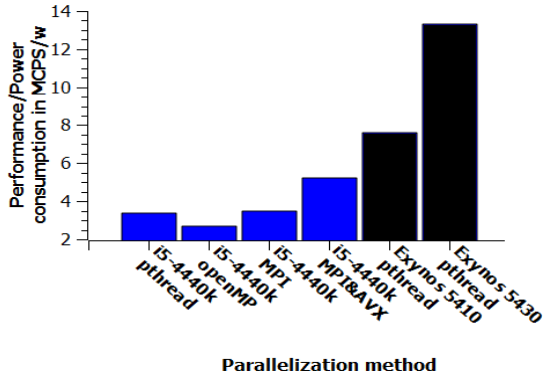

Fig. 7. FDTD performance/power ratio of the Exynos and the Intel i5-4440k.

C. The performance/power consumption of the parallel FDTD compared to other popular computing platforms

One of the features of ARM processors that is constantly emphasized in the popular literature is that the ARM platform consumes very little power. As shown in Fig. 7, the values of FDTD cell throughput normalized by the power consumption seems to verify this for the i5-4440k and Exynos 5410 at least. Table 1 is a comparison of the performance/power ratio of the parallelized FDTD on a variety of computing platforms and illustrates how the FDTD on the Exynos platform relates to these systems. Apart from the FDTD results for the i7 processor [9], all of the parallel FDTD implementations on these platforms originated from the same serial two dimensional FDTD program and was coded by the present authors. It is obvious from this comparison that the processing of the FDTD on the ARM platform does not provide any considerable saving in power consumption. Although the Nvidia GTX 480 appears to have the lowest performance/power rating, it should be noted that this is probably owing to the age of the processor's generation, as predicted by Koomey's law.

The Power PC A2 processor is of particular interest as it processing building block used by IBM's Blue Gene/Q [16] supercomputer. Although released as early as 2011, the Blue Gene/Q still occupies a large proportion of the rankings in Green500 [17] list of energy efficient computers.

The FDTD power efficiency ratings (MCPS per watt) shown in Table 1 agree with the ratings of the top energy efficient processors shown in the Green500 list of November 2014, in that the top 10 positions in the Green 500 list all use Xeon processors similar to the Intel Xeon E5-2640 featuring in Table 1. Although the ARM processors deployed for the FDTD implementations in this work feature near the top of the evaluation in Table 1, they do not appear to feature highly in the current Green500 list.

Table 1: A comparison of the power efficiency of the parallel FDTD on different platforms

Platform	Processor Type	Cores	Release Date	Peak Power (Watt)	Peak MCPS	MCPS Per Core	MCPS Per Watt
GTX 480 Nvidia	GPU	480	2010	320	680	1,4	2,1
IBM Power PC A2	CPU	16 + 2	2010	55	176	11	3,2
C2070 Nvidia	GPU	448	2009	238	780	3,2	3,3
i5-4440 Intel	CPU+AVX	4	2013	56,5*	296	75	5,2
Exynos 5410	CPU	4	2013	2,3*	17,5	4,4	7,6
E5-2640 Intel	CPU+AVX	6	2012	95	1153	192	12,1
Exynos 5430	CPU	4	2014	1,7*	22,7	5,7	13,3
i7-3960x Intel [9]	CPU+AVX	6	2011	130	1800	300	13,8

*Power measurements made manually

IV. FDTD APPLICATIONS ON THE SAMSUNG S4

Despite the limitations of Android platforms on contemporary smartphones as noted in this paper, some quite useful, albeit limited, 2D FDTD simulations can be performed. A commercial application is available on the Android platform to calculate the most suitable position of a WiFi router in an apartment [18]. The FDTD is used to calculate the propagation of the WiFi router's radio transmission throughout the residence so as to determine areas of good and poor WiFi reception.

As a proof of concept, the authors also made computations on the Samsung S4 Smartphone using the two dimensional parallelized FDTD described in this paper. The objective of the computation was to quantify the radio frequency interference shielding provided by a berm (a large earth mound) on a sensitive radio astronomy site in Southern Africa [19]. The results from the FDTD process on the Samsung S4 agreed with those derived from a similar FDTD process modelled on an Intel i5-4440k processor and are shown in Fig. 8. The agreement is satisfactory, given that the application focused on screening, and a 2D model of the 3D berm was used in the simulations, so precise agreement between simulations and measurements was neither expected nor required.

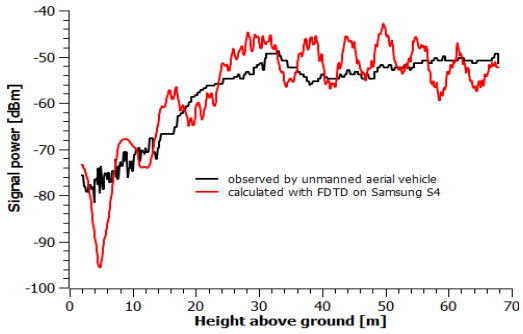

Fig. 8. The signal strength as calculated by the parallel 2D FDTD on the Samsung 4 compared to the signal observed by the unmanned aerial vehicle.

V. CONCLUSION

A comparison of the computational efficiency with the 2D FDTD on other HPC platforms reveals that the ARM processors do not afford a large power saving when computing the FDTD in terms of power-normalized performance. This result may appear surprising, given the claims surrounding low-power processors, but is of course a consequence of their limited performance. For the FDTD at least, most contemporary high performance processors achieve a similar computational efficiency. For applications in large HPC systems, it is the fabric of the system - in particular, the interconnect technology and access to memory - which differentiate systems on the basis of computational efficiency [20]. Nonetheless, as has been described here, the parallel FDTD can be easily deployed in parallel on a Smartphone and used for small-scale rudimentary electromagnetic modeling.

ACKNOWLEDGMENT

DBD and RGI acknowledge the support of SKA South Africa, the South African Research Chairs Initiative of the Department of Science and Technology (DST) and National Research Foundation (NRF), and the Centre for High Performance Computing. The loan of the Alpha Smartphone containing the Exynos 5430 SoC by Samsung is greatly appreciated.

REFERENCES

[1] M. H. Tandel and V. S. Venkitachalam, "Cloud computing in Smartphone: is offloading a better bet?," *Wichita State University*, Wireless Networking and Energy Systems Research Lab., [Online]: http://webs.wichita.edu/?u=WINES&p=/Publications/.

[2] M. Y. Arslan, I. Singh, S. Singh, H. V. Madhyastha, K. Sundaersan, and S. V. Krishnamurthy, "Computing while charging: building a distributed computing infrastructure using Smartphones," *8th International Conference on Networking Experiments and Technologies*, Nice, France, 2012.

[3] R. Ilgner and D. B Davidson, "Price-performance aspects of accelerating the FDTD method using the vector processing programming paradigm on GPU and multi-core clusters," *Applied Computational Electromagnetics Society (ACES) Journal*, vol. 29, no. 5, pp. 351-359, Apr. 2014.

[4] D. Hackenberg, R. Schöne, D. Molka, M. Müller, and A. Knüpfer, "Quantifying power consumption variations of HPC systems using SPEC MPI benchmarks," *Computer Science–Research and Development*, vol. 25, pp. 155-163, Sep. 2010.

[5] J. G. Koomey, S. Berard, M. Sanchez, and H. Wong, "Implications of historical trends in the electrical efficiency of computing," *IEEE Annals of the History of Computing*, vol. 33, pp. 46-54, 2011.

[6] A. Taflove and S. C. Hagness, *Computational Electrodynamics, The Finite-Difference Time-Domain Method*, Third Edition, Artech House, Chapters 3 to 7, 2005.

[7] K. S. Yee, "Numerical solution of initial boundary value problems involving Maxwell's equations in isotropic media," *IEEE Trans. Antennas Propagation*, vol. AP-14, pp. 302-307, 1966.

[8] C. Yuan and Y. Canqun, "Optimizing SIMD parallel computation with non-consecutive array access in inline SSE assembly language," *Fifth International Conference on Intelligent Computation Technology and Automation*, Zhangjiajie, Hunan,

China, pp. 254-257, 2012.
[9] W. Simon, A. Lauer, and A. Wien, "FDTD simulations with 10^{11} unknowns using AVX and SSD on a consumer PC," *IEEE Antennas and Propagation Society International Symposium (APSURSI)*, Chicago, IL, USA, pp. 1-2, July 2012.
[10] A. Asaduzzaman, F. Sibai, and H. El-Sayed, "Performance and power comparisons of MPI Vs Pthread implementations on multi-core systems," *9th International Conference on Innovations in Information Technology*, Abu-Dhabi, 2013.
[11] D. K. Price, A. L. Paolini, K. E. Spagnoli, and J. P. Durbano, "An accelerated GPU FDTD solver using CUDA," *24th Annual Review of Progress in Applied Electromagnetics*, Niagra Falls, Apr. 2008.
[12] L. Zhang, X. Yang, and W. Yu, "Acceleration study for the FDTD method using SSE and AVX instructions," *Conference on Consumer Electronics, Communications and Networks*, Yichang, China, pp. 2342-2344, Apr. 2012.
[13] Exynos Processor Family, [Online]: available at http://en.wikipedia.org/wiki/Exynos.
[14] W. Schroeder, K. Martin, and B. Lorensen, *The Visualization Toolkit*, 4th edition, Kitware Inc., 2006.
[15] A. Henderson, *Paraview Guide, A Parallel Visualization Application*, Kitware Inc., 2007.
[16] IBM, *Introduction to Blue Gene/Q*. 2011. [Online]: available at: http://public.dhe.ibm.com/commonlss ilecm/enldcI12345 usen/ DCL l2345USEN.PDF.
[17] Green500 list November 2014, [Online]: available at http://www.Green500.org.
[18] *Wifi Solver FDTD*. [Online]: available Google Android Playstore.
[19] H. Reader and H. Pienaar, "Model and full scale study of soil berm for Karoo array telescope shielding," *International Symposium on Electromag. Compatibility*, Raleigh, North Carolina, Aug. 2014.
[20] R. G. Ilgner, "A comparative analysis of the performance and deployment overhead of parallelized finite difference time domain (FDTD) algorithms on a selection of high performance multiprocessor computing systems," *Ph.D. Thesis*, Dept. of Electronic and Electrical Eng., Stellenbosch Univ., Stellenbosch, South Africa, 2013.

Robert G. Ilgner obtained his B.Sc. and B.Sc. (Hons) degrees in Geophysics from the University of Witwatersrand in 1982 and 1983 respectively. He received a M.Sc. in Telematics in 1991 from the University of Surrey in Guildford, UK, and was awarded a Ph.D. from the University of Stellenbosch in 2013.

As a Geophysicist he conducted geophysical exploration surveys for mining houses in Southern Africa. He then worked for Siemens (UK) in the Information Technology Industry designing large database systems. He was subsequently employed by Schlumberger in their Seismic Division creating parallel processing applications used for seismic data reduction and modeling. He has built software for the creation of imaging applications and advertising on the internet.

His research interests are in HPC and CEM with the FDTD. He currently manages a variety of commercial IT projects and is a Member of ACES and the South African Geophysical Association.

David B. Davidson received the B.Eng., B.Eng. (Hons), and M.Eng. degrees (all cum laude) from the University of Pretoria, South Africa, in 1982, 1983, and 1986 respectively, and the Ph.D. degree from the University of Stellenbosch, Stellenbosch, South Africa, in 1991.

In 1988, he joined the University of Stellenbosch. He currently holds the South African Research Chair in Electromagnetic Systems and EMI Mitigation for SKA, there in 2014, he was promoted to Distinguished Professor. He has held a number of visiting appointments in Europe, the UK and the USA.

His main research interest through most of his career has been computational electromagnetics (CEM), and he has published extensively on this topic. He is the author "Computational Electromagnetics for RF and Microwave Engineering" (Cambridge, U.K.: Cambridge Univ. Press, 1st ed, 2005, 2nd ed., 2011). Recently, his interests have expanded to include engineering electromagnetics for radio astronomy.

Davidson is a Fellow of the IEEE, a Member of the South African Institute of Electrical Engineers and the Applied Computational Electromagnetic Society, and is a registered professional engineer. He was a recipient of the South African FRD (now NRF) President's Award in 1996. He received the Rector's Award for Excellent Research from the University of Stellenbosch in 2005. He is the Editor of the "EM Programmer's Notebook" column of the IEEE Antennas and Propagation Magazine. He was Chair of the local organizing committee of ICEAA'12-IEEE APWC-EEIS'12, held in Cape Town in September 2012. He received the inaugural IEEE/SAIEE Distinguished Volunteer Award in 2015. He currently serves on South Africa's national Astronomy Advisory Council.

Mode Conversion Caused by Bending in Photonic Subwavelength Waveguides

Y. J. Rodriguez-Viveros [1], D. Moctezuma-Enriquez [2], P. Castro-Garay [1], B. Manzanares-Martinez [1], C. I. Ham-Rodriguez [3], E. Urrutia-Banuelos [3], and J. Manzanares-Martinez [3]

[1] Departamento de Fisica
Universidad de Sonora, Blvd. Luis Encinas y Rosales, Hermosillo, Sonora 83000, Mexico
yohan.jasdid@gmail.com, paola@cifus.uson.mx, betsabe.manzanares@correo.fisica.uson.mx

[2] Instituto Tecnologico de Hermosillo
Av. Tecnológico s/n, Sonora 83170, Mexico
bersek_no1@hotmail.com

[3] Departamento de Investigacion en Fisica
Universidad de Sonora, Blvd. Luis Encinas y Rosales, Hermosillo, Sonora 83000, Mexico
cavanharz@hotmail.com, eurrutia@cifus.uson.mx, jmanza@cifus.uson.mx

Abstract ─ We study the propagation of light in a subwavelength planar waveguide with an angular bend. We observe the mode conversion of a guided wave with a symmetric beam profile impinging into the bending of a waveguide. The guided wave outgoing from the bend is a mixed set of symmetric and asymmetric modes. The amount of mode conversion through the bend is quantified by calculating the Fourier transform of the electric field profile. It is found that the conversion rate is a function of the bending angle.

Index Terms ─ Bending, mode conversion, subwavelength, waveguide.

I. INTRODUCTION

Optical fibers (OF) are dielectric waveguides in the form of cylinders with a diameter (d) larger than the visible range wavelengths (λ=390 nm to λ=700 nm) [1]. OF are flexible waveguides, however, the angle of bending (θ) is limited by a critical angle (θ_c) defined by the principle of total internal reflection (TIR) [1]. They are widely used in optical networks, sensors and other devices [2, 3]. Nowadays to control the flow of data on the Telecom Industry, optical and electronic devices coexist. On the one hand, for long distances photons are transported via optical fibers, which support high bandwidths with low losses. On the other hand, in the electronic circuitry the essential functions of switching and routing are made by manipulating the flow of electrons. The bottleneck for data transfer in this hybrid technology is the operation frequency of the electronic processor which currently is of only a few GHz [4]. To increase the speed of data transfer in optical networks, it has been proposed the development of photonic integrated circuits (PIC) [5, 6]. A PIC does analogous main functions to those of electronic integrated circuits (EIC). The difference is that PIC provides a direct manipulation of the photons traveling in optical waveguides. It is expected that the processing of light in PIC overcome the physical limitations of speed and power dissipation faced by EIC [7].

A progressive development of PIC has been made in the last two decades, which can be classified on three main approaches. A first approach is based on the use of photonic crystals (PC) as a framework for the design of photonic devices to control the flow of light [6]. PC are periodic dielectric structures composed by at least two materials in the unit cell of period (a) which is on the order of the visible wavelength, $a \sim \lambda$ [8]. The fundamental characteristic of PC is the existence of photonic band gaps (PBG) where photons cannot propagate through the periodic lattice. Photonic devices on the order of visible wavelengths can be engineered in PC introducing localized states in the PBG by removing unit cells in the otherwise perfect crystal [9]. A second strategy to design PIC is based on the use of plasmons [10]. Plasmon-based approaches require a precise manipulation of the electromagnetic fields, which are exponentially decaying from the surfaces [11]. It has been suggested the possibility of creating surface-plasmon circuitry with photonic components smaller than the diffraction limit of light [12]. Plasmons however, have substantial optical losses which can severely limit their applicability [13]. To overcome these losses, it has recently been proposed

Submitted On: January 6, 2015
Accepted On: November 7, 2015

the use of gain-loss structures, which introduce unusual possibilities for the propagation of plasmons [14]. A third approach to fabricate PIC is based on the use of nanowires [15-17]. OF and nanowires are both cylindrical waveguides of a diameter d. However, OF have a diameter much bigger than the visible wavelength ($d > \lambda$) which allow a multimodal propagation. In contrast, the nanowire diameter is smaller than the visible wavelength ($d < \lambda$) and as a consequence, only the propagation of a few modes is allowed. This characteristic is desirable for the fabrication of PIC because it is possible to have a more precise control and manipulation of light.

In the last decade, an intensive effort has been made to reduce the width of waveguides [17]. The fabrication of optical waveguides with diameters smaller than the wavelength is a difficult task. For many years it was not possible to attain nanowires with a good quality fabrication because of inherent disorder in the fabrication process such as the existence of surface roughness and diameter variations [16]. In 2003, Tong et al. reported an experimental technique that allowed fabricating wires with diameters as small as 50 nm with an excellent quality [17]. These subwavelength nanowires allowed a higher confinement of photons in small volume regions opening new possibilities for both, the study of fundamental properties and their integration into functional devices [17, 18]. The use of subwavelength waveguides has spun the development of at least five fundamental building blocks for photonic circuitry: i) light sources (lasers) [19], ii) passive components (interconnects) [20], iii) active components (transistors) [21], iv) nonreciprocal optical isolators (diodes) [22], and v) light detectors [23].

Recently Voss et al. investigated the waveguiding at the intersection of two nanowires, which were dissimilar in materials and diameters [24]. One of the main results was the experimental evidence of the excitation of high-order modes, as a result of slight changes in the alignment between subwavelength nanowires. Another important result was the in-situ observation of the generation of high-order modes at imperfections of a nanowire. These results experimentally confirmed the phenomena of mode conversion in subwavelength nanowires

Mode conversion has been recently studied for two other cases of waveguide bends. In the first case, Xing et al. analyzed the propagation of spin-waves passing through a bended magnetic waveguide at the submicron scale using micro-magnetic simulations [25]. In the second case, Zhang et al. studied theoretically and experimentally the TE_{10}-TE_{20} mode conversion of a rectangular waveguide at the microwave regime [26]. In these cases the possibility of separating the fields after the mode conversion into different waveguide branches was reported. In both cases, it has been found that it's possible to have a phase shift between branches as a result of the path difference. In particular, in Ref. [25] it was demonstrated the possibility of creating a kind of Mach-Zehnder interferometer where logic-NOT and logic-AND gates can be tuned in frequency. This result opens the possibility of integrating the mode conversion into interferometric devices.

II. THEORY

The propagation of the electromagnetic fields in a planar waveguide is analyzed by using the curl Maxwell's equations:

$$\nabla \times \mathbf{H}(\mathbf{x}, t) = \frac{\partial}{\partial t}\mathbf{D}(\mathbf{x}, t), \quad (1)$$

$$\nabla \times \mathbf{B}(\mathbf{x}, t) = -\frac{\partial}{\partial t}\mathbf{E}(\mathbf{x}, t). \quad (2)$$

For the Eq. (1) we have considered the case where the density of current is zero, $\mathbf{J}(\mathbf{x}, t) = 0$. Maxwell equations are complemented by the constitutive relations that introduces the material electromagnetic properties of the physical problem. The electric permittivity (ε) provides a description of the macroscopic interaction between the electric field and the dielectric material, whereas the magnetic permeability (μ) describes the interaction of the material with the magnetic field. For the case of a dielectric material (without dispersion), these relations can be written in the form:

$$\mathbf{D}(\mathbf{x}, t) = \varepsilon(\mathbf{x})\mathbf{E}(\mathbf{x}, t), \quad (3)$$

$$\mathbf{B}(\mathbf{x}, t) = \mu(\mathbf{x})\mathbf{H}(\mathbf{x}, t). \quad (4)$$

In Fig. 1 we present the basic geometry of a planar waveguide composed by a slab of high refractive index (n_h) and width d, which is sandwiched between two semi-infinite media of low refractive index (n_l). In this work, we analyze the case of the transversal electric (TE) polarization, where the electric field is parallel to the z-axis, $\boldsymbol{E}(\boldsymbol{x}, t) = \hat{k}E_z(x, y, t)$. The electromagnetic waves inside and outside the slab are propagating and evanescent, respectively.

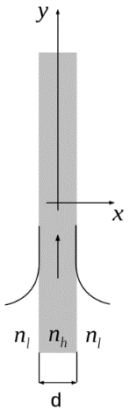

Fig. 1. Planar waveguide of width d and refractive index n_h between two semi-infinite media of refractive index n_l.

The dispersion relation is obtained by solving two well-known transcendental equations [27]. On the one hand, the condition for the modes of even parity with

respect to the *x*-axis is given by the equation:

$$\tan(\pi Q_{x,h}) = Q_{x,l}/Q_{x,h}. \quad (5)$$

On the other hand, the condition for the modes with odd parity is:

$$\cot(\pi Q_{x,h}) = -Q_{x,l}/Q_{x,h}. \quad (6)$$

The reduced wave vectors in the *x*-axis for the high and low refractive index media are:

$$Q_{x,h} = \sqrt{n_h^2\Omega^2 - Q_y^2}, \quad (7)$$

$$Q_{x,l} = \sqrt{Q_y^2 - n_l^2\Omega^2}. \quad (8)$$

The reduced frequency is:

$$\Omega = \omega d/2\pi c. \quad (9)$$

And the reduced wavevector in the *y*-axis is:

$$Q_y = k_y d/2\pi. \quad (10)$$

Figure 2 presents the dispersion relation for the planar waveguide. The high and low refractive indices are n_h=2 and n_l=1, which correspond to the refractive index of ZnO nanowires in air, according to Refs. [18, 24]. Q_y and Ω are the abscissa and ordinate axis, respectively. The light gray zone (Ω<0.3) is the monomodal frequency regime where only one eigenmode is allowed. Conversely, the dark-gray zone (Ω>0.3) is the multimodal frequency regime where two or more eigenmodes are allowed. The TE_0 and TE_1 modes correspond to the first even and odd solutions, respectively. In the monomodal regime, we identify the α eigenmode at (0.32,0.2) which belongs to the TE_0 mode. At the multimodal region we identify the β eigenmode at (0.49,0.4) and the γ eigemode at (0.72,0.4), which correspond to the TE_1 and TE_0 modes, respectively. The arrow line from γ to β illustrates the conversion of modes that we analyze below.

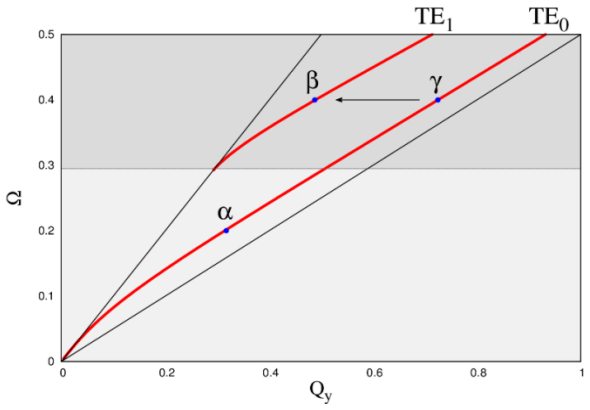

Fig. 2. Dispersion relation for a planar waveguide. The light and dark gray regions are the monomodal and multimodal regimes. The α and γ points belong to the TE_0 mode, while the β point is part of the TE_1 mode.

In Fig. 3 we present the electric field profile for the α, β and γ eigenmodes. We observe that the TE_0 modes corresponding to the α and γ eigenmodes in Fig. 3 (a) and Fig. 3 (c) have an even symmetry. Correspondingly, the TE_1 mode corresponding to the β eigenmode in Fig. 3 (b) has an odd symmetry.

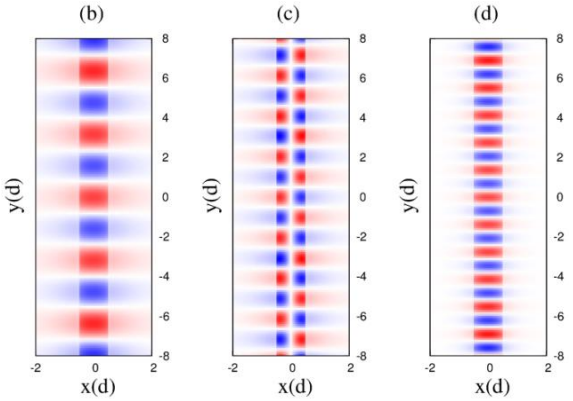

Fig. 3. The electric field profile for the α, β and γ eigenmodes are presented in (a), (b) and (c).

III. NUMERICAL METHOD

We simulate the propagation of the electromagnetic field in the planar waveguide using the finite difference time domain (FDTD) method [28]. The FDTD method is a computational technique used for modeling the temporal evolution of the Maxwell equations. This numerical method is based on the formulation of the differential equations in an associate system of equations in finite differences. The time-dependent Maxwell's equations are discretized using a central-difference approximation to the space and time partial derivatives. The resulting finite-difference system of equations is reformulated in terms of a computational algorithm that can be solved in the time-domain using a recursive process.

In this work, we have simulated the propagation of the electromagnetic field using Phoxonics, the software that we have designed to implement the FDTD technique [29]. Phoxonics is a sophisticated and flexible computational program that allows studying different geometric configurations. In particular, we have analyzed the mode conversion caused by the bending of a planar waveguide.

Considering a polarization of the electric field $\boldsymbol{E}(x,t) = \hat{k}E_z(x,y,t)$, the Maxwell's equations (1) and (2) can be written as three scalar equations in the form:

$$\frac{\partial}{\partial t}D_z(x,y,t) = \frac{\partial}{\partial x}H_y(x,y,t) - \frac{\partial}{\partial y}H_x(x,y,t), \quad (11)$$

$$\frac{\partial}{\partial y}E_z(x,y,t) = -\frac{\partial}{\partial t}B_x(x,y,t), \quad (12)$$

$$\frac{\partial}{\partial x}E_z(x,y,t) = \frac{\partial}{\partial t}B_y(x,y,t). \quad (13)$$

The set of scalar Equations (11)-(13) can be reformulated in terms of finite differences. The finite-difference version of the Equation (11) at the point $(x,y,t) = (i\Delta x, j\Delta y, n\Delta t)$ is:

$$\frac{D_z\left(i,j,n+\frac{1}{2}\right)-D_z\left(i,j,n-\frac{1}{2}\right)}{\Delta t} = \frac{H_y\left(i+\frac{1}{2},j,n\right)-H_y\left(i-\frac{1}{2},j,n\right)}{\Delta x} - \frac{H_x\left(i,j+\frac{1}{2},n\right)-H_x\left(i,j-\frac{1}{2},n\right)}{\Delta y}. \quad (14)$$

The Eq. (12) is written in finite differences for the point $(x,y,t)=\left[i\Delta x,\left(j+\frac{1}{2}\right)\Delta y,\left(n+\frac{1}{2}\right)\Delta t\right]$ as:

$$\frac{B_x\left(i,j+\frac{1}{2},n+1\right)-B_x\left(i,j+\frac{1}{2},n\right)}{\Delta t} = \frac{E_z\left(i,j+1,n+\frac{1}{2}\right)-E_z\left(i,j,n+\frac{1}{2}\right)}{\Delta y}. \quad (15)$$

Finally, the Eq. (13) in finite differences for the point $(x,y,t)=\left[\left(i+\frac{1}{2}\right)\Delta x,j\Delta y,\left(n+\frac{1}{2}\right)\Delta t\right]$ is:

$$\frac{B_y\left(i+\frac{1}{2},j,n+1\right)-B_y\left(i+\frac{1}{2},j,n\right)}{\Delta t} = \frac{E_z(i+1,j,n+1/2)-E_z(i,j,n+1/2)}{\Delta x}. \quad (16)$$

To establish the set of finite difference Equations (14)-(16) in terms of a numerical algorithm, we write these equations in a leapfrog manner that can be solved recursively by using a computational program. To validate the computational implementation of the FDTD method using Phoxonics, we consider a planar waveguide with one or two monochromatic sources embedded inside. These sources are placed at the bottom of our simulation grid to allow seeing the excitation of the eigenmodes. For the case of the α and γ even-modes, they can be excited with a single monochromatic source that is defined by:

$$E_z(x,y,t)=A_1\delta(x-w_{1x})\delta(y-w_{1y})\sin(\omega t). \quad (17)$$

To excite the β mode, it is necessary to consider two monochromatic sources defined by:

$$E_z(x,y,t)=\left[A_1\delta(x-w_{1x})\delta\left(y-w_{1y}\right)+A_2\delta(x-w_{2x})\delta\left(y-w_{2y}\right)\right]\sin(\omega t). \quad (18)$$

The points (w_{1x},w_{1y}) and (w_{2x},w_{2y}) define the position of the monochromatic sources on the x and y axes. A_1 and A_2 are the amplitudes of the sources. The frequency of the monochromatic sources is ω.

The excitation of the α and γ eigenmodes using FDTD is obtained by considering a single monochromatic source, as it is defined in Eq. (17). The position of the monochromatic source is $\left(w_{1x},w_{1y}\right)=(0,-8d)$. In Figs. 4 (a) and 4 (c), the spatial distribution of the TE_0 mode is illustrated when the sources are emitting at the reduced frequencies $\Omega=0.2$ and $\Omega=0.4$, respectively. To obtain the excitation of the β eigenmode we need to use two monochromatic sources as it is defined in Eq. (18). The amplitude of the sources are $A_1=1$ and $A_2=-1$. The position of the sources are $\left(w_{1x},w_{1y}\right)=(-0.4d,-8d)$ and $\left(w_{2x},w_{2y}\right)=(+0.4d,-8d)$, respectively. In Fig. 4 (b) we present the distribution of the TE_1 mode for the case where both monochromatic sources are emitting at a reduced frequency of $\Omega=0.4$.

To validate the excitation of the α, β and γ modes in the planar waveguide using the FDTD technique, we calculate the Fourier transform (FT) of the electric field by using the formula:

$$E_z(Q_y)\cong\frac{1}{\sqrt{2\pi}}\int_0^{L_y}E_z(y)\,e^{i2\pi Q_y y/d}dy. \quad (19)$$

The limits of integration have been switched to consider the finite interval [0:L_y].

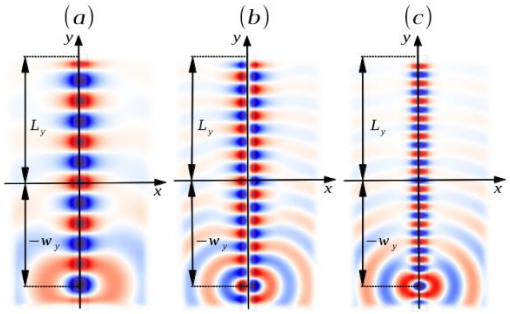

Fig. 4. Simulation of the electric field propagation using FDTD. The excitation of the α, β and γ eigenmodes are presented in (a), (b) and (c), respectively.

In Fig. 5 we present the FT for the electric field on the surface of the planar waveguide. The FT of the electric field distributions in Fig. 3 (a), Fig. 3 (b) and Fig. 3 (c) is presented in Fig. 5 with dotted, dashed and solid lines, respectively. From left to right, the FT peaks around the reduced wavevectors Q_y=0.32, Q_y=0.49 and Q_y=0.72 prove the existence of the α, β and γ eigenmodes, respectively.

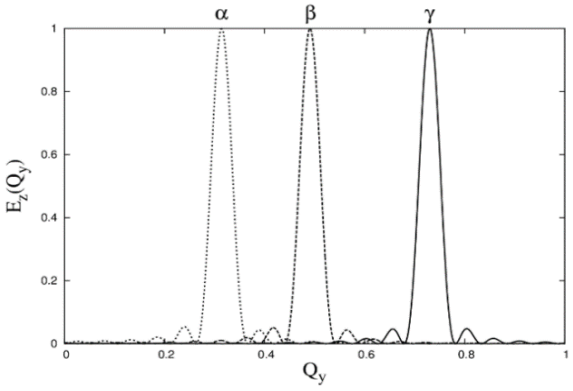

Fig. 5. Fourier transform of the electric field at the surface of the planar waveguide. From left to right, the dotted, dashed and solid lines are the α, β and γ modes.

IV. MODE CONVERSION

In this section, we analyze the mode conversion caused by a bending in a planar waveguide. We consider the case where the TE_0 impinges into the bend. In Fig. 6 is shown a planar waveguide with a bend angle θ at the vicinity of the coordinate system origin.

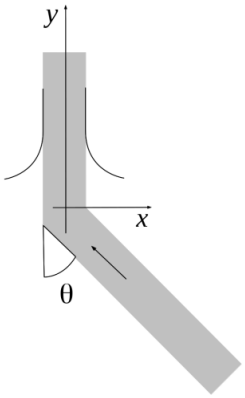

Fig. 6. A planar waveguide with a bend angle θ. The bend is placed at the vicinity of the coordinate system origin.

In Fig. 7 we simulate the propagation of light in the monomodal regime. An even beam profile corresponding to the TE_0 mode with a reduced frequency Ω=0.2 is impinging into the waveguide bend. The cases of waveguides bended with angles of θ=15°, θ=30°, and θ=90°, are presented in (a), (b) and (c), respectively. There are three important observations. The first one is that the incident guided wave passes through the bending without distortion in his symmetry. The second is that the propagation of guided light is not limited by any critical bending angle, as it exists in conventional OF as consequence of the TIR. And the third is that the bending emission increases with the bend angle.

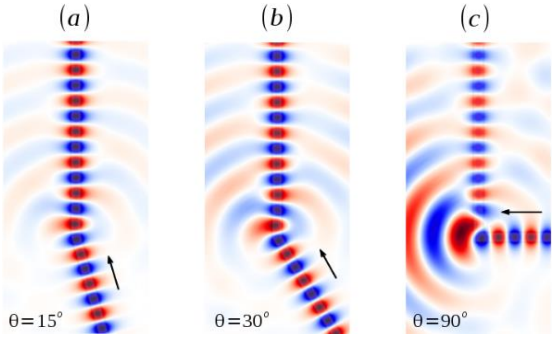

Fig. 7. Propagation at the monomodal regime (Ω=0.2) of the TE_0 mode through a waveguide with an angular bend θ. The cases θ=15°, 30° and 90° are presented in (a), (b) and (c).

In Fig. 8 we simulate the propagation at the multimodal regime. Here, the TE_0 mode is impinging into the bend with a reduced frequency Ω=0.4. For the case of θ=15° illustrated in Fig. 8 (a), we observe that a slight deformation on the geometry of the electric field profile exists. In Fig. 8 (b) is shown the case for θ=30°, for which we observe that after the bend there is a mixed profile of the TE_0 and TE_1 modes where it is not possible to identify a predominant even or odd symmetry. Finally, in Fig. 8 (c) we present the case of θ=90°. It is evident that the incoming mode TE_0 is converted after the bend into the TE_1 mode.

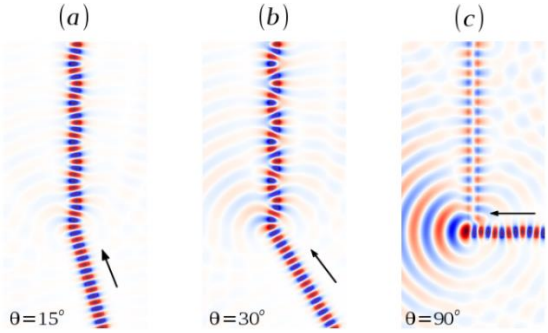

Fig. 8. Propagation at the multimodal regime (Ω=0.4) of the TE_0 mode through a waveguide with an angular bend θ. The cases θ=15°, 30° and 90° are presented in (a), (b) and (c).

The mode conversion can be quantified by using the FT of the electric field as it is defined in in Eq. (19). The FT is calculated for the electric field after the bend on the surface of the planar waveguide. We consider the case presented in Fig. 8, where a guided wave of TE_0 mode is impinging into the bending with a reduced frequency of Ω=0.4.

In Fig. 9 we present the FT for the cases corresponding to an angle of bend θ=0°, 15°, 30° and 60° using black, blue, green and red lines, respectively. We observe that as the angle of bend increases, the amplitude corresponding to the γ mode diminishes. Conversely, as the angle of bend increases the amplitude of the β mode increases. Thus after the bend, the amplitude of the TE_0 mode decreases and the TE_1 mode increases, in both cases as function of the bend angle.

In Fig. 10 we present the variation of the TE_0 and TE_1 modes as a function of the angle θ using a solid and dashed lines, respectively. It is observed that the amount of the TE_0 mode decreases monotonously as a function of the angle of bend. It is found that the TE_0 mode disappear after the bend when is reached θ=80°. In contrast, the amount of the TE_1 mode increases as a function of the angle of bend in the range from 0° to 60°. At 60°, the amount of TE_1 mode starts to decrease. We

observe that for the bend angle θ=90° a complete mode conversion occurs.

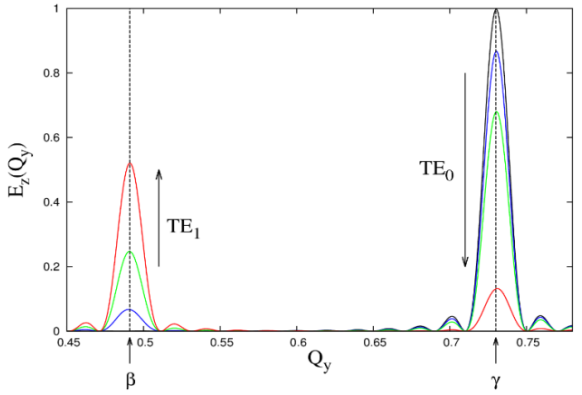

Fig. 9. Fourier transform of the electric field after the bending. The cases θ=0°, 15°, 30° and 60° are presented with black, blue, green and red lines, respectively.

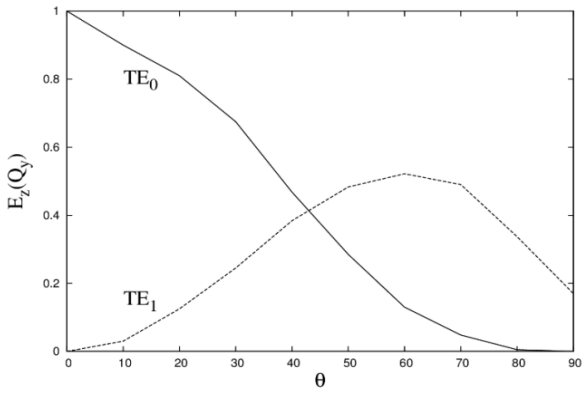

Fig. 10. Fourier transform of the electric field profile as a function of θ. The amplitude of the TE_0 and TE_1 modes are presented with solid and dashed lines, respectively.

V. CONCLUSION

In conclusion, these results demonstrate that subwavelength bend waveguides not just passively transmit light from one point to another. At the multimodal regime, the bend of a subwavelength waveguide acts as a mode converter exciting high-order modes. Therefore, the waveguide bend needs to be intrinsically considered as an active device because it causes a spatial redistribution of the fields. This phenomenon provides an opportunity to create logic devices based in the mode conversion.

We have found a strategy to identify the mode conversion by calculating the FT of the distribution of electric field after the bending. Finally, this study based on the analysis of a two-dimensional geometry is a first step to better understand and utilize the mode conversion in three-dimensional nanowires, which is an essential step for the design of PIC based in subwavelength waveguides.

ACKNOWLEDGMENT

We thank Professor Julio Saucedo for carefully reading the manuscript. This work has been supported by the CONACYT-104151 project. We thank PROMEP-Mexico by special support Grant FOFM-2008.

REFERENCES

[1] J. D. Jackson, *Classical Electrodynamics*, Wiley, New York, 1998.

[2] J. P. Goure and I. Verrier, *Optical Fibre Devices*, CRC Press, New York, 2001.

[3] Optics Communications. *Special Issue: Optical Micro/Nanofibers: Challenges and Opportunities*, vol. 285, no. 4641, 2012.

[4] J. D. Meindl, "Beyond Moore's law: the interconnect era," *Computing in Science Engineering*, vol. 5, pp. 20-24, 2003.

[5] L. Coldren and S. Corzine, *Diode Lasers and Photonic Integrated Circuits*, Wiley, New York, 2012.

[6] J. D. Joannopoulos, P. R. Villeneuve, and S. Fan, "Photonic crystals: putting a new twist on light," *Nature*, vol. 386, pp. 143-149, 1997.

[7] X. Guo, Y. Ying, and L. Tong, "Photonic nanowires: from subwavelength waveguides to optical sensors," *Accounts of Chemical Research*, vol. 47, pp. 656-666, 2014.

[8] E. Yablonovitch, "Inhibited spontaneous emission in solid-state physics and electronics," *Phys. Rev. Lett.*, vol. 58, pp. 2059-2062, 1987.

[9] J. Joannopoulos, R. Meade, and J. Winn, *Photonic Crystals*, Princeton Press, Princeton, 1995.

[10] S. Hayashi and T. Okamoto, "Plasmonics: visit the past to know the future," *Journal of Physics D: Applied Physics*, vol. 45, 433001, 2012.

[11] E. Ozbay, "Plasmonics: Merging Photonics and Electronics at Nanoscale Dimensions", Science, vol. 311, pp. 189-193, 2006.

[12] T. W. Ebbesen, C. Genet, and S. I. Bozhevolnyi, "Surface plasmon circuitry," *Physics Today*, vol. 61, pp. 44-50, 2008.

[13] M. Kuttge, E. J. R. Vesseur, J. Verhoeven, H. J. Lezec, H. A. Atwater, and A. Polman, "Loss mechanisms of surface plasmon polaritons on gold probed by cathodoluminescence," *Applied Physics Letters*, vol. 93, 113110, 2008.

[14] J. Manzanares-Martinez, C. I. Ham-Rodriguez, D. Moctezuma-Enriquez, and B. Manzanares-Martinez, "Omnidirectional mirror based on Bragg stacks with a periodic gain-loss modulation," *AIP Advances*, vol. 4, 017136, 2014.

[15] P. J. Pauzauskie and P. Yang, "Nanowire photonics," *Materials Today*, vol. 9, pp. 36-45, 2006.

[16] F. Ladouceur, "Roughness, inhomogeneity, and integrated optics," *Journal of Lightwave Technology*,

vol. 15, pp. 1020-1025, 1997.

[17] L. Tong, R. Gattass, J. Ashcom, S. He, J. Lou, M. Shen, I. Maxwell, and E. Mazur, "Subwavelength-diameter silica wires for low-loss optical wave guiding," *Nature*, vol. 426, pp. 816-819, 2003.

[18] T. Voss, G. T. Svacha, E. Mazur, S. Mller, C. Ronning, D. Konjhodzic, and F. Marlow, "High-order waveguide modes in ZnO nanowires," *Nano-Letters*, vol. 7, pp. 3675-3680, 2007.

[19] D. O'Carroll, I. Lieberwirth, and G. Redmond, "Microcavity effects and optically pumped lasing in single conjugated polymer nanowires," *Nature Nanotechnology*, vol. 2, pp. 180-184, 2007.

[20] M. Law, D. Sirbuly, J. Johnson, J. Goldberger, R. Saykally, and P. Yang, "Nanoribbon waveguide for subwavelength photonics integration," *Science*, vol. 305, pp. 1269-1273, 2004.

[21] D. Powell, "Light flips transistor switch," *Nature*, vol. 498, pp. 149-149, 2013.

[22] D. Jalas, A. Petrov, M. Eich, W. Freude, S. Fan, Z. Yu, R. Baets, M. Popovic, A. Melloni, J. D. Joannopoulos, M. Vanwolleghem, C. R. Doerr, and H. Renner, "What is -and what is not- an optical isolator," *Nature Photonics*, vol. 7, pp. 579-582, 2013.

[23] J. Wang, M. Gudiksen, X. Duan, Y. Cui, and C. Lieber, "Highly polarized photoluminescence and photodetection," *Science*, vol. 293, pp. 1455-1457, 2001.

[24] T. Voss, "Waveguiding and optical coupling in ZnO nanowires and tapered silica fibers," *Advances in Solid State Physics*, vol. 48, pp. 57-64, 2009.

[25] X. Xing, Y. Yo, S. Li, and X. Huang, "How do spin waves pass through a bend?," *Scientific Reports*, vol. 3, 2958, 2013.

[26] Q. Zhang, C.-W. Yuan, and L. Liu, "Theoretical design and analysis for the TE_{20}-TE_{10} rectangular waveguide mode converters," *IEEE Transactions on Microwave Theory and Techniques*, vol. 60, pp. 1018-1025, 2012.

[27] P. Yeh, *Optical Waves in Layered Media*, Wiley, New York, 1998.

[28] K. S. Yee, "Numerical solution of initial boundary value problems involving Maxwell's equations in isotropic media," *IEEE Trans. Antennas Propagat*., vol. 14, pp. 302-307, 1966.

[29] http://phoxonics.com/software.

A Novel Frequency and Radiation Pattern Reconfigurable Antenna for Portable Device Applications

Wenxing Li, Lei Bao, and Yingsong Li

College of Information and Communications Engineering
Harbin Engineering University, Harbin, 150001, China
liyingsong@ieee.org

Abstract ─ In this paper, a dielectric embedded antenna with frequency and radiation pattern reconfigurable characteristic is proposed for portable terminal applications. The proposed reconfigurable antenna consists of one excitation element, two parasitic elements and eight radio frequency switches. The proposed reconfigurable functions are obtained by controlling the ON/OFF states of the radio frequency switches which are integrated into the excitation elements. As a result, the proposed reconfigurable antenna can operate at two frequencies, 1.9 GHz and 2.8 GHz for supporting DCS1800 (1.71-1.88 GHz) and UMTS (1.92-2.17 GHz), LTE2300 (2.305-2.4 GHz), LTE2500 (2.5-2.69 GHz), WIFI (2.4-2.484 GHz). The radiation pattern reconfigurable characteristic is achieved by controlling the state combination of six radio frequency switches installed on the parasitic elements, resulting in three modes in the radiation pattern at each frequency band. The experimental results demonstrated that the proposed antenna can achieve good frequency and radiation pattern reconfigurable characteristics.

Index Terms ─ Dielectric embedded antenna, frequency and radiation pattern reconfigurable antenna, switchable antenna.

I. INTRODUCTION

With the fast development of wireless communication technology, wireless communication is playing a more salient role in our daily life, and hence, the portable device has become one of popular mobile terminals. However, the electromagnetic radiation emitted from portable device is getting serious. It has been becoming an urgent issue that how to reduce the electromagnetic radiation of the portable device to improve the quality of life and how to reduce harm to health [1-3].

As for the antenna structure, most of the used antennas for portable device can be divided into internal antennas and external antennas, such as cell-phones and Wi-Fi routers. External antennas are mainly realized by using spiral antennas and monopole antennas etc. Internal antennas mainly adopt monopole antennas, including planar inverted F-antennas [4-6], etc. Furthermore, internal antennas have much lower electromagnetic radiation than that of the external antennas. However, they also suffer from the disadvantages of low efficiency and narrow bandwidth [7-9]. Recently, long term evolution (LTE) has been widely studied and investigated. It is desirable to develop a small antenna for portable devices, which can cover at least a few of existing service bands and LTE at the same time, especially before the wide spreading of LTE [10].

The reconfigurable antenna emerges one of the most important research topics and has been widely used in various communication devices. Reconfigurable properties are usually realized by insetting switches, capacitors or phase shifters into the antenna structures. In [11], Zhang et al. uses microstrip Yagi antenna and reconfigurable theory to design a pattern reconfigurable microstrip parasitic array, which can shift the main lobe radiation direction at +35, 0, and -35 in H-plane. In [12-16], wide slot antennas with reconfigurable characteristics for ultra wideband (UWB) wireless communication applications have been reported. The designed antenna can be used as UWB antenna, four band antenna, tri-band antenna, dual-band antenna and notch band UWB antenna by controlling the states of the switches. Recently, a Yagi patch antenna with dual-band and pattern reconfigurable characteristics is systematically discussed in [17]. The beam can scan over the E-plane by controlling the modes of the antenna. In [18], the reconfigurable technology has been applied to design a multi-band antenna for mobile phone. The designed folded loop-inverted F reconfigurable antenna can operate in Hepta-band including GSM850, GSM900, GPS, DCS, PCS, UMTS and WLAN for return loss lower than 6 dB. To expand the application of the reconfigurable antennas, a frequency-reconfigurable antenna for mobile phone with small size was proposed, which consists of a planar inverted F-antenna (PIFA) and a monopole antenna embedded in the same space. A switch was used in the PIFA for providing frequency-reconfigurable operation [10].

Submitted On: December 12, 2014
Accepted On: October 22, 2015

Although the previously designed antennas in [10, 18-21] can cover most existing service bands by altering the reconfigurable frequency bands, most of them cannot realize the frequency and radiation pattern reconfigurable characteristics at the same time to obtain the frequency reconfigurable functions and to reduce the electromagnetic radiation. For this reason, we propose a novel frequency and radiation pattern reconfigurable antenna for portable device applications. Eight radio frequency switches are integrated into the proposed antenna structure to alter the current paths for providing frequency and radiation pattern reconfigurable behaviors. The designed antenna can change the frequency bands to operate at two different frequencies and meanwhile maintains the stable radiation patterns. The radiation pattern reconfigurable characteristics are realized to reduce the electromagnetic radiation according to the position of the portable device toward users at each operating band. When the portable device such as cell phone is standby, the designed antenna can provide omni-directional radiation characteristic. When the portable device is used to communicate with other users, for instance calling other users for cell phone, the radiation pattern will be reconfigured as a directional radiation so that the electric field intensity toward the users can be weakened. Thus, the influence of the electromagnetic radiation for the users is reduced at this mode. By controlling the switches installed on the two parasitic elements, directive and reflective roles of the parasitic elements can be changed and the antenna's maximum radiation direction shifts between 90°and 270°in the H-plane.

II. DESIGN OF THE PROPOSED FREQUENCY AND RADIATION PATTERN RECONFIGURABLE ANTENNA

The geometry of the proposed frequency and radiation pattern reconfigurable antenna is shown in Fig. 1, where S1-S8 are radio-frequency switches. The proposed antenna consists of a driven element, two parasitic elements and eight radio-frequency switches. In this design, the proposed antenna and these switches are embedded into the dielectric substrate whose dielectric constant is 4.4 and the loss tangent is 0.002. The driven element, which is realized by using a stepped dipole that is comprised of a triangle segment and rectangle segment, is approximately a quarter wave length at the resonance frequency of 1.9 GHz in free space. Moreover, the two parasitic elements are set along the driven element at each side. The driven element is fed via a 50 Ohm coaxial cable, which lies in the center of the proposed antenna. Thus, the proposed driven element can be regarded as a dipole antenna. On the basis of the theory of Yagi antennas [9-10], when the switches S1-S3 are turned OFF and the switches S6-S8 are turn ON, the length of the left parasitic element is shorter than the driven element and surface current phase on the left parasitic element is delayed referred to the excitation element. Therefore, the self-impedance of the left parasitic element is capacitive. Furthermore, the length of right parasitic element is longer than the driven element, and the surface current phase is ahead of the driven element. The self-impedance of the right parasitic element is inductive. In this case, the right parasitic element can be regarded as a reflector, while the left parasitic element acts as a director. When the left parasitic element works as a director and the right parasitic element works as a reflector, the H-plane radiation pattern tilts to the positive x axis. Conversely, when the switches S1-S3 are turned ON and the switches S6-S8 are turn OFF, the H-plane radiation pattern tilts to the negative x axis. In this case, the left parasitic element acts as a reflector while the right parasitic element acts as a director. When all the radio frequency switches integrated on the parasitic elements are turned ON, the proposed antenna can provide omni-directional radiation characteristic. In addition, when the two switches, namely S4 and S5, on the excitation element are turned ON, the proposed antenna operates at 1.9 GHz. In this case, the resonance length of the driven element is equal to (L0+D). When these two switches are turned OFF, the antenna works at 2.8 GHz. This is because the resonance length of the excitation element is related to the quarter wave-length which is equal to L0. Thus, switches S4 and S5 are used to alter the resonance length for providing reconfigurable frequency behaviour.

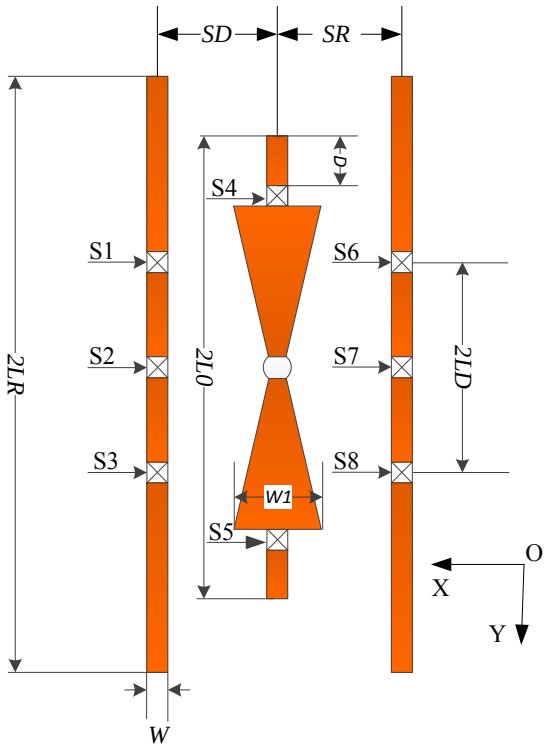

(a) Top view of the antenna

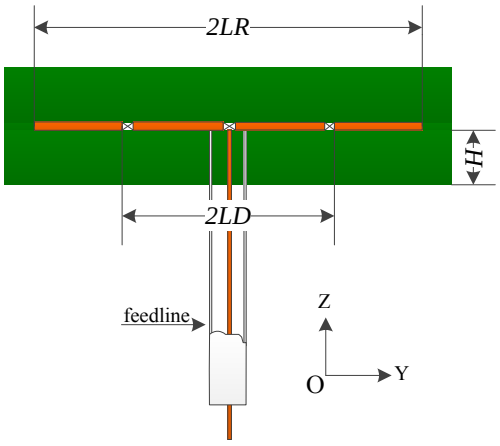

(b) Side view of the antenna

Fig. 1. Geometry of the proposed frequency and radiation pattern reconfigurable antenna.

III. RESULTS AND DISCUSSIONS

In this section, the performance of the proposed antenna is investigated by the use of the high-frequency structure simulator (HFSS). The parameters are optimized and listed as follows: H=2 mm, W=2 mm, W1=6 mm, 2L0=0.26 λ_0, 2LR=0.44 λ_0, 2LD=0.123 λ_0, SD=SR=0.06 λ_0, where λ_0 is the wavelength at the resonance frequency of 1.85 GHz in free space. The operating modes of the proposed antenna are realized by controlling the states of the eight radio-frequency switches shown in Fig. 1, while the operating modes are listed in Table 1. In the simulation, the proposed radio-frequency switches are realized by use of the ideal switch concepts [12-16]. In order to implement these radio frequency switches, the presence of a metal bridge represents the ON state, while its absence represents the OFF state [12-16]. In this paper, metal strips of size 2×2 mm are used for approximating the proposed radio-frequency switches. The VSWR of the proposed antenna at different modes are shown in Fig. 2. It can be seen that the proposed antenna can operate from 1.66 GHz - 2.17 GHz at Mode-1, Mode-2 and Mode-3 for VSWR<2.5. When the proposed antenna works at Modes 4-6, it can cover the bandwidth of 1.95 GHz - 2.97 GHz with VSWR less than 2.5. It can be seen from Fig. 2 that, the impedance bandwidths reach 36.4% and 26.3% at the two operating reconfigurable bands. In order to validate the simulation obtained by HFSS, two prototypes at Mode-4 and Mode-5 are fabricated and shown in Fig. 3. The measured and simulated VSWRs of Mode-4 and Mode-5 are shown in Fig. 4. It can be seen that the measured impedance band is 1.88-3.32 GHz for VSWR<2.5 at Mode-4, while it covers the bandwidth of 1.82-3.02 GHz at Mode-5 with VSWR<2.5. The measured results agree well with simulation ones, which helps to verify the effectiveness of the simulations.

Table 1: Six modes of the proposed reconfigurable antenna

Modes	S1-S3	S4-S5	S6-S8
Mode-1	OFF	ON	OFF
Mode-2	ON	ON	OFF
Mode-3	OFF	ON	ON
Mode-4	OFF	OFF	OFF
Mode-5	ON	OFF	OFF
Mode-6	OFF	OFF	ON

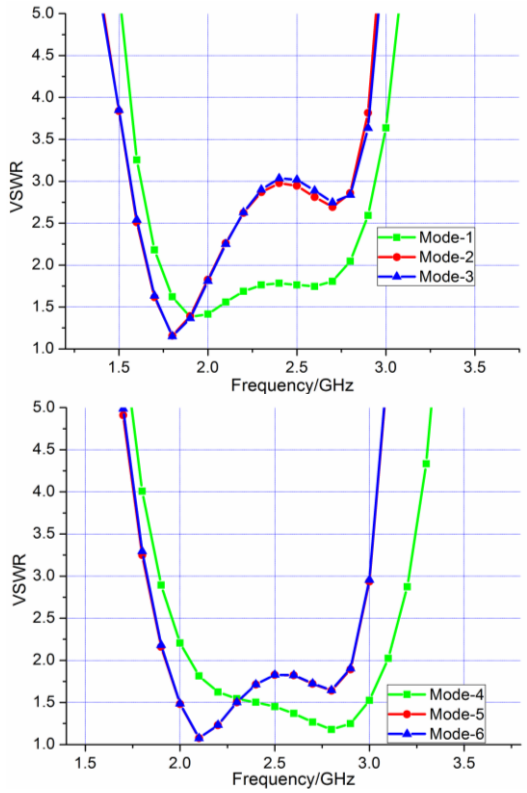

Fig. 2. VSWR of the proposed reconfigurable antenna.

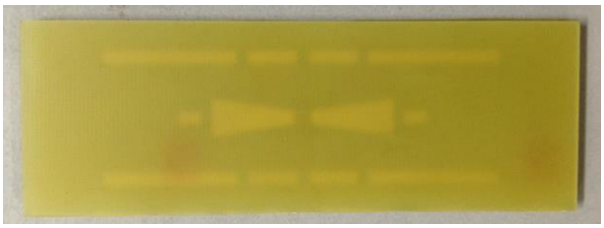

(a) Mode-4

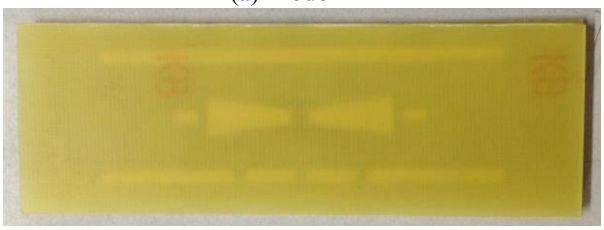

(b) Mode-5

Fig. 3. The prototype of the proposed antenna.

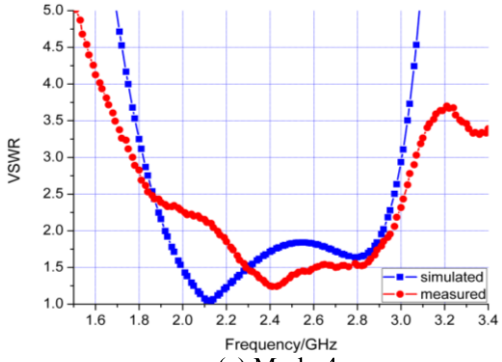

(a) Mode-4

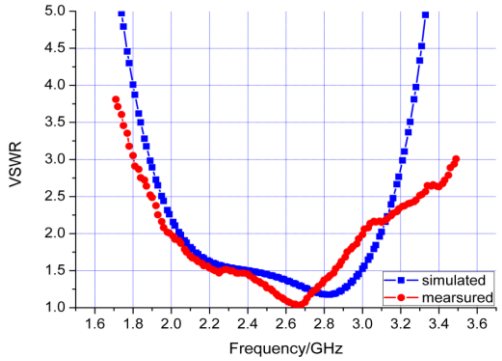

(b) Mode-5

Fig. 4. The measured and simulated VSWR of Mode-4 and Mode-5.

The impedance bandwidths with varying dimensions of SD and SR are shown in Fig. 5. It can be seen from Fig. 5 that the impedance bandwidth of the proposed antenna is decreased with the increment of SD and SR at Mode-2, Mode-3 and Mode-4. The impedance bandwidth is widest when the value of the SD and SR are 8 mm at Mode-1, Mode-5 and Mode-6.

Figure 6 shows the maximal gain of the proposed antenna at the center frequencies and edges of the desired service bands. The maximal gain for the Mode-2 and Mode-3 at 1.9 GHz is about 3.83 dBi. The maximal gain for Mode-5 and Mode-6 at 2.8 GHz is 6.2 dBi.

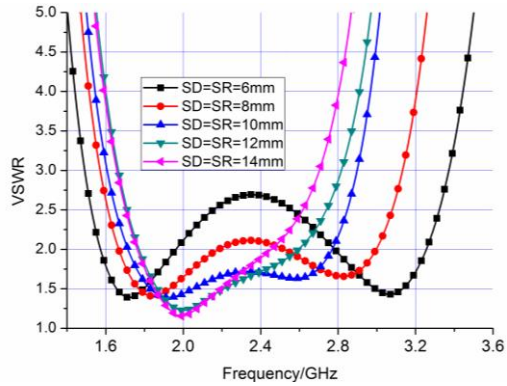

(a) Mode-1

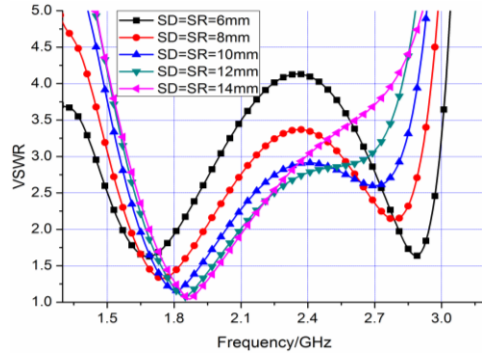

(b) Mode-2

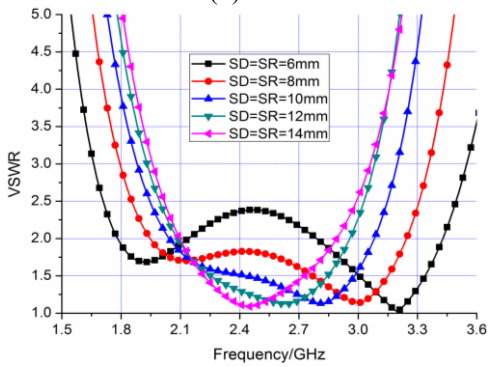

(c) Mode-4

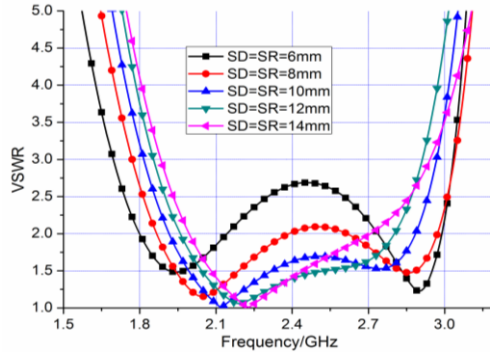

(d) Mode-5

Fig. 5. VSWR of the proposed reconfigurable antenna with different values of SD.

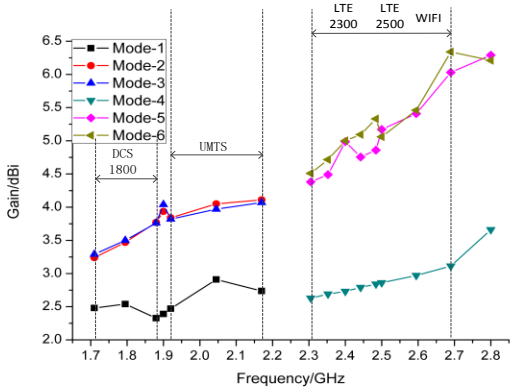

Fig. 6. Gain of the proposed reconfigurable antenna.

The radiation patterns of the proposed antenna at 1.9 GHz and 2.8 GHz are given in Fig. 7. The H-plane is designated as XOZ plane and E-plane is designated as XOY plane. It is shown that the maximum beams are 90° and 270°in the H-plane at 1.9 GHz and 2.8 GHz for Modes 2-3 and 5-6, respectively. Moreover, the half-power beam widths are 179°and 160°degree at Mode-2 and Mode-5, respectively. As for Mode-1 and Mode-4, the proposed antenna can provide a near omni-directional characteristic. According to the design theory of Yagi antenna, the amplitude and phase of surface current on the director and reflector elements can be adjusted to change the space between adjacent elements. The LD effects on the radiation pattern of the proposed antenna are shown in Fig. 8. It is found that the antenna can provide omni-directional radiation patterns for Modes 1 and 4, while it has a directional radiation patterns for other modes with varying LD. The smaller the LD is, the better directional radiation patterns can be achieved.

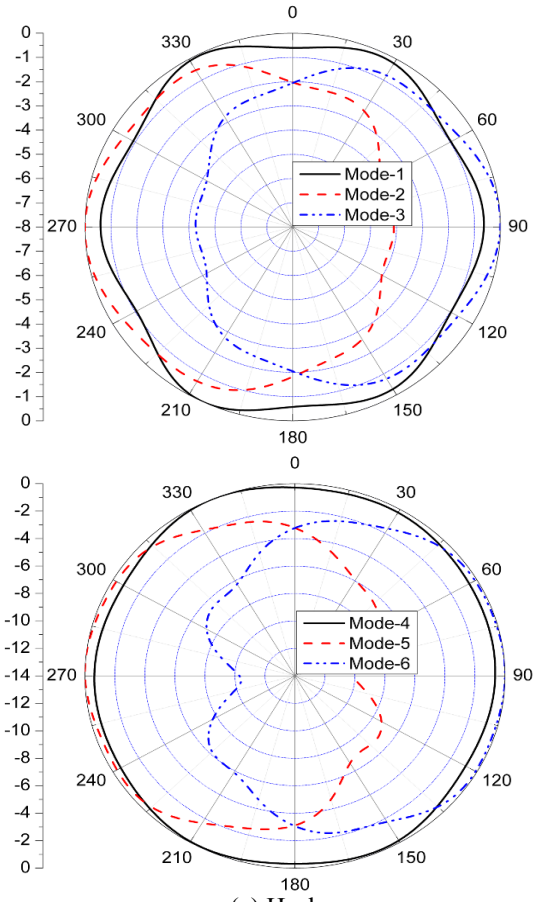

(a) H-plane

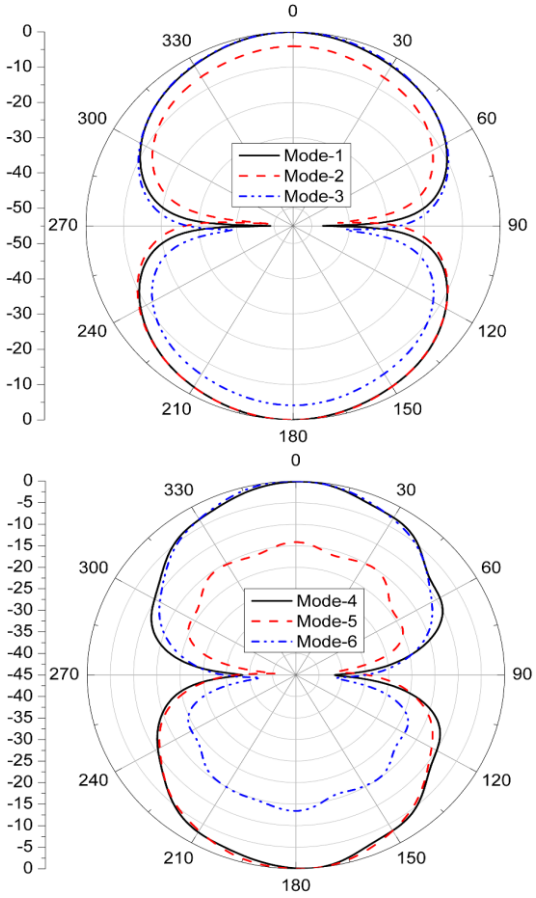

(b) E-plane

Fig. 7. Radiation pattern of the proposed reconfigurable antenna.

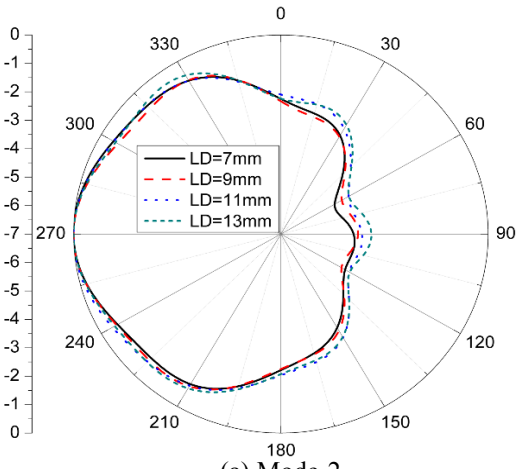

(a) Mode-2

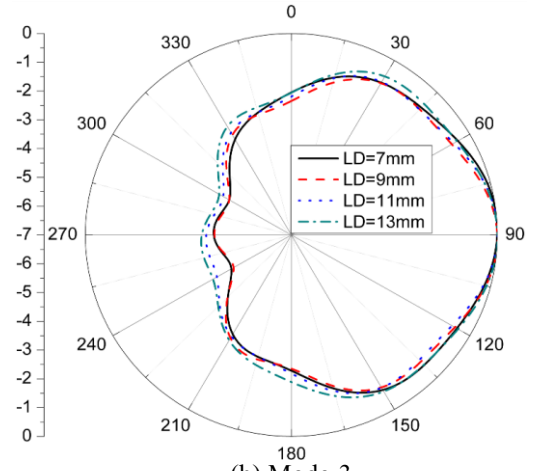

(b) Mode-3

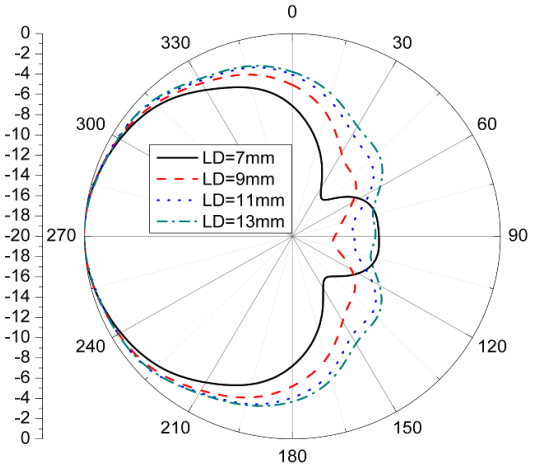

(c) Mode-5

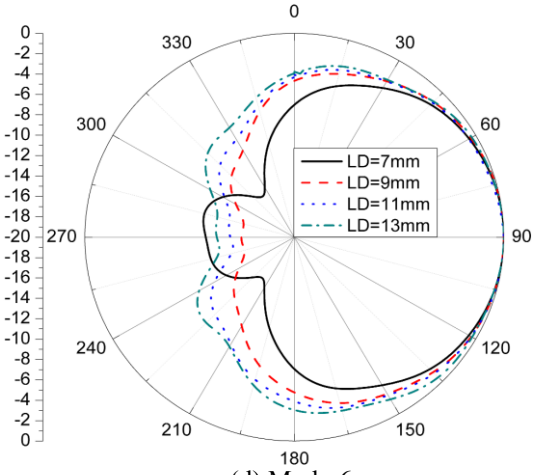

(d) Mode-6

Fig. 8. Radiation pattern of the proposed reconfigurable antenna in the H-plane with different values of LD.

In order to investigate the proposed antenna in detail, the proposed antenna has been compared with standard Yagi antenna at 1.9 GHz. The dimensions of the proposed antenna and standard Yagi antenna are given in Table 2. From Table 2, we can see that the proposed antenna is small in size.

Since all the antenna elements are embedded in the dielectric substrate, the wavelength of the proposed antenna at operation frequency is shorter than the wavelength in free space. In this paper, the effective wavelength in the dielectric substrate is defined in equation (1):

$$\lambda_r = \frac{\lambda_0}{\sqrt{\varepsilon_r}}, \tag{1}$$

where λ_r is the wavelength in the substrate at 1.9 GHz. Therefore, we should consider the dielectric substrate effects when we design our proposed antenna.

Table 2: Dimensions of standard Yagi antenna and the proposed antenna

	Standard Yagi Antenna	The Proposed Antenna
Length of driven element	0.462 λ_0	0.26 λ_0
Length of reflector	0.499 λ_0	0.44 λ_0
Length of director	0.375 λ_0	0.123 λ_0
Spacing between driven element and reflector	0.25 λ_0	0.06 λ_0
Spacing between driven element and director	0.3 λ_0	0.06 λ_0

To further understand the principle of the proposed antenna, the distribution of the electric current at each mode has been shown in Fig. 9. As shown in Fig. 9 (a)-(c), the currents on the directors at Mode-2 and Mode-3 are larger than that of Mode-1. The distribution of the electric currents at Mode-4, Mode-5 and Mode-6 are similar to those of Mode-1, Mode-2 and Mode-3. The electric current on the reflectors at Mode-5 and Mode-6 are smaller than that of Mode-4.

The electric field distribution in XOY plane of the proposed antenna is given in Fig. 10. Compared Fig. 10 (a) with Fig. 10 (b), it can be seen that the electric field intensity around the reflector at Mode-2 is lower than the electric field intensity at Mode-1 because of the electric current distribution. Obviously, the electric field distribution at Mode-2 is almost symmetric to the electric field distribution at Mode-3. When the proposed antenna works at 2.8 GHz, the electric field distribution is similarly shown in Fig. 10 (d)-(f). As shown in Fig. 10 and Fig. 11, the electric field intensity around director at Mode-2, Mode-3, Mode-5 and Mode-6 becomes higher because of the energy conservation law. If the proposed antenna is applied on portable device, the electromagnetic radiation towards the users will be reduced by controlling the modes.

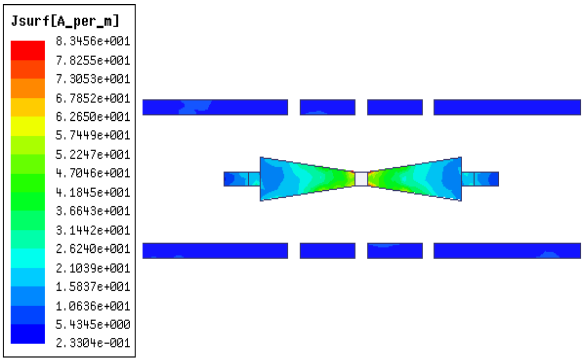

(a) Mode-1

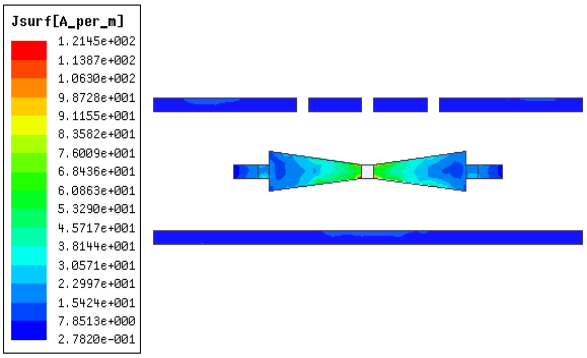

(b) Mode-2

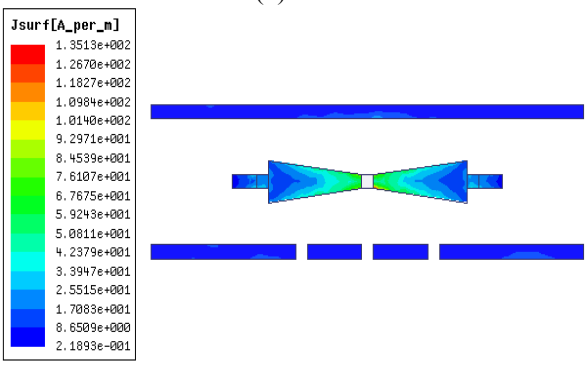

(c) Mode-3

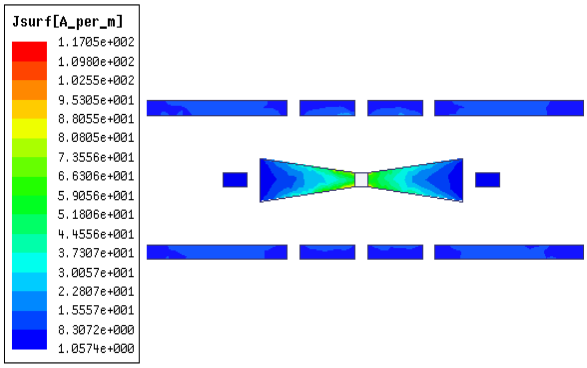

(d) Mode-4

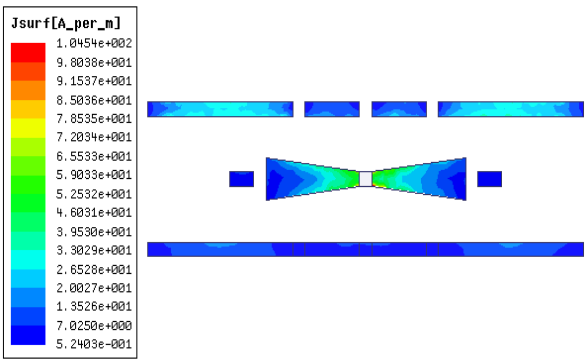

(e) Mode-5

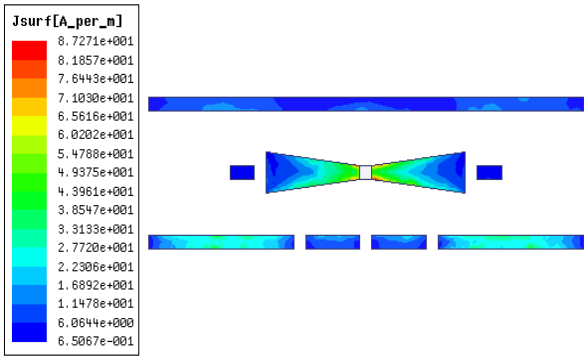

(f) Mode-6

Fig. 9. The distribution of the electric current of the proposed reconfigurable antenna.

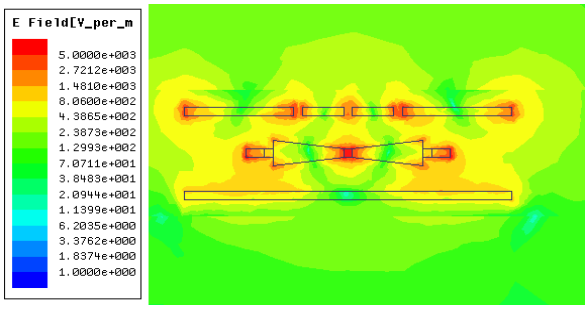

(a) Mode-1

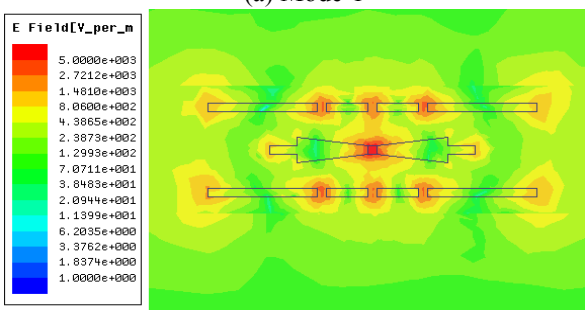

(b) Mode-2

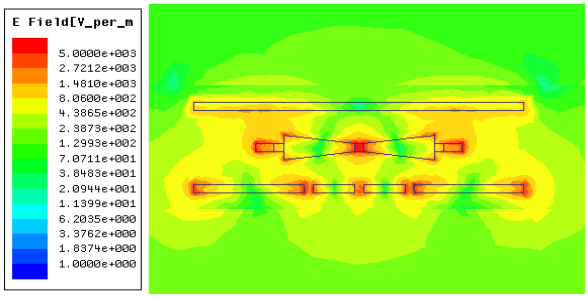

(c) Mode-3

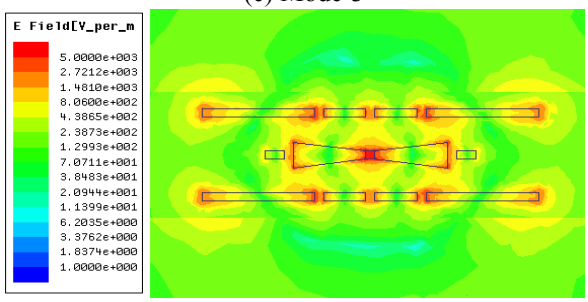

(d) Mode-4

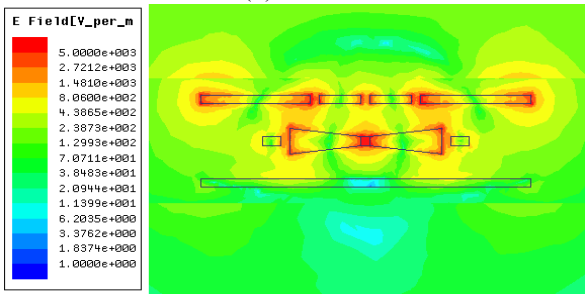

(e) Mode-5

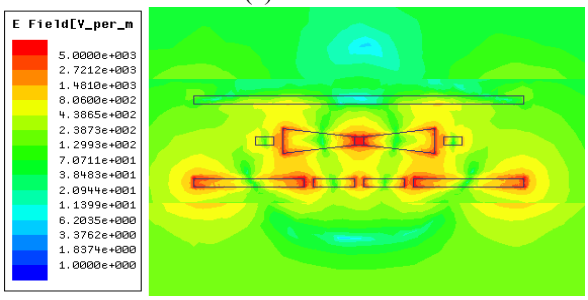

(f) Mode-6

Fig. 10. Electric field distribution in XOY plane of the proposed reconfigurable antenna.

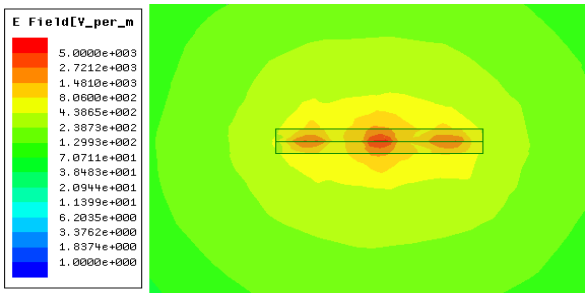

(a) Mode-1

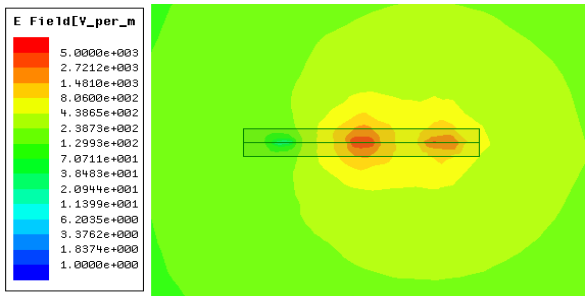

(b) Mode-2

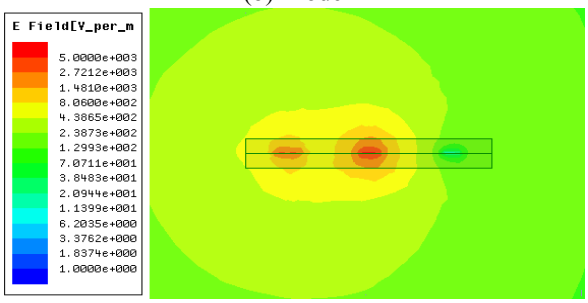

(c) Mode-3

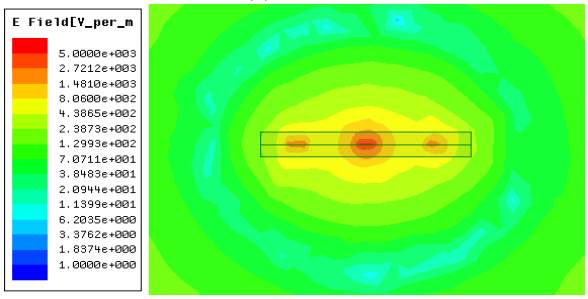

(d) Mode-4

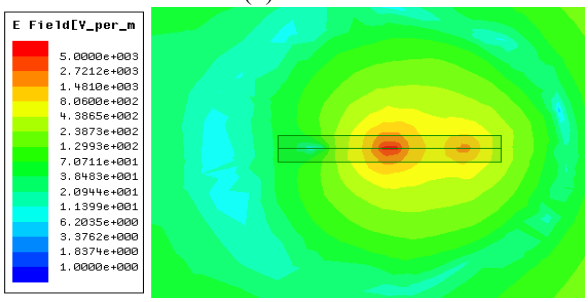

(e) Mode-5

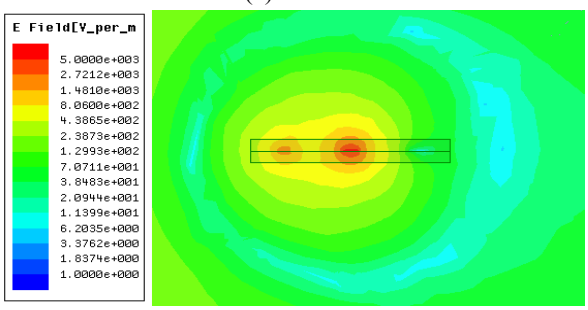

(f) Mode-6

Fig. 11. Electric field distribution in XOZ plane of the proposed reconfigurable antenna.

IV. CONCLUSION

Based on the dielectric embedded technology and the theory of the Yagi antenna, a frequency and radiation pattern reconfigurable antenna has been presented and investigated in detail. The experimental results demonstrated that the proposed antenna can operate at 1.9 GHz and 2.8 GHz, and can provide directional or omni-directional radiation patterns. By controlling the states of the switches, the electric field intensity towards users becomes weak, and hence, the electromagnetic radiation from the portable device can be reduced. The proposed antenna can cover DCS1800 and UMTS at the lower band and can provide support for LTE2300, LTE2500 and WLAN at the upper band. In comparison with the conventional microstrip Yagi reconfigurable antennas, the proposed antenna is relatively small for the given frequency because all the components are buried in the substrate. In the future, we will investigate the proposed antenna by using the PIN diodes switches.

ACKNOWLEDGMENT

This work was partially supported by "973" Basic Research Development Program of China (No. 6131380101). This paper is also supported by Pre-Research Fund of the 12th Five-Year Plan (No. 4010403020102) and Fundamental Research Funds for the Central Universities (HEUCFD1433, HEUCF1508).

REFERENCES

[1] M. T. Santini, G. Rainaldi, and P. L. Indovina, "Cellular effects of extremely low frequency (ELF) electromagnetic fields," *Int. J. Radiat. Biol*., vol. 85, no. 85, pp. 294-313, 2009.

[2] L. Hardell and C. Sage, "Biological effects from electromagnetic field exposure and public exposure standards," *Biomed. Pharmacother*., vol. 62, no. 2, pp. 104-109, 2008.

[3] E. Richter, T. Berman, E. Ben-Michael, et al., "Cancer in radar technicians exposed to radiofrequency/ microwave radiation: sentinel episodes," *Int. J. Occup. Environ. Health*, vol. 6, no. 3, pp. 187-193, 2000.

[4] J. Anguera, A. Andújar, M. C. Huynh, C. Orlenius, C. Picher, and C. Puente, "Advances in antenna technology for wireless handheld devices," *International Journal on Antennas and Propagation*, vol. 2013, Article ID 838364.

[5] C. Rowell and E. Y. Lam, "Mobile-phone antenna design," *IEEE Antennas Propag. Mag*., vol. 54, no. 4, pp. 14-34, Aug. 2012.

[6] J. Anguera, A. Andújar, and C. García, "Multiband and small coplanar antenna system for wireless handheld devices," *IEEE Transactions on Antennas and Propagation*, vol. 61, no.7, pp. 3782-3789, July 2013.e

[7] F. R. Hsiao, H. T. Chen, G. Y. Lee, T. W. Chiou, and K. L. Wong, "A dual-band planar inverted-F patch antenna with a branch-line slit," *Microw. Opt. Technol. Lett*., vol. 32, pp. 310-312, 2002.

[8] C. R. Rowell and R. D. Murch, "A compact PIFA suitable for dual frequency 900/1800-MHz operation," *IEEE Trans. Antennas Propag*., vol. 46, no. 4, pp. 596-598, 1998.

[9] K. L. Wong, W. C. Su, and F. S. Chang, "Wideband internal folded planar monopole antenna for UMTS/WiMAX folder-type mobile phone," *Microw. Opt. Technol. Lett*., vol. 48, pp. 324-327, 2006.

[10] J. Cho, C. W. Jung, and K. Kim, "Frequency-reconfigurable two-port antenna for mobile phone operating over multiple service bands," *IET Journals and Magazines*, vol. 45, no. 20, pp. 1009-1011, 2009.

[11] S. Zhang, G. H. Huff, J. Feng, and J. T. Bernhard, "A pattern reconfigurable microstrip parasitic array," *IEEE Trans. Antennas Propagat*., vol. 52, no. 10, pp. 2273-2776, 2004.

[12] Y. Li, W. Li, and Q. Ye, "Compact reconfigure UWB antenna integrated with SIRs and switches for multimode wireless communications," *IEICE Electronics Express*, vol. 9, no. 9, pp. 629-635, 2012.

[13] Y. Li, W. Li, and W. Yu, "A switchable UWB slot antenna using SIS-HSIR and SIS-SIR for multimode wireless communications applications," *Applied Computational Electromagnetics Society Journal*, vol. 27, no. 4, pp. 340-351, 2012.

[14] Y. Li, W. Li, and Q. Ye, "A reconfigurable triple-notch-band antenna integrated with defected microstrip structure band-stop filter for ultra-wideband cognitive radio applications," *International Journal on Antennas and Propagation*, vol. 2013, Article ID 472645.

[15] Y. Li, W. Li, and Q. Ye, "A CPW-fed circular wide-slot UWB antenna with wide tunable and flexible reconfigurable dual notch bands," *The Scientific World Journal*, vol. 2013, Article ID 402914.

[16] Y. Li, W. Li, and R. Mittra, "Miniaturized CPW-fed UWB antenna with dual frequency rejection bands using stepped impedance stub and arc-shaped parasitic element," *Microwave and Optical Technology Letters*, vol. 56, no. 4, pp. 783-787, 2014.

[17] X. S. Yang, B. Z. Wang, W. Wu, and S. Xiao, "Yagi patch antenna with dual-band and pattern reconfigurable characteristics," *IEEE Trans. Antennas Propagat*., vol. 6, no. 10, pp. 168-171, 2007.

[18] Y. Li, Z. Zhang, J. Zheng, Z. Feng, and M. F. Iskander, "A compact hepta-band loop-inverted F reconfigurable antenna for mobile phone," *IEEE*

Trans. Antennas Propagat., vol. 60, no. 1, pp. 389-392, 2012.

[19] M. Barbuto, F. Bilotti, and A. Toscano, "Design of a multifunctional SRR-loaded printed monopole antenna," *International Journal of RF and Microwave Computer-Aided Engineering*, vol. 22, no. 4, pp. 552-557, July 2012.

[20] D. Rodrigo, B. A. Centiner, and L. Jofre, "Frequency, radiation pattern and polarization reconfigurable antenna using a parasitic pixel layer," *IEEE Transactions on Antennas and Propagation*, vol. 62, no. 6, June 2014.

[21] T. Li, H. Zhai, X. Wang, L. Li, and C. Liang, "Frequency-reconfigurable bow-tie antenna for Bluetooth, WiMAX, and WLAN applications," *IEEE Antennas and Wireless Propagation Letters*, vol. 14, pp. 171-174, 2015.

Design of an Efficient Triple Band RF Energy Harvester

Yunus Uzun

Department of Electrical and Electronics Engineering
Faculty of Engineering, Aksaray University, Aksaray, 68100, Turkey
yunusuzun@aksaray.edu.tr

Abstract ─ In this paper, a new triple band RF energy harvester, considering all the influential parameters, is designed by using Advanced Design System (ADS) simulation software. The most important problem in the RF energy harvesters is low system efficiency. Another problem is that these circuits work on narrow RF bands. The proposed design is found to be much efficient with its current form and provide broadband working frequencies. The output power values and efficiencies of each circuit have been obtained from the software by varying input RF power, load resistance and the number of stages in voltage multiplier at DTV 575 MHz, GSM 900 MHz and WiFi 2.45 GHz frequencies. Thereby a triple band RF energy harvester is proposed for higher efficiency. The system efficiencies for this input power level are obtained about 55% at 575 MHz, 45% at 900 MHz, 30% at 2.45 GHz. The average efficiency is found to be 43% for the individual systems. However, the system efficiency is 68% in the proposed triple band RF energy harvester. This corresponds to an increase rate of 58% for the efficiency. Furthermore, thanks to the proposed RF energy harvester, the efficiencies are increased significantly in cases which only one or two RF signals exist.

Index Terms ─ Efficiency, impedance matching, RF energy harvester, triple band, voltage multiplier.

I. INTRODUCTION

Wireless sensors become very important for our daily life. In general, they consume a little amount of power. These devices are often fed by the batteries. However, the batteries have some disadvantages such as requiring replacement in certain times, increasing the size of device and causing environment pollution [1-5]. In some cases, it is difficult or impossible to replace the batteries of wireless sensors, so lifetime of these devices is equivalent to the lifetime of their batteries [6-8]. These problems motivate the researchers to develop new technologies [9,10]. Recently, low power energy generation methods such as vibration (piezoelectric, electromagnetic and electrostatic), thermoelectric and RF energy harvesting draw attention in terms of an alternative energy source to the batteries. These energy harvesting methods provide a usage without the batteries or an increased battery life of the wireless sensors [11]. There are many signals of different frequencies in our environment, because the wireless communication and equipments are used widely. RF signal sources are TV and radio transmitters, mobile base stations, mobile phones and the other wireless systems [12,13]. It is possible to generate the electrical energy by using RF signals with the properly-designed systems [14,15]. This energy generation method is called RF energy harvesting or RF energy scavenging.

RF energy harvesting method can be especially useful for wireless sensor nodes located in remote places where other energy sources are not feasible [16,17]. Moreover, RF energy harvesting, compared to other energy harvesting methods such as wind and solar etc., does not depend on nature and is available continuously; thus, it is a relatively predictable energy form [18,19]. The main idea of the RF energy harvesting system is capturing RF energy in our surroundings. This energy can supply the electronic equipments with low power consumption or can be stored for future usage [20,21]. Fundamentally, RF energy harvesters include an efficient antenna and an electronic circuit which converts an RF signal to a DC signal. Additionally, source impedance must be equal to the circuit impedance for the maximum power, so an impedance matching circuit is vital in order to obtain the maximum power.

The basic RF energy harvesting system is shown in Fig. 1, which consists of matching circuit, voltage multiplier (RF to DC converter) and storage and load circuits.

The harvested power depends on the RF power level, antenna of system, frequency band and RF to DC converter circuit. Actually, the bases of RF energy harvester are an electromagnetic induction system. So, the higher the RF power, the higher the obtained power. The high gain of the selected antenna and the selection of appropriate frequency band increase the power obtained from the system. In addition, the use of appropriate RF to DC converter and matching circuits

Submitted On: April 29, 2015
Accepted On: November 8, 2015

improve on system efficiency.

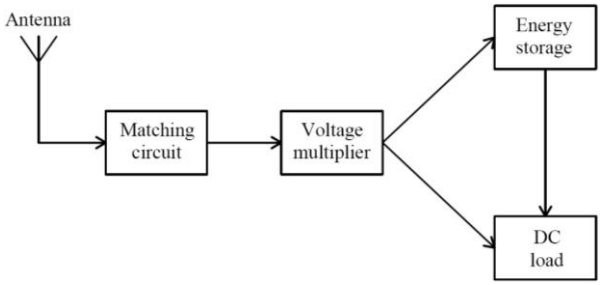

Fig. 1. The block diagram of an RF energy harvesting circuit.

In a wireless system, the received power can be theoretically calculated by the Friis transmission equation as shown in Equation (1):

$$P_r = P_t G_t G_r \left[\frac{\lambda}{(4\pi R)}\right]^2, \quad (1)$$

where P_r is received power, P_t is transmitted power, G_t is gain of the source antenna, G_r is gain of the receiver antenna, λ is wavelength of the transmitted signal, and R is distance between the source and receiver.

As shown in Equation (1), the received power decreases as the distance increases. Therefore, this situation is an important difficulty for the RF energy harvesting concept in far places. Thus, the necessary optimizations should be performed very well to obtain high efficiencies from the system. Considering that the RF signal levels are low in the media, in particular, the impedance matching process should be done properly. In addition, owing to the fact that there are a large number of RF signals at different levels and frequencies in the surrounding media, the increment of the obtained power using the systems that can generate energy from multiple signals is very beneficial.

In this paper, the RF energy harvesters, having three different frequencies which are Digital TV (575 MHz), GSM (900 MHz) and WiFi (2,45 GHz), are analyzed for the voltage multipliers having different number of stages, load impedances, input frequencies and input RF powers using the ADS software. Later, an integrated triple band RF energy harvester being capable of generating energy in the aforementioned frequencies is designed. Thus, optimum parameters for an effective RF energy harvester are determined. And an important increase is obtained in the efficiency using triple band RF energy harvester. In the literature, there are some works including more than one frequency band. 63% efficiency is obtained using a triple band RF energy harvester in Phams' work [22]. Keyrouz *et al.* [23] have designed a triple band RF energy harvester which is combined three different RF energy harvester. The maximum efficiency is 46% in this work. The system efficiency of a dual band RF energy harvester is 57% in Kim *et al.* [24]. The efficiency of proposed system was measured as 68%. This rate is an important improvement in terms of the system efficiency. In addition to this improvement, this RF energy harvester provides high efficiency increase in cases which only one or two RF signals exist.

The paper is organized as follows: In Section 2, the RF energy harvester system including the impedance matching circuit and the voltage multiplier is introduced. In Section 3, some simulation results are presented for different parameters. Finally, the concluding remarks are presented in the last section.

II. ENERGY HARVESTING SYSTEM

RF energy harvester system consists of an antenna, an impedance matching circuit (IMC), a voltage multiplier circuit (VMC), a storage circuit and a load circuit. Antenna with high gain and appropriate frequency band is very important in order to get energy efficiently from the media. Obtained power by an RF energy harvester cannot be sufficient for a load circuit. Due to that, a storage unit must be used to store the obtained energy.

Figure 2 (b) shows a simple 900 MHz RF energy harvester including the *L* type impedance matching circuit and one stage voltage multiplier. The component values of the impedance matching circuit are determined by the software and also calculated analytically by using the following equations [25]:

$$\frac{1}{X_{C\_m}} = \frac{1}{Z_0}\sqrt{\frac{(Z_0 - R_L)}{R_L}}, \quad (2)$$

$$X_{L\_m} = \sqrt{R_L(Z_0 - R_L)} - X_L. \quad (3)$$

Here, X_{C_m} and X_{L_m} are reactances of the impedance matching capacitor and inductor, respectively. Z_0 is input impedance (50 Ω), R_L is real part of the load impedance (31,46 Ω) and X_L is imaginer part of the load impedance (-j340,38 Ω). By solving the following equations, the impedance matching components C_m and L_m are found 2.71 pF and 64.46 nH, respectively.

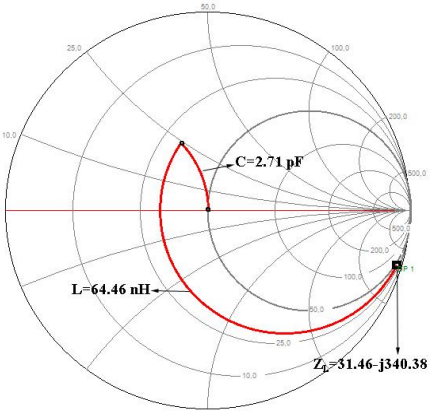

(a)

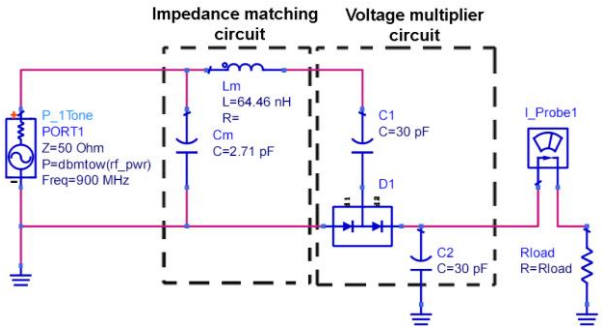

(b)

Fig. 2. (a) The Smith Chart diagram for impedance matching process. (b) 900 Mhz RF energy harvester included IMC and VMC.

In the simulations, this circuit is established at 575 MHz, 900 MHz and 2.45 GHz input frequencies for all number of stages. So, the component values of IMC are determined separately for each stage and input frequency.

A. Impedance matching circuit

In a transmission line, source and load impedances must be equalled to providing the maximum power transfer. Especially, when the input power is low, impedance matching circuits provide a great increase in the system efficiency. RF energy harvester systems should work on low input power levels, because the signal levels surrounding our environment are weak in general. This situation requires that the impedance matching circuits should be used to obtain increased power from such systems. These circuits can be performed in various ways. One of these ways is *L* type impedance matching circuit, which is simple and not bulky. *L* type impedance matching circuit is configured according to the ratio of the load impedance to source impedance.

There are an inductor and a capacitor at *L* type impedance matching circuits. The values of these components depend on the source and the load impedances. The values of components used in this work are shown in Table 1. In the proposed system, while the working frequency is higher, the impedance of the voltage multiplier (i.e., load impedance) is lower due to effect of saturation current. Thus, the values used in the impedance matching circuits are lower at high frequencies.

When the triple band energy harvester is used instead of individual system, total impedance matching component is reduced by 33% as shown in Table 1. Because four matching components are used in the proposed system (3 inductors and 1 capacitor), however the triple band system included three individual harvester use six matching component (3 inductors and 3 capacitors). That causes to decrease the cost and the size of the system. Even though there is an increase at the values of the inductors used in the impedance matching circuit, this situation is not an important increase in terms of cost and size.

Table 1: The components used in one stage individual and triple band energy harvesters

	L (nH)		C (pF)	
	Individual System	Triple Band System	Individual System	Triple Band System
575 MHz	127.2	207.5	0.1	-
900 MHz	64.5	86.0	2.7	-
2.45 GHz	8.6	13.7	2.6	1.6

B. Voltage multiplier circuit

A voltage multiplier circuit can be used to increase voltage signal obtained from the antenna. These circuits convert the RF signals into the DC voltage used in most of the electronic equipments. There are various voltage multiplier circuits. Dickson voltage multiplier circuit is shown in Fig. 3 for this study. The circuit consists of two diodes and two capacitors for each stage. HSMS-2852 Schottky diodes were used in this work due to they have fast switching speed, low forward voltage, low substrate leakage and relatively low junction capacitance. In addition, the system is not bulky, because these diode packages include two series diodes. Therefore, they are suitable for the voltage multiplier circuits.

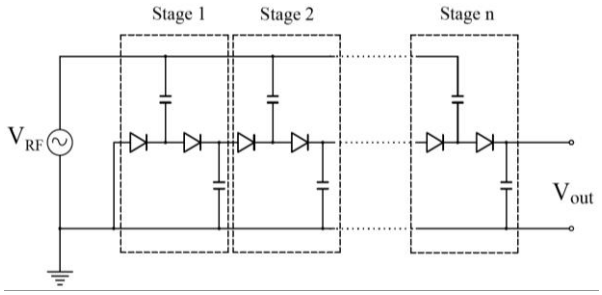

Fig. 3. n stage Dickson voltage multiplier.

The capacitors having different capacity are connected as stage components. But the output voltage does not change too much by using the capacitors that have equal or different capacitance at the stages. For simplicity, same value of the capacitances for all stages is selected. The number of voltage multiplier stages has a significant effect on the efficiency of the RF energy harvesting system [26].

Figure 4 shows equivalent circuit of the Schottky

diode. The overall impedance value of the diode depends on too many variables.

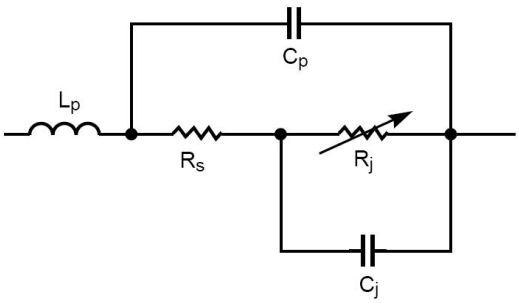

Fig. 4. Equivalent circuit model of diode [27,28].

In Fig. 4, C_j and R_S are the parasitic junction capacitance and series resistance of the diode, respectively. L_P and C_P are the packaging inductance and capacitance respectively. Diode admittance Y_d can be expressed as the following [27]:

$$Y_d = \left(\frac{-jR_j \dfrac{1}{\omega C_j}}{R_j - \dfrac{1}{\omega C_j}} + R_S + j\omega L_P \right)^{-1} + j\omega C_P . \quad (4)$$

R_j is the junction resistance of the diode, and expressed as the following [28]:

$$R_j = \frac{8.33X10^{-5} nT}{I_S + I_B}, \quad (5)$$

where I_S is the diode's saturation current, I_B externally applied bias current, T is temperature (°K) and n is ideality factor.

As seen in Equation (5), the saturation current is an important parameter for diode impedance. Because of the saturation current, diode impedance varies substantially with the increase of frequency [29]. In these diodes, if the input power level exceeds -15 dBm, the impedance (especially real part) increases rapidly [30]. This situation causes a decrease in the efficiency for these input power levels.

Figures 5 (a) and 5 (b) show the real and imaginary parts of the load impedance values depending on the number of stages for three different individual RF energy harvesters. Due to the effects of both the diode junction surfaces and the capacitors used in stages, the load impedance shows the capacitive feature. As seen from Figs. 5 (a) and 5 (b), as the number of stage increases, the load impedance decreases. This means that an incline in the capacitor value to be used in matching circuit and a decline in inductor value with the increasing of stage number.

As seen in Figs. 5 (a) and 5 (b), the value of load impedance decreases by the input frequency. This provides a reduction for the values of the circuit's components used in impedance matching circuit. However, the number of diodes and capacitors will increase with the increasing number of stages, this is an undesirable case in terms of both cost and size. Therefore, the high number of stages should be avoided unless it won't provide a large increase in the efficiency.

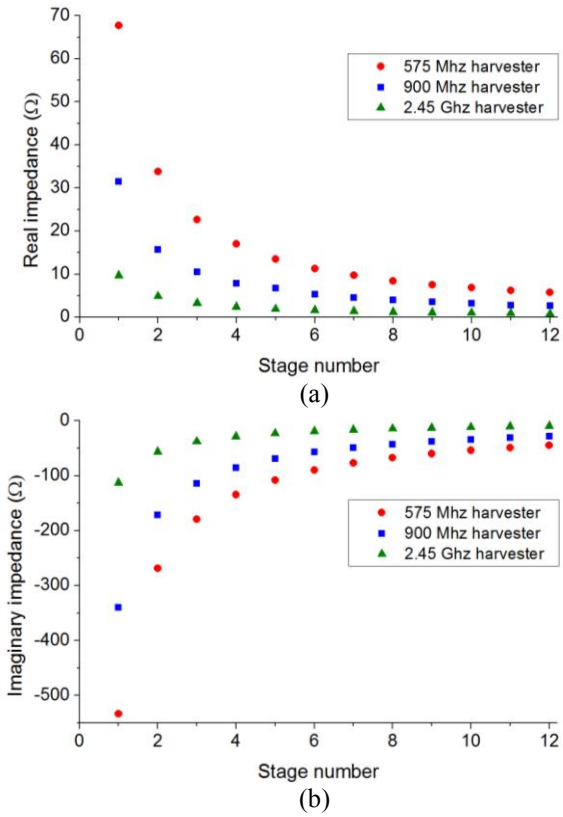

Fig. 5. (a) Real and (b) imaginary parts of the load impedance depending on the number of stages for three different individual RF energy harvesters at 0 dBm.

III. SIMULATION RESULTS

The simulations of the system have been carried out with the ADS software. Initially, the load impedances have been determined at three different frequencies for each number of stages. Then the required impedance matching circuit parameters have been established by the software. Four different systems including 575 MHz, 900 MHz, 2.45 GHz and triple band RF energy harvesters are used in the simulations. The RF input power varying from -50 to 20 dBm have been applied to the systems for to the load resistances from 0.2 to 60 kΩ. As a consequence of this process, the obtained efficiencies have been determined. This process has been tried for all number of stages from one to twelve. The efficiencies calculated are as follows:

$$\eta = \frac{P_r}{P_t} = \frac{V_r^2 / R_L}{P_t}, \quad (6)$$

where P_r and P_t are the received and transmitted powers, respectively, V_r is the obtained voltage, R_L is the load resistance.

In the RF energy harvester systems, one of the most important parameters affecting the output power is the input RF power level. Figure 6 shows efficiencies of the 900 MHz RF energy harvester from the matched and non-matched systems with one stage voltage multiplier for the input power levels from -50 dBm to 20 dBm. As seen from the figure, the impedance matching circuit usage reduces the system efficiency for the input power levels above 5 dBm. This limit value is about 10 dBm and 0 dBm for 575 MHz and 2.45 GHz RF energy harvesters, respectively. For RF signals below these levels, using IMC causes a significant improvement in the efficiency. For instance, if the impedance matching process is done for -20 dBm input signal, the system efficiency is increased nearly seventy-fold. Thus, the determination of the approximate signal level of the media where the system is used is very important to make an appropriate choice of circuit for such applications. The available RF signal level is very important in order to obtain the maximum power from the system whether the impedance matching circuit is used or not. In these applications, the saturation effect is a critical parameter for the system efficiency. In both of matched and unmatched circuits, because of high frequency, the efficiencies decrease by effect of the saturation at the higher than a specific input power. In addition, the efficiency of the diode rectifier will increase until the reverse breakdown voltage of the diode. If the reverse voltage appears across the diode is greater than breakdown voltage, the diode cannot be efficiently rectifier anymore and the rest of the input power is converted to heat in the diode. This results in the decrease in the output efficiency of the RF harvester.

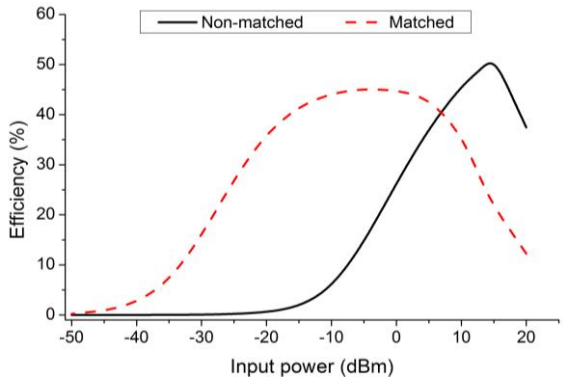

Fig. 6. The efficiency versus the input power for one stage 900 Mhz RF energy harvester.

Figure 7 shows the block diagram of triple band RF energy harvesting system used in this work. As a result of the optimization works, capacitors in the IMCs, which were used for DTV and GSM RF energy harvesters, are deactivated. So the increase in system efficiency is provided and also the cost and the size are decreased. An amount of increase in the values of used inductors has occurred. However, this situation will create any drawback in terms of cost and size.

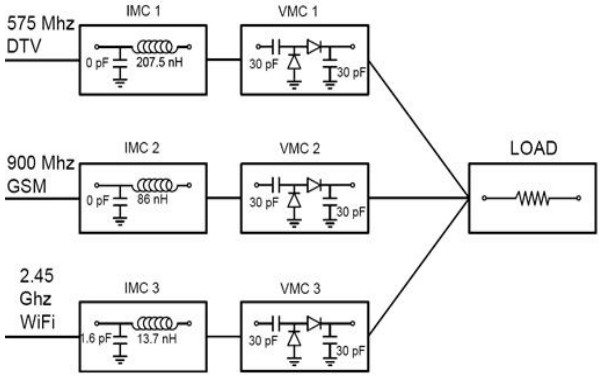

Fig. 7. The block diagram of proposed triple band RF energy harvesting system.

Figure 8 shows the efficiencies of individual DTV (575 MHz), GSM (900 MHz) and WiFi (2.45 GHz) RF energy harvesters depending on the number of the stages at 0 dBm input power. The increase in the input signal frequency decreases the system efficiency because the radiation resistance effects the system at high frequencies. The radiation resistance is directly proportional to the frequency. This resistance has an ohmic effect and causes loss. Therefore, system efficiency is dropped. The system efficiency greatly increases for this input power level as a result of the impedance matching process. But increasing the number of the stage does not cause an increase in the efficiency. As a theoretical rule, if the number of stage in voltage multipliers increases, the obtained voltage is increased, too. But there is not a big increase in the efficiency for higher numbers of stage. Even, there is a decrease in the efficiency. The reason of this situation is the effect of saturation. Considering the effect of saturation, the higher numbers of stage cannot provide a great benefit in every situation. In addition, the system efficiency is dropped the reason of saturation effect at the higher frequencies. Therefore, if the impedance matching circuit is used for this input power, increasing the number of stage is unnecessary. When considered in terms of cost and size, using one stage voltage multiplier is enough.

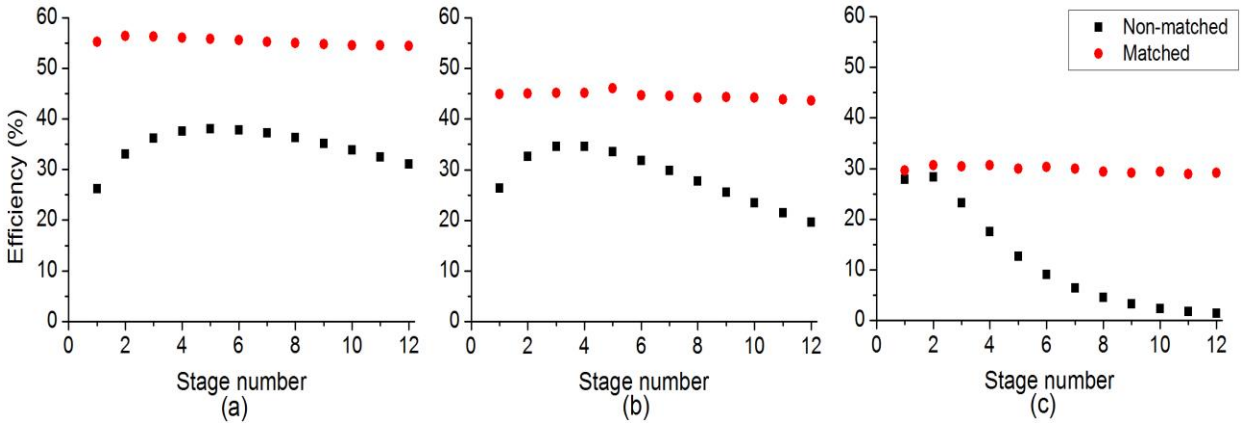

Fig. 8. The efficiency versus the number of the stages for 0 dBm input power: (a) DTV, (b) GSM, and (c) WiFi.

Figure 9 shows the system efficiency of proposed triple band RF energy harvester with one stage voltage multiplier depending on the input RF power level and the load resistance. The system efficiency depends strictly on the input RF power level and the load resistance. The load resistance values which obtained maximum power differ for each RF signal level as shown in Fig. 9. Because the system is optimized according to the 0 dBm input power, the maximum efficiency is obtained from the system while input power is 0 dBm and load resistance is about 6 kΩ. The maximum efficiency is obtained 68% at these values. When the input power level is between -15 dBm and +10 dBm, the system efficiency is realized above 30%. These values are wide range for RF energy harvester systems.

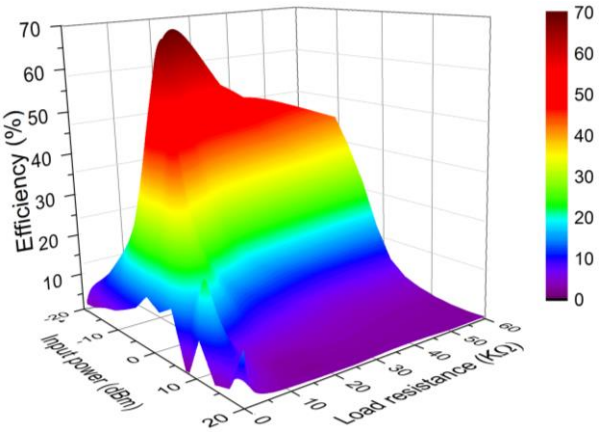

Fig. 9. The efficiency of the proposed system with one stage voltage multiplier depends on the input power and the load resistance.

At the 0 dBm input RF power level, the system efficiency can be obtained as 68% for the load resistance is about 6 kΩ, but this rate decreases to about 20% for 1 kΩ and 20 kΩ. Therefore, accurate determination of the load resistance, connected to the output of RF energy harvester has a great importance. The load impedance cannot be always in these ranges, this problem should be solved via the electronic circuits, which will be connected to the output of the system.

Table 2 shows the obtained powers and the efficiencies at all cases, which three different RF energy harvester have been used individually and one triple band RF energy harvester is used. The system efficiencies are improved significantly with the use of the proposed triple band RF energy harvester. For instance, at 0 dBm input RF power, when the individual DTV, GSM and WiFi RF energy harvesters are used, total obtained power is found to be 1297 μW; whereas, this value becomes 2045 μW for the proposed integrated triple band RF energy harvester. This proves that an increase with approximately 58% occurs in the system efficiency.

The proposed triple band RF energy harvester is increased the efficiency also in the environments where only one or two RF signals exist. The system overcomes the problem of the low efficiency for individual systems with high frequencies such as 2.45 GHz. In a media, where only 2.45 GHz RF signal is available, when the proposed triple band RF energy harvester is used instead of individual RF energy harvester, the obtained efficiency from the system increases by approximately 134%. Thus, the proposed new system can be used with high efficiency in both low and high frequencies. The obtained efficiency from the proposed system is realized as 56.70%, even in the case where only the DTV signal is 0dBm input level.

Table 2: The output powers and efficiencies for one stage individual and triple band RF energy harvesters at 0 dBm

			Individual System		Triple Band System		
575 MHz	900 MHz	2.45 GHz	Power (μW)	Efficiency (%)	Power (μW)	Efficiency (%)	Difference %
✓	✓	✓	1297	43.27	2045	68.18	+57.57
✓	✓		1000	50.02	1324	66.21	+32.36
✓		✓	848	42.41	1289	64.43	+51.92
	✓	✓	745	37.26	1448	72.42	+94.36
✓			552	55.17	567	56.70	+2.77
	✓		449	44.86	726	72.57	+61.77
		✓	297	29.65	694	69.35	

IV. CONCLUSIONS

The voltage multiplier circuits must be used in RF energy harvester, because obtained voltage is very low in scale. The obtained voltage and the harvested power directly depend on the input RF signal level. The impedance matching process significantly increases the obtained power from the system especially at low levels input RF signals. Therefore, if there are low level input signals for the RF energy harvesting, the impedance matching must be used. But the impedance matching process cannot provide a major contribution to the harvested power at the high levels input RF signals such as 20 dBm. The high levels of input RF signal do not always mean the high efficiency. In this work, the maximum efficiency has been obtained in the case, which the input signal is 0 dBm. With the use of proposed triple band RF energy harvester, the efficiency is increased by 58% compared to the conventional individual systems having three different frequencies. Furthermore, the system is increased the efficiency significantly also in environments, where only one or two RF signals exist.

REFERENCES

[1] H. Jabbar, Y. S. Song, and T. T. Jeong, "RF energy harvesting system and circuits for charging of mobile devices," *IEEE Trans. on Consumer Electron.*, vol. 56, no. 1, pp. 247-253, Feb. 2010.

[2] A. Rahimi, O. Zorlu, A. Muhtaroglu, and H. Kulah, "An electromagnetic energy harvesting system for low frequency applications with a passive interface ASIC in standard CMOS," *Sensor Actuat. A-Phys.*, vol. 188, pp. 158-166, Dec. 2012.

[3] Z. W. Sim, R. Shuttleworth, M. J. Alexander, and B. D. Grieve, "Compact patch antenna design for outdoor RF energy harvesting in wireless sensor networks," *Prog. Electromagn. Res.*, vol. 105, pp. 273-294, June 2010.

[4] K. Chang, S. Kang, K. Park, S. Shin, H. S. Kim, and H. Kim, "Electric field energy harvesting powered wireless sensors for smart grid," *J. Electrical Eng. & Tech.*, vol. 7, no. 1, pp. 75-80, Jan. 2012.g

[5] Y. Uzun, S. Demirbas, and E. Kurt, "Implementation of a new contactless piezoelectric wind energy harvester to a wireless weather station," *Elektron Elektrotech.*, vol. 20, no. 10, pp. 35-39, 2014.

[6] M. L. Sichitiu and R. Dutta, "On the lifetime of large wireless sensor networks with multiple battery levels," *Ad Hoc Sens. Wirel.*, vol. 4, no. 1-2, pp. 69-96, 2007.

[7] K. Eguchi, K. Fujimoto, and H. Sasaki, "A hybrid input charge-pump using micropower thermoelectric generators," *IEEJ T. Electr. Electr.*, vol. 7, no. 4, pp. 415-422, 2012.

[8] U. Alvarado, A. Juanicorena, I. Adin, B. Sedano, I. Gutiérrez, and J. de Nó, "Energy harvesting technologies for low-power electronics," *T. Emerg. Telecommun. T.*, vol. 23, no. 8, pp. 728-741, 2012.

[9] T. Wu and H. C. Yang, "On the performance of overlaid wireless sensor transmission with RF energy harvesting," *IEEE J. Sel. Area Comm.*, vol. 33, no. 9, pp. 1-12, 2015.

[10] S. Sudevalayam and P. Kulkarni, "Energy harvesting sensor nodes: survey and implications," *Commun. Surveys Tuts.*, vol. 13, no. 3, pp. 443-461, 2011.

[11] Y. Uzun and E. Kurt, "The effect of periodic magnetic force on a piezoelectric energy harvester," *Sensor Actuat. A-Phys.*, vol. 192, pp. 58-68, 2013.

[12] U. Olgun, C. C. Chen, and J. L. Volakis, "Design of an efficient ambient WiFi energy harvesting system," *IET Microw. Antenna P.*, vol. 6, no. 11, pp. 1200-1206, 2012.

[13] L. Guenda, E. Santana, A Collado, K. Niotaki, N. B. Carvalho, and A. Georgiadis, "Electromagnetic energy harvesting-global information database," *Trans. Emerg. Telecom. Tech.*, vol. 25, no. 1, pp. 56-63, 2014.

[14] A. Costanzo, A. Romani, D. Masotti, N. Arbizzani, and V. Rizzoli, "RF/baseband co-design of switching receivers for multiband microwave energy harvesting," *Sensor Actuat. A-Phys.*, vol. 179, pp. 158-168, June 2012.

[15] D. Masotti, A. Costanzo, M. D. Prete, and V. Rizzoli, "Genetic-based design of a tetra-band high-efficiency radio-frequency energy harvesting

system," *IET Microw. Antenna P.*, vol. 7, no. 15, pp. 1254-1263, 2013.

[16] D. Bouchouicha, F. Dupont, M. Latrach, and L. Ventura, "Ambient RF energy harvesting," *Int. Conf. on Renewable Energies and Power Quality*, Granada, Spain, pp. 1-5, Mar. 2010.

[17] R. Shigeta, T. Sasaki, D. M. Quan, Y. Kawahara, R. Vyas, M. Tentzeris, and T. Asami, "Ambient-RF-energy-harvesting sensor node with capacitor-leakage-aware duty cycle control," *IEEE Sensors J.*, vol. 13, pp. 2973-2983, 2013.

[18] L. Xiao, W. Ping, D. Niyato, and E. Hossain, "Dynamic spectrum access in cognitive radio networks with RF energy harvesting," *IEEE Wirel. Commun.*, vol. 21, no. 3, pp. 102-110, 2014.

[19] K. Xie, Y. M. Liu, H. L. Zhang, and L. Z. Fu, "Harvest the ambient AM broadcast radio energy for wireless sensors," *J. Electromagnet. Wave.*, vol. 25, pp. 2054-2065, 2011.

[20] N. M. Din, C. K. Chakrabarty, A. B. Ismail, K. A. Devi, and W. Y. Chen, "Design of RF energy harvesting system for energizing low power devices," *Prog. Electromagn. Res.*, vol. 132, pp. 49-69, 2012.

[21] C. Wanga, M. Park, W. Zhao, G. Liu, Z. Dilli, and M. Peckerar, "An ultra-low power regulator system for WSNs powered by energy harvesting," *Solid State Electron.*, vol. 101, pp. 38-43, 2014.

[22] B. L. Pham and A. V. Pham, "Triple bands antenna and high efficiency rectifier design for RF energy harvesting at 900, 1900 and 2400 MHz," *IEEE MTT-S International Microwave Symposium Digest*, Seattle, USA, pp. 1-3, June 2013.

[23] S. Keyrouz, H. J. Visser, and A. G. Tijhuis, "Multi-band simultaneous radio frequency energy harvesting," *7th European Conference on Antennas and Propagation*, Gothenburg, Sweden, pp. 3058-3061, Apr. 2013.

[24] P. Kim, G. Chaudhary, and Y. Jeon, "A dual-band RF energy harvesting using frequency limited dual-band impedance matching," *Prog. Electromagn. Res.*, vol. 141, pp. 443-461, 2013.

[25] D. M. Pozar, *Microwave Engineering*, John Wiley & Sons, Inc., USA, 2011.

[26] P. Nintanavongsa, U. Muncuk, D. R. Lewis, and K. R. Chowdhury, "Design optimization and implementation for RF energy harvesting circuits," *IEEE Trans. Emerg. Sel. Topics Circuits Syst.*, vol. 2, no. 1, pp. 24-33, 2012.

[27] A. Nimo, T. Beckedahl, T. Ostertag, and L. Reindl, "Analysis of passive RF-DC power rectification and harvesting wireless RF energy for micro-watt sensors," *AIMS Energy*, vol. 3, no. 2, pp. 184-200, 2015.

[28] HSMS-285x Series, *Surface Mount Zero Bias Schottky Detector Diodes*, Datasheet, Avago Tech., 2009.

[29] A. Nimo, J. Albesa, and L. M. Reindl, "Investigating the effects of parasitic components on wireless RF energy harvesting," *11th Int. Conf. on Multi-Conference on Systems, Signals & Devices*, Barcelona, Spain, pp. 1-6, Feb. 2014.

[30] H. J. Visser, V. Pop, B. O. H. Veld, and R. J. M. Vullers, "Remote RF battery charging," *Proceedings of Power MEMS 2010*, Leuven, Belgium, pp. 37-40, Dec. 2010.

Yunus Uzun received his B.S., M.Sc. and Ph.D. degrees from the Gazi University in 2000, 2004 and 2012, respectively. He worked as a High School Teacher on electrics from his graduation to 2008. He was a Lecturer in the Department of Electrics and Energy of Ahi Evran University for 6 years. Then he was assigned to the Assist. Prof. Dr. position in the Dept. Electrical and Electronics Engineering of Aksaray University in 2014. His main research area focuses on the experimental and theoretical explorations of energy harvesting systems.

Analysis of Dual-Reflector Antenna for Radar Applications

A. Imani [1], M. Soleimani [1], and S. Amiri [2]

[1] Department of Electrical Engineering
Iran University of Science and Technology, Tehran, Iran
aliimani@iust.ac.ir, soleimani@iust.ac.ir

[2] Department of Electrical and Computer Engineering
Iranian Research Organization for Science and Technology, Tehran, Iran
amiri@irost.ir

Abstract ─ A dual-reflector antenna in millimeter wave frequency band is designed at center frequency of 35 GHz. The designed antenna has small size, low weight, fast beam scanning, high efficiency and high gain. Beam rotation of the proposed structure makes it useful for wide angle scanning in modern airborne radar systems. In the literature, beam rotation of similar structures used to be evaluated by two times of the twist-reflector rotation. For the first time, a nonlinear relationship is found between beam rotation and twist-reflector rotation. This nonlinear relation is theoretically extracted in this work. Furthermore, the designed antenna is simulated with a commercial full wave package. The results confirm that the designed goals are addressed. Moreover, the simulation results validate the extracted analytic relationship between beam rotation and twist-reflector rotation. In addition, low VSWR, low cross-polarization and good radiation pattern are observed.

Index Terms ─ Antenna radiation pattern, beam scanning, dual-reflector, feed horn, millimeter wave, polarization, trans-reflector, twist reflector.

I. INTRODUCTION

Airborne radar systems have many requirements such as small size, low weight, fast beam scanning, high efficiency and high gain. A reflector antenna is a good choice for low cost and high efficiency [1-4].

A dual-reflector antenna is compact, like a Cassegrain reflector antenna; but, it delivers high efficiency, high gain and low sidelobe levels of a prime-focus reflector. The dual-reflector antenna, as a compact option for the Cassegrain, has performed more comparably to a prime-focus reflector antenna. The antennas in millimeter wave frequency bands can have physically small sizes; yet, they can achieve gains in excess of 30 dB [5-11].

This antenna is composed of three parts: the main reflector (twist reflector), sub-reflector (trans-reflector) and feed horn. Details of the design method of a dual-reflector antenna and its parts are explained below.

Trans-reflector is a parabola structure which acts as both a reflector antenna and a radome. The trans-reflector is made of conductive-strip grating embedded in a shaped dielectric molding [12]. It is easy to see that a large sub-reflector blocks effective area of the main reflector (aperture blocking phenomenon). However, if only one polarization is permissible, this adverse effect can be considerably decreased.

Consider the antenna in transmitting mode, as in Fig. 2. A feed horn antenna with linear polarization illuminates the trans-reflector that its electric field vector is aligned parallel to the conductive strip grating. The strips are arranged orderly beside each other so that the trans-reflector collects and then reflects the incident wave with considerable reduction in escaping waves to the space. While the twist-reflector receives the reflected radiation from the trans-reflector, the twist-reflector rotates field vector 90 degrees and then redirects it toward the trans-reflector. The electric field polarization is perpendicular to the trans-reflector's strips grating direction, and then it passes through the trans-reflector into the space with an inconsiderable loss.

The attenuation versus frequency diagram for oxygen and water vapor is shown in Fig. 1 [13]. This diagram shows some minimum attenuation at special frequencies such as 35, 94 and 225 GHz. Here, the antenna design frequency is selected 35 GHz.

In this article, analysis, design, simulation and optimization of dual-reflector antenna is described. A dual-reflector antenna is designed in millimeter wave frequency band. The theory and relations of this design are also extracted in this work. Then, it is focused on design methods of antenna parts, including the trans-reflector, twist-reflector and feed horn.

Submitted On: April 22, 2014
Accepted On: October 22, 2015

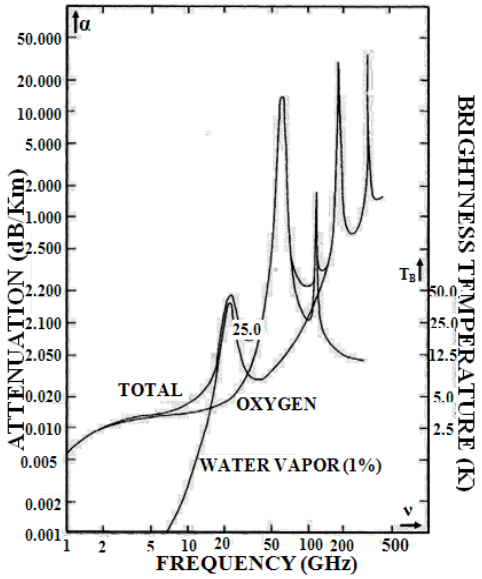

Fig. 1. Attenuation versus frequency diagram for oxygen and water vapor.

II. ANTENNA CONFIGURATION

The proposed antenna is divided to three parts: a feed horn, a trans-reflector, and a twist-reflector as revealed in Fig. 2. The design method of any part is discussed below.

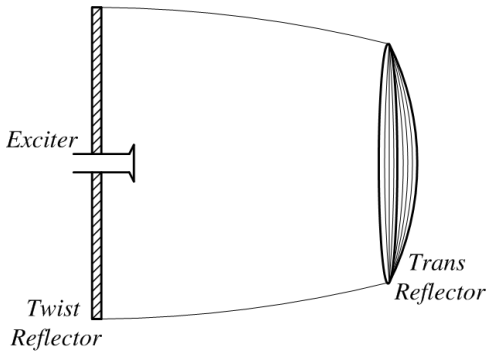

Fig. 2. Configuration of the proposed antenna.

A. Feed horn design

The feed horn antenna is designed specifically for the millimeter wave frequency band for which, the most essential requirements are as follows: 1- to keep the input return loss high throughout the operating frequency interval, and 2- to optimize the E- and H-plane beam width maximizing performance (gain). Figure 3 shows the designed horn antenna and its dimensions.

Dimensions of the designed horn antenna are a=9 mm, b=10 mm, and l=20 mm as noted in Fig. 3. The simulation results for return loss of the antenna are shown in Fig. 4 which confirms the satisfactory return loss suitable for feeding.

Figure 5 demonstrates the simulated power radiation patterns at the center frequency (35 GHz) in both E- and H-planes.

Since the horn antenna has a phase center, the best performance of dual-reflector antenna can be achieved when the phase center of horn antenna is located at the trans-reflector focal point.

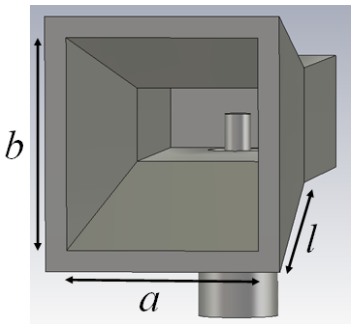

Fig. 3. Designed horn antenna.

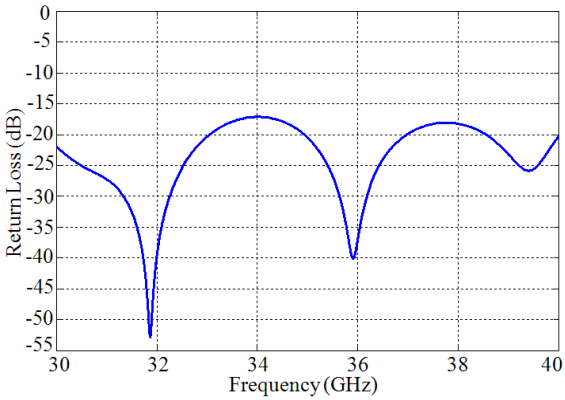

Fig. 4. Return loss of the horn antenna.

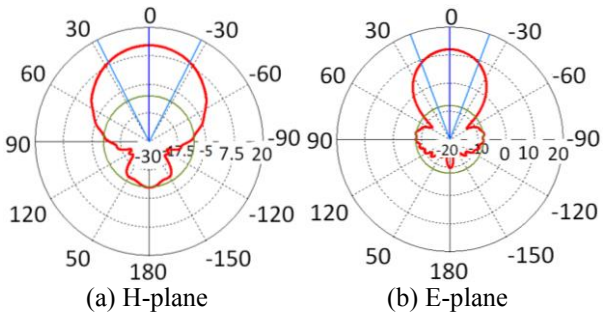

Fig. 5. Radiation pattern of the horn antenna for 35 GHz.

B. Trans-reflector design

The trans-reflector has a periodic structure which includes a set of embedded conductive strips grating inside a dielectric layer, as shown in Fig. 6. This structure does two functions: first, it acts as a reflector which collocates feed-horn radiation and second, it is a

radome to collocate the returned energy from the twist-reflector. The function of the trans-reflector is almost dependent on the polarization of the incident electric field.

Whenever the electric field is parallel to the strips (as in Fig. 6) we call it a reflect-polarized because the field reflects; otherwise we call it a thru-polarized because the field passes through the strip grating. Since the grating has not a continuous conductive surface, there is some loss in the reflected polarization. For the thru-polarized signal, the trans-reflector acts like a radome.

This structure has a parabolic shape. The dimensions of the proposed antenna are as follows: W_t=1 mm and S_t=1 mm, where W_t is the strip width and S_t is the space between the strips.

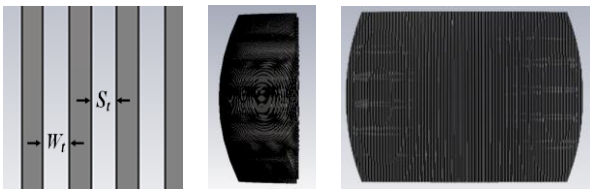

(a) Strip grating (b) Side view (c) Front view

Fig. 6. Trans-reflector structure.

C. Twist-reflector design

A planar reflection structure has been used to rotate the incident electromagnetic wave. For economical reasons, a dielectric twist-reflector is used: a quarter-wave, ground-plane-backed and dielectric layer printed with conductive strip grating.

Figure 7 shows the twist-reflector and a vertically polarized incident electric field on its conductive strips grating. The conductive strips and the incident electric field are making 45 degrees angle.

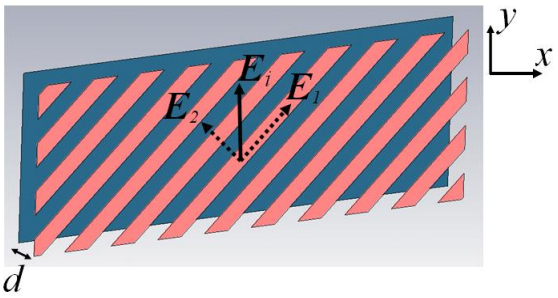

Fig. 7. Twist-reflector structure.

The incident electric field can be decomposed into parallel and perpendicular components with respect to the strips which will be reflected and transmitted, respectively. The transmitted perpendicular component travels through the dielectric substrate and will be reflected by the ground plane.

Assume the incident electric field vector is y-directed,

$$E_i = E_0\, e^{-j\beta z}\, \hat{y}, \tag{1}$$

where E_0 is the incident electric field amplitude, β is the wave number and z is the propagation direction. Then, the parallel and perpendicular components are:

$$\begin{aligned} E^i_{r1} &= E_i \cos\theta\left(\hat{x}+\hat{y}\right) = E_0\, e^{-j\beta z}\cos\theta \quad \left(\hat{x}+\hat{y}\right), \\ E^i_{t1} &= E_i \cos\theta\left(-\hat{x}+\hat{y}\right) = E_0\, e^{-j\beta z}\cos\theta\,\left(-\hat{x}+\hat{y}\right), \end{aligned} \tag{2}$$

where E^i_{r1} is parallel component and E^i_{t1} is perpendicular component and their reflection of the ground plane are:

$$\begin{aligned} E^r_{r2} &= E_i \cos\theta\left(\hat{x}+\hat{y}\right) = E_0\, e^{+j\beta z}\cos\theta\left(\hat{x}+\hat{y}\right), \\ E^r_{t2} &= E_i\, e^{-j\beta d\times 2}\cos\theta\left(\hat{x}-\hat{y}\right) \\ &= E_0\, e^{+j\beta z}\, e^{-j\beta d\times 2}\cos\theta\,\left(\hat{x}-\hat{y}\right), \end{aligned} \tag{3}$$

where E^r_{r2} is the reflection of E^r_{r1}, E^r_{t2} is the reflection of E^i_{t1} and d is the substrate thickness. Therefore, the total field is:

$$\begin{aligned} E^r_t &= E^i_{r1} + E^r_{t2} \\ &= E_0\, e^{j\beta z}\cos\theta\left(\hat{x}+\hat{y}+e^{j\beta d\times 2}\left(-\hat{x}+\hat{y}\right)\right) \\ &= E_0\cos\theta e^{j\beta z}\left\{\hat{x}\left(1-e^{-j2\beta d}\right)+\hat{y}\left(1+e^{-j2\beta d}\right)\right\}, \end{aligned} \tag{4}$$

where E^r_t is the total reflected field.

To transmit the reflected wave through the trans-reflector, the electric field polarization must be horizontal (perpendicular to the trans-reflector conductive strips grating). Therefore, the reflected electric field polarization must be rotated 90 degrees relative to the incident electric field polarization.

By choosing the strip width and spacing and the substrate thickness properly, the phase difference between the two electric field components can be set as 180 degrees. Thus, rotating the total reflected electric field 90° relative to the incident electric field.

So, the electric field component in y direction must be zero:

$$\begin{aligned} &1+e^{-j2\beta d}=0 \;\Rightarrow -2\beta d=-\pi \quad , \quad \beta=\frac{2\pi}{\lambda} \\ &2\times\frac{2\pi}{\lambda}\times d=\pi \;\Rightarrow\; d=\frac{\lambda}{4}. \end{aligned} \tag{5}$$

Therefore, the substrate thickness is λ/4. The dual-reflector antenna dimensions are much larger than the operational wavelength. Therefore, the edge effects can be ignored.

III. THE RELATION BETWEEN THE TWIST-REFLECTOR ROTATION ANGLE AND THE BEAM ROTATION ANGLE

The antenna coordination is shown in Fig. 8, where –z is the direction of the incident wave and the normal unit vector on the twist-reflector is:

$$\hat{n}=\cos(el)\sin(az)\hat{x}+\sin(el)\hat{y}+\cos(az)\cos(el)\hat{z}, \quad (6)$$

where the *az* and *el* are rotation angles in azimuth and elevation directions, respectively.

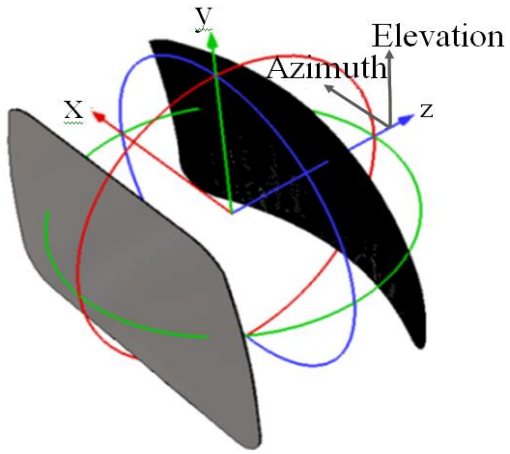

Fig. 8. Antenna coordination.

The propagation direction vector can be into the tangential and perpendicular components as:

$$\hat{I}_t=\left(\hat{I}.\hat{n}\right)\hat{n}, \quad (7)$$

$$\hat{I}_p=\hat{I}-\hat{I}_t=\hat{I}-\left(\hat{I}.\hat{n}\right)\hat{n}, \quad (8)$$

where I_t and I_p are the tangential and perpendicular components, respectively.

As is revealed in the Fig. 9, the perpendicular vector direction remains the same for both incident and reflection states; but, the tangential component direction inverses from the reflection state to the incident state. Therefore,

$$\begin{aligned}\hat{r}&=\hat{I}_p-\hat{I}_t\\&=\hat{I}-\left(\hat{I}\cdot\hat{n}\right)\hat{n}-\left(\hat{I}\cdot\hat{n}\right)\hat{n}=\hat{I}-2\left(\hat{I}\cdot\hat{n}\right)\hat{n},\end{aligned} \quad (9)$$

where $\hat{r}$ is the reflection vector direction. By use of equation (6) into equation (9),

$$\begin{aligned}\hat{r}&=\sin(2az)\cos^2(el)\hat{x}+2\cos(az)\cos(el)\sin(el)\hat{y}\\&+\left(a\cos^2(az)\cos^2(el)-1\right)\hat{z},\end{aligned} \quad (10)$$

where *az* and *el* are twist-reflector rotation angles in azimuth and elevation directions, respectively. Then, the beam vector direction is:

$$\begin{aligned}\hat{r}&=\cos(el_r)\sin(az_r)\hat{x}+\sin(el_r)\hat{y}\\&+\cos(az_r)\cos(el_r)\hat{z},\end{aligned} \quad (11)$$

where the az_r and el_r are the beam rotation angles in azimuth and elevation directions, respectively.

Using equations (10) and (11), the beam rotation angles are:

$$el_r=\sin^{-1}\left(2\cos(az)\cos(el)\sin(el)\right), \quad (12)$$

$$az_r=\tan^{-1}\left[\frac{\sin(2az)\cos^2(el)}{2\cos^2(az)\cos^2(el)-1}\right]. \quad (13)$$

In this state, the beam rotation angle will clear when the *az* and *el* is known.

Assuming (az_r,el_r) as the antenna vector direction, as shown in the Fig. 8, the normal vector is:

$$\hat{n}=\frac{\hat{r}-\hat{I}}{\left|\hat{r}-\hat{I}\right|}, \quad (14)$$

$$\begin{aligned}\hat{n}=&\frac{\sqrt{2}\cos(el_r)\sin(az_r)}{2\sqrt{\cos(az_r)\cos(el_r)+1}}\hat{x}+\frac{\sqrt{2}\sin(el_r)}{2\sqrt{\cos(az_r)\cos(el_r)+1}}\hat{y}\\&+\frac{\sqrt{2\cos(az_r)\cos(el_r)+2}}{2}\hat{z}.\end{aligned} \quad (15)$$

The normal vector direction in azimuth and elevation rotation angles (*az*, *el*) is:

$$\begin{aligned}\hat{n}=&\cos(el)\sin(az)\hat{x}+\sin(el)\hat{y}\\&+\cos(az)\cos(el)\hat{z}.\end{aligned} \quad (16)$$

Equations (15) and (16) give the antenna rotation angles:

$$el=\sin^{-1}\left(\frac{\sqrt{2}\sin(el_r)}{2\sqrt{\cos(az_r)\cos(el_r)+1}}\right), \quad (17)$$

$$az=\tan^{-1}\left(\frac{\frac{\sqrt{2}\cos(el_r)}{\sqrt{\cos(az_r)\cos(el_r)+1}}\times}{\frac{\sin(az_r)}{\sqrt{2\cos(az_r)\cos(el_r)+2}}}\right). \quad (18)$$

According to the above equations, the twist-reflector rotation angle versus beam rotation angle in azimuth and elevation directions are indicated in Fig. 10, in which the difference between the linear state (mirror law) and nonlinear state (the above equations) is clear.

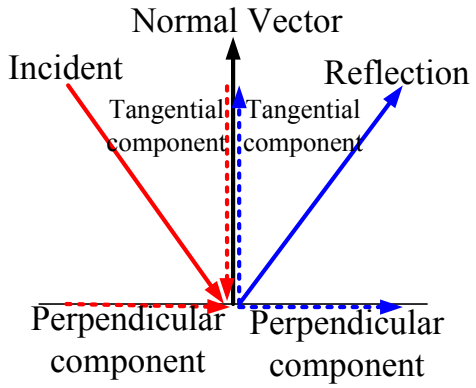

Fig. 9. Incident and reflection state.

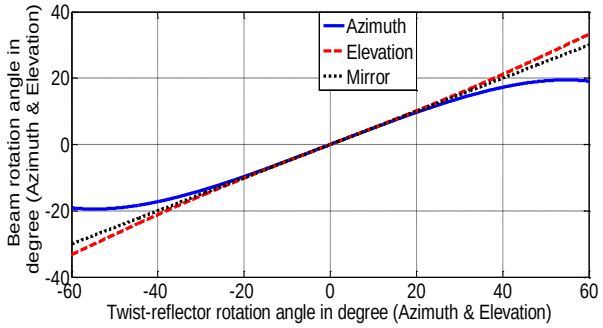

Fig. 10. The twist-reflector rotation angle versus beam rotation angle in azimuth and elevation.

IV. SIMULATION AND RESULTS

Configuration of the dual-reflector antenna is given in Fig. 11. The proposed antenna is simulated with commercially available packages such as CST microwave studio in the operating frequency range. This antenna has very high gain, narrow beam-width and very good sidelobe level. The simulated radiation pattern of the dual-reflector antenna is shown in Fig. 12.

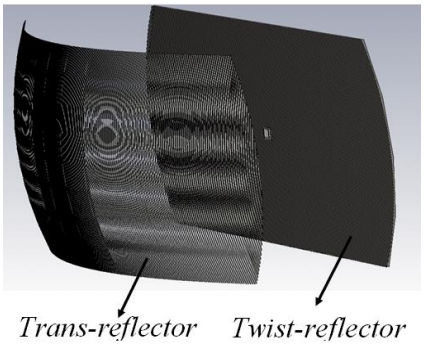

Fig. 11. Configuration of dual-reflector antenna.

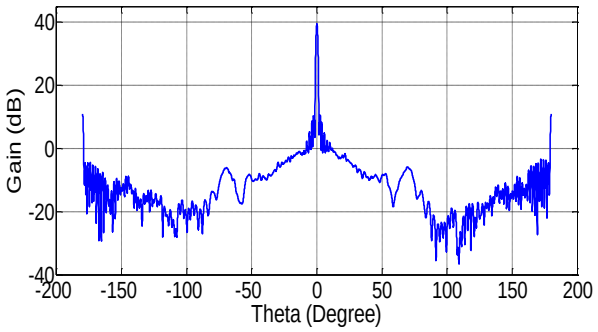

Fig. 12. Simulated radiation pattern at frequency of 35 GHz.

This antenna has fast beam scanning capability. The radiation patterns for various azimuth scan angles (0°, 30° and 60°), *el*=0, and for various elevation scan angles (0°, 20° and 30°), *az*=0, are respectively shown in Figs. 13 and 14 that their specifications are numerically listed in Table 1.

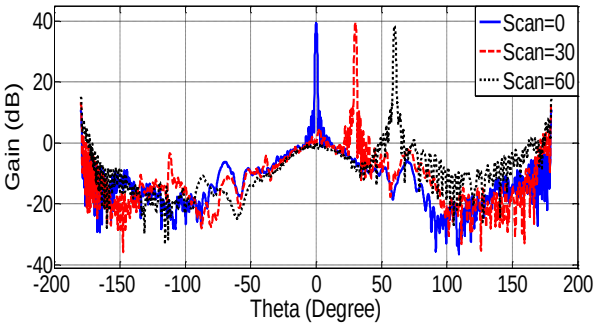

Fig. 13. Radiation pattern in azimuth scan.

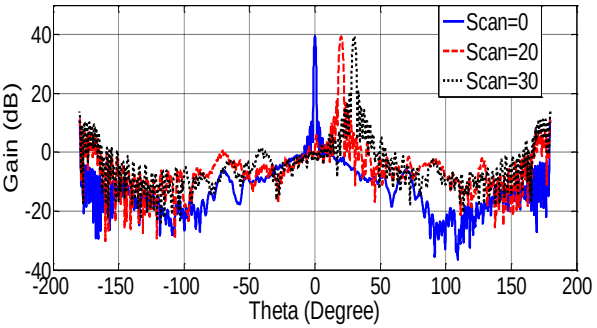

Fig. 14. Radiation pattern in elevation scan.

Table 1: Specification of radiation pattern

Scan Angle (degree)	0°	30°	60°
Gain (dB)	39.4	39.2	38.5
HPBW (degree)	1.2	1.2	1.3
S.L.L	-28.5	-26.1	-23.3

The linear and nonlinear equations (Eqs. 12 and 13) are equal in a specific circumstance whenever *el*=0 or *az*=0. Otherwise, if the *az* and *el* angles are not zero simultaneously, the radiation pattern will become different for two mentioned equations. For instance, if *el*=10 and *az*=15 are putted in linear and nonlinear equations, results will be el_r=20 and az_r=30, el_r=19.29 and az_r=30.91 respectively.

Regarding to simulation results, the radiation pattern is shown in Fig. 15 for two elevation planes, el_r=20 and el_r=19.29. It is apparent that the peak of pattern is located in el_r=19.29 rather than el_r=20. This trend is also repeated for two azimuth planes, az_r=30 and az_r=30.91 in Fig. 16. A plane included the peak of pattern is desirable. Therefore, the proposed nonlinear equation is absolutely correct. For more clarifications of Figs. 15 and 16, specifications of the radiation patterns are numerically listed in Table 2.

Regarding to the Table 2, the gain is decreased 6.3 dB in the plane az_r=30 rather than az_r=30.91 in azimuth direction, and 1.3 dB in the plane el_r=20 rather than el_r=19.29. As a result, the beam scanning is not correct without the using of nonlinear equation for this structure.

Figurre 17 shows simulated co- and cross-polar far-field radiation patterns at frequency of 35 GHz. From this figure, it is seen that the designed antenna exhibits low cross-polarization which its level is less than -40 dB.

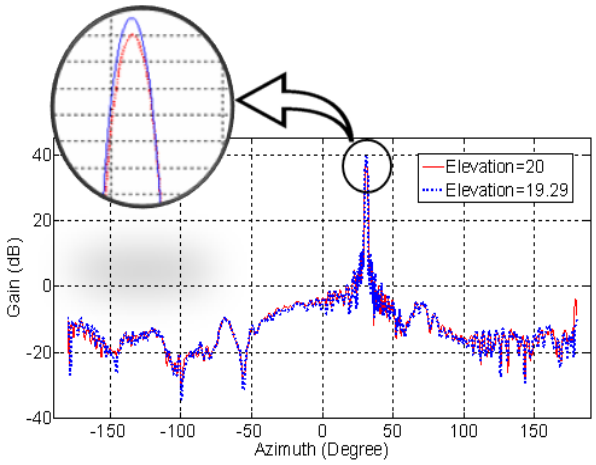

Fig. 15. Radiation pattern in elevation scan.

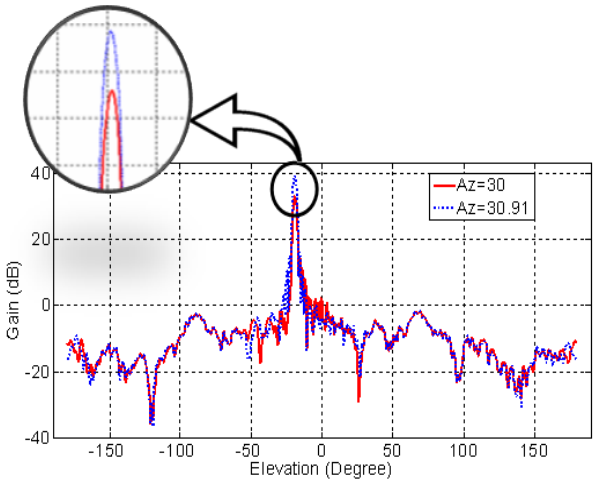

Fig. 16. Radiation pattern in azimuth scan.

Table 2: Specification of radiation pattern

Direction / Specification	In Azimuth		In Elevation	
Angle (degree)	30	30.91	20	19.29
Gain (dB)	33	39.3	38	39.3
HPBW(degree)	2.2	2.2	1.3	1.3
SLL (dB)	-18.4	-23.2	-28.3	-28.6

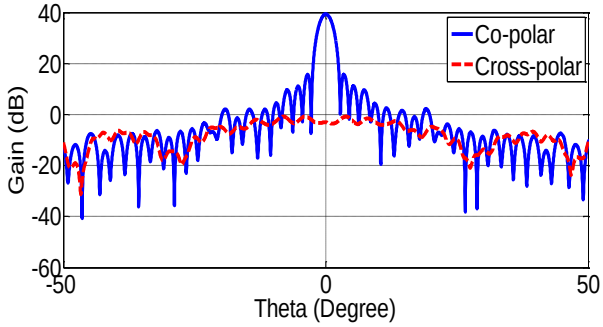

Fig. 17. Comparison of co- and cross-polarization.

V. CONCOLUSION

In this paper, a dual-reflector antenna has been presented at center frequency of 35 GHz. This antenna is a type of Cassegrain which equipped with two reflectors: a flat (twist-reflector) and a parabola (trans-reflector). A new formula is extracted in the relation between the twist-reflector mechanical movement and the beam rotation angle. Without this formula the beam scanning is not correct. This antenna has small size, low weight, fast beam scanning, wide angle beam scanning, low cross-polarization, high efficiency and high gain. The designed antenna has good far-field radiation characteristics in the entire operating bandwidth in both azimuth and elevation directions. The antenna presents beam scanning capability ±60° in azimuth and ±30° in elevation by mechanical movement of the twist-reflector. Based on these characteristics, the proposed antenna can be useful for airborne radar systems and millimeter wave applications.

REFERENCES

[1] J. Shalit, "The manufacture of airborne Cassegrain antenna," *IEEE Symposium on Mechanical Engineering in Radar*, pp. 220-224, Nov. 1977, IEEE Pub 77CH1250-0-AES.

[2] B. L. Lewis and J. P. Shelton, "Mirror scan antenna technology," *International Radar Conference*, pp. 279-283, Apr. 1980.

[3] D. D. Howard, D. C. Cross, and H. Poor, "Mirror-antenna dual band lightweight mirror design," *IEEE Transaction on Antenna and Propagation*, vol. 33, pp. 286-294, Mar. 1985.

[4] D. C Cross, D. D. Howard, and J. W. Titus, "Mirror-antenna radar concept," *Microwave Journal*, vol. 29, pp. 323-324, May 1986.

[5] K. S. Kellejer and G. Hyde, *Reflector Antennas*, in R. C. Johnson and H. Jasik (eds.), Antenna Engineering Handbook, Second Edition, New York, McGraw-Hill, ch. 17, p. 29, 1984.

[6] E. L. Holzman, "Transreflector antenna design for millimeter-wave wireless links," *IEEE Antennas*

and Propagation Magazine, vol. 47, no. 5, pp. 9-22, Oct. 2005.

[7] H. Haiden, L. Xiumei, and C. Zhangliang, "Design of fast-scanning millimeter-wave monopulse antenna," *International Conference on Radar*, pp. 1-4, Oct. 2006.

[8] Z. Hussein, K. Green, E. Im, and S. Durden, "Design of offset reflector with elliptical flat scan mirror and its applications to a dual-frequency, dual-polarization airborne rain radar observation," *IEEE International Symposium on Antennas and Propagation Society*, vol. 1, pp. 642-645, 2002.

[9] L. K. De Size and J. F. Ramsay, *Reflecting Systems*, in R. C. Hansen (ed.), Microwave Scanning Antennas, Los Altos, CA, Peninsula Press, pp. 127-128, 1985.

[10] C. A. Cochrane, *High Frequency Radio Aerials*, US Patent 2,736,895, Feb. 28, 1956.

[11] E. O. Houseman, "A millimeter wave polarization twist antenna," *IEEE International Symposium on Antennas and Propagation Society*, vol. 16, pp. 51-54, May 1978.

[12] R. A. Vandendolder and G. D. Winslow, *Insert Mold Process for Forming Polarizing Grid Element*, US Patent 6,246,381, June 12, 2001.

[13] http://www.propagation.gatech.edu/ECE6390/project/Fall2012/Team07/Space%20Reach%20Website/index_files/Page785.htm.

Ali Imani was born in Iran in 1982. He received the B.S. degree in Electrical Engineering from Tabriz University, Tabriz, Iran, in 2006 and M.S. degree in Electrical Engineering from Shahed University, Tehran, Iran, in 2009. He is currently working toward the Ph.D. degree at Iran University of Science and Technology, Tehran, Iran. His research interests include slot antennas, wideband antennas, millimeter-wave antennas, analysis and design of microstrip antennas, radar systems and electromagnetic theory.

Mohammad Soleimani received the B.S. degree in Electrical Engineering from the University of Shiraz, Shiraz, Iran, in 1978 and the M.S. and Ph.D. degrees from Pierre and Marie Curio University, Paris, France, in 1981 and 1983, respectively.

Currently, he is a Professor with the Iran University of Sciences and Technology, Tehran, Iran. His research interests include computational electromagnetic and antennas.

Shervin Amiri was born in Iran in 1966. He received the B.S., M.S., and Ph.D. degrees in Electrical Engineering from the Iran University of Science and Technology, Tehran, in 1988, 1994, and 1999, respectively. He is currently an Assistant Professor in the Electrical and Computer Engineering Department of IROST. His research interests include satellite communication and microwave and millimeter-wave antennas.

Series Solution to the Radiation from Slotted Antenna on Elliptic Cylinder Coated by Biaxial Anisotropic Material

A-K. Hamid

Dept. of Electrical and Computer Engineering, College of Engineering
University of Sharjah, UAE
akhamid@sharrjah.ac.ae

Abstract — Radiation characteristics of an axially slotted circular or elliptical antenna coated by biaxial anisotropic material are investigated using series solution. The fields inside and outside the coating regions are expressed in terms of appropriate Mathieu functions with unknown field coefficients. The boundary conditions at the conducting and dielectric coating surfaces are invoked to obtain the unknown field expansion coefficients. Numerical results are presented graphically for the radiation pattern with various geometries and electrical parameters.

Index Terms — Axially slotted elliptic antenna, biaxial anisotropic material, Mathieu functions, series solution.

I. INTRODUCTION

Numerous scholars in the literature have studied the characteristic radiation by dielectric coated slotted circular and elliptical cylinders [1-6]. Investigation on the radiation by axially N slotted elliptical antenna coated with lossy dielectric material was conducted by Hussein and Hamid [7]. Recently, materials possessing both lossy and lossless metamaterials as well as chiral material have gained considerable attention by several researchers [8-10], while possessing anisotropic materials have been studied by [11-13]. The anisotropic material coating is important to investigate since the electrical characteristics of coated antenna are not uniform in all directions [14-15]. Antennas with anisotropic dielectric coating may have application in satellite communication, space aircraft and airplanes industries.

To the best of our knowledge, the radiation produced by an axially slotted circular or elliptical cylinder coated with biaxial anisotropic material has not been investigated using series solution.

This paper presents series solution to the radiation by an axially slotted antenna on a conducting elliptic cylinder coated with biaxial anisotropic material based on the boundary value method. The presented numerical results will show the effect of biaxial anisotropic material coating on the radiation pattern of slotted antenna.

II. FORMULATION

The geometry of conducting elliptic cylinder with axially slotted antenna covered by biaxial anisotropic material is shown in Fig. 1. The antenna is assumed to be infinite in the z-axis. The antenna parameters a_c and b_c represent the conducting core semi-major and semi-minor axes, respectively, while a and b are the semi-major and semi-minor axes of the dielectric coating material. The axial antenna slot coordinates are denoted by v_1 and v_2. The relation between the elliptical (u, v, z) and Cartesian coordinate systems (x, y, z) is:

$$x = F\cosh(u)\cos(v), \tag{1}$$

$$y = F\sinh(u)\sin(v), \tag{2}$$

where F is the semifocal length of the elliptical antenna. The radiated electric field exterior to the biaxial anisotropic dielectric coating (region I and $\xi > \xi_1$) can be expressed in terms of Mathieu functions as follows [16]:

$$E_z^I = \sum_{q,m}^{\infty} C_{qm} R_{qm}^{(4)}(c\ ,\xi) S_{qm}(c_0, \eta), \tag{3}$$

where $q = e, o$, C_{qm} are the unknown radiated field expansion coefficients, S_{qm} are the angular Mathieu functions of order m, while $R_{qm}^{(4)}$ are the radial Mathieu functions of the fourth kind. It should be noted that $\xi = \cosh u$, $\eta = \cos v$, $c = kF$, and $k = \omega\sqrt{\mu\varepsilon}$.

The relative permittivity and permeability tensors of the anisotropic material referred to the coordinate axes ξ, η, z are assumed to be biaxial and written as [17-19]:

$$\overline{\overline{\varepsilon}}_r = \begin{bmatrix} \varepsilon_{r1} & 0 & 0 \\ 0 & \varepsilon_{r2} & 0 \\ 0 & 0 & \varepsilon_{r3} \end{bmatrix}, \quad \overline{\overline{\mu}}_r = \begin{bmatrix} \mu_{r1} & 0 & 0 \\ 0 & \mu_{r2} & 0 \\ 0 & 0 & \mu_{r3} \end{bmatrix}. \tag{4}$$

The Maxwell's equations for an anisotropic region can be written as:

$$\nabla \times \mathbf{E} = -jkZ\overline{\overline{\mu}}_r \cdot \mathbf{H}, \tag{5}$$

$$\nabla \times \mathbf{H} = j(k/Z)\overline{\overline{\varepsilon}}_r \cdot \mathbf{E}, \tag{6}$$

Submitted On: June 8, 2015
Accepted On: September 8, 2015

where Z is the free space wave impedance, and a bold symbol referring to a vector sign. The electric and magnetic field components within the anisotropic elliptic cylinder can be written using equation (5) and (6) as:

$$H_u^{II} = \frac{j}{k\ Z\ \mu_{r1} h}\frac{\partial E_z^{II}}{\partial v}, \tag{7}$$

$$H_v^{II} = -\frac{j}{k\ Z\ \mu_{r2} h}\frac{\partial E_z^{II}}{\partial u}, \tag{8}$$

$$E_z^{II} = \frac{jZ}{k\ \varepsilon_{r3} h^2}\left[\frac{\partial}{\partial v}\left(hH_u^{II}\right) - \frac{\partial}{\partial u}\left(hH_v^{II}\right)\right]. \tag{9}$$

Substituting for H_u^{II}, H_v^{II} in (9) from equations (7) and (8), we obtain:

$$\frac{\partial^2 E_z^{II}}{\partial v^2} + \frac{\mu_{r1}}{\mu_{r2}}\frac{\partial^2 E_z^{II}}{\partial u^2} + c^2\mu_{r1}\varepsilon_{r3}(\cosh^2 u - \cos^2 v)E_z^{II} = 0. \tag{10}$$

If E_z^{II} is written as the product $g_1(v)g_2(u)$, then by using the method of separation of variables, equation (10) can be separated into the two differential equations:

$$\frac{\partial^2 g_1(v)}{\partial v^2} - (c_{13}^2\cos^2 v - b^2)\, g_1(v) = 0, \tag{11}$$

$$\frac{\partial^2 g_2(u)}{\partial u^2} + \left\{c_{23}^2\cosh^2 u - b^2\,\frac{\mu_{r2}}{\mu_{r1}}\right\} g_2(u) = 0, \tag{12}$$

satisfied by $Sq_n(c_{13},\cos v)$, $Rq_p^{(1)}(c_{23},\cosh u)$, respectively, with $p = m\sqrt{\mu_{r2}/\mu_{r1}}$, $c_{13} = F\omega\sqrt{\mu_{r1}\varepsilon_{r3}}$, $c_{23} = F\omega\sqrt{\mu_{r2}\varepsilon_{r3}}$, $h = F\sqrt{(\cosh^2 u - \cos^2 v}$, and b^2 being the separation constant.

The electric field inside the biaxial anisotropic dielectric coating (region II) for $\xi_c < \xi < \xi_1$ can be written in terms of Mathieu functions as:

$$E_z^{II} = \sum_{q,m}^{\infty}[A_{qm}R_{qp}^{(1)}(c_{23},\xi) + B_{qm}R_{qp}^{(2)}(c_{23},\xi)]S_{qm}(c_{13},\eta), \tag{13}$$

where A_{qm} and B_{qm} are the unknown transmitted field expansion coefficients, $R_{qp}^{(1)}$ and $R_{qp}^{(2)}$ are the radial Mathieu functions of the first and second kind, respectively. The magnetic field components in regions (I) and (II) are derived using Maxwell's equations and written as:

$$H_v^{I} = \frac{-j}{\omega\mu h}\left\{\sum_{q,m}^{\infty} C_{qm}R_{qm}'^{(4)}(c_0,\xi)S_{qm}(c\ ,\eta)\right\}, \tag{14}$$

$$H_v^{II} = \frac{-j}{\omega\mu_{r2} h}\left\{\sum_{q,m}^{\infty}[A_{qm}R_{qp}'^{(1)}(c_{23},\xi) + B_{qm}R_{qp}'^{(2)}(c_{23},\xi)]S_{qm}(c_{13},\eta)\right\}. \tag{15}$$

The prime in equations (14) and (15) refers to the derivative with respect to u.

The electric field E_z should be continuous across the dielectric layer at $\xi = \xi_1$, this leads to:

$$[A_{qn}R_{qp}^{(1)}(c_{23},\xi_1) + B_{qn}R_{qp}^{(2)}(c_{23},\xi_1)]N_{qn}(c_{13}) = \sum_m^{\infty} C_{qm}R_{qm}^{(4)}(c_0,\xi_1)M_{qnm}(c_{13},c_0), \tag{16}$$

where $N_{qn}(c_{13})$ and $M_{qnm}(c_{13},c_0)$ are defined as:

$$N_{qn}(c_{13}) = \int_0^{2\pi}[S_{qn}(c_{13},\eta)]^2\, dv, \tag{17}$$

$$M_{qnm}(c_{13},c) = \int_0^{2\pi} S_{qn}(c_{13},\eta)S_{qm}(c,\eta)dv. \tag{18}$$

The tangential magnetic field components at $\xi = \xi_1$ should also be continuous and require that:

$$[A_{qn}R_{qp}'^{(1)}(c_{23},\xi_1) + B_{qn}R_{qp}'^{(2)}(c_{23},\xi_1)]N_{qn}(c_{13}) = \mu_{r2}\sum_m^{\infty} C_{qm}R_{qm}'^{(4)}(c_0,\xi_1)M_{qnm}(c_{13},c). \tag{19}$$

The tangential electric field on the conducting surface ($\xi = \xi_c$) must be zero except at the slot surface. This leads to:

$$\sum_{q,m}^{\infty}[A_{qm}R_{qp}^{(1)}(c_{23},\xi_c) + B_{qm}R_{qp}^{(2)}(c_{23},\xi_c)]S_{qm}(c_{13},\eta) = \begin{cases} F(v) & \nu_1 < \nu < \nu_2 \\ 0, & \text{elsewhere.} \end{cases} \tag{20}$$

Multiplying both sides of (20) by $S_{qn}(c_{13},\eta)$ and integrating over $0 < \nu < 2\pi$, we obtain:

$$[A_{qn}R_{qp}^{(1)}(c_{23},\xi_c) + B_{qn}R_{qp}^{(2)}(c_{23},\xi_c)]N_{qn}(c_{13}) = F_{qn} = \int_{\nu_1}^{\nu_2} F(v)\,S_{qn}(c_{13},\eta)d\nu. \tag{21}$$

The integral in equation (21) may be computed numerically by expressing the field at the slot surface as [6,7]:

$$F(\nu) = E_0\cos[\pi(\nu_0 - \nu)/(2\alpha)], \tag{22}$$

$$\nu_0 = (\nu_1 + \nu_2)/2, \tag{23}$$

$$\alpha = (\nu_2 - \nu_1)/2. \tag{24}$$

The angular Mathieu functions are written in terms of Fourier series as:

$$S_{en}(c_{13},\eta) = \sum_k D_e^k(c_{13},n)\cos(k\nu), \tag{25}$$

$$S_{on}(c_{13},\eta) = \sum_k D_o^k(c_{13},n)\sin(k\nu). \tag{26}$$

Substituting equations (25)-(26) into equation (21), F_{en} and F_{on} can finally be written as:

$$F_{en} = E_o\sum_k D_e^k(c_{13},n)\int_{\nu_1}^{\nu_2}\cos\left[\pi(\nu - \nu_0)/(2\alpha)\right]\cos(k\nu)d\nu, \tag{27}$$

$$F_{on} = E_o \sum_k D_o^k(c_{13}, n) \int_{\nu_1}^{\nu_2} \cos\left[\pi(\nu - \nu_0)/(2\alpha)\right] \sin(k\nu) d\nu. \quad (28)$$

Solving for B_{en} by equation (21) and incorporating the result in equations (16) and (19) by eliminating A_{en}, we obtain the radiated field coefficients C_{en}. Similar procedure may be followed to obtain the odd coefficients C_{on}.

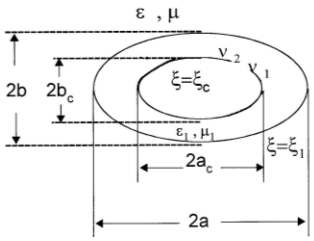

Fig. 1. Slotted antenna on elliptic cylinder with biaxial anisotropic material coating.

III. NUMERICAL RESULTS

After computing the radiated field coefficients C_{qn}, the far-field radiation pattern, antenna gain, and the aperture conductance may be evaluated. The slotted antenna far field can be written as:

$$E_z^I(\rho, \varphi) = \sqrt{\frac{j}{k\rho}} e^{-jk\rho} \left[\sum_{q,n}^{\infty} j^n C_{qn} S_{qn}(c, \cos\varphi) \right], \quad (29)$$

where ρ and φ represent the polar coordinates in the cylindrical coordinate system. The antenna gain is expressed as [6,7]:

$$G(\varphi) = \frac{1}{Z\, k\rho} \left[\left| \sum_{q,n}^{\infty} j^n C_{en} S_{en}(c, \cos\varphi) \right|^2 \right]. \quad (30)$$

The accuracy of the obtained numerical results is checked against slotted circular and elliptic antennas coated with conventional dielectric material [6,8]. Figure 2 shows the radiation pattern numerical results (gain versus φ) obtained for a conventional dielectric coating material represented by solid line ($\varepsilon_r = 2$ and $\mu_r = 1$), while biaxial anisotropic coating represented by dotted μ_{r2} = 4 and circled μ_{r2} = 9 lines. The slot location is at $\nu_0 = 90^o$ where $\alpha = 2.8657^o$. The parameters for the biaxial medium are $\varepsilon_{r1} = 1.0$, $\varepsilon_{r2} = 1.0$, $\varepsilon_{r3} = 2.0$, $\mu_{r1} = 1.0$, $\mu_{r3} = 1.0$, while for cylinder geometries are $ka_c = 1.0$, $kb_c = 0.6$, $ka = 1.13$, $kb = 0.8$. It can be seen the gain of the antenna is slightly dropped at the location of the antenna by increasing the value μ_{r2} from 4 to 9 while the gain is increased for the range -100° to 0° and 150° to 250°.

Figure 3 is similar to Fig. 2 except for circular antenna with $ka_c = 1.0$, $kb_c = 1.0$, $ka = 1.6$, $kb = 1.6$. The gain is not affected by increasing the value μ_{r2} at the location of the antenna while it is significantly decreased at the side lobes locations.

Figure 4 shows the again for an elliptic antenna by fixing the value μ_{r2} at 4.0 while changing the value of ε_{r3} from 2.0 to 4.0. Increasing the value of $\varepsilon_{r3} = 2.0$ has little on the antenna except for minor increase at the side lobe locations. Figure 5 is similar to 4 except for circular antenna it behaves like elliptical antenna.

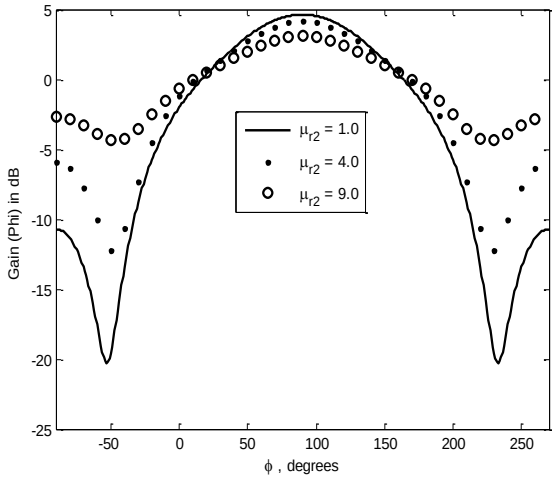

Fig. 2. Radiation pattern of slotted elliptic antenna coated with biaxial anisotropic material and different values of μ_{r2} ($\varepsilon_{r1} = 1.0$, $\varepsilon_{r2} = 1.0$, $\varepsilon_{r3} = 2.0$, $\mu_{r1} = 1.0$, $\mu_{r3} = 1.0$, $ka_c = 1.0$, $kb_c = 0.6$, $ka = 1.13$, $kb = 0.8$).

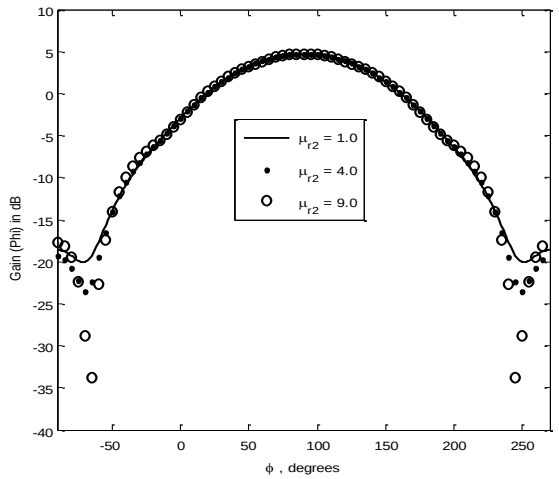

Fig. 3. Radiation pattern of slotted circular antenna coated with biaxial anisotropic material and different values of μ_{r2} ($\varepsilon_{r1} = 1.0$, $\varepsilon_{r2} = 1.0$, $\varepsilon_{r3} = 2.0$, $\mu_{r1} = 1.0$, $\mu_{r3} = 1.0$, $ka_c = 1.0$, $kb_c = 1.0$, $ka = 1.6$, $kb = 1.6$).

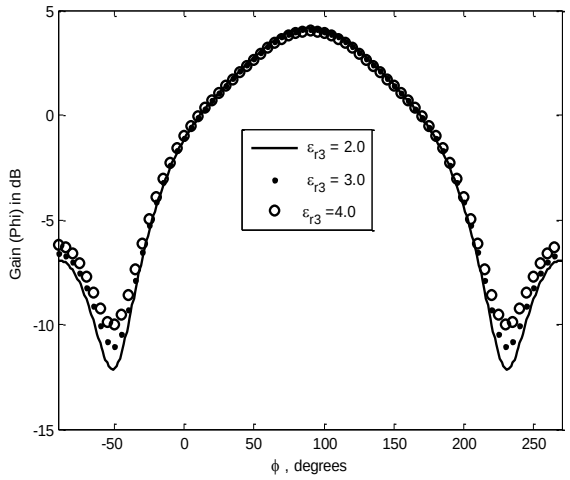

Fig. 4. Radiation pattern of slotted elliptic antenna coated with biaxial anisotropic material and different values of ε_{r3} ($\varepsilon_{r1}=1.0,\ \varepsilon_{r2}=1.0,\ \mu_{r1}=1.0,\ \mu_{r2}=4.0,\ \mu_{r3}=1.0,\ \mathrm{ka_c}=1.0,\ \mathrm{kb_c}=0.5,\ \mathrm{ka}=1.1,\ \mathrm{kb}=0.7$).

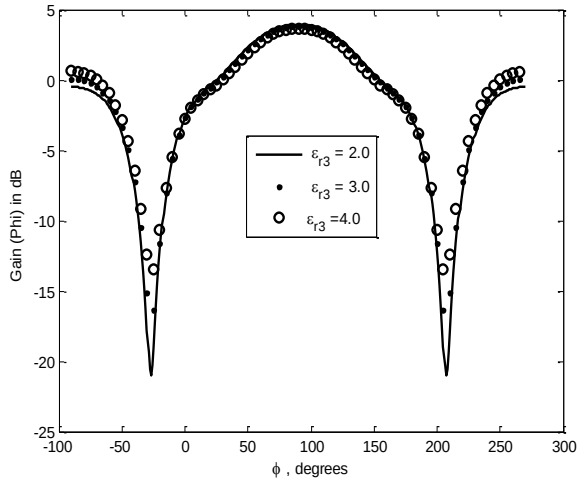

Fig. 5. Radiation pattern of slotted circular antenna coated with biaxial anisotropic material and different values of ε_{r3} ($\varepsilon_{r1}=1.0,\ \varepsilon_{r2}=1.0,\ \mu_{r1}=1.0,\ \mu_{r2}=4.0,\ \mu_{r3}=1.0,\ \mathrm{ka_c}=1.0,\ \mathrm{kb_c}=1.0,\ \mathrm{ka}=2.0,\ \mathrm{kb}=2.0$).

In Fig. 6 we plotted the gain versus the anisotropic dielectric material thickness for the cases kb = 0.7 and kb = 1.0. It can be noticed for these cases, the side lobes decrease and the antenna bandwidth increase. Figure 7 is similar to Fig. 6 except for circular antenna for thickness kb = 1.3 and kb = 1.5.

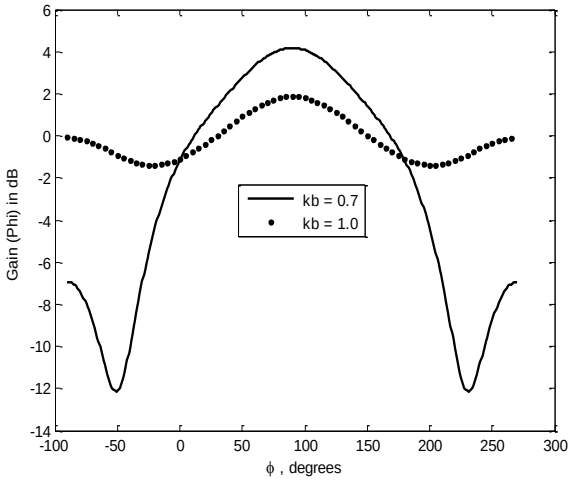

Fig. 6. Radiation pattern of slotted elliptic antenna coated with biaxial anisotropic material and different values of kb ($\varepsilon_{r1}=1.0,\ \varepsilon_{r2}=1.0,\ \varepsilon_{r3}=2.0,\ \mu_{r1}=1.0,\ \mu_{r2}=4.0,\ \mu_{r3}=1.0,\ \mathrm{ka_c}=1.0,\ \mathrm{kb_c}=0.5$).

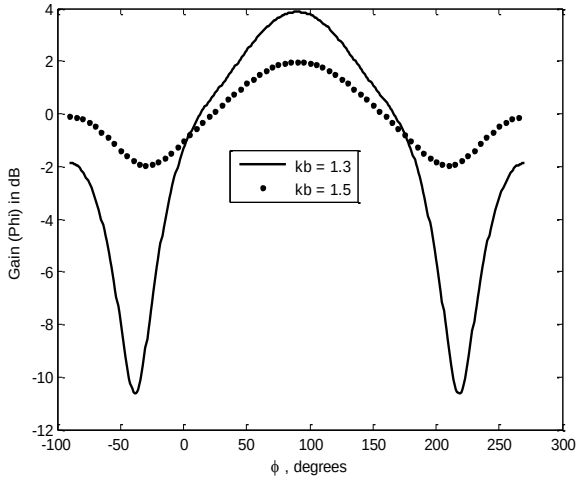

Fig. 7. Radiation pattern of slotted circular antenna coated with biaxial anisotropic material and different values of kb ($\varepsilon_{r1}=1.0,\ \varepsilon_{r2}=1.0,\ \varepsilon_{r3}=2.0,\ \mu_{r1}=1.0,\ \mu_{r2}=4.0,\ \mu_{r3}=1.0,\ \mathrm{ka_c}=1.0$).

IV. CONCLUSIONS

The radiation characteristics of an axially slotted circular, for comparison, or elliptical antenna coated by biaxial anisotropic material were investigated using series solution. It was shown that the presence of biaxial anisotropic material coating with specific

characteristic values and thickness lead to reducing the side lobes and enhancing the bandwidth of the antenna.

ACKNOWLEDGMENT

The author would like to acknowledge the support by the University of Sharjah, United Arab Emirates.

REFERENCES

[1] C. M. Knop, "External admittance of an axial slot on a dielectric coated metal cylinder," *Radio Sci*., vol. 3, pp. 803-818, Aug. 1968.

[2] L. Shafai, "Radiation from an axial slot antenna coated with a homogenous material," *Canadian J. Phys*., vol. 50, no. 23, 1972.

[3] J. Y. Wong, "Radiation pattern of slotted elliptic cylinder antenna," *IEEE Trans. Antennas Propagat*., vol. AP-3, pp. 200-203, Oct. 1955.

[4] J. Y. Wong, "Radiation conductance of axial and transverse slots in cylinders of elliptical cross section," *Proc. IRE*, vol. 41, pp. 1172-1177, Sep. 1953.

[5] J. H. Richmond, "Axial slot antenna on dielectric coated elliptic cylinder," *IEEE Trans. Antennas Propagat*., vol. AP-37, pp. 1235-1241, Oct. 1989.

[6] H. A. Ragheb, A. Sebak, and L. Shafai, "Radiation by axial slots on dielectric coated nonconfocal conducting elliptic cylinder," *IEE Proc. Microw. Antennas Propagat*., vol. 143, no. 2, pp. 124-130, Apr. 1996.

[7] M. I. Hussein and A-K. Hamid, "Radiation characteristics of N axial slots on a conducting elliptical antenna coated by a lossy dielectric layer," *Canadian Journal of Physics*, vol. 82, no. 2, pp. 141-149, 2004.

[8] B. N. Khatir, M. Al-Kanhal, and A. Sebak, "Electromagnetic wave scattering by elliptic chiral cylinder," *Journal of Electromagnetic Waves and Applications*, vol. 20, no. 10, pp. 1377-1390, 2006.

[9] B. N. Khatir and A. R. Sebak, "Slot antenna on a conducting elliptic cylinder coated by chiral media," *Electromagnetics*, vol 29, pp 522-540, 2009.

[10] B. N. Khatir and A. Sebak, "Slot antenna on a conducting elliptic cylinder coated by nonconfocal chiral media," *Progress in Electromag. Research Journal, PIER 93*, 125-143, 2009.

[11] Z-S. Wu, S-C. Mao, and L. Yang, "Two-dimensional scattering by a conducting elliptic cylinder coated with a homogeneous anisotropic shell," *IEEE Trans. Antennas Propagat*., vol. 57, pp. 3638-3645, Nov. 2009.

[12] N. Montaseri, M. Soleimani, and A. Abdolali, "Realization of the perfect electromagnetic conductor circular cylinder using anisotropic media," *Prog. Electromag. Res. M*, vol. 25, pp. 173-184, 2012.

[13] X-B. Wu and W. Ren, "Axial slot antenna on an anisotropic dielectric-coated circular cylinder," *IEE Proceedings - Microwaves, Antennas and Propagation*, vol. 141, iss. 6, pp. 527-530, 1994.

[14] G. Enrico, L. Carbonini, and A. Bruno, "Effects of anisotropic dielectric materials on a sandwich wire antenna (SWA)," *European Microwave Conference*, 2006.

[15] K. K. Mei and M. Meyer, "Solutions to spherical anisotropic antennas," *IEEE Transaction on Antennas and Propagation*, vol. 12, pp. 459-463, 1964.

[16] P. M. Morse and H. Feshbach, *Methods of Theoretical Physics*, vols. I and II, McGraw-Hill, New York, 1953.

[17] N. Montaseri, A. Abdolali, M. Soleimani, and V. Nayyeri, "Plane wave scattering by a circular PEMC cylinder coated with anisotropic media," *Int. J. RF and Microwave CAE*, vol. 23, pp. 225-231, 2013.

[18] A-K. Hamid and F. Cooray, "Scattering of a plane wave by a homogeneous anisotropic elliptic cylinder," *IEEE Transactions on Antennas and Propagation*, vol. 63, no. 8, pp. 3579-3587, 2015.

[19] A-K. Hamid, "Axially slotted antenna on elliptic cylinder coated with biaxial anisotropic material," *9th European Conference on Antennas and Propagation (EuCAP 2015)*, Lisbon, Portugal, Apr. 12-17, 2015.

A-K. Hamid received the B.Sc. degree in Electrical Engineering from West Virginia Institute of Technology and University, West Virginia, U.S.A. in 1985, M.Sc. and Ph.D. degrees from the University of Manitoba, Winnipeg, Manitoba, Canada in 1988 and 1991, respectively, both in Electrical Engineering. From 1991-1993, he was with Quantic Laboratories Inc., Winnipeg, Manitoba, Canada, developing two and three dimensional electromagnetic field solvers using boundary integral method. From 1994-2000 he was with the Faculty of Electrical Engineering at King Fahd University of Petroleum and Minerals, Dhahran, Saudi Arabia. Since Sep. 2000, he is with the Dept. of Electrical and Computer Engineering at the University of Sharjah, Sharjah, United Arab Emirates. His research interest includes EM wave scattering from two and three dimensional bodies, FDTD simulation of cellular phones, inverse scattering using neural networks and investigating thermal PV system experimentally.

UWB Monopole Antenna with Switchable Band-Notch Characteristic Using a Novel MEMS Afloat

Arash Nemati and Bahram A. Ganji

Department of Electrical & Computer Engineering
Babol Noshirvani University of Technology, Babol, Mazandaran, Iran
Arash.nemati@stu.nit.ac.ir, baganji@nit.ac.ir

Abstract ─ In this paper, a novel microelectro-mechanical system (MEMS) U-shaped afloat is designed and used instead of a simple slot to activate and deactivate the band notch characteristic of an ultra wideband (UWB) monopole antenna at the WLAN band (5.15-5.825 GHz) without extra DC bias lines. The novelty of this work is design of MEMS afloat that can stay in down state permanently. When the dc actuation voltage, about 20 volts, is applied to the microstrip center line, the λ/2 long U-shaped afloat moves down and creates a slot (resonating element) in its vacant place. Whereas no voltage is applied, the afloat remains in the up position and serves as a part of the antenna, which eliminates the resonance. The proposed design for MEMS afloat has least negative effect on gain, reflection coefficient, and pattern of the antenna. The gain of the antenna is about 3.2 dBi over the entire UWB frequency band (3.1-10.6 GHz), while it decreases sharply over 7 dB at the rejection band. More-over, the time-domain characteristics of the antenna is investigated, which shows 1 ns delay over the UWB frequency band for 20 cm. Due to a novel afloat design, the addition of the resonance element does not affect on the radiation performance, reflection coefficient, gain, and group delay of the antenna outside of notched band frequencies.

Index Terms ─ MEMS U-shaped afloat, switchable band notch, UWB antenna.

I. INTRODUCTION

In recent years, due to the attractive features, such as low cost, small size, ease of fabrication, and wide frequency bandwidth, there has been more attention in ultrawideband (UWB) monopole antennas. The Federal Communication Commission (FCC) has allocated 3.1-10.6 GHz for commercial ultrawideband (UWB) communication systems [1]. Several antenna structures have been proposed for UWB applications [2-5]. The frequency range for UWB system will cause interference to some other existing narrowband services. One of them is wireless local-area network (WLAN), which operates in the 5.15-5.875 GHz band. However, using filters the complexity of the UWB system will increase. To over-come this problem, the structures with band-rejection characteristic such as parasitic inverted-U strip [6], U-shaped slot [7-9], arc-shaped slot [10], H-shaped conductor backed plane [11], and rectangle-shaped plane [12] are proposed to integrate with the previous antennas. However, none of them had reconfigurable band notch characteristics. The main challenge for researchers in UWB antenna design is the design of a single antenna that can provide reconfigurable rejected band. Reconfigurability is obtained by employing two ideal switches on SIS-HSIR and SIS-SIR [13]. A pin diode is used in [14] to switch ON or OFF the notch band. However, the switches were actuated using DC bias lines. MEMS switches are used in [15] to reach the reconfigurability without bias lines. However, to reach this capability, a floating ground was used in MEMS switch. Therefore, the switch could not stay in down position permanently.

In this paper, an UWB monopole antenna with U-shaped MEMS afloat that can be actuated to place a band notch at the WLAN frequencies is presented. The MEMS afloat is designed so that it does not require extra bias lines and the switch can stay in down position permanently.

II. DESIGN OF ANTENNA AND MEMS AFLOAT

Figure 1 shows the geometry of the reconfigurable WLAN band rejection UWB elliptical monopole antenna. The antenna was designed on a 28 mm × 37 mm liquid crystal polymer (LCP) substrate with a low permittivity ($\varepsilon r \approx 3$), low-loss ($tan\ \delta \approx 0.002$), and a thickness of 0.3 mm. All of these characteristics make it an ideal substrate for antennas, particularly at high frequencies. The width of the 50 ohm microstrip feed line is 0.75 mm and the thickness of the antenna and the ground plane is 5 μm. In this paper, a novel MEMS afloat is designed and used instead of a simple slot in the antenna. The afloat is held by several beams, which are connected to the antenna in 10 points, shown with red points [Fig. 1 (c)]. The dimensions of the antenna, afloat, beams, bridges,

Submitted On: December 1, 2014
Accepted On: October 22, 2015

and ground plane are summarized in Table 1.

The lengths of the beams are:

$$L_{b1} + L_{b2} / 2, \quad (1)$$

$$L_{b1} + L_{b3} / 2, \quad (2)$$

$$L_{b1} + L_{b4} / 2. \quad (3)$$

There is an air gap between afloat and ground plane with depth of h=45 μm.

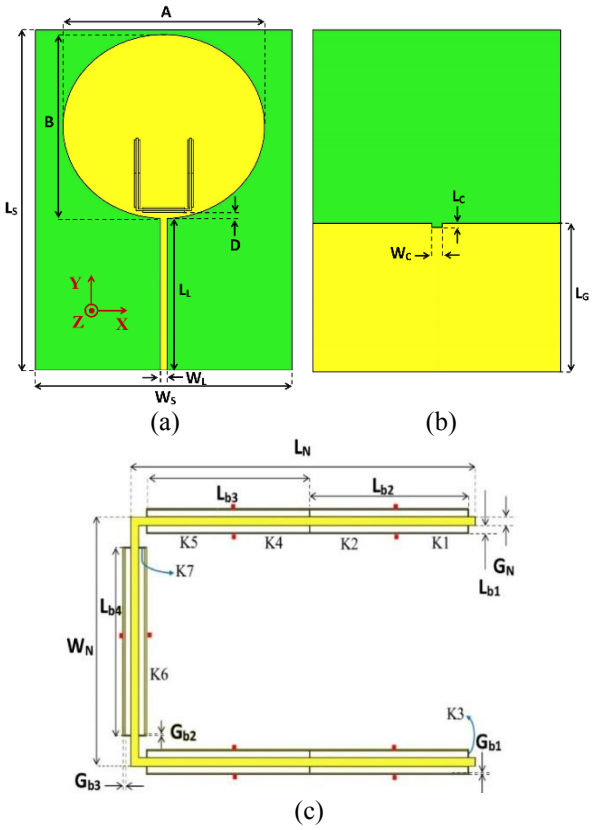

Fig. 1. Schematic diagram of: (a) antenna's front view, (b) antenna's back view, and (c) U-shaped afloat.

Table 1: Antenna and afloat dimensions

Parameter	Length (mm)	Parameter	Length (mm)
L_S	37.000	L_N	7.900
W_S	28.000	G_N	0.200
A	22.000	W_N	6.045
B	20.000	L_{b1}	0.190
L_L	16.500	L_{b2}	3.640
D	0.820	L_{b3}	3.740
L_G	16.400	L_{b4}	4.540
W_L	0.750	G_{b1}	0.030
L_C	0.300	G_{b2}	0.010
W_C	1.000	G_{b3}	0.045

A 1 μm thick high resistive sheet, underneath a passivation layer is at the bottom of air gap, which is connected to the ground plane. When the dc actuation voltage is applied to the microstrip center line, the *λ/2* long U-shaped afloat moves down (h=45 μm) and creates a slot (resonating element) in its vacant place [Fig. 2 (b)]. Whereas no voltage is applied, the afloat remains in the up position and serves as a part of the antenna, which eliminates the resonance [Fig. 2 (a)].

The pull-in voltage V_{PI} can be expressed as [16]:

$$V_{PI} = \sqrt{\frac{8Kh^3}{27\varepsilon_0 A}}, \quad (4)$$

where h is the original gap between afloat and ground plane, ε_0 is the dielectric constant of the air, A is the surface area of the afloat, which for the afloat design can be expressed as:

$$A = \left(2\left(G_N \times L_N\right) + \left(G_N \times W_N\right)\right), \quad (5)$$

and K is the effective spring constant of the 20 T-shaped and L-shaped beams [Fig. 1 (c)], which can be written as:

$$K = 4\begin{bmatrix}\left(K_1 \| K_3\right) + \left(K_2 + K_4\right) \| K_3 + \\ + \left(K_5 \| K_3\right) + \left(K_6 \| K_7\right)\end{bmatrix}, \quad (6)$$

where:

$$K_i = \frac{EG_iT_i^3}{L_i^3}, \qquad (i = 1, 2, ..., 7) \quad (7)$$

where L_i, G_i, and T_i are the length, width, and thickness of the beams, and E is the Young's modulus of the aluminum. Firstly, the values of Table 1 should be put in Eq. 7 to calculate the K_i for all of the beams. Secondly, the results from Eq. 7 should be put in Eq. 6 to calculate the effective spring constant of the afloat.

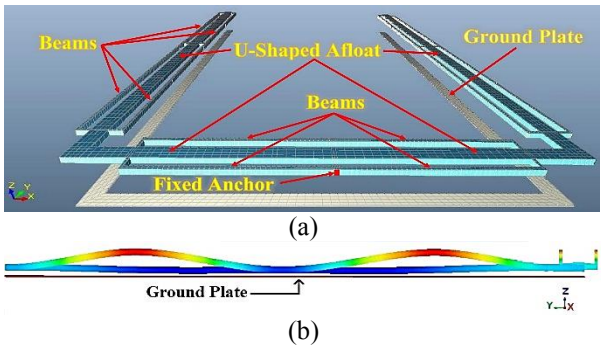

Fig. 2. Schematic diagram of U-shaped MEMS afloat and ground plate in: (a) up position and (b) down position.

The radiating structure, located at a distance 0.1 mm from the end of the ground plane, is an elliptical antenna, which has a major axis A=22 mm and a secondary axis B=20 mm. Depending on the lowest frequency of operation (f_l=3.1 GHz) and effective dielectric constant of substrate, A and B are calculated as:

$$\frac{1}{2}\left(\pi \cdot \frac{(A+B)}{2}\right) + L_L = c \Big/ \left(2 f_\ell \sqrt{\varepsilon_{eff}}\right), \quad (8)$$

where:

$$\varepsilon_{eff} = (\varepsilon_r + 1)/2, \quad (9)$$

where c is the speed of light. The left side of the Eq. 8 is the half of the circumference of the antenna and its transmission line. The antenna and its transmission line together act as a monopole antenna. Hence, their total length should be equal to half of the frequency which the antenna is supposed to radiate. Since the UWB antenna radiates at very large range of frequency, the lowest frequency determines the total size of the antenna. Next, attenuation would happen at twofold the lowest frequency and the next one at threefold that frequency. As a result, A and B are chosen and then according to Eq. 8, L_L is calculated. Figure 3 shows optimization of parameters A and B to achieve best result for the reflection coefficient of the antenna. The best values for A and B is selected to have the lowest S_{11} over the entire UWB frequency band (3.1-10.6 GHz).

Additionally, the antenna performance in the high frequency band (between 9 GHz to 11 GHz) can be further improved by cutting a rectangular slot on the middle of the ground plane. Figure 4 shows the optimization of parameter L_C to achieve best result for the reflection coefficient of the antenna. L_C =0.3 mm is selected to decrease the reflection coefficient and also does not affect other frequency ranges so much.

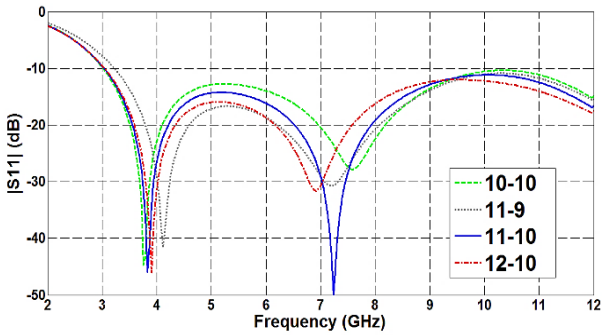

Fig. 3. Effect of antenna size on reflection coefficient (A/2 – B/2).

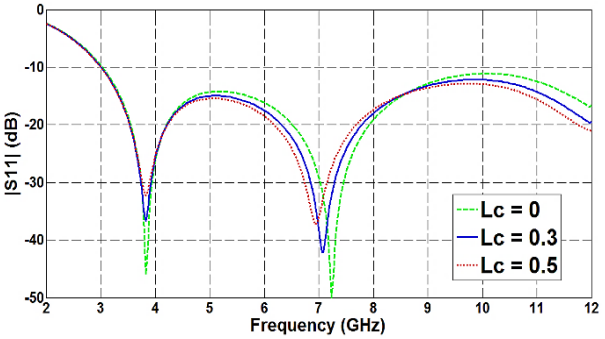

Fig. 4. Effect of L_C on reflection coefficient.

III. OPERATION PRINCIPLE

The total length of the slot is approximately λ/2 at the frequency which the rejection band is desired (around 5.5 GHz). The relation between central notched frequency and afloat dimensions can be approximately considered as [17]:

$$f_U = c/\left(4\left(L_N + (W_N/2) - G_N\right)\sqrt{\varepsilon_{eff}}\right), \quad (10)$$

where L_N, W_N, and G_N are the length, width, and thickness of the afloat, and ε_{eff} is the effective dielectric constant of the air.

Figure 5 shows the surface current distribution in two frequencies. As shown in Fig. 5 (a), at the notch frequency of 5.5 GHz, when the afloat is in down position the current density in the edges of the U-shaped slot is stronger than other areas. The directions of the currents in the inner and outer side of the U-shaped slot are opposite to each other as presented in [16]. Therefore, they cancel each other and the antenna does not radiate. On the other hand, in Fig. 5 (b), we can see stronger current distributions concentrated near the outer edges of the antenna at the center frequency of the corresponding notched band. At a pass band frequency of 8 GHz (outside the notched band), the distribution of the surface current is uniform near the outer edges of the antenna, as shown in Fig. 5 (c).

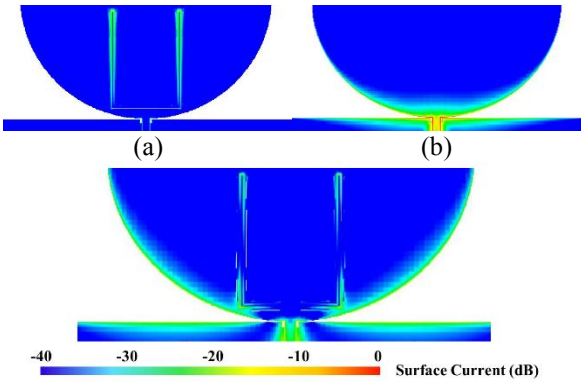

Fig. 5. Simulated surface current distributions: (a) afloat down at 5.5 GHz, (b) afloat up at 5.5 GHz, and (c) afloat down at 8 GHz.

The slot can be modeled by a short circuit terminated series stub in a transmission line model as shown in Fig. 6. The presence of the slot is modeled as a long, short circuit terminated series stub, which is similar to a spur line filter. If the afloat is down [Fig. 6 (a)], the spur line filter is connected to the circuit, and at the stub resonant frequency, there is an equivalent series open circuit that reflects the signal. However, when the afloat is up, the spur line filter is not connected to the circuit [Fig. 6 (b)]. Therefore, radiation occurs at all frequencies.

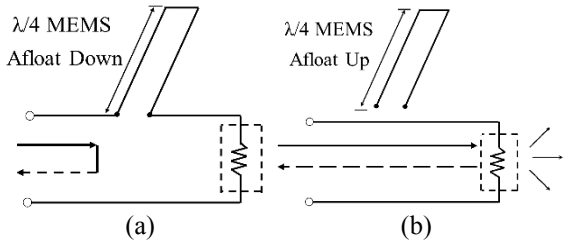

Fig. 6. Transmission line model for antenna with: (a) U-shaped afloat down, and (b) U-shaped afloat up.

IV. RESULTS AND DISCUSSION

In this paper, the MEMS mechanical structure is simulated using Intellisuite, which is a multi-physics simulator that uses the finite element method (FEM). For the mechanical simulations, it was assumed that aluminum afloat with a thickness of 5 µm is suspended 45 µm above the ground plane. Aluminum has a Young's modulus (E) of 70 GPa, a Poisson's ratio (v) of 0.33, and a density (ρ) of 2700 kg/m^3. Figure 7 shows the afloat displacement versus bias voltage from 0 V to 16 V. The deflection as a function of voltage increases slightly until a drastic change occurs that indicate pull in voltage. The pull-in voltage of the afloat is about 15.9 V, which is low comparing to previous designs, and the switching is permanent. This means that the switch has the ability to stay in down position constantly. The calculated pull-in voltage using Eq. 4 is 16.4 V. Hence, for considerably large structure of the afloat comparing to previous MEMS switches, there is good agreement between analatical and simulation result for afloat pull-in voltage.

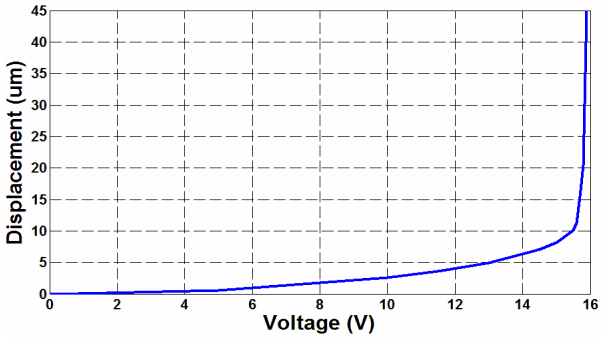

Fig. 7. Afloat displacement vs. DC voltage.

Figure 8 shows the simulated S_{11} results for the proposed antenna. When the afloat is up, the simulated plots for the antenna (afloat up) and the "Reference" antenna (the antenna presented in Fig. 1 without afloat) are in very good agreement. This agreement indicates the efficiency of the afloat has least effect on the antenna's performance. When the afloat is down, the presented reflection coefficient verifies the good performance of the MEMS afloat and the suggested effectiveness.

As shown in Fig. 9, the antenna's gain decreases sharply over 7 dB in the notched band. For other frequencies, out of the notched band, the antenna exhibits moderate gain about 3.2 dBi.

Figure 10 shows the simulated S_{11} characteristics for different values of D. As D increases from 0.82 to 1.82 mm, the bandwidth of notched band is varied from 560 to 410 MHz. From this result, the band width of notched band is controllable by changing of the slot. By decreasing of D, the slot gets closer to the edges and bottom of antenna so it can absorb waves easier in the wider ranges of frequency from center resonant frequency. It can be seen that by changing D, the center frequency of notched band remains almost fixed.

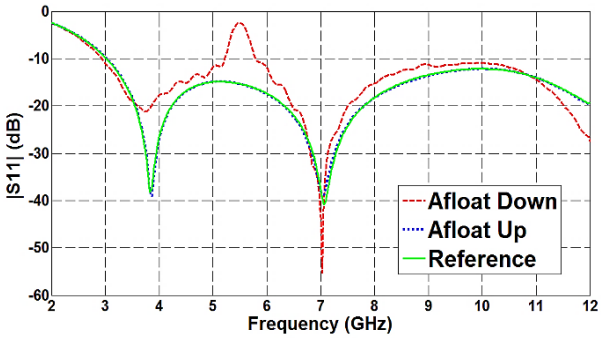

Fig. 8. Simulated reflection coefficient of the antenna.

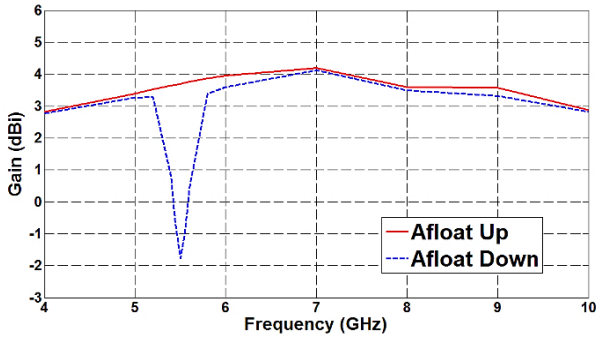

Fig. 9. Simulated realized gain of the antenna.

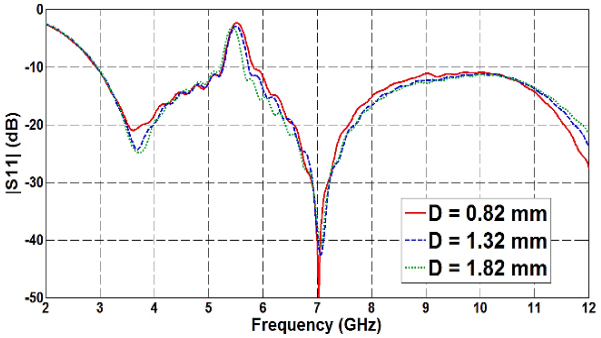

Fig. 10. Slot position effect on reflection coefficient.

Figure 11 shows the simulated S_{11} characteristics for different values of L_N. As L_N increases from 7.1 to 8.7 mm, the center frequency of notched band is varied from 5.88 to 5.12 GHz. From this result, the frequency of notched band is controllable by changing length of the slot and it decreases 47.5 MHz for every 1 mm increase of L_N, which agrees with Eq. 10. It can be seen that by changing L_N, the bandwidth of notched band remains almost fixed.

Figure 12 shows the simulated S_{11} characteristics for different values of h. As the height h increases from 25 to 65 μm, the center frequency of notched band is varied from 5.43 to 5.63 GHz. From this result, the frequency of notched band increases 50 MHz for every 10 μm increase of h. By increasing the height of h the ε_{eff} decreases, and according to Eq. 10, the resonant frequency increases. It can be seen that the bandwidth of notched band remains almost fixed.

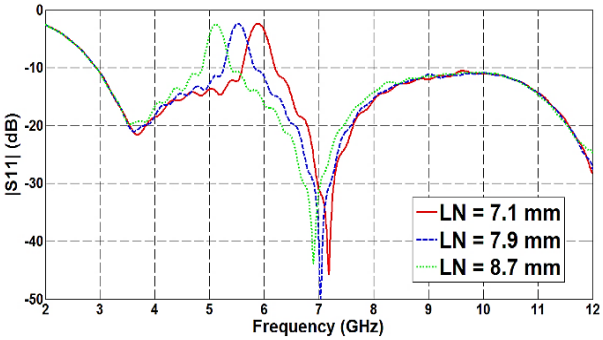

Fig. 11. Slot length effect on reflection coefficient.

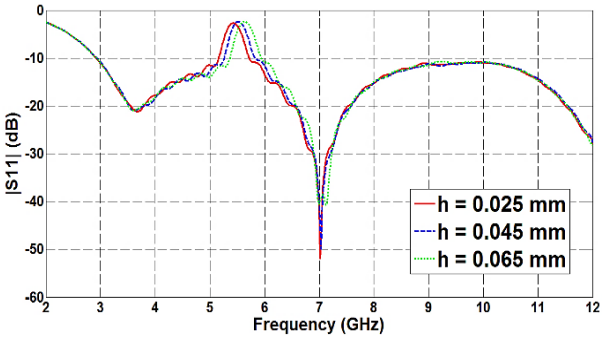

Fig. 12. Slot height effect on reflection coefficient.

Although, the proposed antenna presents very wide frequency band, the good frequency domain performance cannot necessarily ensure that the antenna also behaves well in time-domain. As a result, in order to verify the effectiveness of the antenna for time-domain applications, its time-domain response must be examined. The time-domain characteristic of the antenna is simulated in a manner shown in Fig. 13. The two identical proposed antennas are put face to face in a distance of 20 cm. The simulated group delay of the antenna is shown in Fig. 14. While the afloat is up, the variation of the group delay of the antenna is about 1 ns across the whole UWB. If the group delay variation exceeds 1 ns, the phases are no longer to be linear in far-field region and a pulse distortion is caused. It can be a serious problem in UWB communication systems. On the other hand, while the afloat is down, the maximum group delay of 6.5 ns happens in notched frequency. Figure 15 shows the group delay of the antenna, while the antennas are put side by side in a distance of 20 cm. While the afloat is up, the group delay of the antenna is about 1 ns across the whole UWB. On the other hand, while the afloat is down, the maximum group delay of 11.5 ns happens in notched frequency. This study has shown that band-notched antenna has a good time-domain characteristic and a small pulse distortion as well.

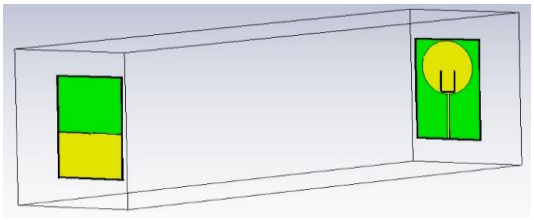

Fig. 13. The setup of the group delay simulation.

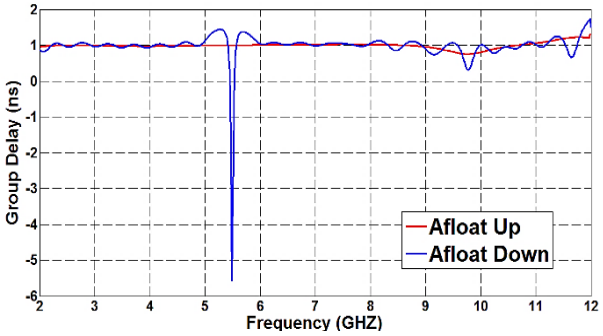

Fig. 14. Simulated group delay of the antenna in face to face position.

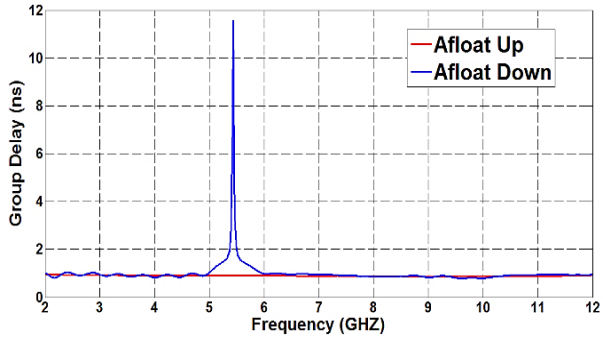

Fig. 15. Simulated group delay of the antenna in side by side position.

Figure 16 and 17 shows the radiation patterns for the antenna. Simulations at 5.5 and 8 GHz are presented in both E (x-y) and H (x-z) planes. The two states (afloat up and down) of the reconfigurable antenna are compared with the "Reference" antenna. Radiation patterns at 8 GHz show that the addition of the resonating elements does not affect the radiation performance of the antenna, outside the of the notch band frequencies [Figs. 16 (a) and (b)]. On the other hand, within the band-notch range (radiation patterns at 5.5 GHz) and with the appropriate MEMS afloat state the radiated field intensity is degraded [Figs. 17 (a) and (b)]. It can be seen from Figs. 16 and 17 that, the presence of the afloat has least effect on the radiation patterns except when it goes down.

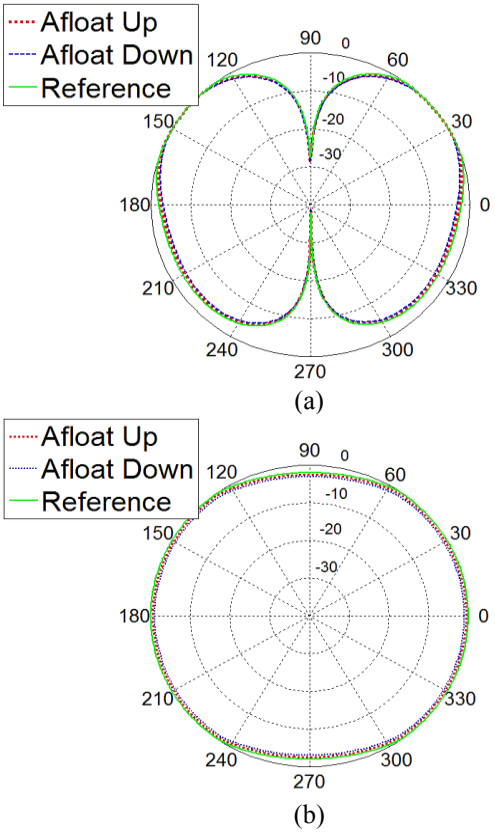

Fig. 16. Simulated radiation pattern at: (a) E plane at 8 GHz and (b) H plane at 8 GHz.

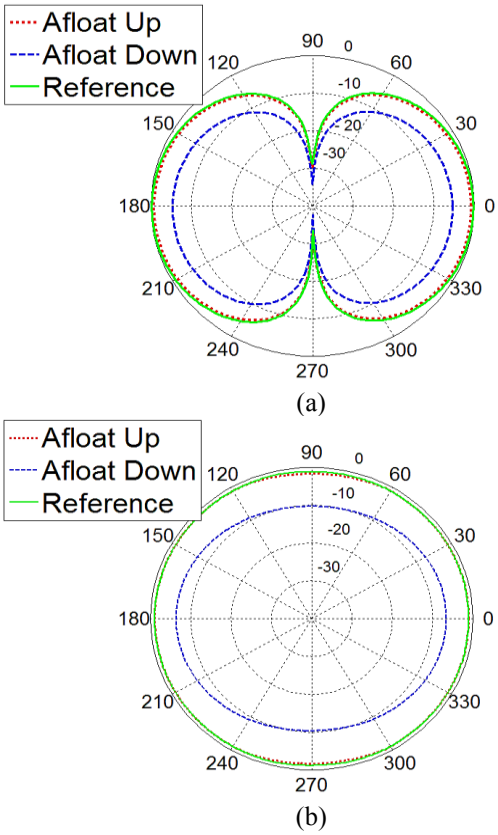

Fig. 17. Simulated radiation pattern at: (a) E plane at 5.5 GHz and (b) H plane at 5.5 GHz.

VI. CONCLUSION

An ultra wideband (UWB) elliptical monopole antenna fed by microstrip line with reconfigurable rejection band characteristic at the WLAN band (5.15-5.825 GHz) is proposed in this paper. To obtain reconfigurability, a *λ/2* long U-shaped MEMS afloat is used, which is actuated through the RF signal path without DC bias lines. Using extra DC bias lines could reduce the radiation performance of the antenna because of RF leakage through the bias lines. The effects of the various geometrical parameters on the notched frequency band are studied. The pull in voltage of the afloat was low and its switching was permanent. Due to a novel afloat design, the proposed antenna has good omnidirectional pattern in different frequencies and the addition of the resonance element does not affect on the radiation performance outside of notched band frequencies.

REFERENCES

[1] Federal Communications Commission Re-vision of Part 15 of the Commission's Rules Regarding Ultra-wideband Transmission System" Tech. Rep., ET-Docket 98-153, FCC02-48, 2002.

[2] R. Chair, A. A. Kishk, K. F. Lee, C. E. Smith, and D. Kajfez, "Microstrip line and CPW fed ultra-wideband slot antennas with U-shaped tuning stub and reflector," *Progress In Electromagnetics Research*, vol. 56, pp. 163-182, 2006.

[3] D. Chen and C. H. Cheng, "A novel compact ultra-wideband (UWB) wide slot antenna with via holes," *Progress In Electromagnetics Research,* vol. 94, pp. 343-349, 2009.

[4] K. P. Ray and Y. Rang, "Ultra wideband printed elliptical monopole antennas," *IEEE Transactions on Antennas and Propagation*, vol. 55, no. 4, pp.

1189-1192, 2007.

[5] N. Ojaroudi, M. Ojaroudi, and Sh. Amiri, "Enhanced bandwidth of small square monopole antenna by using inverted U-shaped slot and conductor-backed plane," *Applied Computational Electromagnetics Society (ACES) Journal*, vol. 27, no. 8, pp. 685-690, Aug. 2012.

[6] R. Fallahi, A.-A. Kalteh, and M. Golparvar Roozbahani, "A novel UWB elliptical slot antenna with band-notched characteristics," *Progress In Electromagnetics Research*, vol. 82, pp. 127-136, 2008.

[7] Y. J. Cho, K. H. Kim, D. H. Choi, S. S. Lee, and S-O. Park, "A miniature UWB planar monopole antenna with 5-GHz band-rejection filter and the time-domain characteristics," *IEEE Trans Antennas Propag.*, vol. 54, no. 5, pp. 1453-1460, 2006.

[8] T. P. Vuong, A. Ghiotto, Y. Duroc, and S. Tedjini, "Design and characteristics of a small U-slotted planar antenna for IR-UWB," *Microwave Opt. Technol. Letters*, vol. 49, iss. 7, pp. 1727-1731, 2007.

[9] M. Majidzadeh and C. Ghobadi, "Compact microstrip fed monopole antenna with modified slot ground plane for UWB applications," *Applied Computational Electromagnetics Society (ACES) Journal*, vol. 27, no. 10, pp. 801-807, Oct. 2012.

[10] S. Khan, J. Xiong, and S. He, "Low profile and small size frequency notched planar monopole antenna from 3.5 to 23.64 GHz," *Microwave Opt. Technol. Letters*, vol. 50, iss. 1, pp. 235-236, Jan. 2008.

[11] R. Zaker, C. Ghobadi, and J. Nourinia, "Novel modified UWB planar monopole antenna with variable frequency band-notched function," *IEEE Antennas Wireless Propag. Letters*, vol. 7, pp. 112-114, 2008.

[12] W. Chen and K. Yang, "CPW-fed planar ultra-wideband antenna having a frequency band-rejected function," *Proc. Int. Conf. TENCON2007*, pp. 1-3, 2007.

[13] Y. Li, W. Li, and W. Yu, "A switchable UWB slot antenna using SIS-HSIR and SIS-SIR for multi-mode wireless communications applications," *Applied Computational Electromagnetics Society (ACES) Journal*, vol. 27, no. 4, pp. 340-351, Apr. 2012.

[14] V. A. Shameena, M. N. Suma, K. Raj Rohith, P. C. Bybi, and P. Mohanan, "Compact ultra-wideband planar serrated antenna with notch band ON=OFF control," *Electron. Lett.*, vol. 42, no. 23, pp. 1323-1324, Nov. 2006.

[15] S. Nikolaou, N. D. Kingsley, G. E. Ponchak, J. Papapolymerou, and M. Tentzeris, "UWB elliptical monopoles with a reconfigurable band notch using MEMS switches actuated without bias lines," *IEEE Trans. Antennas Propag.*, vol. 57, no. 8, pp. 2242-2251, 2009.

[16] D.-M. Fang, S. Fu, Y. C. Yong, and X.-L. Zhao, "Surface micromachined RF MEMS variable capacitor," *Microelectronics Journal*, vol. 38, no. 8-9, pp. 855-859, 2007.

[17] W.-S. Lee, D.-Z. Kim, K.-J. Kim, and J. W. Yu, "Wideband planar monopole antennas with dual band-notched characteristics," *IEEE Trans. Microw. Theory Tech.*, vol. 54, no. 6, pp. 2800-2806, Jun. 2006.

Arash Nemati was born in Ghaemshahr, Iran, in 1989. He received the B.S. degree in Electrical Engineering from University of Mazandaran, Babolsar, Iran, in 2011 and M.S. degree in Electronics from Babol University of Technology, Babol, Iran, in 2014.

Since February 2014, he has been a Lecturer at the Department of Electrical and Computer Engineering, Babol University of Technology, Babol, Iran. His research interests include RF Microelectronics, RF-MEMS, Reconfigurable Antennas and Filters, and CMOS Analog Integrated Circuit Design.

Bahram Azizollah Ganji is an Associate Professor of Micro-Electronics with the Babol Noshirvani University of Technology. He received his Ph.D. degree in Micro-Engineering and Nano-Electronics from the University Kabangsaan Malaysia (UKM) in 2007, his B.Sc. degree in Electronics from Mashhad University in 1987, and his M.Sc. degree in Electronics from Tehran University in 1983.

His current interests are design and fabrication of MEMS/NEMS sensors, RFMEMS, BiOMEMS, MOEMS and Nano-Electronics. He has published more than 70 academic research papers.

Analysis of TM and TE Modes in Eccentric Coaxial Lines Based on Bipolar Coordinate System

Jun Zhou [1], Meiyan Chen [2], Renbin Zhong [1], and Shenggang Liu [1]

[1] Terahertz Research Center, School of Physical Electronics
University of Electronic Science and Technology of China, Chengdu, Sichuan 610054, China
zhoujun123@uestc.edu.cn, zhoujun@uestc.org

[2] Southwestern Institute of Physics, Chengdu, Sichuan 610041, China
mychen0014@126.com

Abstract ─ The cutoff wavenumbers, cutoff frequencies, field distributions and dispersive characteristics of TM and TE modes (higher order modes) in eccentric coaxial lines are carefully calculated by a new method directly based on the finite difference method (FDM) in bipolar coordinate system (BCS). Detailed comparisons with the previous results in the literature demonstrate the accuracy of the proposed method. Several characteristic features of the field distributions and the dispersion relations are also indicated. This method and its variations are very suitable and efficient for the computation of electromagnetic field problems in transmission lines with eccentric parallel cylinders.

Index Terms ─ Bipolar coordinate system, eccentric coaxial line, finite-difference method, transmission line, waveguide.

I. INTRODUCTION

The coaxial transmission lines have been widely used in different devices for various applications from the early 1900s. As a special case, the coaxial line with an eccentric inner conductor is termed as the eccentric coaxial line, which has been suggested to be used as an adjustable quarter-wave transformer for TEM mode propagation [1]. The effect of the displacement of the inner conductor on the electromagnetic characteristics of this kind of transmission lines was firstly investigated in 1960s [2]. As the eccentricity between the two conductors increases, higher order TM and TE modes may be excited at relatively high frequencies. For this problem, lots of methods mainly based on the conformal mapping and/or the boundary value approach have been reported in the literature continuously [2-11]. These methods have proven to be powerful for the solution of various wave-field problems. However, they are often found to be somewhat complex in practical applications. Analysis of TM and TE modes (higher order modes) in eccentric coaxial lines still remains interesting and challenging in the theory of electromagnetism.

The aim of this paper is to present a relatively simple method for the numerical analysis of eccentric coaxial lines through a computational approach. A new method which is directly based on the finite difference method (FDM) [12] in bipolar coordinate system (BCS) [13] is selected for much of this modeling effort. The FDM is a versatile and powerful technique for the computation of electromagnetic field problems, which is sufficient to allow us to investigate the higher order TM and TE modes in eccentric coaxial lines. The BCS has been successfully applied to the calculation of scattering from circular cylinders [14,15], which is much more convenient than the translational addition theorem of Bessel functions for transferring the fields component between two cylindrical coordinate systems [16].

This paper is organized as follows. We begin by discussing the methodology in Section II. The numerical results are then explored in detail and their comparisons with the previous results discussed in Section III. Finally, further discussion and conclusions are drawn in Section IV and Section V, respectively.

II. MODELING USING 2-D FDM IN BCS

A. Modeling in BCS

In uniform waveguides and transmission lines, the waveguiding structures are not changed along the propagating direction. The cross section of an eccentric coaxial line is shown in Fig. 1 (a). It contains a circular outer conductor and an eccentric circular inner conductor. The radii of the outer and inner circles are r_1 and r_2 respectively, and d is the distance between their centers.

This kind of waveguiding structure can be easily defined in the bipolar coordinate system (ξ, η, z) as shown in Fig. 1 (b) [13]. Let P_1 and P_2 be two fixed points in any z-plane with the coordinates (a, 0) and (-a, 0) respectively. The equations:

Submitted On: September 30, 2013
Accepted On: October 22, 2015

$$(x - a\coth\xi)^2 + y^2 = a^2\,\mathrm{csch}^2\,\xi\,, \tag{1}$$

$$x^2 + (y - a\cot\eta)^2 = a^2\csc^2\eta\,, \tag{2}$$

describe two families of orthogonal circles. Equation (1) describes the circles whose centers lie on the *x*-axis. The point P_1 at (a, 0) corresponds to $\xi = +\infty$, whereas its image P_2 at (-a, 0) corresponds to $\xi = -\infty$, and the *y*-axis is approached when $\xi = 0$. Equation (2) describes the circles whose centers lie on the *y*-axis and all of which pass through the fixed points P_1 and P_2. The parameter η is confined to the range $0 \le \eta \le 2\pi$. A value less than π is assigned to the arc above the *x*-axis, while the lower arc is denoted by a value of η equal to π plus the value of η assigned to the upper segment of the same circle.

The relation between BCS and Cartesian coordinate system can be described as:

$$x = h_1\sinh\xi\,, \tag{3}$$

$$y = h_2\sin\eta\,, \tag{4}$$

$$z = h_3 z\,, \tag{5}$$

where the metrical coefficients are:

$$h_1 = h_2 = \frac{a}{\cosh\xi - \cos\eta} = h,\ h_3 = 1\cdot \tag{6}$$

Suppose the two circles in Fig. 1 (a) both lie to the right of the *y*-axis in Fig. 1 (b), as shown in Fig. 1 (c), the parameters stated above are related by the following equations:

$$d = a(\coth\xi_1 - \coth\xi_2)\,, \tag{7}$$

$$r_1 = a\,\mathrm{csch}\,\xi_1\,, \tag{8}$$

$$r_2 = a\,\mathrm{csch}\,\xi_2\,. \tag{9}$$

Then, we can get the transformation relations:

$$a = \frac{\sqrt{\left[(r_1+r_2)^2 - d^2\right]\left[(r_1-r_2)^2 - d^2\right]}}{2d}\,, \tag{10}$$

$$\xi_1 = \mathrm{arcsinh}\frac{a}{r_1}\,, \tag{11}$$

$$\xi_2 = \mathrm{arcsinh}\frac{a}{r_2}\cdot \tag{12}$$

Here, in order to define the entire region in BCS, the parameter ξ is confined to the range $\xi_1 \le \xi \le \xi_2$, in order to define the entire region in BCS together with the other confinement $0 \le \eta \le 2\pi$.

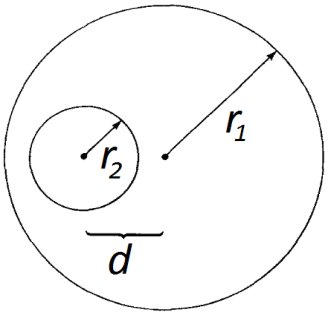

(a)

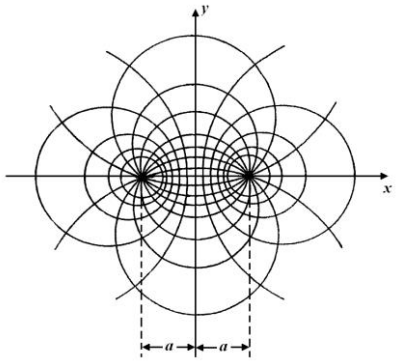

(b)

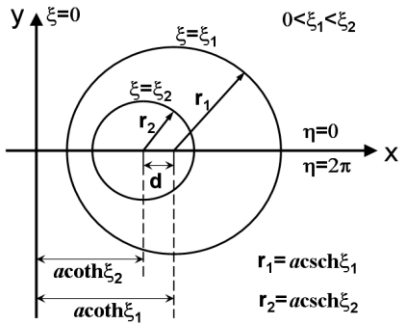

(c)

Fig. 1. Modeling in bipolar coordinate system: (a) cross section of eccentric coaxial line, (b) bipolar coordinate system, and (c) relations between the parameters.

B. Helmholtz equation and boundary conditions

Maxwell equations for the potential $\varphi(\xi, \eta, z)$ of an eccentric coaxial line lead to the following homogeneous Helmholtz equation in BCS:

$$\nabla_\perp^2\varphi + k_c^2\varphi = 0\,, \tag{13}$$

where $\nabla_\perp^2 = \frac{1}{h^2}\left(\frac{\partial^2}{\partial\xi^2} + \frac{\partial^2}{\partial\eta^2}\right)$, $k_c^2 = k^2 - k_z^2$, $k = \frac{\omega}{c}$, and c is the speed of light.

For TEM mode, $k = k_z$, when $\mathrm{ch}\xi - \cos\eta \ne 0$ we can get the Laplace equation:

$$\left(\frac{\partial^2}{\partial\xi^2} + \frac{\partial^2}{\partial\eta^2}\right)\varphi = 0\,, \tag{14}$$

which can be analytically solved by means of the variable separation approach.

For TM and TE modes, the Helmholtz equation is:

$$\frac{(\cosh\xi - \cos\eta)^2}{a^2}\left(\frac{\partial^2}{\partial\xi^2} + \frac{\partial^2}{\partial\eta^2}\right)\varphi + k_c^2\varphi = 0\,. \tag{15}$$

It has been proven strictly in mathematics that this equation can't be solved by means of the variable separation approach. Fortunately, this problem can be easily solved by means of the numerical methods such as the FDM and the finite element method (FEM).

For TM modes, $\varphi = E_z$, the Dirichlet boundary condition $\varphi = 0$ is employed on the boundaries $\xi = \xi_1$ and

$\xi = \xi_2$. While for TE modes, $\varphi = H_z$, the Neumann boundary condition $\partial\varphi/\partial n = 0$ is used. In addition, with consideration of the rotational symmetry, the periodic boundary conditions should be applied on the boundaries $\eta = 0$ and $\eta = 2\pi$.

C. FDM applied to the Helmholtz equation

According to Eq. (15), we can easily obtain the difference form of the Helmholtz equation in BCS on an orthogonal mesh. Based on the equation and the boundary conditions, a differentiation matrix A can be obtained for solving the eigenvalue problem:

$$A\Phi = k_c^2\Phi = \lambda\Phi, \tag{16}$$

where Φ is the eigenvector of φ values and $\lambda = k_c^2$ is the required eigenvalue.

Finally, the cutoff wavenumbers, the cutoff frequencies, the field distributions and the dispersive characteristics can all be achieved from the solution of this eigenvalue problem.

III. NUMERICAL RESULTS

Based on the above methodology, a special code has been constructed using the Microsoft Visual C++ programming language. The aim of this code is to solve the eigenvalue problems in BCS, print and save numerical results, and plot the field distributions. This code is very fast, it takes less than half a minute to calculate the first twenty eigenvalues for each case listed in the tables below on a single personal computer.

According to the previous publications, in order to be convenient for comparison and conversion, the results are always given for an outer circle of unit radius, the radius of the inner circle being denoted $\alpha = r_2 / r_1$ and the distance between the centers of the circles denoted $\beta = d / r_1$. To convert these frequencies to those of a similar region with outer circle of radius r_1, divide these frequencies by r_1. When comparing the results of other authors, their frequencies were normalized to an outer circle of radius 1. In this case, the transformation relations demonstrated in Eqs. (10)-(12) can be rewritten as:

$$a = \frac{\sqrt{\left[(1+\alpha)^2 - \beta^2\right]\left[(1-\alpha)^2 - \beta^2\right]}}{2\beta}, \tag{17}$$

$$\xi_1 = \operatorname{arcsinh} a, \tag{18}$$

$$\xi_2 = \operatorname{arcsinh} \frac{a}{\alpha}. \tag{19}$$

In our calculations, the values of α and β for which Kuttler [3] presented tables are selected. The main parameters used in the present calculations are summarized in Table 1. For purposes of direct comparisons, the cutoff wavenumbers obtained by the present calculations together with those evaluated by Kuttler [3], Vishen [4], Zhang [6] and Das [9] for symmetric and asymmetric TM as well as TE modes are given in Tables 2 to 5.

Table 1: Main parameters for the calculations

Parameters	Values
r_1	1
r_2	The value of α
d	The value of β
Range of ξ	Calculated from Eqs. (17)-(19)
Range of η	$[0, 2\pi]$
$\Delta\xi$	0.01
$\Delta\eta$	0.01

From the tables we can find that for TM modes, our results coincide with those of Vishen [4] and Zhang [6], which are all within the bounds reported by Kuttler [3]. For TE modes, our results do not agree with those of [4,6] very well, but most of them are within the bounds reported by Kuttler, and are all very close to the upper bounds. Obviously, for both TM and TE modes, our results do not agree with those of Das [9], we think the main reason is that the small numbers of the grid nodes (corresponding to the large spatial steps) used in [9] cause rough mesh and low precision in their calculations.

Then, based on the cutoff wavenumbers listed in the tables, the eigenvalues and the corresponding eigenvectors in Eq. (16) can be easily achieved from the relation $\lambda = k_c^2$. After that, the field distributions can be directly plotted using the φ values in the eigenvectors and the mode numbers can be easily determined from the field distribution plots. In Fig. 2 and Fig. 3, we detail the field distributions of the longitudinal field components for the lowest TM and TE modes corresponding to the case of $\alpha = 0.5$ and $\beta = 0.2$, respectively. Here, we use the prefix "e" for even (symmetric) modes and "o" for odd (asymmetric) modes [2,17].

Finally, the cutoff angular frequencies ω_c, the cutoff frequencies f_c and the dispersive characteristics can be easily achieved from the relations $\omega_c = 2\pi f_c = f_c c$, $\omega^2 = \omega_c^2 + k_z^2 c^2$. The cutoff frequencies for the lowest TM and TE modes corresponding to the case of $\alpha = 0.5$ and $\beta = 0.2$ are given in Table 6, and the dispersion curves for these modes are shown in Fig. 4.

From the field distributions and the dispersion curves we can find several characteristic features: (1) each of the TE_{mn} and TM_{mn} modes splits up into one even mode and one odd mode when $m \neq 0$; (2) the TM_{0n} modes are all even modes, and the TE_{0n} modes do not exist; (3) the cutoff frequencies of the TE_{mn} modes are much lower than those of the TM_{mn} modes with the same mode numbers m and n; (4) the cutoff frequencies of the eTE_{mn} modes and the oTE_{mn} modes with the same mode numbers are very close to each other, so their dispersion curves nearly overlap.

Table 2: Cutoff wavenumbers for symmetric TM modes

Case	Our Results	Das [9]	Zhang [6]	Vishen [4]	Kuttler Bounds [3]	
					Lower	Upper
α=0.5 β=0.1	5.4695	5.432	5.46953	5.4695	5.46911	5.47043
	6.4747	6.431	6.47472	6.4747	6.47403	6.47547
	7.3062	7.257	7.30617	7.3062	7.30527	7.30683
	7.8692	7.815	7.86924	7.8692	7.86823	7.86982
	8.4965	8.433	8.49647	8.4965	8.495	8.4972
α=0.5 β=0.2	4.8106	4.792	4.8106	4.8106	4.80935	4.81191
	6.1724	6.127	6.1724	6.1724	6.1703	6.1735
	7.3945	7.386	7.3945	7.3945	7.3907	7.3957
	8.4974	8.445	8.4974	8.4974	8.4894	8.4991
	9.3409	9.158	9.3409	9.3409	9.2694	9.3488
α=0.5 β=0.3	4.3071	4.293	4.3071	4.3071	4.3042	4.3118
	5.8903	5.828	5.8903	5.8903	5.8736	5.8944
	7.3197	7.198	7.3197	7.3197	7.24	7.325
	8.2909	7.953	8.2909	8.2909	8.081	8.316
	8.6388	8.365	8.6388	8.6388	8.382	8.646
α=2/3 β=0.2	6.2399	6.217	6.2399	6.2399	6.2379	6.242
	7.6769	7.65	7.6769	7.6769	7.6728	7.6787
	9.0439	8.99	9.0439	9.0439	9.0323	9.0456
	10.3535	10.309	10.3534	10.3536	10.318	10.356
	11.6134	11.523	11.6134	11.6184	11.539	11.616
α=0.25 β=0.25	3.4723	3.446	3.4723	3.4723	3.4687	3.4752
	4.9221	4.897	4.9221	4.9221	4.911	4.9249
	5.9268	5.862	5.9268	5.9268	5.893	5.93
	6.7154	6.58	6.7154	6.7154	6.591	6.723
	6.7527	6.626	6.7527	6.7527	6.622	6.767
α=0.25 β=0.5	2.9824	2.981	2.9824	2.9824	2.887	2.996
	4.7868	4.781	4.7868	4.7868	4.088	4.827
	5.8084	5.777	5.8084	5.8084	-	5.877
	6.2439	6.234	6.2439	6.2439	-	6.323
	7.5586	7.356	7.5586	7.5592	-	7.735

Table 3: Cutoff wavenumbers for asymmetric TM modes

Case	Our Results	Das [9]	Zhang [6]	Vishen [4]	Kuttler Bounds [3]	
					Lower	Upper
α=0.5 β=0.1	5.9918	5.953	5.99176	5.9918	5.99121	5.99257
	6.9203	6.878	6.92031	6.9203	6.91953	6.92102
	7.7123	7.619	7.71232	7.7123	7.7113	7.71299
	8.4845	8.371	8.4845	8.4845	8.483	8.4852
	9.3564	9.204	9.3564	9.3564	9.3542	9.3572
α=0.5 β=0.2	5.5114	5.485	5.5114	5.5114	5.5098	5.5125
	6.7991	6.729	6.7991	6.7991	6.7964	6.8002
	7.9607	7.931	7.9607	7.9607	7.9559	7.9619
	9.0091	8.897	9.0091	9.0091	8.9996	9.0106
	9.9556	-	9.9556	9.9556	9.9316	9.9577
α=0.5 β=0.3	5.1224	5.088	5.1224	5.1222	5.1179	5.1257
	6.621	6.563	6.621	6.621	6.5994	6.6251
	7.991	7.839	7.991	7.991	7.876	7.997
	9.1877	8.814	9.1877	9.1877	8.829	9.21
	9.2676	8.975	9.2676	9.2676	8.9	9.276
α=2/3 β=0.2	6.9683	6.887	6.9683	6.9683	6.9654	6.9702
	8.3682	8.347	8.3682	8.3682	8.3631	8.37
	9.7053	9.61	9.7053	9.7053	9.6922	9.7071
	10.9892	10.932	10.9892	10.9892	10.947	10.992
	12.2266	-	12.2266	12.2266	12.128	12.229
α=0.25 β=0.25	4.264	4.248	4.264	4.264	4.2583	4.268
	5.5393	5.488	5.5393	5.5393	5.5239	5.5425
	6.6357	6.552	6.6357	6.6357	6.582	6.641
	7.7135	7.46	7.7135	7.7135	7.443	7.723
	7.7243	-	7.7243	7.7243	7.488	7.735
α=0.25 β=0.5	4.0338	3.973	4.0338	4.0338	3.858	4.043
	5.5432	5.494	5.5432	5.5432	4.58	5.575
	6.9144	6.914	6.9144	6.9144	-	6.992
	7.156	7.144	7.156	7.156	-	7.208
	8.1858	-	8.1858	8.1858	-	8.355

Table 4: Cutoff wavenumbers for symmetric TE modes

Case	Our Results	Das [9]	Zhang [6]	Vishen [4]	Kuttler Bounds [3]	
					Lower	Upper
α=2/3 β=0.2	1.322	1.318	1.3222	1.2522	1.32027	1.32221
	2.4458	2.422	2.4445	2.4365	2.4408	2.4446
	3.6216	3.565	3.6217	3.6209	3.6157	3.6218
	4.7881	4.672	4.7897	4.7897	4.7804	4.7901
	5.9378	5.717	5.9378	5.9379	5.9218	5.9385
α=0.475 β=0.315	1.5195	-	1.5158	1.4407	1.5132	1.5159
	2.7341	-	2.7343	2.7256	2.727	2.7345
	3.9275	-	3.9237	3.924	3.8978	3.9248
	4.3704	-	4.4035	-	4.342	4.407
	5.0806	-	5.0801	5.0799	4.977	5.084
α=1/3 β=2/9	1.5808	1.569	1.5806	1.5619	1.5766	1.5807
	2.9063	2.863	2.9065	2.9064	2.8968	2.9067
	4.1164	4.016	4.1152	4.1152	4.0944	4.1161
	4.2334	4.56	4.2342	4.422	4.2146	4.2356
	5.2649	5.083	5.2673	5.2669	5.219	5.27
α=0.5 β=0.2	1.4076	1.401	1.40792	1.3793	1.40694	1.40793
	2.6863	2.659	2.6861	2.6849	2.6837	2.6862
	3.9296	3.918	3.9295	3.9295	3.9247	3.9298
	5.0178	4.872	5.0175	-	4.9937	5.0192
	5.1135	5.512	5.1133	5.1131	5.1031	5.1139
α=0.25 β=0.25	1.6848	1.633	1.681	1.665	1.6768	1.6811
	2.9616	2.908	2.9679	2.9678	2.9445	2.9684
	3.9744	3.899	3.9861	-	3.939	3.988
	4.145	4.352	4.165	4.1191	4.105	4.168
	5.2913	5.055	5.2946	5.2942	5.111	5.303
α= 0.15875 β=0.379	1.8089	-	1.7944	1.7769	1.7603	1.7948
	3.0013	-	2.9992	2.9932	2.871	3.004
	3.7523	-	3.7703	3.8632	3.432	3.775
	4.1806	-	4.1824	4.1808	3.76	4.21

Table 5: Cutoff wavenumbers for asymmetric TE modes

Case	Our Results	Das [9]	Zhang [6]	Vishen [4]	Kuttler Bounds [3]	
					Lower	Upper
α=2/3 β=0.2	1.1928	1.189	1.19175	1.1917	1.19001	1.19176
	2.4297	2.418	2.4304	2.4307	2.4267	2.4305
	3.6196	3.415	3.6202	3.6203	3.6142	3.6203
	4.7879	4.669	4.7896	4.7896	4.7804	4.7899
	5.9324	-	5.9379	5.9379	5.9231	5.9385
α=0.475 β=0.315	1.3783	-	1.3741	1.374	1.3715	1.3741
	2.7257	-	2.7196	2.7187	2.7125	2.7198
	3.9152	-	3.9237	3.9244	3.9069	3.9247
	5.0657	-	5.0793	5.0796	5.041	5.083
	5.4061	-	5.4232	5.3686	5.325	5.427
α=1/3 β=2/9	1.5461	1.532	1.5435	1.5435	1.5393	1.5436
	2.9063	2.863	2.9064	2.9058	2.8966	2.9067
	4.1164	4.016	4.1152	4.1152	4.0955	4.1161
	5.1588	5.053	5.1651	5.1606	5.131	5.167
	5.2705	-	5.2758	5.2758	5.237	5.279
α=0.5 β=0.2	1.3522	1.344	1.35218	1.3522	1.35114	1.35219
	2.6843	2.657	2.6834	2.6838	2.6815	2.684
	3.9268	3.892	3.9295	3.9296	3.9247	3.9298
	5.1128	4.982	5.1131	5.1131	5.1036	5.1138
	5.8274	-	5.8315	5.8106	5.793	5.834
α=0.25 β=0.25	1.6458	1.633	1.6489	1.649	1.6446	1.649
	2.9671	2.915	2.9678	2.9667	2.9547	2.9682
	4.145	3.972	4.1581	4.1579	4.12	4.16
	5.0636	4.654	5.0581	5.0616	4.978	5.06
	5.3089	-	5.2964	5.2965	5.175	5.302
α= 0.15875 β=0.379	1.7544	-	1.7583	1.7584	1.733	1.7584
	2.9884	-	2.9879	2.9848	2.873	2.989
	4.164	-	4.1614	4.159	3.78	4.17

Table 6: Cutoff frequencies for the lowest TM and TE modes with $\alpha = 0.5$ and $\beta = 0.2$

Modes		k_c	ω_c ($\times 10^9$)	f_c (GHz)
TM modes	eTM_{01}	4.8106	1.4432	0.2297
	oTM_{11}	5.5114	1.6534	0.2631
	eTM_{11}	6.1724	1.8517	0.2947
	oTM_{21}	6.7991	2.0397	0.3246
	eTM_{21}	7.3945	2.2184	0.3531
	oTM_{31}	7.9607	2.3882	0.3801
TE modes	oTE_{11}	1.3522	0.4057	0.06457
	eTE_{11}	1.4076	0.4223	0.06721
	oTE_{21}	2.6843	0.8053	0.1282
	eTE_{21}	2.6863	0.8059	0.1283
	oTE_{31}	3.9268	1.178	0.1875
	eTE_{31}	3.9296	1.1789	0.1876

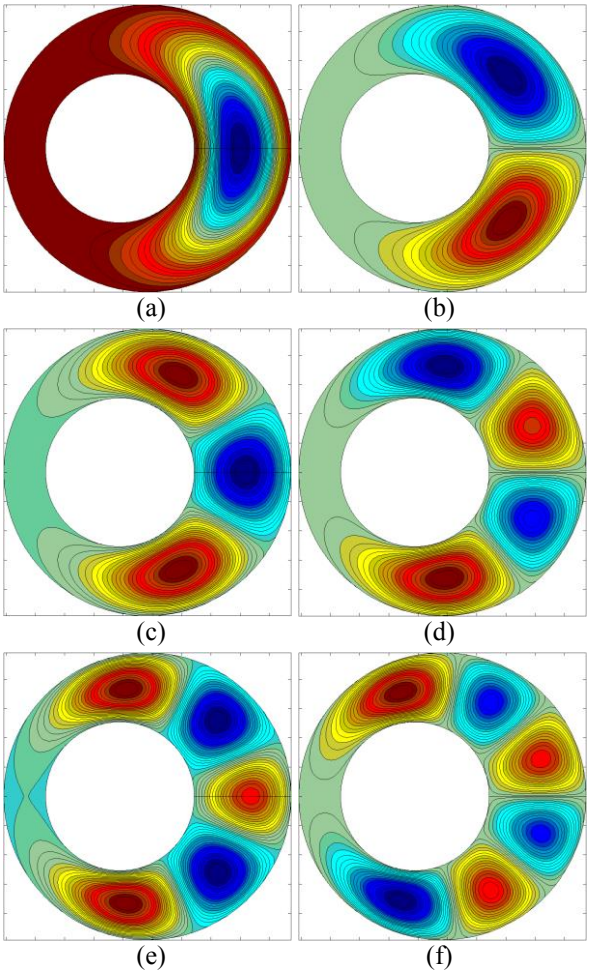

Fig. 2. Field distributions of E_z for the lowest TM modes with $\alpha = 0.5$ and $\beta = 0.2$: (a) eTM_{01} mode, (b) oTM_{11} mode, (c) eTM_{11} mode, (d) oTM_{21} mode, (e) eTM_{21} mode, and (f) oTM_{31} mode.

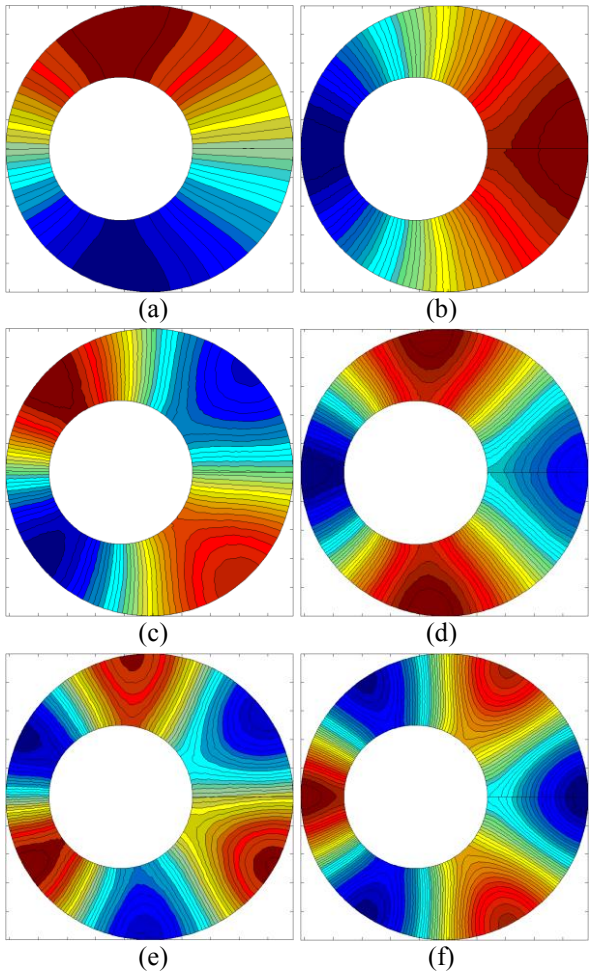

Fig. 3. Field distributions of H_z for the lowest TE modes with $\alpha = 0.5$ and $\beta = 0.2$: (a) oTE_{11} mode, (b) eTE_{11} mode, (c) oTE_{21} mode, (d) eTE_{21} mode, (e) oTE_{31} mode, and (f) eTE_{31} mode.

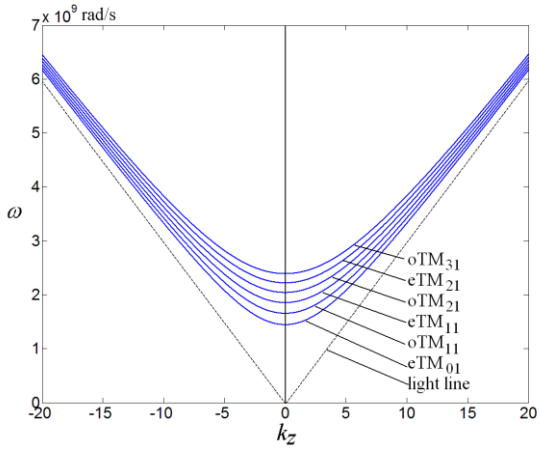

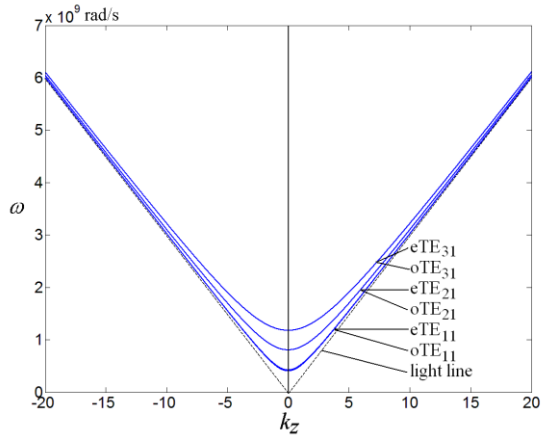

(b)

Fig. 4. Dispersion curves for the lowest TM and TE modes with α = 0.5 and β = 0.2: (a) TM modes, and (b) TE modes.

The dependence of the cutoff frequency on the eccentricity of the coaxial line has been intensively analyzed in the literature, so we will not discuss here. The deviation between the numerical results calculated by the present method and those presented in the literature is very small. This agreement justifies the validity of the present analysis. Because BCS is very suitable for transmission lines with eccentric parallel cylinders, the success of the present method encourages its use for other problems, such as the analysis of lunar waveguides mentioned in [3] and two-wire waveguides [18,19]. For these problems, only some variations of the boundary conditions in the present method are required.

IV. DISCUSSION

A. Accuracy and convergence rate

It is necessary to discuss the characteristics of the proposed method. Here, we will discuss the accuracy and convergence rate, which are two of the most essential characteristics of a numerical method.

The accuracy obtained by the proposed method is mainly due to the easy definition of eccentric coaxial waveguiding structure in BCS. Given an arbitrary cross section of an eccentric coaxial line, we can easily get the required parameters in BCS through the transformation relations demonstrated in Eqs. (10)-(12). Since the inner and outer boundaries are all parallel to the ξ-axis in BCS, there is no need to worry about the errors from the saw-tooth shaped boundaries, which has long been suffered by the FDM in other coordinate systems, as shown in Fig. 5.

From the Taylor series of $\varphi_{i,j}$ in BCS, we obtain:

$$\frac{\partial^2 \varphi_{i,j}}{\partial \xi^2} = \frac{\varphi_{i+1,j} - 2\varphi_{i,j} + \varphi_{i-1,j}}{(\Delta\xi)^2} + O\left[(\Delta\xi)^2\right], \qquad (20)$$

$$\frac{\partial^2 \varphi_{i,j}}{\partial \eta^2} = \frac{\varphi_{i,j+1} - 2\varphi_{i,j} + \varphi_{i,j-1}}{(\Delta\eta)^2} + O\left[(\Delta\eta)^2\right], \qquad (21)$$

which indicate that the second derivative of $\varphi_{i,j}$ is second-order accurate. So, in the case of $\Delta\xi = \Delta\eta = 0.01$ we used for the calculations, an accuracy of 0.0001 can be achieved. Even higher accuracy can also be easily achieved by reducing the spatial step size.

In order to solve the eigenvalue problem demonstrated in Eq. (16) with high efficiency, the Arnoldi method has been adopted for the fast computations. The Arnoldi method is well known for solving large matrix eigenvalue problems. For this classical method, the convergence rate has been intensively analyzed in the publications in mathematics [20,21], so we will not analyze it any more.

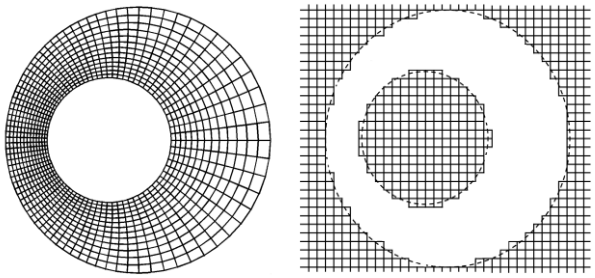

(a) (b)

Fig. 5. Comparison of meshes in different coordinate systems: (a) mesh with smooth boundaries in BCS, (b) and mesh with saw-tooth shaped boundaries in Cartesian coordinate system.

B. Comparisons with other methods

Among all the numerical methods, the FDM is the oldest and also the simplest. Its simplicity, however, makes it very robust and efficient [12]. It is essential to compare the proposed method with other commonly used numerical methods. Here, we will give the comparisons among the FDM, the finite difference time-domain (FDTD) method, the FEM method and the method of moments (MoM).

The FDM used in this paper is a numerical procedure for converting partial differential equations (PDEs) of a boundary-value problem into a set of algebraic equations to obtain approximate solutions, it is very suitable and efficient for the problem analyzed here. The method has been widely used in a variety of engineering fields. For a practical problem, if the coordinate system is properly chosen, the saw-tooth shaped boundaries can be well avoided and the degree of accuracy can reach a very high level, which has just been discussed.

The applications of FDM to the analysis of electromagnetic problems was empowered by the development of a unique scheme for the discretization of

the time-domain Maxwell's equations, which is known today as the FDTD method. With the further development, the FDTD became probably the most popular numerical technique for solving complex electromagnetic problems [12]. But, the FDTD is well suited to time-domain full-wave analysis. There is no need to solve the eigenvalue problems using the FDTD method.

Like the FDM, the FEM is a numerical procedure to convert partial differential equations into a set of linear algebraic equations to obtain approximate solutions. Instead of approximating the differential operators, the FEM approximates the solution of a partial differential equation. Today, the FEM is recognized as a general preeminent method applicable to a wide variety of engineering and mathematical problems [12]. Generally, when compared with the FDM, the FEM has better accuracy and stability, but its realization is too complicated. Furthermore, it requires larger computer memory and longer computation time.

The MoM, also known as the moment method, is another powerful numerical technique in electromagnetics. Like the FEM, the MoM transforms the governing equation of a boundary-value problem into a matrix equation to enable its solution on digital computers. Today, it has become one of the most predominant methods in computational electromagnetics [12]. But the MoM is particularly well suited to open-region electromagnetic problems such as wave scattering and antenna radiation, and its realization is also too complicated when compared with the FDM.

To conclude, according to the above comparisons, it is easy to see that the FDM in BCS used in this paper is the most convenient, efficient and straightforward numerical method with high simplicity and practicality for the analysis of TM and TE modes in eccentric coaxial lines and other transmission lines with eccentric parallel cylinders.

V. CONCLUSION

A new method directly based on the FDM in BCS is developed, which is very suitable and efficient for calculating TM and TE modes in eccentric coaxial lines. Making use of this method, the cutoff wavenumbers, cutoff frequencies, field distributions and dispersive characteristics of higher order TM and TE modes in eccentric coaxial lines are given. Our results agree well with the previous results in the literature. In addition, several characteristic features of the field distributions and the dispersion relations are also indicated.

The accuracy of this method is mainly due to the easy definition of eccentric coaxial waveguiding structure in BCS. Furthermore, some variations of this method can be applied to the computation of electromagnetic field problems in other transmission lines with eccentric parallel cylinders (connected or not), such as lunar waveguides, two-wire waveguides, and so on.

ACKNOWLEDGMENT

Jun Zhou wishes to express his sincere thanks to Prof. Zhaoyun Duan, Prof. Wei Shao and Prof. Shengjian Lai in School of Physical Electronics of UESTC for their kind help and comments. This work was supported by the Natural Science Foundation of China under Grant No. 61505022.

REFERENCES

[1] P. Grivet, *Physics of Transmission Line at High and Very High Frequency*, Academic Press, London, 1970.

[2] H. Y. Yee and N. F. Audeh, "Cutoff frequencies of eccentric waveguides," *IEEE Trans. Microwave Theory Tech.*, vol. 14, no. 10, pp. 487-493, Oct. 1966.

[3] J. R. Kuttler, "A new method for calculating TE and TM cutoff frequencies of uniform waveguides with lunar or eccentric annular cross section," *IEEE Trans. Microwave Theory Tech.*, vol. 32, no. 4, pp. 348-354, Apr. 1984.

[4] A. Vishen, G. P. Srivastava, G. S. Singh, and F. Gardiol, "Calculation of cutoff wavenumbers for TE and TM modes in tubular lines with offset center conductors," *IEEE Trans. Microwave Theory Tech.*, vol. 34, no. 2, pp. 292-294, Feb. 1986.

[5] M. Davidovitz and Y. T. Lo, "Cutoff wavenumbers and modes for annular-cross-section waveguide with eccentric inner conductor of small radius," *IEEE Trans. Microwave Theory Tech.*, vol. 35, no. 5, pp. 510-515, May 1987.

[6] L. Zhang, J. Zhang, and W. Wang, "Correct determination of TE and TM cutoff wavenumbers in transmission lines with circular outer conductors and eccentric circular inner conductors," *IEEE Trans. Microwave Theory Tech.*, vol. 39, no. 8, pp. 1416-1420, Aug. 1991.

[7] A. A. Kishk, R. P. Parrikar, and A. Z. Elsherbeni, "Electromagnetic scattering from an eccentric multilayered circular cylinder," *IEEE Trans. Antennas Propag*., vol. 40, no. 3, pp. 295-303, Mar. 1992.

[8] B. N. Das and O. J. Vargheese, "Analysis of dominant and higher order modes for transmission lines using parallel cylinders," *IEEE Trans. Microwave Theory Tech.*, vol. 42, no. 4, pp. 681-683, Apr. 1994.

[9] B. N. Das and S. B. Chakrabarty, "Evaluation of cut-off frequencies of higher order modes in eccentric coaxial line," *IEE Proc. - Microwave Antennas Propag*., vol. 142, no. 4, pp. 350-356, Aug. 1995.

[10] X. Zhou, Z. Yu, and W. Lin, "Characteristics of eccentric coaxial line using conformal mapping and finite-difference time-domain method,"

Microwave and Optical Tech. Lett., vol. 16, no. 11, pp. 249-252, Nov. 1997.

[11] S. B. Chakrabarty, S. B. Sharma, and B. N. Das, "Higher-order modes in circular eccentric waveguides," *Electromagnetics*, vol. 29, no. 5, pp. 377-383, 2009.

[12] J. M. Jin, *Theory and Computation of Electromagnetic Fields*, John Wiley & Sons, Inc., New Jersey, 2010.

[13] J. A. Stratton, *Electromagnetic Theory*, McGraw-Hill, New York, 1941.

[14] J. M. Jarem, "Rigorous coupled wave analysis of bipolar cylindrical systems: scattering from inhomogeneous dielectric material, eccentric, composite circular cylinders," *Progress in Electromagnetics Research*, vol. 43, pp. 181-237, 2003.

[15] R. Herschmann and O. Büchel, "Radiation characteristics of a coaxial waveguide with eccentric inner conductor for application in hyperthermia and microwave reflex therapy," *Advances in Radio Science*, vol. 5, pp. 189-195, 2007.

[16] H. A. Yousif and A. Z. Elsherbeni, "Oblique incidence scattering from two eccentric cylinders," *Journal of Electromagnetic Waves and Applications*, vol. 11, no. 9, pp. 1273-1288, 1997.

[17] E. Abaka and W. Baier, "TE and TM modes in transmission lines with circular outer conductor and eccentric circular inner conductor," *Elec. Lett.*, vol. 5, no. 11, pp. 251-252, May 1969.

[18] H. Pahlevaninezhad, T. E. Darcie, and B. Heshmat, "Two-wire waveguide for terahertz," *Opt. Expr.*, vol. 18, no. 7, pp. 7415-7420, Mar. 2010.

[19] R. Zhong, J. Zhou, W. Liu, and S. Liu, "Theoretical investigation of a terahertz transmission line in bipolar coordinate system," *Science China Information Sciences*, vol. 55, no. 1, pp. 35-42, Jan. 2012.

[20] Y. Saad, *Numerical Methods for Large Eigenvalue Problems*, SIAM, Philadelphia, 1992.

[21] G. H. Golub and C. F. Van Loan, *Matrix Computations*, Third edition, The Johns Hopkins University Press, 1996.

Jun Zhou was born in Hubei Province, China, in 1980. He received the B.S. degree in Applied Physics and the Ph.D. degree in Plasma Physics from the University of Electronic Science and Technology of China (UESTC), Chengdu, China, in 2003 and 2009, respectively.

From October 2008 to May 2009, he was a Visiting Student in Queen Mary, University of London, UK. In 2009, he joined the faculty of UESTC. He is currently engaged in research in the Terahertz Science and Technology Research Center at UESTC in the areas of terahertz sources, terahertz spectroscopy and imaging, terahertz transmission lines and antennas, and computational electromagnetics.

Meiyan Chen was born in Shandong Province, China, in 1981. She received the B.S. degree in Applied Physics from the Liaocheng University, Liaocheng, China, in 2004, the M.S. degree in Condensed Matter Physics from the University of Electronic Science and Technology of China (UESTC), Chengdu, China, in 2007 and the Ph.D. degree in Nuclear Energy Technology and Development from the Southwestern Institute of Physics (SWIP), Chengdu, China, in 2012.

She is currently with the SWIP. Her research interests include theory, simulation and experimental works on novel materials and components.

Renbin Zhong was born in Jiangxi Province, China, in 1973. She received the M.S. degree in Optics from the Southwest Jiaotong University, Chengdu, China, in 2003 and the Ph.D. degree in Plasma Physics from the University of Electronic Science and Technology of China (UESTC), Chengdu, China, in 2012.

She is currently with the Terahertz Science and Technology Research Center, UESTC. Her research interests include terahertz sources, terahertz transmission and related components.

Shenggang Liu received the B.S. degree from the Southeast University (formerly Nanjing Polytechnic Institute), Nanjing, China, in 1995 and the Ph.D. degree in Physical Electronics from the University of Electronic Science and Technology of China (UESTC), Chengdu, China, in 1958.

Since 1964, he has been leading various research projects on gyrotrons, free electron lasers, and plasma electronics. He was a Distinguished Visiting Professor with Old Dominion University, Norfolk, VA, and the College of William and Mary, Williamsburg, VA, where he worked in the field of microhollow cathode discharges, microwave plasma excited excimer lasers, and electromagnetic field effect on biological cells. In 1980, he was elected Academician of the Chinese Academy of Sciences. In 1984, he was appointed Vice-President of UESTC and then served as President from 1986 to 2001. He is a Member of International Organizing Committee of IRMMW-THz Conferences, K. J. Button Prize Committee, et al. He serves as the Chair of the International Committee of SICAST Conferences. He is currently Professor and Director of the Terahertz Science and Technology Research Center, UESTC. His research interests include terahertz physics, microwave electronics, relativistic electronics, free electron laser, optics, and plasma physic.

Microstrip Dielectric Substrate Material Characterization with Temperature Effect

B. Ravelo [1], A. Thakur [2], A. Saini [2], and P. Thakur [2]

[1] IRSEEM EA
4353 Avenue Galilée, F-76801 Saint Etienne du Rouvray, France
ravelo@esigelec.fr

[2] Centre of Excellence in Nanotechnology and Materials Science
Shoolini University, Solan, H.P., 173212, India

Abstract ─ This paper describes a dielectric substrate materials electromagnetic (EM) characterization method in the ultra-wideband (UWB) frequencies from DC to 5 GHz by taking into account the temperature influence. The proposed method theoretical principle is described and fundamentally built with the analytical formulation from the microstrip transmission line (TL) theory. From this basic concept, the analytical equations enabling to determine the dielectric material relative permittivity and loss tangent from the given S-parameters are established. The characterization method is validated with numerical and experimental tests. As proof of concept, a prototype of microstrip TL printed on FR4 epoxy substrate was designed, fabricated and experimented. The relative permittivity and loss tangent were extracted in the UWB frequency from DC to 5 GHz in the range of temperature varied from 40°C to 140°C. This innovative characterization method is useful for the investigation on the frequency dependent and especially by taking into account the temperature influence on the substrate materials; for example, during the microstrip circuits design phase.

Index Terms ─ Measurement method, microstrip line, relative permittivity, substrate material, temperature effect.

I. INTRODUCTION

With the tremendous trend on the electronic circuit design shirking size, the electromagnetic compatibility/ interference (EMC/EMI), the signal integrity and the temperature influence become critical effects [1-5] which must be integrated to the design and fabrication phases. These undesirable physical phenomena are more and more crucial for the deep submicron VLSI [1-2]. It was found that the thermal effects can induce particular phenomenon as the electromigration in the integrated circuits [3-4]. Moreover, the clock signal performances can be degraded due to the thermal influence on the substrate [5]. More recently, electronic research and design engineers were experimented that the temperature effect and the moisture are susceptible to degrade the printed circuit boards (PCBs) global performance [6]. Due to the constant increase of integration density, the substrate material characterization with the frequency and temperature dependence becomes a challenging subject for the microwave and integrated circuit designers and manufacturers [2,7]. Until now, very few investigations on the temperature influence to the electronic devices performance as the integrated [8] and hybrid [9] circuits are available in the literature. Despite the developed electromagnetic (EM) classical modeling, simulation and test techniques [10-11], the simultaneous influence of electrical, EM and temperature effects on the microwave circuits and devices remains an open question for the electronic research and design engineers. Furthermore, most of the existing classical EM characterization techniques dedicated to the dielectric materials are based on the consideration of S-parameters by using waveguide structures. Some of the available techniques are essentially carried out with the through, reflect, line calibration [11], coplanar lines [12-14], and split ring resonators [15]. However, those techniques present a heavy process complexity and they do not include the temperature effect and require sophistical analytical approaches. The existing measurement technique of complex permittivity which takes into account the temperature variation as proposed in [16] was set with different shapes of resonant cavity. Nevertheless, such a characterization technique is particularly limited in terms of the operating frequency. Furthermore, it cannot be used for predicting the material characteristics in the baseband and microwave frequencies, which can be regularly required for the digital and microwave or mixed signal integrity analysis [17].

To overcome such technical limits, a relevant characterization method enabling to predict the substrate

Submitted On: February 26, 2015
Accepted On: July 28, 2015

material parameters in the ultra-wideband (UWB) frequency (with baseband frequency up to some GHz) with the use of microstrip technology can be envisaged. In addition to the flexibility of microstrip line theoretical approach, it enables a particularly simple experimental process as can be found in [17].

This paper addresses the EM characterization technique of dielectric substrate material with the temperature influence based on the miscrostrip line theory. For the better understanding, the paper is principally organized in three main sections. Section 2 is focused on the methodological approach of the substrate material characterization method under study. The fundamental formulas enabling to determine the permittivity will be proposed. The experimental application of the analytical approach constitutes Section 3. A microstrip test structure printed on FR4 epoxy will be investigated. The conclusion of the paper is drawn in the last section.

II. METHODOLOGY OF THE PROPOSED DIELECTRIC MATERIAL CHARACTERIZATION

The theoretical approach of this substrate material characterization method is elaborated in the present section. The method is essentially built with the consideration of microstrip structure. After brief introduction of the structure geometrical definitions and its S-parameters, the formulas allowing the extraction of the parameters to be determined will be proposed.

A. Description of the structure for the proposed substrate material EM characterization

The most accurate experimental way to perform a substrate material EM characterization in the base band and broadband microwave frequency dependence is based on the S-parameters measurement consideration. Thanks to the design simplicity and the flexibility of the analytical approach, the transmission line (TL) and resonator structures are the most popular technology to realize this characterization technique. In fact, by considering the exploitation of S-parameters analytical definition in function of the geometrical parameters, the substrate EM parameters as the permittivity formulation can be extracted. Along the paper, the TL implemented in microsrip structure will be investigated to establish the theoretical approach.

The configuration of the structure using the dielectric substrate characteristic measurement method under study is shown in Fig. 1. It acts as a microstrip TL with physical length *d*, metallization width *w* and thickness *t* which is printed on dielectric substrate with height *h*. The substrate complex permittivity versus frequency *f* and temperature *T* will be extracted from the TL measured two-port S-parameters.

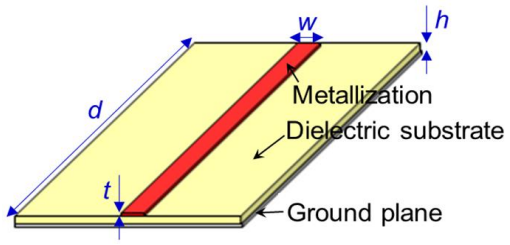

Fig. 1. Microstrip line structure and its physical parameters.

Along the paper, the reference impedance is denoted Z_0=50 Ω. The two-port system S-to-Z transform applied to the microstrip structure proposed in Fig. 1 allows to determine the access and transfer impedances. From where, the input and transmitted impedance versus the frequency *f* with respect to the S-parameters measurement versus the environment temperature *T* are defined as:

$$Z_{11}(jf,T)=\frac{\begin{array}{l}Z_0\cdot(1+S_{11}(jf,T)-S_{22}(jf,T)\\-S_{11}(jf,T)\cdot S_{22}(jf,T)\\+S_{12}(jf,T)\cdot S_{21}(jf,T))\end{array}}{\begin{array}{l}1-S_{11}(jf,T)-S_{22}(jf,T)\\+S_{11}(jf,T)\cdot S_{22}(jf,T)\\-S_{12}(jf,T)\cdot S_{21}(jf,T)\end{array}}, \quad (1)$$

$$Z_{21}(jf,T)=\frac{\begin{array}{l}Z_0\cdot 2S_{21}(jf,T)\\1+S_{11}(jf,T)+S_{22}(jf,T)\\-S_{11}(jf,T)\cdot S_{22}(jf,T)\\+S_{12}(jf,T)\cdot S_{21}(jf,T)\end{array}}{}, \quad (2)$$

with *j* is the complex number. In the one hand, these expressions permit to determine the TL matrix impedances from the measured S-parameters by using a VNA. In the other hand, by assuming that the TL is Z_0-loaded and non-dispersive, the same input and transfer impedances can be determined knowing the characteristic impedance Z_c and the propagation constant γ via the following expressions:

$$Z_{11}=Z_c\frac{\cosh(\gamma\cdot d)}{\sinh(\gamma\cdot d)}, \quad (3)$$

$$Z_{21}=\frac{Z_c}{\sinh(\gamma\cdot d)}. \quad (4)$$

The equality of these analytical formulations combined with the microstrip line properties constitutes the building block of the determination method of the substrate material parameters under study described in the next paragraphs.

B. Analytical equations of the dielectric substrate parameter extraction with frequency dependence including the temperature influence

First and foremost, the dielectric characteristics are established from the microstrip line analysis combined

with the Bahl and Trivedi theory [17]. By definition, the TL propagation constant is defined in function of the per-unit loss α and the phase constant β via the basic expression $\gamma(jf,T)=\alpha(f,T)+j\beta(f,T)$. From the member to member division of Equations (3) and (4), the following expression of the propagation constant can be obtained:

$$\gamma(jf,T)=\frac{1}{d}\arg\cosh\left[\frac{Z_{11}(jf,T)}{Z_{21}(jf,T)}\right]. \quad (5)$$

Then, the effective relative permittivity $\varepsilon_{r_{eff}}(f,T)$ of the dielectric material constituting the microstrip TL can be established from the phase constant thanks to the relation:

$$\varepsilon_{r_{eff}}(f,T)=\left[\frac{c\cdot\partial\beta(f,T)}{2\pi\partial f}\right]^2, \quad (6)$$

with c is the light speed in the vacuum. From where, the substrate relative permittivity can be extracted with the expression [17]:

$$\varepsilon_r(f,T)\approx\frac{2\varepsilon_{r_{eff}}(f,T)-1+a(w/h)}{1+a(w/h)}, \quad (7)$$

where the mathematical function $a(.)$ is defined by:

$$a(x)=\begin{cases}\dfrac{1}{\sqrt{1+12/x}}+0.04(1-x)^2 & for\ x<1\\ \dfrac{1}{\sqrt{1+12/x}} & for\ x\geq 1\end{cases}. \quad (8)$$

Finally, the loss tangent can be extracted from the equation:

$$\tan\left[\delta(f,T)\right]\approx\frac{c\cdot\alpha(f,T)}{\pi\cdot f\sqrt{\varepsilon_{r_{eff}}(f,T)}}. \quad (9)$$

During the numerical modelling, those analytical relations were implemented as Matlab program. The computed results will be discussed in the next section.

III. EXPERIMENTAL INVESTIGATION

After introduction of the experimental setup, the measurement results exploitation will be presented in this section based on the previous analytical approach.

A. Circuit under test design and experimental setup

The microstrip TL assumed as the circuit under test is photographed in Fig. 2. It can be seen that this TL presents physical parameters w=1.5 mm and d=164 mm. The circuit is printed on FR4 epoxy substrate with height h=0.8 mm and copper etched with thickness t=35 µm. The S-parameters of the circuit under test were measured with the Agilent VNA 8502C from DC to 5 GHz. Moreover, after calibration, it was placed in the furnace provided by THITEC® depicted in Fig. 3. The furnace presents the physical size 50cm×47cm×50cm or volume 117 liters. The furnace operates with a digital function allowing to program the temperature of its internal chamber. For the present study, the temperature chamber was increased from ambient T=40°C to 140°C. In order to consider the temperature influence on the circuit under test, the sampling of the measured $S(jf,T)$-parameters was recorded at least after five minutes of the temperature change.

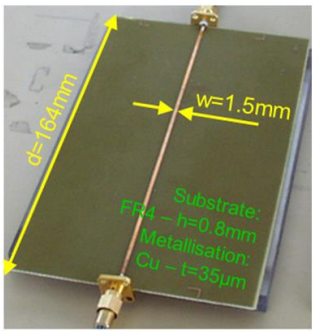

Fig. 2. Photograph of the circuit under test.

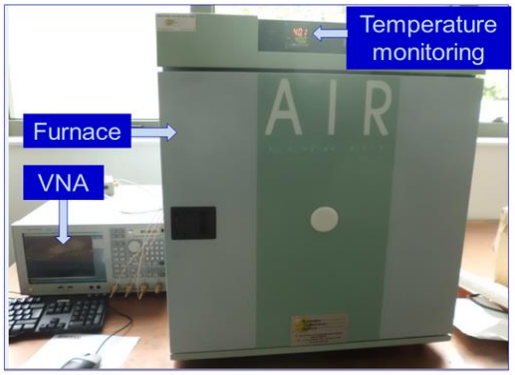

Fig. 3. Photograph of the experimental test bench including the VNA and the furnace.

To check the relevance of the proposed method, preliminary numerical tests with EM computation based on the method of moment (MoM) were performed.

B. Numerical tests with method of moment simulation

To perform the numerical tests, the inputs parameters are the physical dimensions of the tested line, the operating frequency band and the given S-parameters. Two microstrip TLs supposed with different physical lengths d_1=82 mm and d_2=164 mm printed on the dielectric substrate with relative permittivity ε_r=4.5, loss tangent $\tan(\delta)$=0.018 and h=0.8 mm etched with Cu-conductor were designed and simulated in the ADS/Momentum environment. The comparisons between the super UWB substrate characteristics extracted from the simulated S-parameters are displayed in Fig. 4.

A good correlation between the extracted dielectric characteristics is observed. However, a relative variation lower than 8% is occurred compared to the ideal

parameters, mainly due to the MoM numerical inaccuracy. This preliminary result confirms the feasibility of the characterization method under study independently to the TL physical length and to operate notably in the UWB frequency.

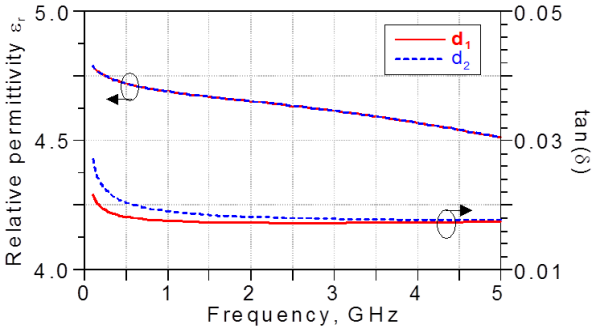

Fig. 4. Comparisons between relative permittivity and loss tangent versus frequency from MoM simulations.

Based on the full wave approach, it can be pointed out that the present method generates numerical relative errors lower than 10%. Furthermore, comparisons between the performances of the coplanar-, cavity- and microstrip-structure based methods are addressed in Table 1.

Table 1: Comparison between the coplanar, cavity and microstrip structure based dielectric characterization methods

Methods	Coplanar	Cavity	Microstrip
Bandwidth	Not adapted to lower frequencies	Limited by resonant effect	Limited To tens GHz
Complexity	Low	High	Low
Temperature	Adapted	Difficult	Adapted

C. Extraction of dielectric material in the UWB frequency with temperature-dependent

Based on the experimental setup shown in Fig. 3, the DUT S-parameters were measured from DC to 5 GHz by increasing the temperature step by step. For the sake of simplicity and temperature influence illustration, only the measured $S_{11}(f,T)$ reflection and $S_{21}(f,T)$ transmission parameters at T={40°C, 60°C, 85°C, 100°C, 120°C, 140°C} are presented respectively in Fig. 5 (a) and in Fig. 5 (b). It is noteworthy that during the test, there is no significant difference between $S_{11}(f,T)$ and $S_{21}(f,T)$, for T varied from the ambient temperature of about 20°C to 40°C and the TL losses increase with the temperature. Then, the UWB characteristics of the FR4 constituting the DUT substrate from DC to 5 GHz can be determined from expressions (7) and (9).

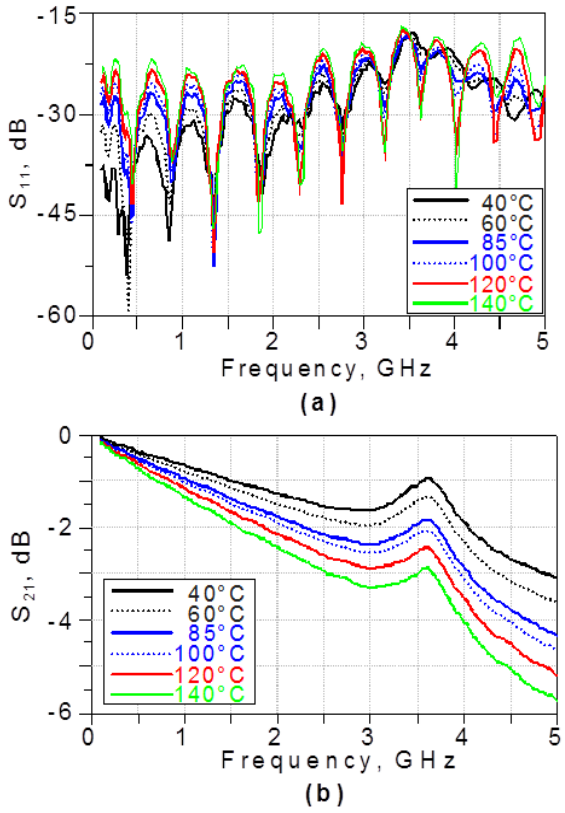

Fig. 5. Measured S-parameters of the DUT of Fig. 2 for T={40°C, 60°C, 85°C, 100°C, 120°C, 140°C}.

Consequently, the measured dielectric constant $\varepsilon_r(f,T)$ is plotted in Fig. 6 (a). It can be emphasized that the obtained relative permittivity $\varepsilon_r(f,T)$ is proportionally inverse of the temperature T. Moreover, $\varepsilon_r(f,T)$ presents an absolute variation of about 0.27 when increasing the temperature from 40°C to 140°C. Furthermore, Fig. 6 (b) depicts the loss tangent in the same temperature range. The loss tangent tan[$\delta(f,T)$] increases with T from about 0.025 with margin of about 0.02. The loss tangent is sensitivity to the TL resonance frequencies. This temperature effect can be reduced by choosing material with less thermal coefficient of expansion and low losses. The envelop of loss tangent can be estimated by using other methods like strip line ring resonator using proper calibration method and by reducing the systematic error and instrumental error through repeated characterization. Compared to the existing characterization techniques introduced in [10-11], the proposed method is simpler and allows to operate in UWB frequency from DC to several GHz. In addition, it enables the microwave structure modelling versus temperature.

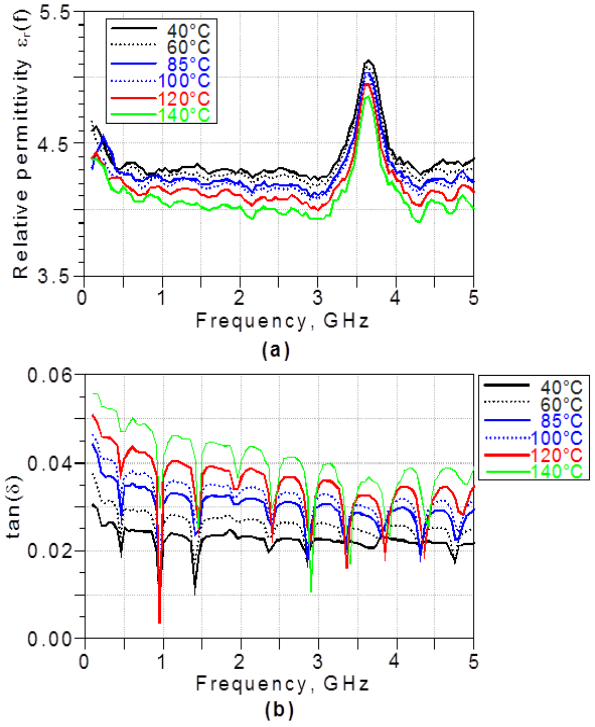

Fig. 6. (a) Measured FR4 substrate dielectric constant, and (b) loss tangent vs frequency and temperature.

D. Discussion the potential application with the extraction of the frequency dependent RLCG-model with the temperature consideration

Several applications of the proposed EM characterization method can be envisaged for the PCB design engineering as the signal and power integrity analyses. It can be emphasized that the developped method is beneficial thanks to the proposed EM characteristic with the temperarature influence. To do this, the performant TL behavioural model as the RLC-network modelling can be utilized. It can be recalled that given the characterisitc impedance $Z_c(jf,T)$ and the propagation constant $\gamma(jf,T)$, the TL RLC-model can be extracted. As suggested in [7], the per unit-length parameters R_u, L_u, C_u and G_u can be calculated with the following expressions:

$$R_u(f,T)=\frac{\Re\{\gamma(jf,T).Z_c(jf,T)\}}{d}, \quad (10)$$

$$L_u(f,T)=\frac{\Im\{\gamma(jf,T)\cdot Z_c(jf,T)\}}{2\pi f\cdot d}, \quad (11)$$

$$C_u(f,T)=\frac{\Im\left\{\dfrac{\gamma(jf,T)}{Z_c(jf,T)}\right\}}{2\pi f\cdot d}, \quad (12)$$

with $\Re[z]$ and $\Im[z]$ are respectively the real and imaginary parts of the complex number z. The TL RLC-model can be extracted based on the model presented in [17]. The feasibility of this future application can be understood with the variation of the TL per unit length RLC-parameters $R_u(T)$, $L_u(T)$ and $C_u(T)$ at 1 GHz addressed in Table 2.

Table 2: Per unit length RLC-parameters $R_u(T)$, $L_u(T)$ and $C_u(T)$

T	R_u (Ω/m)	L_u (nH/m)	C_u (pF/m)
40°	1.29	344	138
60°	1.62	353	138
85°	1.93	360	137
100°	2.12	369	135
120°	2.33	370	133
140°	3.54	370	127

The thermo-electromagnetic characterization method under study presents potential applications for:

- The EMC engineering in particular with the EM shielding effectiveness prediction [18-20] by overcoming the limitation in terms of the frequency band in addition to the temperature effects.
- The RF engineering with the use of unknown complex structure material absorption in the broadband frequency band [21].
- And facing to the open questions on the integration of the composite materials in the different areas, the present characterization method offers a possibility of the effective parameter modelling of the innovative materials as the complex composites [22].

IV. CONCLUSION

A simple and efficient characterization method of dielectric substrate constant and loss tangent is developed. The method is particular innovative with its possibility to operate in super UWB frequency with temperature influence. The proposed method is based on the use of microstrip TL properties. The analytical concept illustrating the methodology principle is presented. To illustrate the proposed method functionality, a proof of concept was designed, fabricated, simulated and experimented. The relevance of the method was verified with MoM numerical tests. Then, an application with a prototype of microstrip TL printed on FR4 epoxy substrate is presented. The dielectric constant $\varepsilon_r(f,T)$ and loss tangent $\tan[\delta(f,T)]$ from DC to 5 GHz was extracted by considering the temperature variation from 40°C to 140°C. Moreover, since the linear thermal coefficient of copper is 18.10^{-6}m/mK, the temperature from 40°C to 140°C, i.e., by 100°C will increase the length of microstrip line from 164 mm to 164.3 mm, i.e., by 0.18%.

The present method is limited to the prediction of the PCB substrate global characteristic. The main drawback is for the characterization of typically

micrometric size materials. In addition, the method is particularly sensitive to the measurement artefacts.

The exploitation of the proposed method for the microwave PCBs reliability prediction, the EM compatibility investigation and signal integrity analysis with respect to the temperature influence is in progress.

ACKNOWLEDGMENT

Acknowledgement is made to the Upper Normandy Region for the PULSAT project support of this research work through the FEDER fund.

REFERENCES

[1] K. Banerjee, A. Mehrotra, A. Sangiovanni-Vincentelli, and H. Chenming, "On thermal effects in deep sub-micron VLSI interconnects," *Proc. 36th ACM/IEEE-CAS/ EDAC Design Automation Conf.*, New Orleans, LA, USA, pp. 885-891, June 21-25, 1999.

[2] Y. Cheng, C. Tsai, C. Teng, and S. Kang, *Electrothermal Analysis of VLSI Systems*, Kluwer Academic Publishers, Boston/Dordretch/London, 2000.

[3] H. A. Schafft, "Thermal analysis of electromigration test structures," *IEEE Trans. on Electron Device*, vol. Ed-34, no. 3, pp. 664-672, 1987.

[4] A. A. Bilotti, "Static temperature distribution in IC chips with isothermal heat sources," *IEEE Trans. on Electron Device*, vol. Ed-21, no. 3, pp. 217-226, 1974.

[5] A. H. Ajami, M. Pedram, and K. Banerjee, "Effects of non-uniform substrate temperature on the clock signal integrity in high performance designs," *Proc. IEEE Conf. Custom Integrated Circuits*, San Diego, CA, USA, pp. 233-236, May 6-9, 2001.

[6] J. R. Miller, Y. Li, K. Hinckley, G. Blando, B. Guenin, I. Novak, A. Dengi, A. Rebelo, and S. McMorrow, "Temperature and moisture dependence of PCB and package traces and the impact on signal performance," *Proc. of Design Con. 2012*, Santa Clara, CA, USA, pp. 1-27, Jan. 30 - Feb. 2, 2012.

[7] J. Zhang and T. Y. Hsiang, "Extraction of subterahertz transmission-line parameters of coplanar waveguides," *Progress In Electromagnetics Research Symposium (PIERS) Online*, vol. 3, no. 7, Beijing, China, pp. 1102-110, Mar. 26-30, 2007.

[8] A. H. Ajami, K. Banerjee, M. Pedram, and L. P. P. P. van Ginneken, "Analysis of non-uniform temperature-dependent interconnect performance in high-performance ICs," *Proc. 38th ACM/IEEE-CAS/EDAC Design Automation Conference* (*DAC'01*), Las Vegas, NV, USA, pp. 567-572, June 18-22, 2001.

[9] B. Ravelo, A. Perennec, M. Le Roy, and Y. Boucher, "Active microwave circuit with negative group delay," *IEEE Microwave Wireless Component Letters*, vol. 17, no. 12, pp. 861-863, Dec. 2007.

[10] L. F. Chen, C. K. Ong, C. P. Neo, V. V. Varadan, and V. K. Varadan, *Microwave Electronics: Measurement and Materials Characterization*, Wiley, NJ, USA, Jan. 2005.

[11] R. K. Challa, D. Kajfez, J. R. Gladden, A. Z. Elsherbeni, and V. Demir, "Permittivity measurement with a non-standard waveguide by using TRL calibration and fractional linear data fitting", *Progress In Electromagnetics Research (PIER) B*, vol. 2, pp. 1-13, 2008.

[12] J. Hinojosa, "S-Parameter broadband measurements on-coplanar and fast extraction of the substrate intrinsic properties," *IEEE Microwave Wireless Component Letters*, vol. 11, no. 2, pp. 80-82, 2001.

[13] A. Kumar and G. Singh, "Measurement of dielectric constant and loss factor of the dielectric material at microwave frequencies," *Progress In Electromagnetics Research (PIER)*, vol. 69, pp. 47-54, 2007.

[14] X.-C. Zhu, W. Hong, K. Wu, H.-J. Tang, Z.-C. Hao, and H.-X. Zhou, "Characterization of substrate material using complementary split ring resonators at terahertz frequencies," *Proc. of IEEE Int. Wireless Symp.* (*IWS*) *2013*, Beijing, China, pp. 1-4, Apr. 14-18, 2013.

[15] J. Krupka, J. Breeze, A. Centeno, N. Alford, T. Claussen, and L. Jensen, "Measurements of permittivity, dielectric loss tangent, and resistivity of float-zone silicon at microwave frequencies," *IEEE Trans. Microwave Theory and Techniques*, vol. 54, no. 11, pp. 3995-4001, Nov. 2006.

[16] T. Eudes, B. Ravelo, and A. Louis, "Experimental validations of a simple PCB interconnect model for high-rate signal integrity," *IEEE Trans. Electromagnetic Compatibility*, vol. 54, no. 2, pp. 397-404, Apr. 2012.

[17] I. J. Bahl and D. K. Trivedi, "A designer's guide to microstrip line," *Microwaves*, pp. 174-182, May 1977.

[18] C. D. Raj, G. S. Rao, P. V. Y. Jayasree, B. Srinu, and P. Lakshman, "Estimation of reflectivity and shielding effectiveness of three layered laminate electromagnetic shield at X-band," *Progress In Electromagnetics Research* (*PIER) B*, vol. 20, pp. 205-223, 2010.

[19] C. Morari, I. Balan, J. Pintea, E. Chitanu, and I. Iordache, "Electrical conductivity and electromagnetic shielding effectiveness of silicone rubber filled with ferrite and graphite powders," *Progress In Electromagnetics Research (PIER) M*, vol. 21, pp. 93-104, 2011.

[20] K. Lakshmi, H. John, K. T. Mathew, R. Joseph,

and K. E. George, "Microwave absorption, reflection and EMI shielding of PU/PANI composite," *Journal of Acta Materialia*, vol. 57, pp. 371-375, 2009.

[21] M. Y. Koledintseva, J. Drewniak, and R. DuBroff, "Modelling of shielding composite materials and structures for microwave frequencies," *Progress In Electromagnetics Research (PIER) B*, vol. 15, pp. 197-215, 2009.

[22] V. Preault, R. Corcolle, L. Daniel, and L. Pichon, "Shielding effectiveness of composite materials: effect of inclusion shape," *IEEE Trans. Magnetics*, vol. 49, no. 5, pp. 1941-1944, May 2013.

B. Ravelo holds his Ph.D. degree in 2008 from Univ. Brest and his dissertation to lead research ("HDR=Habilitation à Diriger des Recherches") in 2012 from Univ. Rouen. He is currently Assistant Prof. at ESIGELEC/IRSEEM in Rouen/France. His research interests cover the microwave circuit design, EMC/EMI and signal integrity engineering. He is a pioneer of the development of negative group delay (NGD) RF/analog circuits and its applications. He is (co)-author of more than 100 papers and regularly involved in national/ international research projects.

A. Thakur is Ph.D. in Physics from Himachal Pradesh University-Shimla, India. He is post doctorate from University of Brest, France and Taiwan National University Taiwan. Recently, he is working as Professor in Centre of Excellence in Nanotechnology and Materials Science at Shoolini University, Solan. He is recipient of Young Scientist Award from Department of Atomic Energy and Department of Science & Technology, Government of India. His areas of research are magneto-dielectric materials for antenna miniaturization, water purification and high density memory storage devices. He has published more than 50 papers in International Journals.

A. Saini is an Electronics Engineer having Masters degree from IIT Kanpur with specialization in Microelectronics and VLSI. Presently he is pursuing a Ph.D. on Microstrip Antenna with Magneto-dielectric substrate from Shoolini University, Solan, India. His research interest includes design, simulation and modeling of microstrip antenna on magneto-dielectric substrate for various applications in defence and communication. His other research interest includes design and development of various sensors for Fuzes, MEMS based impact switches and electronic circuit design.

P. Thakur is Gold Medalist in Master's degree in Electronics and Ph.D. from Himachal Pradesh University-Shimla, India. Presently, she is working as Head in the School of Physics & Materials Science Shoolini University. She is also recipient of Young Scientist Award from Department of Science & Technology, Government of India. She is working on dielectric and multiferroic materials for different applications. She has published more than 50 papers in International Journals.

A Novel Printed Antenna with Square Spiral Structure for WiMAX and WLAN Applications

P. Beigi and J. Nourinia

Department of Electrical Engineering
Urmia Branch, Islamic Azad University, Urmia, Iran
Payam.beigi@yahoo.com, j.nourinia@urmia.ac.ir

Abstract ─ A new printed antenna with multiband characteristic suitable for WiMAX and WLAN operating frequency bands is presented. For this purpose, two square spiral arms as radiating elements and partial ground plane are considered in the antenna structure. By adding the square spirals and adjusting the number of turns of the square spirals, new resonances are excited and desired resonant frequencies at 2.56, 3.94, 5.20, 5.80, and 10.18 GHz can be achieved to cover WLAN and WiMAX systems. Parametric simulation of the main parameters affecting the antenna performance are presented and discussed. The designed antenna with full size of 20×20 mm^2 is fabricated and tested. The radiation pattern is approximately omnidirectional in operating bands. The simulated and the experimental results are in acceptive agreement and confirm good performance for the offered antenna.

Index Terms ─ Multiband characteristic, square spiral arms.

I. INTRODUCTION

It is now common practice to integrate several radios in a single wireless platform that uses one antenna or one single radio device to handle multiple standards. To this end, the antennas need to cover multiple frequency bands [1]. Multiband antennas are one of the desirable candidates to be employed in services with various operating bands. The characteristic of the printed antenna can easily satisfy the technical requirements for high performance, being light weight and low profile. So, printed monopole antennas and the dipole antennas play an important role in many aspects of multiband antennas [2]. Wireless local area network (WLAN) and worldwide interoperability for microwave access (WiMAX) with standard operating frequency bands including 2.4 GHz (2.4-2.484 GHz)/5.2 GHz (5.15-5.356 GHz)/5.8 GHz (5.725-5.825 GHz) and 2.56 GHz (2.5-2.69 GHz)/3.5 GHz (3.4-3.696 GHz)/5.5 GHz (5.25-5.85 GHz), respectively, have been widely applied in mobile devices such as handheld computers and intelligent phones [3]. Recently, several multiband printed monopole and dipole antennas for WLAN and WiMAX applications have been presented in [2-13]. A dipole antenna using double-side layer and the flared arms is presented in [2]. The proposed antenna consists of three branch strips. The longer strip is employed as a reflector and the shorter one is as a director. The desired operating bands can be achieved by optimizing the length of the branch strips. In [3], a hybrid design of a microstrip-fed parasitic coupled ring fractal monopole antenna is investigated. By adding fractal strip and inserting parasitic element in the back side, WiMAX and WLAN operating bands can be covered. In [4], a coplanar waveguide-fed (CPW) antenna includes a square spiral patch to increase resonance frequencies and two L-shaped strips for achieving wider impedance bandwith. In [5], a monopole antenna with one branch strip and two hook-shaped strips suited for WLAN/WiMAX applications is designed.The return loss curves of the presented antenna is significantly influenced by the rectangular slit in the ground plane. In [6], two rectangular split-ring resonators subjoined on the radiating patch to obtain a tri-band resonant characteristic. In [7], folded Γ-shaped arms are used to tune frequency bands. Also, H-shaped slot on the ground plane has an important effect on producing wider impedance bandwidth. In [8], a novel PIFA configuration is proposed of T-shaped on the radiating patch and rectangular slot in the ground plane. These modifications lead to enhanced impedance bandwidth. In [9], a monopole antenna has a dual-layer metallic structure which is embedded on both sides of the substrate. 3 GHz and 5 GHz frequency bands can be achieved by adding the S-shaped strip to the feed line and a special structure on the bottom layer, respectively. In [10], a monopole antenna with several narrow strips, acted as resonance paths, are connected to a 50-ohm CPW feed line. In the offered antenna, multiband characteristic can be obtained by using quarter-wavelength long patch.

In this paper, a simple printed antenna with a novel configuration is suggested for WLAN and WiMAX applications. The proposed antenna consists of two square spiral arms connected to a microstrip feed line

Submitted On: May 27, 2015
Accepted On: November 8, 2015

on the top layer of the substrate and a defected ground plane on the bottom layer. By using square spirals, new resonances are generated, and so multiband operation can be achieved. Modified turns of the square spirals and optimized dimensions of the ground plane lead to favorable frequency bands of 245 MHz (2.498-2.743 GHz), 254 MHz (3.789-4.043 GHz), 365 MHz (5.063-5.428 GHz), 397 MHz (5.601-5.998 GHz), and 580 MHz (9.911-10.491 GHz). The presented structure has an efficient performance with the lower cost and simple design. The final size of presented antenna is smaller than most multiband antennas which are mentioned recently. Good return loss and radiation characteristics are gained in the frequency band of interest.

II. ANTENNA CONFIGURATION AND DESIGN

Figure 1 shows geometrical configuration of the suggested antenna which is printed on an FR4 substrate with a size of 20(x-axis)×20(y-axis)×1 mm^3, relative permittivity of 4.4, and loss tangent of 0.022. Two square spirals as radiating element and 50 Ω microstrip line with fixed width (W_0) and length (L_0) is used on the upper side of the substrate. The partial ground plane with constant width of L_G = 6 mm is embedded on the other side of substrate. The square spirals have critical effects on exciting new resonances and controlling frequency resonances. To investigate the importance of square spirals, four steps of the designing process, as illustrated in Fig. 2, for different turns of the square spirals are presented and studied. Ansoft simulation software high-frequency structure simulator (HFSS) [14] is used for the parametric analysis and optimization of the designs. All the optimized values of the parameters are written in Table 1.

At first, the main innovation of the design including two special arms with unequal strips [see Fig. 2 (a)] is considered. In the second, third, and last steps [see Figs. 2 (b), 2 (c), and 2 (d)], excess strips are sequentially added to the arms to configure the turns of the square spirals. By connecting any strip to the arms, additional current paths on the radiating elements is generated. In this case, the new coupling paths between square spirals and ground plane can be obtained, and thus, the number of frequency resonance is increasing. Return loss curves for all the mentioned steps are demonstrated in Fig. 3.

Table 1: The final dimensions of the designed antenna

Param.	mm	Param.	mm	Param.	mm
L_0	8	L_1	9	L_2	7
L_3	2.4	L_4	4	L_5	2.4
W_0	1.7	W_1	0.3	W_2	7.4
W_3	6.5	W_4	4.5	W_5	4.4
W_6	3.5	L_G	6	h_{sub}	1
W_{sub}	20	L_{sub}	20		

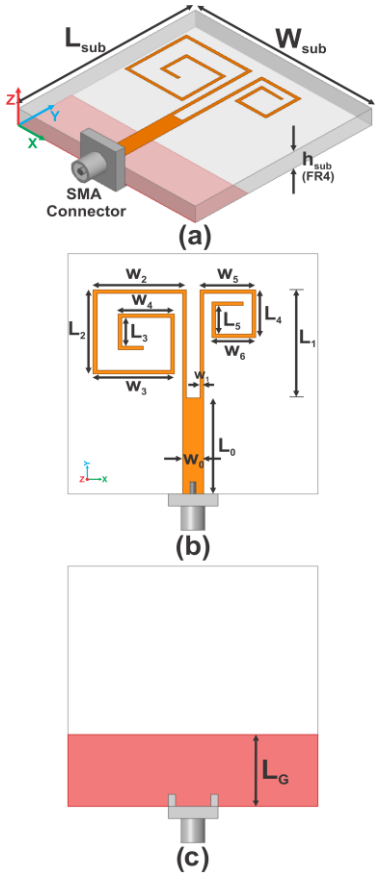

Fig. 1. Geometry of the proposed antenna: (a) side view, (b) top view, and (c) bottom view.

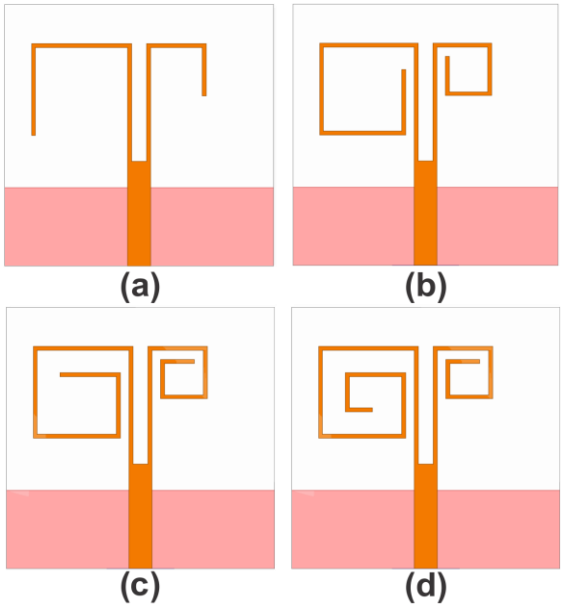

Fig. 2. (a) The antenna in step 1, (b) the antenna in step 2, (c) the antenna in step 3, and (d) the proposed antenna in step 4.

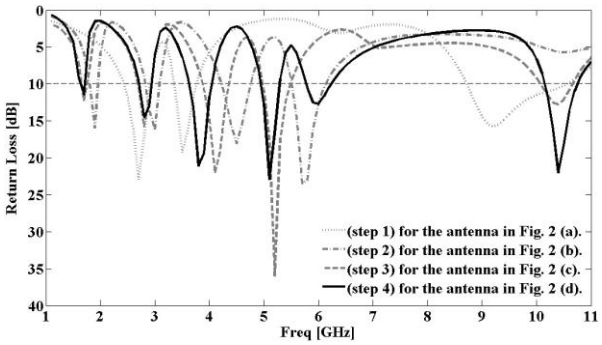

Fig. 3. Simulated return loss characteristics for antennas shown in Figs. 2 (a), (b), (c) and (d).

In the optimized case, resonant frequencies at 1.6, 2.7, 3.7, 5.1, 5.8, and 10.4 GHz are educed. For more expression of the significance of the dimension of square spiral arms, parametric study for the substantial parameters of the arms have been done. Note that in parametric analysis, one parameter is changed while the others are fixed. Simulated return loss curves with different values of key parameters named W_3, W_6, L_3, L_5, and W_4 are shown in Fig. 4, Fig. 5, and Fig. 6. From Fig. 4, it is found that the increment of the W_3 and W_6 has a great effect on moving resonant frequency to lower frequencies. As illustrated in Fig. 5, various values of the L_3 and L_5 control the impedance matching of the higher resonant frequencies. Finally, as indicated in Fig. 6, by increasing W_4, the matching and the location of higher frequency bands can be improved.

For more clarification of the frequency performance of the square spirals, current distribution of the exhibited proposed antenna for desirable resonant frequencies at 2.7, 3.7, 5.1, and 5.8 GHz are displayed in Fig. 7. From Fig. 7 (a) and Fig. 7 (b), it is clearly observed that the surface current distribution is concentrated around small and large square spiral arms at 2.7 and 3.7 GHz, respectively. Furthermore, as seen in Fig. 7 (c) and Fig. 7 (d), surface currents are nearly equal around both arms. Therefore, multiband operation can be achieved by different radiated parts of square spirals.

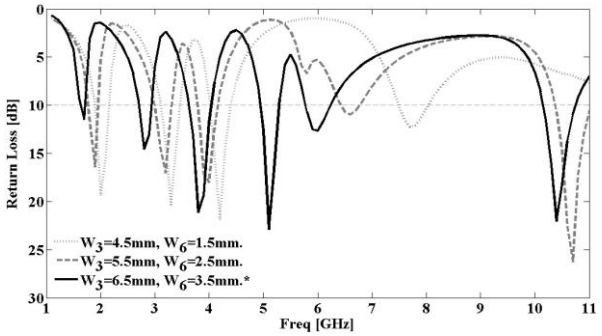

Fig. 4. Simulated return loss characteristics for the antenna with different values of the W_3 and W_6.

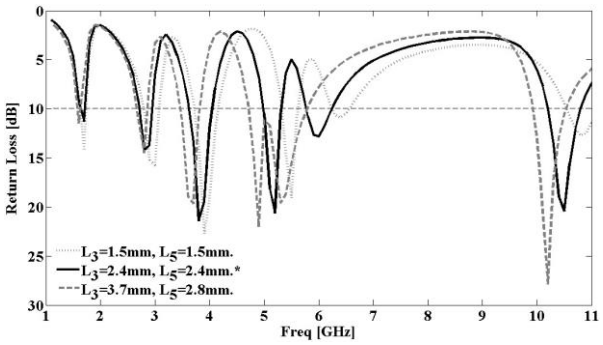

Fig. 5. Simulated return loss characteristics for the antenna with different values of the L_3 and L_5.

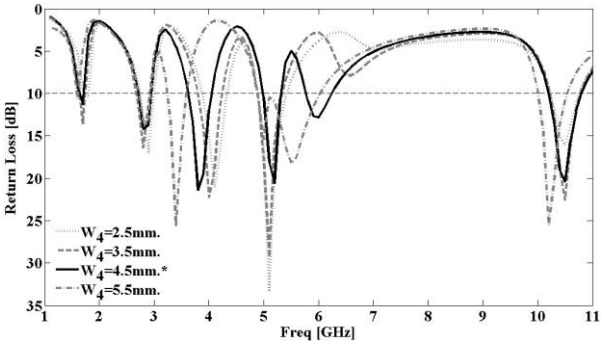

Fig. 6. Simulated return loss characteristics for the antenna with different values of the W_4.

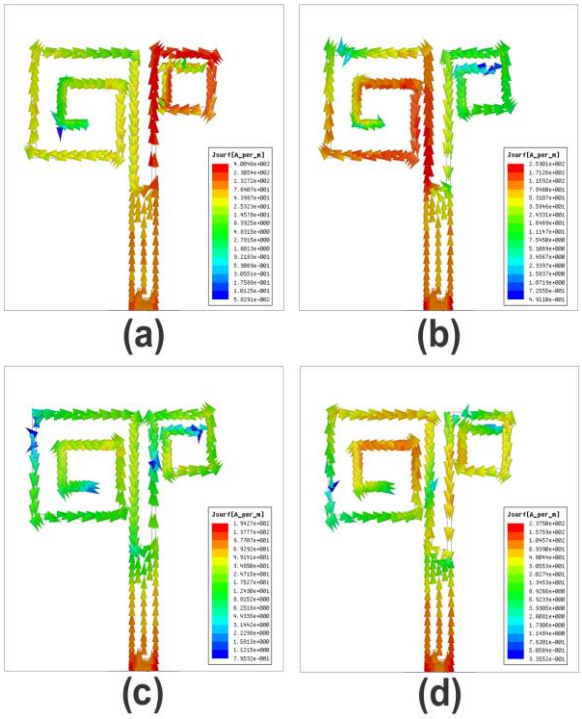

Fig. 7. Simulated surface current distributions on the radiating patch at: (a) 2.7, (b) 3.7, (c) 5.1, and (d) 5.8 GHz.

III. RESULTS AND DISCUSSIONS

The photograph of the manufactured antenna is shown in Fig. 8. Simulated and measured return loss characteristics of the discussed antenna are plotted in Fig. 9. Figure 9 indicates that there is a discrepancy between the simulated and measured results. This discrepancy is commonly due to the a number of parameters, such as the wider range of simulation frequencies, the fabricated antenna dimensions as well as the thickness, and dielectric constant of the substrate, on which the antenna is fabricated. To confirm the accurate return loss characteristics for the designed antenna, it is recommended that the manufacturing and measurement process need to be performed carefully; besides, SMA soldering accuracy and FR4 substrate quality need to be taken into consideration [15].

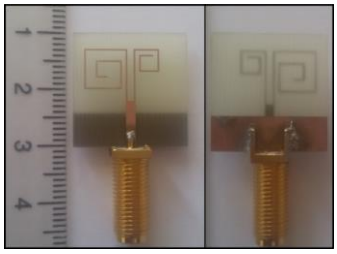

Fig. 8. Photograph of the fabricated antenna prototype with proposed patch.

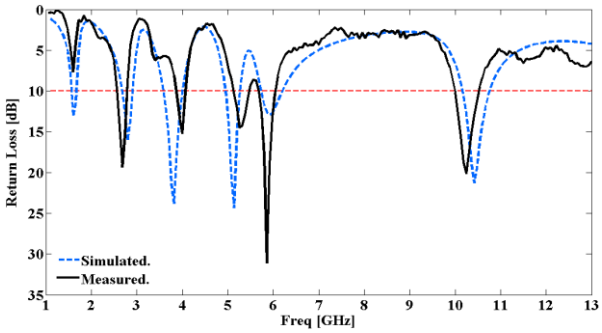

Fig. 9. Measured and simulated return losses of the proposed antenna.

As shown in Fig. 9, multiband operation at 245 MHz (2.498-2.743 GHz), 254 MHz (3.789-4.043 GHz), 365 MHz (5.063-5.428 GHz), 397 MHz (5.601-5.998 GHz), and 580 MHz (9.911-10.491 GHz) can be attained to cover WiMAX frequency bands at 2.5 GHz (2500-2690 MHz), and WLAN frequency bands at 5.2/5.8 GHz (5150-5350 MHz)/(5725-5825 MHz). The simulated and measured peak gains for the proposed antenna for the lower, middle and higher bands are shown in Fig. 10. The normalized co-polarization and cross-polarization radiation patterns of the antenna at 2.56, 3.94, 5.2, and 5.8 GHz are illustrated in Fig. 11. The radiation pattern in x-z plane is approximately omnidirectional.

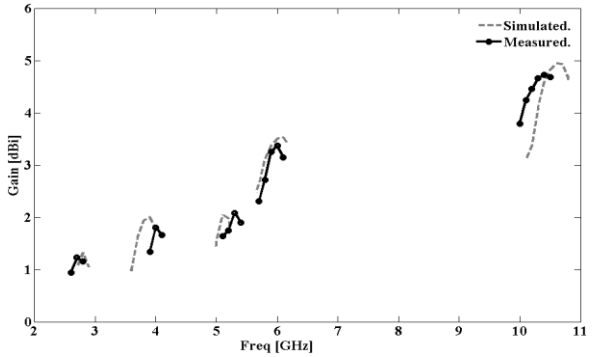

Fig. 10. Measured and simulated gain curves of the proposed antenna.

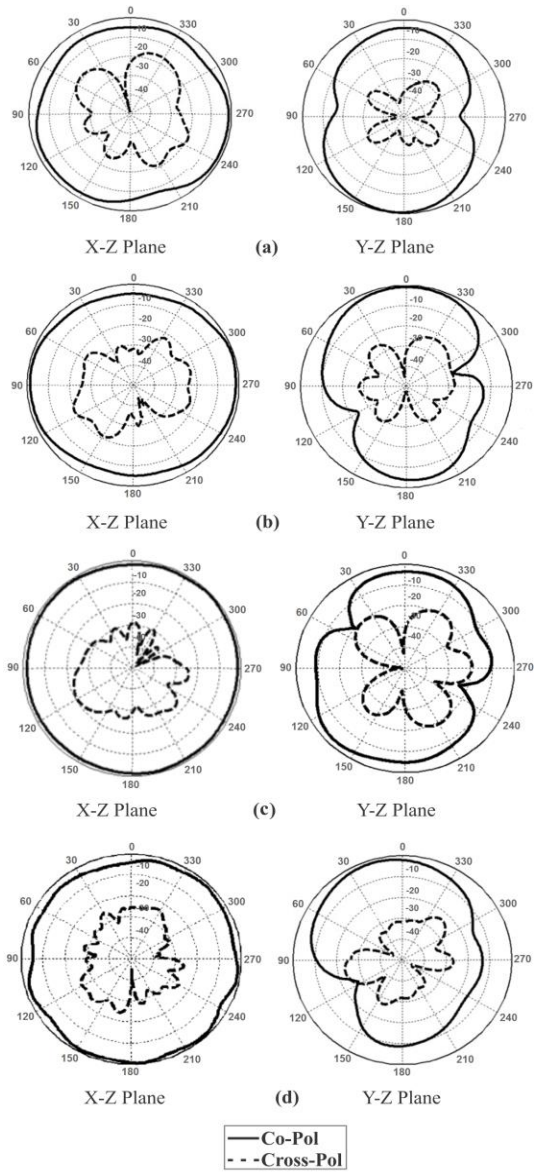

Fig. 11. Normalized radiation patterns of the proposed antenna at: (a) 2.56, (b) 3.94, (c) 5.2, and (d) 5.8 GHz.

IV. CONCLUSION

A novel multiband printed antenna for WiMAX/ WLAN applications has been reported. We showed that by using two square spiral arms as radiating elements and a partial ground plane, five frequency bands at 245 MHz (2.498-2.743 GHz), 254 MHz (3.789-4.043 GHz), 365 MHz (5.063-5.428 GHz), 397 MHz (5.601-5.998 GHz), and 580 MHz (9.911-10.491 GHz) can be obtained, so WiMAX/WLAN standard frequency bands can be covered. Also, the radiation patterns in both H-plane and E-plane are omnidirectional at covered frequency bands. The proposed antenna is attractive and can be practical for various multi frequency systems.

REFERENCES

[1] P. Y. Qin, A. R. Weily, Y. J. Guo, T. S. Bird, and C. H. Liang, "Frequency reconfigurable quasi-Yagi folded dipole antenna," *IEEE Trans. Antennas Propag*., vol. 58, no. 8, pp. 2742-2747, Aug. 2010.

[2] Z.-X. Yuan, Y.-Z. Yin, Y. Ding, B. Li, and J. J. Xie, "Multiband printed and double-sided dipole antenna for WLAN/WiMAX applications," *Microwave Opt. Technology Letters*, vol. 54, no. 4, Apr. 2012.

[3] J. Pourahmadazar, Ch. Ghobadi, J. Nourinia, and H. Shirzad, "Multiband ring fractal monopole antenna for mobile devices," *IEEE Antennas Wireless Propag. Lett*., vol. 9, pp. 863-866, 2010.

[4] P. Beigi, J. Nourinia, Y. Zehforoosh, and B. Mohammadi, "A compact novel CPW-fed antenna with square spiral-patch for multiband applications," *Microwave and Opt. Technology Letters*, vol. 57, no. 1, Jan. 2015.

[5] J. H. Yoon, Y. C. Rhee, and Y. K. Jang, "Compact monopole antenna design for WLAN/WiMAX triple-band operations," *Microwave and Opt. Technology Letters*, vol. 54, no. 8, Aug. 2012.

[6] L. Kang, H. Wang, X. H. Wang, and X. Shi, "Compact ACS-fed monopole antenna with rectangular SRRs for tri-band operation," *Electronics Letters*, vol. 50 no. 16, pp. 1112-1114, Jul. 2014.

[7] H. Lavakhamseh, Ch. Ghobadi, J. Nourinia, and M. Ojaroudi, "Multiresonance printed monopole antenna for DCS/WLAN/WiMAX applications," *Microwave Opt. Technology Letters*, vol. 54, no. 2, Feb. 2012.

[8] M. Ojaroudi, M. Hassanpour, Ch. Ghobadi, and J. Nourinia, "A novel planar inverted-F antenna (PIFA) for WLAN/WiMAX applications," *Microwave Opt. Technology Letters*, vol. 53, no. 3, Mar. 2011.

[9] Y. Xu, Y.-C. Jiao, and Y.-C. Luan, "Compact CPW-fed printed monopole antenna with triple-band characteristics for WLAN/WiMAX applications," *Electronics Letters*, vol. 48, no. 24, Nov. 2012.

[10] A. Mallahzadeh, A. Foudazi, and S. M. A. Nezhad, "A small-size pentaband handshaped coplanar waveguide-fed monopole antenna," *Microwave and Opt. Technology Letters*, vol. 53, no. 7, July 2011.

[11] N. Ojaroudi, M. Ojaroudi, and N. Ghadimi, "A new design of printed monopole antenna with multi-resonance characteristics for DCS/WLAN/WiMAX applications," *Applied Computational Electromagnetics Society (ACES) Journal*, vol. 28, no. 8, Aug. 2013.

[12] K. L. Sheeja, P. K. Sahu, S. K. Behera, and N. Dakhli, "Compact tri-band metamaterial antenna for wireless applications," *Applied Computational Electromagnetics Society (ACES) Journal*, vol. 27, no. 11, Nov. 2012.

[13] H. B. Mustafa and Y. E. Erdemli, "Triple-band microstripline-fed printed wide-slot antenna for WiMAX/WLAN operations," *Applied Computational Electromagnetics Society (ACES) Journal*, vol. 29, no. 10, Oct. 2014.

[14] Ansoft High Frequency Structure Simulation (HFSS), ver. 15, Ansoft, Corporation, 2013.

[15] A. Valizade, Ch. Ghobadi, J. Nourinia, and M. Ojaroudi, "A novel design of reconfigurable slot antenna with switchable band notch and multi-resonance functions for UWB applications," *IEEE Antennas Wireless Propag. Lett., (AWPL)*, vol. 11, pp. 1166-1169, 2012.

Payam Beigi was born in 1987 in Urmia, Iran. He received his B.Sc. degree in Electrical Engineering from Azad University, Urmia Branch and M.Sc. degree in Electrical Engineering from the Department of Electrical Engineering, Science and Research Branch, Islamic Azad University, West Azerbaijan, Iran. His research interests include monopole antenna, slot antennas, microstrip antennas, small antennas for wireless communications and reconfigurable structure.

Javad Nourinia received his B.Sc. in Electrical and Electronic Engineering from Shiraz University, M.Sc. degree in Electrical and Telecommunication Engineering from Iran University of Science and Technology, and Ph.D. degree in Electrical and Telecommunication from University of Science and Technology, Tehran Iran in 2000. From 2000 he was an Assistant Professor and now he is a Professor in the Department of Electrical Engineering of Urmia University, Urmia, Iran. His primary research interests are in antenna design, numerical methods in electromagnetic, microwave circuits.

A 340-400 GHz Zero-Biased Waveguide Detector Using an Self-Consistent Method to Extract the Parameters of Schottky Barrier Diode

Tianhao Ren [1], Yong Zhang [1*], Ruimin Xu [1], Jingtao Zhou [2], Chengyue Yang [2], and Zhi Jin [2]

[1] School of Electronic Engineering
University of Electronic Science and Technology of China, Chengdu, +86 611731, China
ren_tian_hao@163.com, yongzhang@uestc.edu.cn, rmxu@uestc.edu.cn

[2] Department of Microwave IC
Institute of Microelectronics of Chinese Academy of Sciences, Beijing, +86 100029, China
zhoujingtao@ime.ac.cn, yangchengyue@ime.ac.cn, jinzhi@ime.ac.cn

Abstract — A type of low-barrier Schottky barrier diode (SBD), based on InGaAs/InP, is designed and fabricated, and then a 340-400 GHz zero-biased waveguide detector utilizing this diode is proposed. To predict the performance of the SBD, firstly we present a self-consistent analytical method to find the accurate values of the parameters of the SBD by using the on-wafer measured S-parameter under different bias conditions up to 40 GHz and an auxiliary de-embedding structure. The extracted values show a very good agreement with the theoretical values. Then a concept called effective capacitance is proposed to model the high frequency (340-400 GHz) properties of the SBD. This concept has greatly improved the consistency of the simulated and measured results of the detector. The measured maximum voltage responsivity and the minimum noise effective power (NEP) of the detector are 800 mV/mW and 3.46×10^{-11} W/Hz$^{0.5}$ at 382 GHz, respectively.

Index Terms — Detector, effective capacitance, InGaAs/InP, low barrier, modeling technology, parameter extraction, Schottky barrier diode.

I. INTRODUCTION

Terahertz (THz) detection technology is becoming more and more attractive for its applications in astronomy, imaging and bio-sensing [1,2].There is a number of ways to achieve THz detection [3]. Bolometers are extremely sensitive, providing responsivity up to 10^5 V/W, and noise equivalent power (NEP) about 10^{-13} W/Hz$^{0.5}$. But relatively speaking, they have a slow temporal response and require cryogenic condition [4]. A room temperature THz detector which has high responsivity, high stability, and low cost of fabrication will greatly promote the application of THz technologies. Schottky barrier diode (SBD) detectors have long been used in millimeter-wave (MMW) and THz regions because of their high sensitivity, ability to operate at an ambient or cryogenic temperature and fast response time. When the diode is optimized to have a low forward turn-on voltage, the detectors can achieve excellent frequency response and bandwidth, even with zero-bias. InGaAs/InP is verified to be a very promising material system for the detection at MMW and THz frequencies. Superior to traditional material, such as GaAs, its lower Schottky barrier height provides zero-bias detection ability that not only eliminates shot noise and hence improves crucially signal-to-noise ratio, but also simplifies the detection system [5].

In this study, a planar SBD using InGaAs/InP material system with low barrier height is designed and fabricated at Institute of Microelectronics of Chinese Academy of Sciences (IMCAS). Based on this SBD, a 340-400 GHz zero-biased waveguide detector is proposed.

The hardest and most important part of the solid-state circuit design is the modeling of the device. The deviation between the simulated and measured results is mainly due to the inaccurate modeling technique. Here, we propose a self-consistent modeling technique of SBD which is based on an analytic method to extract the parameters of SBD from the on-wafer measured S-parameter data. The extracted values of the parameters agree well with the theoretical values. Then an extrapolation process and a concept called effective capacitance are also presented, which greatly improve the consistency between the simulated and measured results.

II. DESIGN AND MODELING OF THE SBD

A common structure of a planar SBD is depicted in Fig. 1 (a). As mentioned above, detectors based on SBDs with low forward turn-on voltage can achieve excellent frequency response and bandwidth. Hence, InGaAs/InP material system which has a low barrier height is used here. The doping levels and the thicknesses of epitaxial

Submitted On: January 18, 2015
Accepted On: November 8, 2015

layer and buffer layer need to be carefully designed to meet the demand of the detector. In order to minimize the series ohmic contact resistance, the buffer doping concentration (N_{buffer}) should be as high as possible; for instance, 3×10^{19} cm^{-3}, which is near to the upper limit of InGaAs. The thickness of buffer layer (t_{buffer}) should be larger than one skin depth at the operating frequency, but larger thickness leads to larger cost. So the trade-off value is chosen to be 1.5 μm. Both epitaxial doping concentration (N_{epi}) and epi-layer thickness (t_{epi}) should be considered at the same time. t_{epi} should be slightly larger than the maximum depletion depth, which is also relative to N_{epi}. The decision of N_{epi} is a compromise between series resistance and reverse breakdown voltage. Here, N_{epi} and t_{epi} are chosen as 2×10^{17} cm^{-3} and 0.2 μm, respectively. The diameter of the Schottky contact was chosen as 2 μm to obtain a reasonable junction capacitance which satisfies the demand of the detector at specified frequencies [6,7].

The fabrication process of the SBD is described briefly as follows. Firstly, the epitaxial lattice matched $In_{0.53}Ga_{0.47}As$ structure including a 1.5 μm thick heavily doped n^+-type buffer layer and a 0.2 μm thick n-type epitaxial layer was grown on a semi-insulating (SI) InP substrate using molecular beam epitaxy (MBE). The doping concentration of the two layers are 3×10^{19} cm^{-3} and 2×10^{17} cm^{-3}, respectively. Secondly, the ohmic contact was formed at the epi-layer by etching through the n-type buffer layer and depositing a Ti-Pt-Au metal. Thirdly, a SiO_2 layer was deposited on the epi-layer to provide passivation and insulation. Fourthly, the Schottky contact was formed by opening a current window on the insulating layer followed by depositing a metal contact on the epi-layer. Fifthly, a narrow metal connection was formed across the surface-channel to route the Schottky anode path towards a large anode contact pad. This narrow metal connection is known as the air-bridge finger. Finally, the $In_{0.53}Ga_{0.47}As$ material beneath the air-bridge finger was removed to isolate the anode and cathode pads. Here, the SI-InP substrate serves as a supporting structure for the diode [8].

Figure1 (b) illustrates the equivalent circuit model of the SBD, which is the basis of our extraction method. The Schottky junction is modeled as voltage-dependent junction capacitance (C_j) and resistance (R_j) [9]. R_s is the series resistance. The fringing field between both pads is modeled as a pad-to-pad capacitance (C_{pp}). The finger-to-pad coupling is modeled as C_{fp} and the self-inductance of the air-bridge finger is modeled as L_f [10].

Although the equivalent circuit is very mature and has been used for years, but a self-consistent method to find the accurate values of these parameters is still lacking. Here, we use the on-wafer measured S-parameter under different bias condition up to 40 GHz and an auxiliary de-embedding structure to find the accurate values. Then we compare the extracted values with the theoretical values, which are deduced from the DC-IV curve of SBD.

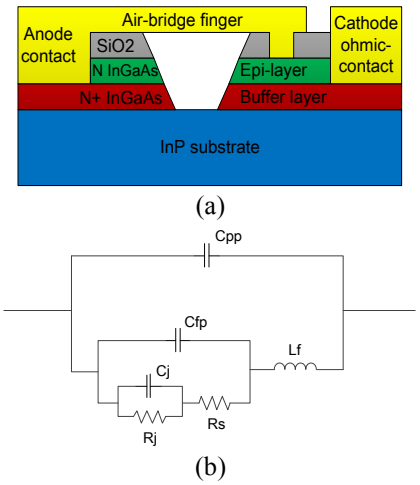

Fig. 1. (a) Cross section view and (b) equivalent circuit model of the InP/InGaAs based planar SBD.

Figure 2 shows the images of the diode which is identical to the one used in the detector and its auxiliary de-embedding structure. They are both in coplanar waveguide (CPW) configuration, since the ground-signal-ground (GSG) probe is used in the on-wafer S-parameter measurement.

In the extraction process, three equivalent circuits are used, which are "open", "short" and "actual", as shown in Fig. 3. "Open" represents the auxiliary de-embedding structure as shown in Fig. 2 (b). "Short" represents the SBD which is working at relatively large forward bias conditions, such as 1V. "Actual" represents the SBD which is working at bias conditions ranging from -1 V to 0.15 V. Notice that in all the three equivalent circuits, there should be a series resistance (denoted by R_{pad}) which represents the probe connection resistance and the resistance of the microstrip line. R_{pad} is removed from the circuits since it is very small (less than 1 Ω). The coupling between the signal and ground lines is modeled as C_{pad}. The self-inductance of the signal line is modeled as L_{pad}. For planar diodes, L_f is in the range of several to tens pico-henrys, whereas the capacitances are in the range of a tenth to tens of a femto-farad. At the measured frequencies, capacitances are dominant, compared to the inductance. Thus, L_f is negligible in the equivalent circuit. In the "short" mode, C_j is extremely small and R_s is negligible, compared to L_{pad}. And in "actual" mode, R_s is negligible small in comparison with the junction resistance.

In "open" mode, C_{pad} is extracted by using:

$$C_{pad} = \frac{\mathrm{Im}(Y_{11\_open})}{\omega}. \quad (1)$$

In "short" mode, L_{pad} is extracted by using:

$$L_{pad} = \frac{1}{\omega} \cdot \frac{1}{\mathrm{Im}(Y_{11\_open} - Y_{11\_short})}. \quad (2)$$

In "actual" mode, the total capacitance (C_{pp}+C_{fp}+C_j) is extracted by using:

$$C_{total} = \frac{1}{\omega} \cdot \frac{1}{\frac{1}{\mathrm{Im}(Y_{11\_actual} - Y_{11\_open})} + \frac{1}{\mathrm{Im}(Y_{11\_open} - Y_{11\_short})}}, \quad (3)$$

where Y is the Y-parameter calculated from the on-wafer measured S-parameter, and ω is the angular frequency.

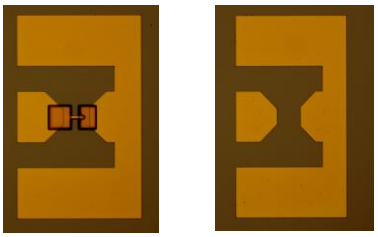

Fig. 2. Microscope images of: (a) diode and (b) auxiliary de-embedding structure in CPW configuration.

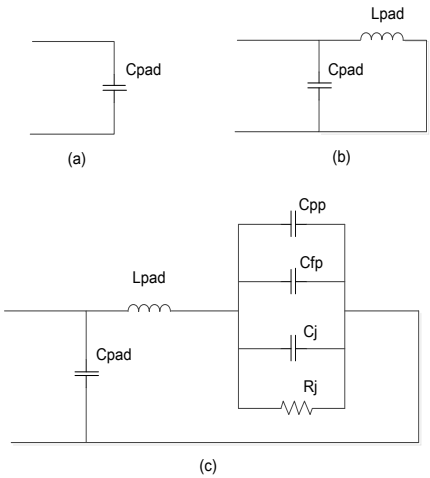

Fig. 3. Equivalent circuits for: (a) "open", (b) "short", and (c) "actual".

The measured S-parameter is from 10 to 40 GHz. Within this range, the extracted values of C_{pad}, L_{pad}, and C_{total} are about 19 fF, 95 pH and 18 fF, respectively, as shown in Fig. 4 (a), which is the case of the zero-bias condition. C_{pad} and L_{pad} do not change with different bias conditions, while C_{total} does; since it contains C_j, which is the voltage-dependent junction capacitance. The values of C_{total} under different bias conditions are shown in Fig. 4 (b), which is the case of 40 GHz.

According to the Schottky theory, the total capacitance is described as:

$$C_{total} = C_{j0}(1 - \frac{V}{V_{bi}})^{-0.5} + C_{par}, \quad (4)$$

where C_{j0} is the zero-bias junction capacitance, V is the bias voltage, V_{bi} is the build-in potential and C_{par} is the total parasitic capacitance (C_{pp} + C_{fp}).

By fitting (3) to (4), C_{j0}, V_{bi}, and C_{par} are extracted, which are useful in the design and simulation of the detector. From the curve-fitting procedure at 40GHz, C_{j0}, V_{bi}, and C_{par} are extracted as 9.6 fF, 0.26 V, and 8.8 fF, respectively. A comparison between the extracted and fitted C_{total} is depicted in Fig. 4 (b), showing a very good agreement. By using the same equation and values of C_{j0}, V_{bi}, and C_{par}, good agreements are also obtained at the band of 10-40 GHz.

The theoretical values of C_{j0} and V_{bi} are deduced from the DC-IV curve as 9.56 fF and 0.25 V respectively, which are consistent with the extracted values. Details of the deduction can be found in [6]. The values of these parameters are listed in Table 1.

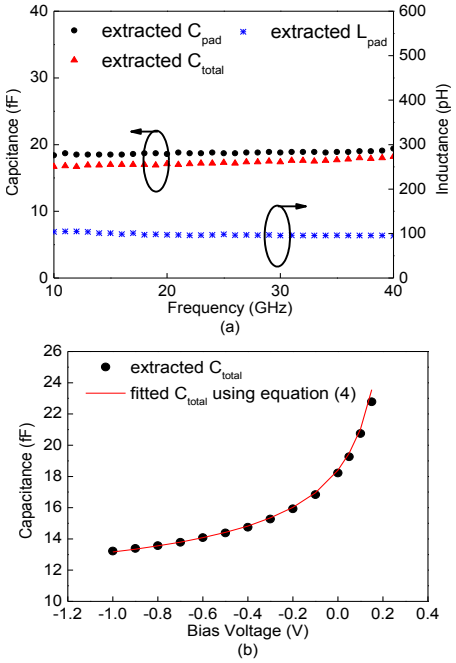

Fig. 4. (a) Extracted C_{total}, C_{pad}, and L_{pad} versus frequency at zero-biased voltage, and (b) extracted and fitted C_{total} versus bias voltage at 40 GHz.

Table 1: Summary of the values of parameters

Parameter	DC-IV Theory Value	Extracted Value (40 GHz)	Effective Value (400 GHz)
C_{j0}	9.56 fF	9.6 fF	$C_{j0,eft}$=15.7 fF
V_{bi}	0.25 V	0.26 V	$V_{bi,eft}$=0.26 V
C_{par}	-	8.8 fF	$V_{bi,eft}$=0.26 V
C_{pad}	-	19 fF	
L_{pad}	-	95 pH	

To verify our extraction method further, S-parameter comparison between equivalent circuit model simulation and diode measurement is presented. Figure 5 shows the simulated equivalent circuit as well as the value of each parameter which is obtained by our extraction method. The values of R_j is calculated by the DC-IV curve using:

$$R_j = \frac{dV}{dI} = \frac{1}{I} \cdot \frac{\eta kT}{q}, \tag{5}$$

where η is the ideal factor, q is the elementary charge, k is the Boltzmann's constant and T is the ambient temperature. The comparison between the simulated and measured S11 is shown in Fig. 6. Good agreements of both magnitude and phase are observed. Only S11 is compared here since the one-port measurement setup is used.

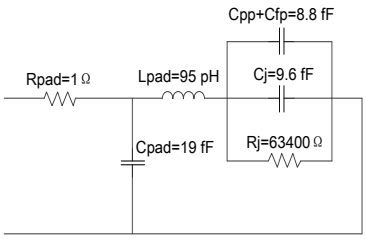

Fig. 5. Equivalent circuit simulation model with the values extracted by the proposed method.

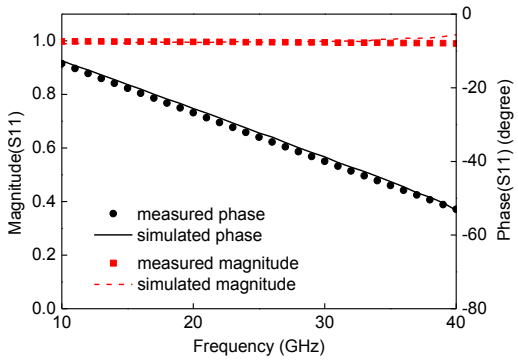

Fig. 6. Comparison between the simulated and measured S11 of the SBD.

The results in Fig. 4, Table 1 and Fig. 6 indicate that our method aiming at finding the accurate values of the parameters is valid, self-consistent and useful. The accurate values not only help us to get a deep insight of the diode which can help us to improve the diode, but also are the key to the diode modeling which is very important in the following detector design process.

However, the diode is expected to be used in a 340-400 GHz detector, which is beyond the extraction range (10-40 GHz). To solve this problem, an extrapolation process is conducted up to 400 GHz, as shown in Fig. 7. Only C_{total} is extrapolated since C_{pad} and L_{pad} are used to model the GSG configuration which has nothing to do with the modeling of the detector. It is observed that C_{total} varies with the frequency. The reason is that the parasitic effect becomes stronger at higher frequencies, which makes the circuit model in Fig. 1 (b) and Fig. 3 insufficient. However, fully considering the parasitic effect at high frequencies leads to a very complex question.

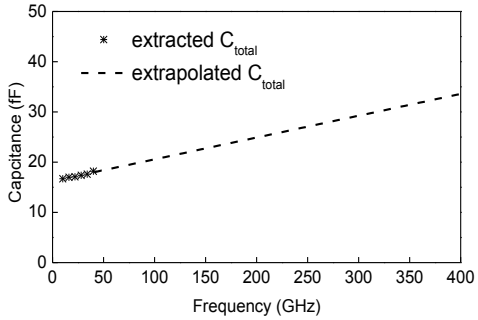

Fig. 7. Extracted and extrapolated C_{total} versus frequency at zero-biased voltage (markers are the extracted data calculated from the 10-40 GHz measured S-parameter, and dashed lines are the corresponding extrapolation up to 400 GHz).

So we proposed a concept called effective capacitance, which contains the high frequency parasitic effect while maintaining the same simplicity. In Section IV, we will see that the effective capacitance has greatly improved the consistency between the simulated and measured results of the detector. Figure 7 is the case of zero-biased condition. Extrapolation at other biased-conditions can be conducted in a similar way. Then a fitting procedure, which is similar to that in Fig. 4 (b) is conducted to obtain the effective C_{j0}, V_{bi} and C_{par} under 400 GHz, noted as $C_{j0,eft}$, $V_{bi,eft}$ and $C_{par,eft}$, respectively. All the values of the parameters are summarized in Table 1. It is observed that V_{bi} keeps the same value at DC, 40 GHz and 400 GHz, which is consistent with the physical properties of the material. $C_{j0,eff}$ and $C_{par,eff}$ are different from C_{j0} and C_{par}, since they now contain the high frequency parasitic effect.

In conclusion, the procedure of our modeling technology is as follows. Firstly, the extracted values at 10-40 GHz are obtained by using the proposed parameter extraction method. Then, an extrapolation process up to the operation frequency (400 GHz) is conducted to obtain the effective capacitance, which contains the high frequency effect and are used in the final circuit simulation. There are many other modeling technologies for SBD. For example, the model of drift-diffusion [11], hydrodynamic [12], and Monte Carlo [13] contains some physical effects, all of which could increase the accuracy, but are very complex and hard to implement with the conventional CAD tools. Other equivalent circuit models are always based on an I-V or C-V fitting procedure at low frequencies [14], which have too little physical insight.

And the lack of the extrapolation process makes the model inaccurate at high frequencies.

III. DESIGN OF THE DETECTOR

Generally, the detector can be divided into two parts, the linear part and the nonlinear part, which are analyzed by Ansoft's High Frequency Structure Simulator (HFSS) and Agilent's Advanced Design System (ADS), respectively. The proposed detector consists of four parts: waveguide (WG) to microstrip line transition, input matching, diode part, and output matching with low pass filter (LPF). The design process is shown in Fig. 8. Details of the design process are discussed as follows.

A 3D electromagnetic (EM) simulation model of the diode part including the connection to microtrip line is built in HFSS, as depicted in Fig. 9. This model is based on accurate geometric dimensions with the setup shown in Table 2. The definition of wave port representing the entrance to the Schottky junction is very important to achieve a correct simulation, which is defined as a circular sheet between the epi-layer and buffer layer with a perfect cylindrical conductor through the epi-layer.

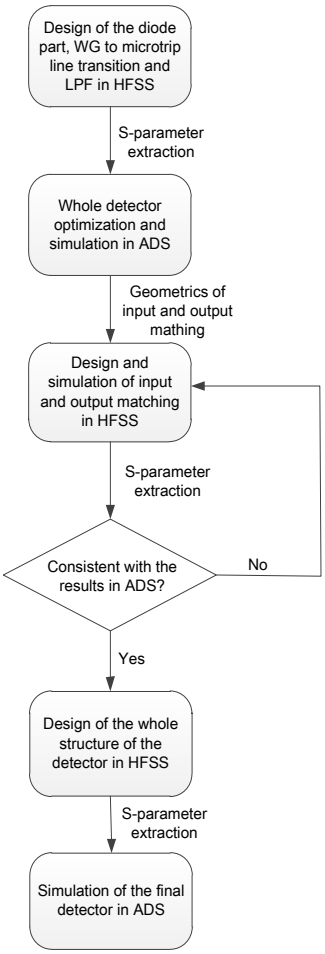

Fig. 8. Design flow of the detector.

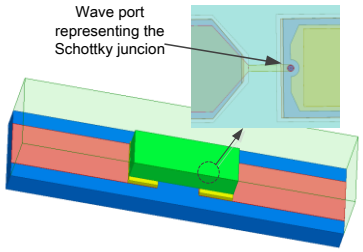

Fig. 9. 3D EM simulation model of the diode part and the definition of the wave port.

Table 2: Material properties setup in HFSS

Material	Relative Permittivity	Bulk Conductivity (S/m)
n^+ InGaAs	-	PEC
n InGaAs	12.3	0
SiO_2	4	0
InP	12.5	0

The passive linear parts of detector are designed and analyzed in HFSS and the nonlinear simulation is carried on in ADS by harmonic balance (HB) method. The circuit design process is introduced as follows. First, a WG to microstrip line transition and a LPF which stops the RF signal from leaking into the output port are designed. With the S-parameter data of the two structures, an ideal whole detector circuit model is built in ADS. After the optimization process, the initial structures of the input and output matching parts are obtained, which are then re-built in HFSS to verify the simulated results for the operating frequency is very high (340-400 GHz). The models in HFSS are modified to obtain the simulated results which are similar to those in ADS. Finally, the whole detector is built in HFSS, as depicted in Fig. 10, and simulated in ADS. A photograph of the detector is shown in Fig. 11.

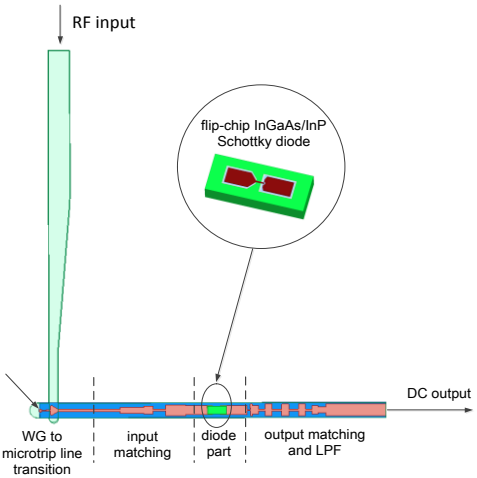

Fig. 10. Whole structure of the detector.

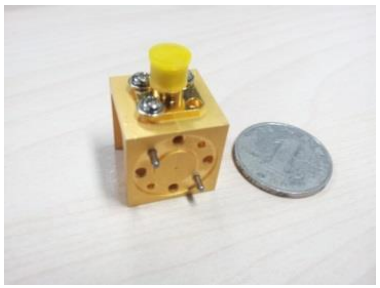

Fig. 11. Photograph of the detector.

IV. RESULTS

Voltage responsivity and NEP are two important characters of detectors. Voltage responsivity is defined as:

$$R_v = \frac{mag(V_{out})}{P_{in}}, \tag{6}$$

where V_{out} is the output voltage and P_{in} in the power of the pumped signal. The terahertz signal is pumped into the detector and then the output voltage is measured by a phase-locked amplifier. A comparison between the simulated and measured voltage responsivity of the detector is shown in Fig. 12. It is observed that the maximum measured voltage responsivity is 800 mV/mW at 382 GHz. Two different values of C_{j0} are used in the simulation. One is deduced from the DC-IV theory or extracted at 40 GHz, and the other is the effective value at 400 GHz using the concept of effective capacitance (see Table 1). Both the simulated results show the same trend of the measured result. However, a much better agreement is observed when using the effective capacitance at 400 GHz, which proves that our parameter extraction method, the corresponding extrapolation process and the concept of effective capacitance are valid and correct. Frankly speaking, there still exists some deviation, which may be due to the processing and assembling errors or even still the modeling technology. Although the deviation problem at high frequencies has not yet been completely solved, the proposed concept of effective capacitance is a very promising attempt.

NEP is defined as:

$$NEP = \frac{N_v}{R_v}, \tag{7}$$

where N_v is the noise voltage of detector, which is measured by noise analyzer. Commonly N_v is measured with zero RF power. Under this condition only thermal noise is generated, which is different from the actual condition. In fact, as the input power increases, excess noise such as flicker noise, is generated. Flicker noise becomes increasingly important as the input power is increased [15]. N_v is measured as 27.7×10^{-9} V/Hz$^{0.5}$ with a RF power level of about 4 μW, and then NEP is calculated, as shown in Fig. 13. The minimum NEP is 3.46×10^{-11} W/Hz$^{0.5}$ at 382 GHz.

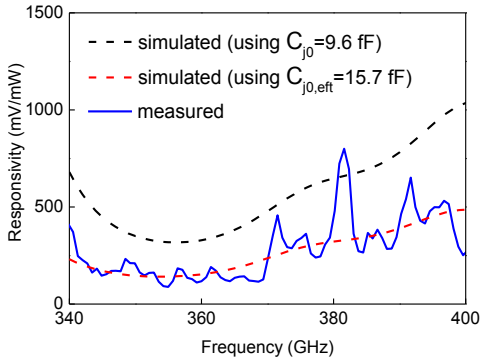

Fig. 12. Comparison between the measured and simulated voltage responsivity.

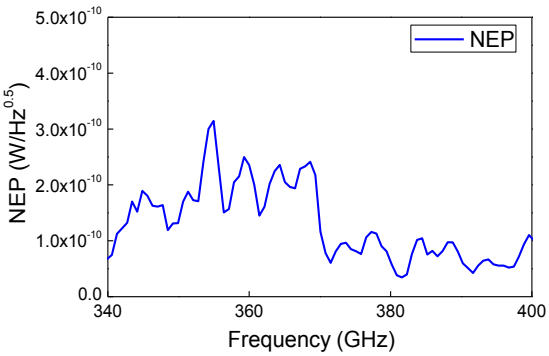

Fig. 13. Measured NEP of the detector.

V. CONCLUSION

In this study, firstly, we design and fabricate a type of InGaAs/InP material system based planar SBD with the feature of low barrier height which can improve the performance of detectors.

Secondly, a modeling technology for SBD is presented, which is based on an analytical parameter extraction method (working at 10-40 GHz) and a corresponding extrapolation process up to 400 GHz. The concept of effective capacitance is proposed to describe the high frequency effect, which greatly improve the consistency between the simulated and measured results of the detector.

Finally, based on the proposed SBD and the modeling technology, a 340-400 GHz zero-biased waveguide detector is designed and measured. By utilizing the topology of zero-bias (no DC path), the proposed detector becomes simple, compact and low cost. The measured results show that the maximum voltage responsivity and the minimum NEP are 800 mV/mW and 3.46×10^{-11} W/Hz$^{0.5}$ at 382 GHz, respectively. The consistency between the simulated and measured results of the detector has been greatly improved with the help of the effective capacitance.

ACKNOWLEDGMENT

This work is supported by the National High Technology Research and Development Program of China (863 Program) (2011AA010203), the National Basic Research Program of China (973 Program) (2011CB201704, 2010CB327502) and the National Nature Science Foundation of China (61434006).

REFERENCES

[1] J. Zmuidzinas and P. L. Richards, "Superconducting detectors and mixers for millimeter and submillimeter astrophysics," *Proceedings of the IEEE*, vol. 92, no. 10, pp. 1597-1616, 2004.

[2] D. L. Woolard, T. R. Globus, et al., "Submillimeter-wave phonon modes in DNA macromolecules," *Physical Review E*, vol. 65, no. 5, 051903, 2002.

[3] P. R. Griffiths and C. C. Homes, *Instrumentation For Far-Infrared Spectroscopy*, Handbook of Vibrational Spectroscopy, 2006.

[4] M. Tonouchi, "Cutting-edge terahertz technology," *Nature Photonics*, vol. 1, no. 2, pp. 97-105, 2007.

[5] A. Semenov, O. Cojocari, et al., "Application of zero-bias quasi-optical Schottky-diode detectors for monitoring short-pulse and weak terahertz radiation," *IEEE Electron. Device Letters*, vol. 31, no. 7, pp. 674-676, 2010.

[6] D. W. Porterfield, "Millimeter-wave planar varactor frequency doublers," *University of Virginia*, 1998.

[7] K. S. Saini, "Development of frequency multiplier technology for ALMA," *ALMA Memo 337*, 2003.

[8] J. Zhou, C. Yang, et al., "Planar InGaAs Schottky barrier diodes for terahertz applications," *Journal of Semiconductors*, 06, 2013.

[9] S. A. Maas, *Microwave Mixers*, Norwood, MA, Artech House, Inc., 368 p.1, 1986.

[10] A. Y. Tang, V. Drakinskiy, et al., "Analytical extraction of a Schottky diode model from broadband S-Parameters," *IEEE Transactions on Microwave Theory and Techniques*, vol. 61, pp. 1870-1878, May 2013.

[11] J. Grajal, V. Krozer, et al., "Modeling and design aspects of millimeter-wave and submillimeter-wave Schottky diode varactor frequency multipliers," *IEEE Trans. Microw. Theory Techn.*, vol. 48, no. 4, pp. 700-711, Apr. 2000.

[12] C. Lee, B. Gelmont, et al., "A modified harmonicbalance analysis of Schottky diode multipliers based upon a hydrodynamic transport model," in *Proc. 10th Int. Symp. Space Terahertz Tech.*, Charlottesville, VA, USA, pp. 312, Mar. 1999.

[13] R. Lipsey, S. Jones, et al., "Monte Carlo harmonic-balance and drift-diffusion harmonic-balance analyses of 100-600 GHz Schottky barrier varactor frequency multipliers," *IEEE Trans. Electron. Devices*, vol. 44, no. 11, pp. 1843-1850, Nov. 1997.

[14] C. Zhao, "Modelling and characterisation of a broadband 85/170 GHz Schottky varactor frequency doubler," *Chalmers University of Technology*, 2011.

[15] J. L. Hesler and T. W. Crowe, "Responsivity and noise measurements of zero-bias Schottky diode detectors," *18th Intl. Symp. Space Terahertz Tech.*, Pasadena, CA, 2007.

Tianhao Ren (Ph.D. candidate) received the B.S. degrees from University of Electronic Science and Technology of China (UESTC), Chengdu, China in 2012. He is now working for his Ph.D. in UESTC. His current research interests include millimeter-wave and terahertz systems and their applications, the modeling technology of terahertz devices, the terahertz monolithic integrated circuit (TMIC) technology, and some new technologies in the millimeter-wave and terahertz region.

Yong Zhang (Ph.D., Professor, Senior Member of IEEE) received the B.S., M.S., and Ph.D. degrees from University of Electronic Science and Technology of China (UESTC), Chengdu, China in 1999, 2001, and 2004, respectively. He was invited as a Visiting Scholar of Illinois Institute of Technology, USA, in 2009-2010. His current research interests include the design and application of passive and active components at microwave and millimeter wave frequencies, solid state terahertz technology, etc.

Optimization of Electromagnetics Problems Using an Improved Teaching-Learning-Based-Optimization Technique

Houssem R. E. H. Bouchekara [1] and Mouaaz Nahas [2]

[1] Constantine Electrical Engineering Laboratory, LEC, Department of Electrical Engineering
University of Constantine 1, 25000 Constantine, Algeria
bouchekara.houssem@gmail.com

[2] Department of Electrical Engineering, College of Engineering and Islamic Architecture
Umm Al-Qura University, P.O. Box: 5555, Makkah, 21955 Saudi Arabia
mmnahas@uqu.edu.sa

Abstract ─ Teaching-learning-based optimization (TLBO) is a rising star technique among metaheuristic techniques with highly competitive performance. This technique, which has been recently introduced, is based on the effect of influence of a teacher on learners and learners on their colleagues. This paper intends to apply an improved version of TLBO in the field of electromagnetics. To demonstrate its effectiveness in this area, the proposed technique is applied to two benchmarks related to brushless direct current wheel motor problem and testing electromagnetic analysis methods problem number 22. The quality of the results presented shows that the proposed technique is very competitive with other well-known optimization techniques; hence, it is a promising alternative technique for optimization in the field of electromagnetics.

Index Terms ─ electromagnetics, metaheuristics, optimization, teaching-learning-based-optimization.

I. INTRODUCTION

Optimization is a commonly encountered mathematical problem in all engineering disciplines where the efficient and effective design of products and systems is crucial [1]. It is even so in the field of electromagnetics, where the designers are faced with the challenge of optimizing ever more complex components, devices and systems [2], [3], [4]. Many electromagnetic problems require optimization; some examples are electrical machines design, antenna design, target image reconstruction, anti-reflective coating design for low radar cross section and microstrip filters design.

Recently, a new metaheuristic that is the teaching–learning-based optimization (TLBO) technique has been introduced. This technique has not yet received much attention by the electromagnetic optimization community. This technique is mainly based on the effect of influence of a teacher on learners and the interaction between learners themselves.

The main contribution of this paper is developing and applying an improved version of the TLBO technique to solve electromagnetics optimization problems (this will be referred to as ITLBO). Furthermore, in order to assess the performance of the developed technique, it is compared with that of other techniques provided in the literature.

The remainder of this paper is organized as follows. Section 2 introduces the concept and main features of the TLBO technique and the improvements that have been made. In Section 3, the brushless DC wheel motor (BLDC) and testing electromagnetic analysis methods (TEAM) number 22 benchmarks are presented. In Section 4, ITLBO is tested on the considered benchmarks and the results detailed. Finally, the paper conclusions are drawn in Section 5.

II. TEACHING-LEARNING-BASED-OPTIMIZATION

Design optimization process comprises three elements: objective functions, feasible solutions and optimization methods [5]. The optimization method searches for the optimal design among all available feasible designs. Generally, nature-inspired heuristic optimization methods seem to work better than traditional (deterministic) methods, and hence, are widely used [5]. Among all nature-inspired techniques, genetic algorithm (GA) is the most widely used which provides a near optimal solution for a `complex design problem with large number of variables and constraints [5]. However, the algorithm performance is affected by its specific control parameters [6]. This triggers the need for parameter-free optimization techniques where no algorithm parameters are required.

TLBO is a parameter-less metaheuristic technique introduced recently by Rao and colleagues [5]. In contrast with the other techniques, TLBO only requires such

Submitted On: February 9, 2015
Accepted On: October 19, 2015

controlling parameters as population size and maximum number of iterations for its operation [6]. Moreover, TLBO outperforms some other widespread metaheuristics with regard to constrained benchmark functions, constrained mechanical design, and continuous non-linear numerical optimization problems [7].

TLBO is a population-based optimization technique that uses a population of solutions to advance to the global solution [5], [8]. The technique is based on the principle of sharing knowledge by a teacher with his students in a classroom environment (i.e., Teacher Phase) and then sharing knowledge by learners with their classmates (i.e., Learner Phase) [7]. Therefore, TLBO works on the influence of a teacher on learners and influence of learners on their colleagues. The influence is usually manifested by the learners' results or outcomes. Better results of a class are typically represented by the students' mean grade. In general, the teacher attempts to distribute knowledge among learners to increase their knowledge level and help them enhance their grades. Consequently, the teacher will increase the mean grade of the class according to his capability. On the other hand, students will not only gain knowledge based on teaching quality, but also on the quality of students sitting in the class. Quality of the students is assessed through the mean value of the population. Moreover, the teacher puts effort to increase the mean of students to a higher level, at which students will require another teacher of better quality to teach them [5]. The TLBO algorithm is given in Algorithm 1.

Algorithm 1: TLBO pseudocode.

```
n: dimension of the problem
m: population size
MAXITER: maximum number of iterations
Initialization()
while ITER<MAXITER
    Elite ←SelectBest(P,Elite)
    for i=1:m
        T_F=round(1+rand)
        X_mean ← mean(X_i)
        X_teacher ← best(X_i)
        X_new,i = X_i + rand · (X_teacher-(TF · X_mean))
        if f(X_new,i)<f(X_i)
            X_i ←X_new,i
        end if
        j ←randi(m)
        if j≠i
            if f(X_i)<f(X_j)
                X_new,i = X_i + rand · (X_i – X_j)
            else
                X_new,i = X_i + rand · (X_j – X_i)
            end if
        end if
        if f(X_new,i)<f(X_i)
            X_i←X_new,i
        end if
    end for
    P ←ReplaceWorstWithElite(P,Elite)
    P ←RemoveDuplicateIndividuals(P)
    ITER = ITER +1
end while
```

As aforesaid, the process of TLBO is divided into two phases namely: the 'Teacher Phase' and the 'Learner Phase'.

In the teacher phase, consider M_i as the mean and T_i as the teacher at any iteration i. T_i will try to move mean M_i towards its own (new) level denoted by M_{new}. The solution is modified according to the difference between the existing and the new mean given by:

$$\text{Difference\_Mean}_i = r_i(M_{new} - T_F M_i), \quad (1)$$

where T_F is a teaching factor that decides the value of mean to be changed, and r_i is a random number in the range [0,1]. T_F has the value of either 1 or 2, which is a heuristic step and decided randomly with equal probability as T_F = round[1 + rand(0, 1){2 − 1}]. This difference updates the existing solution using the following expression:

$$X_{new,i} = X_{old,i} + \text{Difference\_Mean}_i. \quad (2)$$

In the learner phase, a learner interacts randomly with other learners through group discussions, presentations, formal communications, etc. A learner increases his knowledge if the other learner is more knowledgeable than him. To express the learner modification, if X_i and X_j are two different learners ($i \neq j$), and X_i is more knowledgeable than X_j, then:

$$X_{new,i} = X_{old,i} + r_i(X_i - X_j). \quad (3)$$

On the contrary, if X_j is more knowledgeable than X_i, then:

$$X_{new,i} = X_{old,i} + r_i(X_j - X_i). \quad (4)$$

In order to implement the TLBO for optimization problem, the following five steps are required: 1) Define the optimization problem and initialize the optimization parameters; 2) Initialize the population; 3) Apply the teacher phase; 4) Apply the learner phase; and 5) Apply the termination criterion.

In the first step, the population size (m), the maximum number of iterations (MAXITER), the number of design variables (n) need to be initialized, and design variables limits defined (U_L, L_L). Moreover, the optimization problem should be defined as: minimize $f(X)$, where $f(X)$ is the objective function, X is a vector for design variables such that $L_{L,i} \leq x_i \leq U_{L,i}$, and $X_i \in x_i = 1, 2, \ldots, n$.

In the second step, a random population is generated according to the population size and number of design variables.

In the third step, mean of the population is calculated to give the mean for the particular subject as:

$$M_n = [m_1, m_2, \ldots, m_n]. \quad (5)$$

For each iteration, the best solution acts as a teacher; that is:

$$X_{teacher} = X_{f(X)=min}. \quad (6)$$

The teacher will try to move the mean value towards $X_{,teacher}$, which will act as a new mean for the iteration: see (1).

The value of T_F is selected as 1 or 2. The obtained difference is added to the current solution to update its values using the relation in (2).

X_{new} is then accepted if it gives better function value, and so on.

In the fourth step, learners increase their knowledge through their interaction with their colleagues: see (3) and (4).

In the fifth step, if the stopping criterion is achieved, for example the maximum number of iterations, the whole process is stopped; otherwise, it will be repeated from the third step, and so on.

III. THE IMPROVED TEACHING-LEARNING-BASED-OPTIMIZATION

In the improved version of the TLBO (i.e., ITLBO), the lines between 16 – 25 in Algorithm 1 are replaced by the lines between 16 – 31 in Algorithm 2. The objective of introducing this improvement is to test the new vector X_{new} after every update in the k dimension of this vector ($k = 1: n$). This improvement is inspired, somehow, from the differential evolution algorithm where only one dimension (not all the vectors) is updated at a time.

Algorithm 2: ITLBO pseudocode.

```
1  n: dimension of the problem
2  m: population size
3  MAXITER: maximum number of iterations
4  Initialization()
5  while ITER<MAXITER
6      Elite ←SelectBest(P,Elite)
7      for i=1:m
8          TF=round(1+rand)
9          Xmean ← mean(Xi)
10         Xteacher ← best(Xi)
11         Xnew,i = Xi + rand · (Xteacher-(TF · Xmean))
12         if f(Xnew,i)<f(Xi)
13             Xi ←Xnew,i
14         end if
15         j ←randi(m)
16         if j≠i
17             if f(Xi)<f(Xj)
18                 for k=1:n
19                 Xnew,i (k) = Xi(k) + rand · (Xi(k) – Xj(k))
20                 if f(Xnew,i)<f(Xi)
21                     Xi(k)←Xnew,i(k)
22                 end if
23             end for
24             for k=1:n
25               Xnew,i (k)= Xi (k)+ rand · (Xj(k) – Xi(k))
26               if f(Xnew,i)<f(Xi)
27                   Xi(k)←Xnew,i(k)
28               end if
29             end for
30           end if
31       end if
32   end for
33   P ←ReplaceWorstWithElite(P,Elite)
34   P ←RemoveDuplicateIndividuals(P)
35   ITER = ITER +1
36 end while
```

IV. APPLICATIONS

A. BLDC benchmark

The application of TLBO in electromagnetics optimization is first illustrated on the BLDC benchmark designed for a race solar vehicle. This benchmark is presented in [9]. The authors proposed a benchmark with five design variables and one objective function to be maximized, that is the efficiency (which is equivalent to minimizing the motor losses) [10]. Figure 1 shows the prototype of the motor and Table 1 summarizes the five design variables with mapping ranges used in this study. In addition to the constraints imposed on the design variables, the problem is subject to six inequality constraints. These last constraints are related to technological and operational considerations regarding the specific wheel motor [10]. Thus, the optimization problem can be formulated as follows:

$$\text{OF} = -\eta. \quad (7)$$

Subject to:

$$M_{tot} \leq 15 \text{ [kg]}, \quad (8)$$

$$D_{ext} \leq 340 \text{ [mm]}, \quad (9)$$

$$D_{int} \geq 76 \text{ [mm]}, \quad (10)$$

$$I_{max} \geq 125 \text{ [A]}, \quad (11)$$

$$\text{discr}(D_s, \delta, B_d, B_e) \geq 0, \quad (12)$$

where, OF is the objective function (the minus sign is for transforming the minimization problem to a maximization one), η is the efficiency, M_{tot} is the total mass of the active parts, D_{ext} is the outer diameter, D_{int} is the inner diameter, I_{max} the current in the phases and discr(D_s, δ, B_d, B_e) is the determinant used for the calculation of the slot height. One of the main advantages of the BLDC benchmark is the availability of the source code to compute the objective function and constraints. Thus, the comparison of optimization results for different techniques is independent of differences in the calculation. These features make this benchmark ideal for comparing the performance of different techniques.

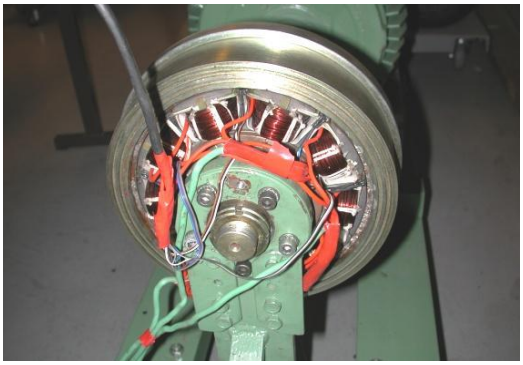

Fig. 1. Prototype of the wheel motor. The inner stator is visible with the coils rolled up around the teeth [9].

Table 1: Design variables and their ranges for the BLDC benchmark

Parameter	Description	Min	Max
D_s [mm]	Bore (stator) diameter	150	330
B_e [T]	Air gap induction	0.50	0.76
δ [A/mm^2]	Conductor current density	2.0	5.0
B_d [T]	Teeth magnetic induction	0.9	1.8
B_{cs} [T]	Stator back iron induction	0.6	1.6

B. TEAM22 benchmark

The TEAM Workshop Problem 22 or TEAM22 concerns the optimal design of a superconducting magnetic energy storage (SMES) device (Fig. 2). The goal of the optimization is to find the SMES configurations that offer an energy stored as close as possible to a defined reference value and a value for the stray field, as small as possible compared to a reference value [14], [15], [16].

There are two formulations of TEAM22 benchmark, based on the number of design variables of the optimization problem. The problem studied in this paper consists in the continuous, constrained, eight-parameter problem, shown in Fig. 2. The design variables are given in Table 2. Moreover, the system has two constraints: the first one is a design constraint where the solenoids should not overlap each other, and the second one is that the superconducting material should not violate the quench condition that links together the value of the current density and the maximum value of magnetic flux density. Thus, the optimization problem can be formulated as follows [14], [15]:

$$\mathrm{OF} = \frac{\mathrm{B}^2_{stray}}{\mathrm{B}^2_{norm}} + w\frac{\left|E - E_{ref}\right|}{E_{ref}}. \tag{13}$$

Subject to:

$$R_1 + \frac{d_1}{2} < R_2 - \frac{d_2}{2}, \tag{14}$$

$$\left|\mathbf{J}\right| = \left(-6.4\left|\mathrm{B}_{\max}\right| + 54\right)\ A/\mathrm{mm}^2, \tag{15}$$

where, E_{ref} is the reference value of the energy and it is equal to 180MJ, B_{norm} is the reference value of the stray field and it is equal to 200μT, B_{max} represent the maximum values of the magnetic induction, w is a penalty factor with value equal to 100 (this factor has been introduced in [15] in order to make the two terms of the objective function, i.e., the stray field and energy terms error, of roughly the same magnitude) and the stray field B_{stray} (evaluated along 22 equidistant points along line a and line b in Fig. 2) is defined as:

$$\mathrm{B}^2_{stray} = \frac{\sum_{i=1}^{22}\left|B_{stray,i}\right|^2}{22}. \tag{16}$$

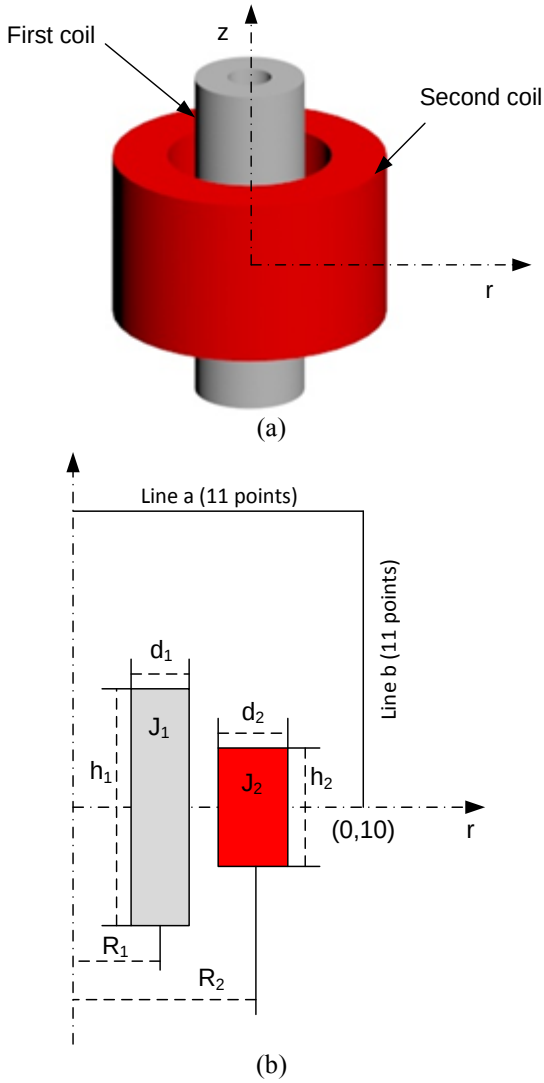

Fig. 2. TEAM22 configuration: (a) 3D representation of the SMES device, and (b) representation of the right-half transverse cut over the SMES device.

Table 2: Design variables and their ranges for TEAM22 benchmark

Parameter	Min	Max
R_1 [m]	1	4
R_2 [m]	1.8	5
h_{12} [m]	0.2	3.6
h_{22} [m]	0.2	3.6
d_1 [m]	0.1	0.8
d_2 [m]	0.1	0.8
J_1 [MA/m^2]	10	30
J_2 [MA/m^2]	-30	-10

V. OPTIMIZATION RESULTS

A. BLDC benchmark

In order to show the robustness and effectiveness of both the TLBO and ITLBO techniques, they have been applied to the BLDC benchmark, where 100 independent trials have been performed for four cases corresponding to four different population sizes. The results of this investigation are shown in Table 3. We can notice that the best, the mean, the median and the worst values of the objective function for the four cases after 100 trials are very close. This is also shown by the low values of standard deviations calculated.

A small comparison or results obtained using the TLBO and the ITLBO techniques, shows the effect of the improvements that has been introduced. We can see clearly that the ITLBO technique outperforms the standard TLBO technique. Furthermore, this investigation reveals the effectiveness of the ITLBO technique and its ability to reach either the optimum value or very near to it in every trial and with different sizes of population. The results obtained here using the TLBO and ITLBO techniques are compared to some other well-known techniques reported in the literature, i.e., sequential quadratic programming (SQP) genetic algorithm (GA), ant colony optimization (ACO), partcile swarm optimization (PSO) and modified imperialist competitive algorithm (MICA).

The results of this comparison are reported in Table 4. It appears from this table that the results obtained using the proposed ITLBO technique correspond to the optimal motor configuration as reported in the literature.

Table 3: Simulation results of the BLDC benchmark in 100 trials

Population Size	Method	Worst	Mean	Median	Best	SD
10	TLBO	94.92	95.29	95.31	95.32	0.0549318
	ITLBO	95.11	95.30	95.31	95.32	0.0453629
20	TLBO	95.30	95.32	95.32	95.32	0.00270286
	ITLBO	95.31	95.32	95.32	95.32	0.00066817
30	TLBO	95.31	95.32	95.32	95.32	0.00083383
	ITLBO	95.32	95.32	95.32	95.32	0.0003585
40	TLBO	95.31	95.32	95.32	95.32	0.00062436
	ITLBO	95.32	95.32	95.32	95.32	0.00023746
50	TLBO	95.32	95.32	95.32	95.32	0.00036394
	ITLBO	95.32	95.32	95.32	95.32	0.00017832

Table 4: Comparison of results using different optimization techniques

Method	D_s [mm]	B_e [T]	δ [A/mm²]	B_d [T]	B_{cs} [T]	η [%]	M_{tot} [kg]	I_{max} [A]	D_{int} [mm]	D_{ext} [mm]	T_a [°C]
ITLBO	201.37	0.6481	2.051	1.8	0.89	95.32	15	125	76.5	239.1	95.26
TLBO	201.24	0.6482	2.044	1.8	0.8963	95.32	15	125	76.0	238.9	95.35
SQP [11]	201.20	0.6481	2.044	1.8	0.8959	95.32	15	125	76	238.9	95.35
GA [12]	201.50	0.648	2.060	1.8	0.8817	95.31	15	125	76.9	239.2	95.21
GA & SQP [12]	201.20	0.6481	2.062	1.8	0.87	95.31	15	125	76	238.9	95.31
ACO [13]	201.20	0.6481	2.044	1.8	0.8959	95.32	15	125	76	238.9	95.35
PSO [13]	202.10	0.6476	2.042	1.8	0.9298	95.32	15	125	79.2	239.8	94.98
MICA [10]	201.20	0.6481	2.044	1.8	0.8959	95.32	15	125	76	238.9	95.35

B. TEAM22 benchmark

The second example studied in this paper is the TEAM 22 benchmark. The numerical experiments were conducted for 30 independent trials. The parameters of the optimal configurations found using the TLBO and the ITLBO techniques are tabulated in Table 5. Further,

the magnetic flux equipotentials and the magnetic flux density of the optimal configuration found using the ITLBO are represented in Fig. 3 and Fig. 4, respectively.

In Table 6, the ITLBO technique is compared with the TLBO technique and with some other optimizations techniques that are GA, PSO, differential evolution (DE), league championship algorithm (LCA) and electromagnetism-like mechanism (EM). From this comparison, it is worth to mention the superiority of the proposed ITLBO technique over some well-known optimization techniques. In addition, it is to be noted that, the ITLBO performances are better than the standard TLBO. In other words, the ITLBO is more efficient and more robust than the TLBO.

Table 5: Optimal configuration of TEAM22 benchmark obtained using ITLBO

	Value	
Parameter	TLBO	ITLBO
R_1 [m]	1.27	1.20
R_2 [m]	1.96	1.95
h_{12} [m]	2.09	2.80
h_{22} [m]	2.97	3.60
d_1 [m]	0.61	0.80
d_2 [m]	0.10	0.11
J_1 [MA/m^2]	14.85	10.29
J_2 [MA/m^2]	-27.65	-23.35
OF	0.40	0.18
E [MJ]	179.55	179.96
B_{stray} [mT]	0.08	0.08

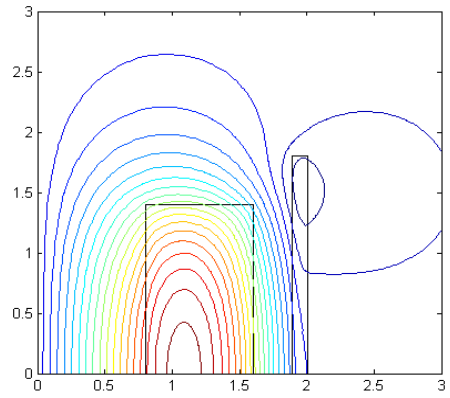

Fig. 3. Magnetic flux equipotentials of the optimal configuration obtained using ITLBO.

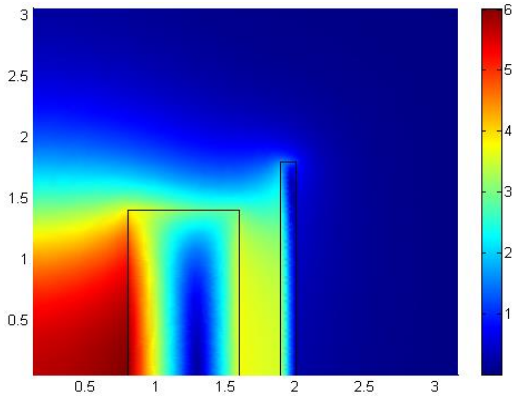

Fig. 4. Magnetic flux density distribution of the optimal configuration obtained using ITLBO.

Table 6: Comparison of results using different optimization techniques after 30 trials

Method	Worst	Mean	Median	Best	Standard Deviation
ITLBO	2.08	0.66	0.54	0.18	0.46
TLBO	11.59	3.06	1.51	0.40	2.71
GA	32.71	15.95	14.16	5.93	7.33
PSO	101.88	26.79	10.82	0.03	32.29
DE	57.11	6.33	3.52	0.01	10.38
LCA	88.44	41.76	43.48	1.65	20.97
EM	22.33	13.12	12.14	7.80	3.99

VI. CONCLUSION

This paper starts by describing the TLBO technique which is a powerful yet easy technique for optimization of various design problems including electromagnetic ones. The TLBO has the advantage of being a parameter-less optimization technique, i.e., its algorithm has no specific control parameters to tune.

In this study, an improved version of the TLBO technique was developed and applied to the BLDC and TEAM22 benchmarks. Considering the quality of the obtained results, it is possible to conclude that the ITLBO constitutes an efficient and robust technique for optimization in electromagnetics area. Further benchmarks for other common electromagnetic problems are currently under investigation. Also, implementing multi-objective ITLBO is a possible extension of the current work in the area concerned with in this study.

REFERENCES

[1] H. R. E. H. Bouchekara, "Electromagnetic device optimization based on electromagnetism-like mechanism," *Appl. Comput. Electromagn. Soc. J.*, vol. 28, no. 3, pp. 241-248, 2013.

[2] D. Vieira, A. C. Lisboa, and R. R. Saldanha, "An

enhanced ellipsoid method for electromagnetic devices optimization and design," *IEEE Transactions on Magnetics*, vol. 46, no. 8, pp. 2843-2851, 2010.

[3] P. Alotto, "A hybrid multiobjective differential evolution method for electromagnetic device optimization," *COMPEL: The International Journal for Computation and Mathematics in Electrical and Electronic Engineering*, vol. 30, no. 6, pp. 1815-1828, 2012.

[4] J. Ouyang and D. A. Lowther, "Comparison of evolutionary and rule-based strategies for electromagnetic device optimization," *IEEE Transactions on Magnetics*, vol. 48, no. 2, pp. 371-374, 2012.

[5] R. Rao, V. J. Savsani, and D. P. Vakharia, "Teaching-learning-based optimization: a novel method for constrained mechanical design optimization problems," *Computer-Aided Design*, vol. 43, no. 3, pp. 303-315, 2011.

[6] R. V. Rao and V. Patel, "An elitist teaching learning based optimization algorithm for solving complex constrained optimization problems," *International Journal of Industrial Engineering Computations*, vol. 3, no. 4, pp. 535-560, 2012.

[7] M. Črepinšek, S. H. Liu, and L. Mernik, "A note on teaching-learning-based optimization algorithm," *Information Sciences*, vol. 212, pp. 79-93, 2012.

[8] R. Venkata Rao and V. D. Kalyankar, "Parameter optimization of modern machining processes using teaching-learning-based optimization algorithm," *Engineering Applications of Artificial Intelligence*, vol. 26, no. 1, pp. 524-531, 2013.

[9] S. Brisset and P. Brochet, "Analytical model for the optimal design of a brushless dc wheel motor," *COMPEL: The International Journal for Computation and Mathematics in Electrical and Electronic Engineering*, vol. 24, no. 3, pp. 829-848, 2005.

[10] L. Coelho, L. Afonso, and P. Alotto, "A modified imperialist competitive algorithm for optimization in electromagnetics," *IEEE Transactions on Magnetics*, vol. 48, no. 2, pp. 579-582, 2012.

[11] F. Moussouni and S. Brisset, "A benchmark for a mono and multi objective optimization of the brushless dc wheel motor," *Laboratory of Electrical Engineering and Power Electronics, University of Science and Technology of Lille*, 2007. [Online]. Available: http://l2ep.univ-lille1.fr/come/benchmark-wheel-motor.htm. [Accessed 20 Apr. 2013].

[12] F. Moussouni, S. Brisset, and P. Brochet, "Some results on design of brushless dc wheel motor using SQP and GA," *International Journal of Applied Electromagnetics and Mechanics*, vol. 26, no. 3-4, pp. 233-241, 2007.

[13] F. Moussouni, S. Brisset, and P. Brochet, "Comparison of two multi-agent algorithms: ACO and PSO," *in Proc. 13th Int. Symp. Electromagnetic Fields Mechatron., Elect. Electron. Eng*., Czech Republic, 2007.

[14] P. G. Alotto, U. Baumgartner, F. Freschi, M. Jaindl, A. Kostinger, Ch. Magele, W. Renhart, and M. Repetto, *SMES Optimization Benchmark: TEAM Workshop Problem 22*, [Online]. Available: http://www.compumag.org/jsite/team.html.

[15] L. Dos Santos Coelho, C. Da Costa Silveira, C. A. Sierakowski, and P. Alotto, "Improved bacterial foraging strategy applied to TEAM workshop benchmark problem," *IEEE Transactions on Magnetics*, vol. 46, no. 8, pp. 2903,2906, Aug. 2010.

[16] A. Berbecea, "Multi-level approaches for optimal system design in railway applications," *Ph.D. Thesis*, Laboratoire L2EP à l'Ecole Centrale de Lille, 2012.

Houssem R. E. H. Bouchekara is an Associate Professor in the Electrical Engineering Department of University of Constantine 1. He received his B.S. in Electrical Engineering from University Mentouri Constantine, Algeria, in 2004, his Master in Electronic Systems and Electrical Engineering from Polytechnic School of the University of Nantes, France, in 2005, and his Ph.D. in Electrical Engineering from Grenoble Institute of Technology, France, in 2008. His research interest includes optimization techniques, magnetic refrigeration, electromagnetics, electric machines and power systems.

Mouaaz Nahas received the B.Sc. degree (Electrical Engineering) from Jordan University of Science and Technology, Jordan, in 2001, the M.Sc. degree (Communications Engineering) from Loughborough University, UK, in 2002, and the Ph.D. degree (Embedded Systems) from the University of Leicester, UK, in 2009. He is currently an Assistant Professor in the Department of Electrical Engineering at Umm Al-Qura University, Makkah, Saudi Arabia. His main research interest is in embedded systems, electromagnetics and wireless communications.

Frequency and Time Domain Investigation of Compact UWB Slot Antenna with Triple Band Notched Characteristics

Seyed Ramin Emadian, Javad Ahmadi-Shokouh, Abdolmalek Raeesi, Abdolbaset Askani, and Jalal Nazari

Department of Telecommunication Engineering
University of Sistan and Baluchestan, Zahedan, Iran
ramin.emadian@gmail.com, jahmadis@ieee.org, Abdolmalek.raeisi@gmail.com, abdolbaset.askani@gmail.com, nazari_jalal@yahoo.com

Abstract ─ In this paper, a simple compact ultrawideband (UWB) microstrip slot antenna with triple band notched characteristics is presented. In the proposed antenna, a good impedance matching over a very wide frequency range is achieved by adding two rectangular stubs to the bottom section of the simple rectangular patch. Moreover, by employing an inverted T-shaped stub connected to the ground plane and two U-shaped and Ω-shaped slots in the modified patch, triple band notched properties are obtained. This proposed triple band notched antenna with dimensions of 26×26 mm^2 has a very wide bandwidth from 2.5 GHz up to 19 GHz, which is about 150% fractional bandwidth of the center frequency. Unlike the most previous works reported in the literature, the triple band notched feature applied in the proposed antenna does not deteriorate the impedance bandwidth at higher frequencies. The radiation results such as gain, efficiency and radiation patterns as well as time domain properties of the proposed antenna show that it can be a good candidate for new super wideband applications.

Index Terms ─ Band notched characteristics, radiation patch, resonant slots, system fidelity factor.

I. INTRODUCTION

With advances in wireless communications and portable devices, designing of small planar UWB antennas has attracted more attentions. These planar antennas have many advantages such as simple structure, easy fabrication, and omnidirectional radiation pattern. More importantly, they have wide impedance bandwidth which comes up with an increased transmission data rate. Lately, many methods have been used to enhance the antenna impedance bandwidth, for instance, using L-shaped stubs on the back of the substrate [1], inverse T-shaped slots cut in the ground plane [2], employing truncated radiation patch [3], and a trident shaped feedline [4]. Due to the low power of UWB signals, low interferences with other narrowband signals can inherently occur. However, many techniques are presented to avoid interferences between UWB systems and other narrowband wireless systems such as WiMAX (3.3-3.6), WLAN (5.15-5.35 and 5.75-5.85), and X band with downlink frequency bandwidth 7.25-7.75 GHz. Hence, the structures with proper shape and size should be used to design band notched functions. They should reject only the undesired bands while their effects over the other pass band frequencies should be negligible. Some of these techniques include etching split ring resonators in the radiation patch [5] and embedding a pair of rotated V-shaped slots in the ground plane [6]. In this paper, a simple and compact UWB slot antenna with triple notched bands is presented. Two rectangular stubs with proper dimensions are added to the bottom of the rectangular radiation patch to enhance the impedance bandwidth to about 19 GHz. An inverted T-shaped stub connected to the ground plane and two resonant slots etched out from the radiation patch are employed to create triple band notched characteristics of the proposed antenna. In most antennas reported in the literature, band notched structures have limited upper edge of the frequency band. In fact, the higher-order harmonics of the band notched structures occur at the higher frequencies and deteriorate the impedance bandwidth. In [7], two methods have been presented to design a triple band notched antenna. One method uses multiple etched slots on the radiation patch, and the other one uses split ring resonators (SRRs) coupled to the feed line. In both of the above methods, a spurious stop-band emerged in vicinity of 10 GHz and accordingly, the bandwidth of the antenna is limited at higher frequencies. Moreover, the UWB antennas presented in [8-10] are the other examples that their band notched structures generate a spurious stop band at higher frequencies. The proposed triple band notched structure presented in this paper does not generate spurious stop bands at higher frequencies. Hence, the impedance bandwidth of the proposed antenna with and without band notched structure is almost the same at higher frequencies. The rest of the

Submitted On: June 7, 2015
Accepted On: November 8, 2015

paper is organized as follows. In Section II, the antenna structure is described. The antenna design analogy is explained in Section III. In the next section, the radiation characteristics of the proposed antenna such as gain, radiation efficiency and patterns are discussed and explained. Moreover, time domain behaviors of the proposed antenna are studied at Section V. Finally, Section VI concludes the paper.

II. ANTENNA STRUCTURE

The proposed antenna contains a wide quasi-circle slot with radius of 12 mm in the ground plane and a simple rectangular radiation patch with size of 6.6×8 mm^2. Figure 1 shows the structure of the proposed triple band notched UWB slot antenna. A 50 Ω coplanar waveguide (CPW) feed line including a center strip of width 2.6 mm and two gaps of width 0.3 mm is used to excite the antenna. The antenna is fabricated on FR4 substrate with relative permittivity ε_r = 4.4, loss tangent of 0.018 and height of 1.6 mm. For good impedance matching over the operating bandwidth, two rectangular stubs are added to the bottom of the rectangular patch as shown in Fig. 1. An inverse T-shaped resonant stub inside the quasi-circle slot connected to the ground plane, and two Ω-shaped and U-shaped resonant slots cut from the radiation patch are employed to achieve notched bands. The proposed antenna has a simple structure and compact size of 26×26 mm^2.

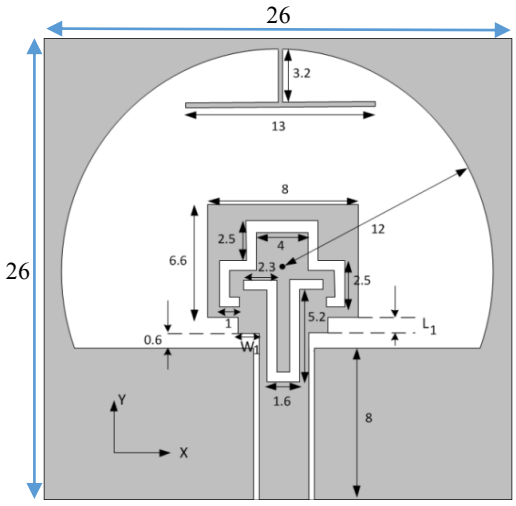

Fig. 1. Geometry of the proposed antenna (mm).

III. ANTENNA DESIGN AND DISCUSSIONS

A. Full-band UWB antenna design

High frequency structure simulator (HFSS) software, which works based on finite element method, is employed to obtain the simulation results. A quasi-circle slot and simple rectangular patch with proper dimensions are employed to satisfy UWB requirements. To further enhance the impedance bandwidth, two rectangular stubs with dimensions of $L_1 \times W_1$ are added to the lower section of the radiation patch as shown in Fig. 1. Figure 2 shows the VSWR diagrams of the antenna with and without these rectangular stubs. It can be seen from the figure that the lower cut off frequency is slightly decreased, and the VSWR at higher frequencies of the band is greatly improved. The middle band is slightly damaged but it is still acceptable (VSWR < 2).

Furthermore, to better clarify the role of these rectangular stubs, the VSWR diagrams of the modified antenna for different values of L_1 and W_1 are depicted in Fig. 3 and Fig. 4, respectively. In Fig. 3, L_1 varies from 0.5 mm to 1.5 mm, while W_1 is fixed at 0.8 mm. It can be seen that by increasing parameter L_1 to a specified value, the impedance bandwidth is improved at higher frequencies. However, further increasing the parameter L_1 causes the lower cutoff frequency to increase. The optimum value of L_1 is equal to 1 mm. Figure 4 shows the variations of W_1 when L_1 is fixed at 1 mm. Like the previous case, it is seen from the figure that by increasing W_1 to a specified value the impedance bandwidth can be improved, while further increasing W_1 deteriorates the bandwidth at lower frequencies. The optimum value of W_1 is obtained equal to 0.8 mm.

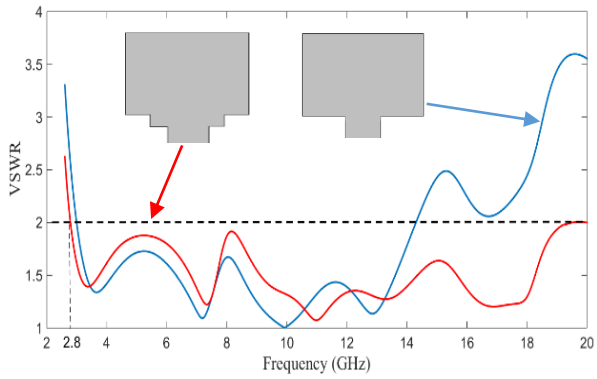

Fig. 2. VSWR of the antenna with and without rectangular stubs.

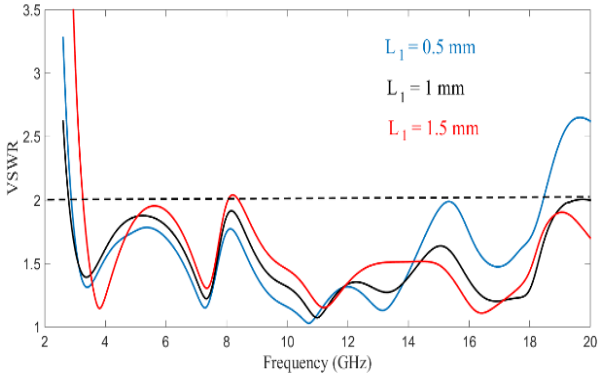

Fig. 3. VSWR of the antenna with different values of L_1 when W_1 is fixed at 0.8 mm.

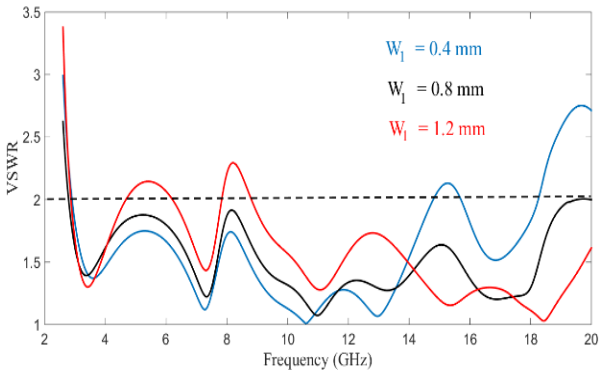

Fig. 4. VSWR of the antenna with different values of W_1 when L_1 is fixed at 1 mm.

B. Band notched structures design

To prevent the interferences between the UWB and WiMAX systems, an inverse T-shaped stub is connected to the ground plane of the proposed UWB antenna in order to provide a band notched property at WiMAX frequency band. The T-shaped stub, with a horizontal arm of 13 mm and a vertical arm of 3.2 mm, acts as a quarter wavelength resonator at 3.8 GHz (center frequency of the first notched band). At this frequency, the electrical current is mainly concentrated on the T-shaped stub and due to its resonance feature a band notched characteristic with center frequency of 3.8 GHz appears. To create band notched properties for WLAN band (5-6 GHz band), the Ω-shaped resonant slot with given values is etched out from the radiating patch. Finally, to reject the 7-8 GHz band, a U-shaped slot is cut from the radiating patch. The width of the T-shaped stub is fixed at 0.3 mm, while the width of the Ω-shaped and U-shaped slots are fixed at 0.5 mm. Figure 5 depicts the VSWR diagram of the three different single band notched antennas.

The proposed antenna, simultaneously applies these band notched structures in a single design and therefore an UWB antenna with triple band notched characteristics can be achieved.

Figure 6 shows the simulated and measured VSWR of the proposed antenna. The computer simulation technology (CST) software is also used to emphasize accuracy of the antenna design. As seen from the figure, by combining the band notched structures in the proposed antenna, the resonant frequencies are shifted to lower values. It is due to the mutual coupling of these filtering structures on each other. This phenomenon is more visible for WLAN and X band, because both the Ω-shaped and U-shaped slots are inserted in the radiation patch and placed near each other. Consequently, they have more effects on each other. Moreover, in the final design the size of these resonant stub and slots are slightly modified to have better impedance matching over the entire band.

It can be seen that the measured and simulated results are in good agreement. As mentioned earlier, unlike most antennas reported recently, the triple band notched structure introduced in this paper does not deteriorate the bandwidth of the proposed antenna, especially at higher frequencies. It is noted that by tuning the length of these filtering structures (inverse T-shaped stub, Ω-shaped and U-shaped slots), the center frequency of the notched bands can be controlled.

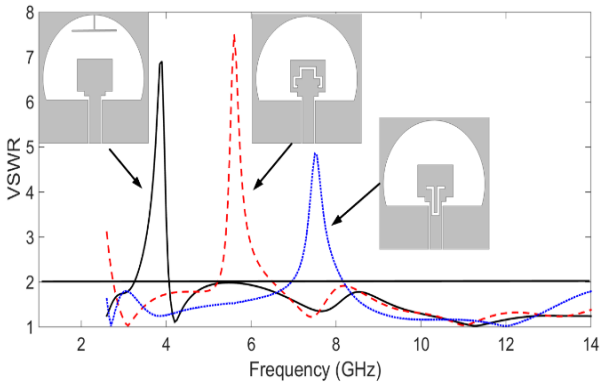

Fig. 5. VSWR of different single band notched antennas.

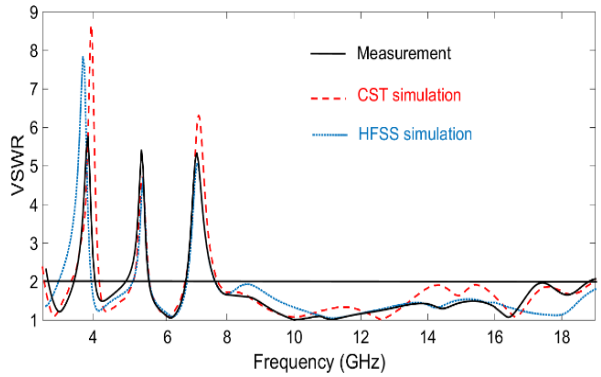

Fig. 6. Measured and simulated VSWR of proposed antenna.

IV. FAR FIELD RADIATION CHARACTERISTICS

Figure 7 shows the measured gain and simulated radiation efficiency of the proposed antenna. It is observed from the figure that the gain is almost constant with variations of less than 3.5 dB over the entire operating bandwidth, except at the notched bands. There are three high reductions in the gain and radiation efficiency diagrams due to the effect of the band notched structures. Figure 8 shows the radiation patterns of the proposed antenna in the two cut planes, E-plane (y-z plane) and H-plane (x-z plane) at three sample frequencies (2.8, 7.5 and 12 GHz). The radiation patterns are almost constant and omnidirectional in the H-plane and bi-directional in the E-plane.

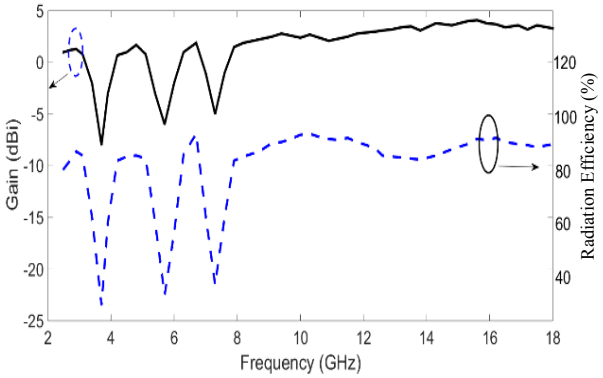

Fig. 7. Measured gain and simulated radiation efficiency of proposed antenna.

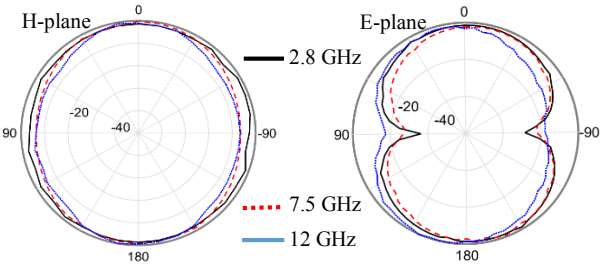

Fig. 8. Normalized far field radiation patterns of proposed antenna.

V. TIME DOMAIN CHARACTERISTICS

A significant property of UWB systems is the transmission of very narrow pulses in time. Antenna designing in the pulse-based UWB systems (impulse radio UWB communication systems), has a unique collection of design requirements. Therefore, further studies and investigations should be performed on time domain behavior of an UWB antenna.

In this section, two transmitting and receiving antenna systems including the reference antenna (antenna without band notched structures) system and proposed antenna (antenna with triple band notched structures) system in face to face and side by side scenarios are investigated. The CST software is employed to simulate time domain behaviors. In both scenarios, two identical antennas placed at a distance of 30 cm from each other, are employed for transmitting and receiving the UWB signal. A sixth derivative Gaussian pulse with a frequency spectrum corresponding to 3.1-10.6 GHz is used as the input signal. Figure 9 shows the input and received signals of the reference and proposed antenna systems in face to face and side by side scenarios, respectively. Figure 10 also demonstrates their power spectral density. FCC's outdoor and indoor mask are also shown for comparison. It can be seen that the proposed antenna system has a more distortion in the received pulse compared to the reference antenna system. It is due to the band notched properties of the proposed antenna. The power spectral density of the proposed antenna has three sharp nulls at the notched frequencies. It indicates that a portion of the input signal cannot be received effectively as shown in Fig. 10. Moreover, it can be seen that compared to the face-to-face scenario, both reference and proposed antenna system experience more distortion in received pulse for side-by-side scenario. This is due to the maximum radiation of the antenna in the Z-direction (see Fig. 1).

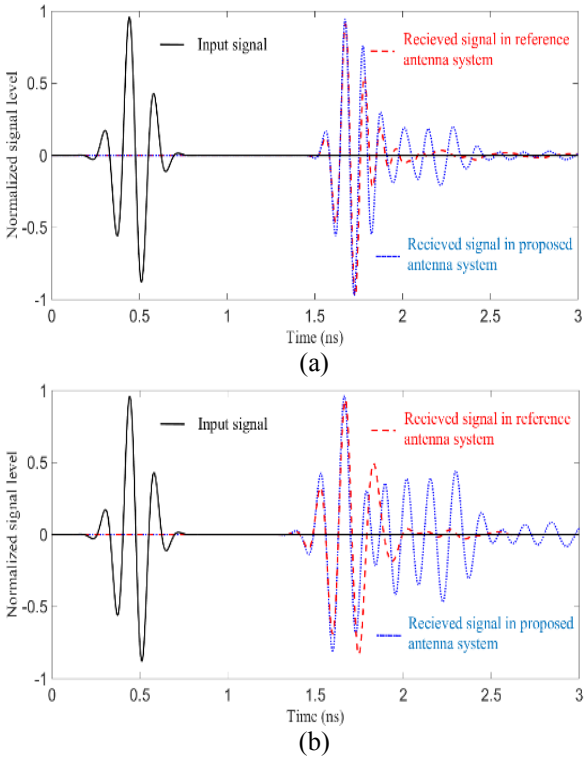

Fig. 9. Input signal and received signals for reference antenna system and proposed antenna system: (a) in face to face scenario, and (b) in side by side scenario.

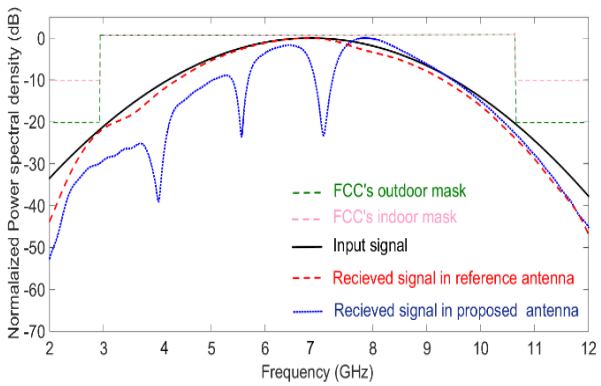

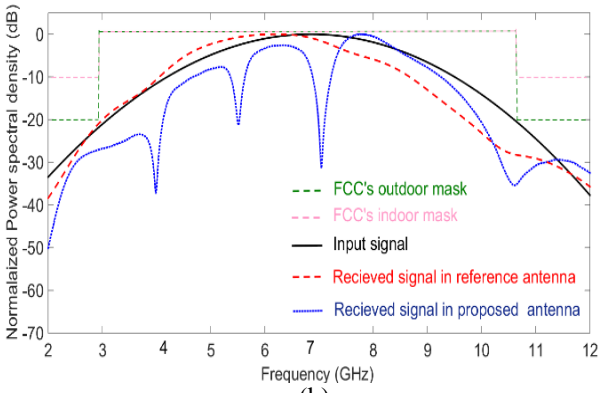

(b)

Fig. 10. PSD of input signal and received signals for reference antenna system and proposed antenna system: (a) in face to face scenario, and (b) in side by side scenario.

In the time domain method, an important factor indicating the performance of the antenna is the fidelity factor. The fidelity is employed as a factor of similarity between the input and received signal and obtained as follows [11]:

$$F = \mathrm{Max}_{\tau} \left| \frac{\int_{-\infty}^{+\infty} S(t) r(t-\tau) dt}{\sqrt{\int_{-\infty}^{+\infty} S(t)^2 \int_{-\infty}^{+\infty} r(t)^2}} \right|, \quad (1)$$

where S(t) and r(t) are the input and received signals, respectively. The values of the system fidelity factor vary between 0 and 100%. A system fidelity factor value of 100% shows that the received signal perfectly fits the input signal, while a value of 0 indicates that the received signal is completely different than the input signal. A distortion higher than 50% can cause the pulse approximately unrecognizable [12]. The system fidelity factor of the reference antenna system and proposed antenna system in both face-to-face and side-by-side scenarios is calculated and reported in Table 1. It is observed that the system fidelity factor of the reference antenna pair is good (more than 90%). For the proposed antenna pair, the fidelity factor is slightly deteriorated because of the filtering structures of the proposed antenna.

Table 1: System fidelity factor for different scenarios

Different Scenarios	Fidelity Factor
Reference antenna system in face to face scenario	94%
Reference antenna system in side by side scenario	91%
Proposed antenna system in face to face scenario	84%
Proposed antenna system in side by side scenario	77%

VI. CONCLUSION

In this paper, a novel and simple triple band notched slot antenna is presented. In this antenna, the impedance bandwidth is highly improved by inserting two rectangular stubs between the rectangular patch and CPW feed line. Moreover, by using an inverse T-shaped stub connected to the ground plane, and two Ω-shaped and U-shaped slots in the radiation patch, triple band notched characteristics are achieved. The results reveal that the radiation properties as well as time domain behavior of the proposed antenna are satisfied. Due to these advantages, the proposed antenna can be a proper candidate for super wide band applications.

REFERENCES

[1] S. R. Emadian, M. Mirmozafari, C. Ghobadi, and J. Nourinia, "Bandwidth enhancement of dual band-notched circle-like slot antenna," *Electronics Letters*, vol. 48, no. 7, pp. 356-357, Mar. 2012.

[2] S. R. Emadian and J. Ahmadi-shokouh, "Modified ground circle like-slot antenna with dual band-notched characteristics for super UWB applications," *Applied Computational Electromagnetics Society (ACES) Journal*, vol. 30, pp. 436-443, 2015.

[3] S. R. Emadian and J. Ahmadi-shokouh, "Very small dual band notched rectangular slot antenna with enhanced impedance bandwidth," *IEEE Trans. Antennas Propag.*, vol. 63, no. 10, pp. 4529-4534, 2015.

[4] S. R. Emadian, C. Ghobadi, J. Nourinia, M. Mirmozafari, and J. Pourahmadazar, "Bandwidth enhancement of CPW-fed circle-like slot antenna with dual band-notched characteristic," *IEEE Antennas Wireless Propag. Lett.*, vol. 11, pp. 543-546, 2012.

[5] D. Sarkar, K. Srivastava, and S. Saurav, "A compact microstrip-fed triple band-notched UWB monopole antenna," *IEEE Antennas Wireless Propag. Lett.*, vol. 13, pp. 396-399, 2014.

[6] S. Venkata, M. Rana, P. Bakariya, S. Dwari, and M. Sarkar, "Planar ultrawideband monopole antenna with tri-notch band characteristics," *Progress In Electromagnetics Research C*, vol. 46, pp. 163-170, 2014.

[7] Y. Zhang, W. Hong, C. Yu, Z. Kuai, Y. Don, and J. Zhou, "Planar ultrawideband antennas with multiple notched bands based on etched slots on the patch and/or split ring resonators on the feed line," *IEEE Trans. Antennas Propag.*, vol. 56, no. 9, pp. 3063-3068, 2008.

[8] C. Zhang, J. Zhang, and L. Li, "Triple band-notched UWB antenna based on SIR-DGS and fork-shaped stubs," *Electronics Letters*, vol. 50, no. 2, pp. 67-69, Jan. 2014.

[9] F. Zhu, S. Gao, A. Ho, A. Abd-Alhameed, C. See, T. Brown, J. Li, G. Wei, and J. Xu, "Multiple band-notched UWB antenna with band-rejected elements integrated in the feed line," *IEEE Trans. Antennas Propag*., vol. 56, no. 9, pp. 3063-3068, 2008.

[10] Y. Zhang, W. Hong, C. Yu, J. Zhou, and Z. Kuai, "Design and implementation of planar ultra-wideband antennas with multiple notched bands based on stepped impedance resonators," *IET Microw. Antennas Propag*., vol. 3, no. 12, pp. 1051-1059, 2008.

[11] A. Dastranj and H. Abiri, "Bandwidth enhancement of printed E-shaped slot antennas fed by CPW and microstrip line," *IEEE Trans. Antenna Propag*., vol. 58, pp. 1402-1407, 2010.

[12] G. Quintero, J.-F. Zürcher, and A. K. Skrivervik, "System fidelity factor: a new method for comparing UWB antennas," *IEEE Trans. Antennas Propag*., vol. 59, no. 7, pp. 2502-2512, July 2011.

Numerical Evaluation of the Radar Cross Section of Human Breathing Models

Marta Cavagnaro, Erika Pittella, and Stefano Pisa

Dept. of Information Engineering, Electronics and Telecommunications (DIET)
Sapienza University of Rome, Rome, Italy
[cavagnaro, pittella, pisa]@diet.uniroma1.it

Abstract ─ In this paper, anatomical models of the human body are used to evaluate the radar cross section (RCS) of breathing subjects. The study is performed by using a self-developed finite difference time domain (FDTD) code implemented in the message passing interface environment (MPI). The realized models represent three different phases of the breathing activity taking into account the respiration physiology and the pulmonary mechanics. In particular, the end expiration phase (resting state), the end of a normal inspiration phase (tidal), and the end of a deep inspiration phase (deep) were considered. Computed results show RCS values of the resting state model in agreement with literature data, and appreciable variations of the RCS determined by the breathing activity. Simulations performed with homogeneous body models suggest that these differences depend both on the model anatomy and on the tissue dielectric properties.

Index Terms ─ Breathing models, electromagnetic scattering, radar cross section.

I. INTRODUCTION

Ultra-wide band (UWB) radars for remote sensing of vital signs, as the breath and cardiac activity, can be useful for monitoring the breathing of patients during hospital confinement, for through-the-wall sensing, and for the rescue of people under rubbles or snow. UWB radars detect the time of arrival and the amplitude variations of UWB pulses once reflected by the human body to evaluate the thorax and heart movements, and then derive the cardio-respiratory activities [1]. The knowledge of the radar cross section (RCS) of men in correspondence of different respiration phases is of great importance for the design of UWB radars for remote monitoring of respiratory activity. In particular, the RCS is essential in predicting the time behavior of the radar-received signal, thus helping designing stand-alone apparatuses [1].

In literature, few works deal with the RCS of the human body including experimental investigations [2]-[5] and recent numerical studies [1], [6]-[7]. These works indicate RCS absolute values of the order of 1 m^2, with large fluctuations with the frequency. However, these limited data are based on man models at rest and they do not consider variations of the tissue properties with frequency.

In this paper, a finite-difference time-domain (FDTD) parallel code was used to evaluate the RCS of anatomical models of the human body as a function of the frequency. Models of men in resting state and previously developed models representing a tidal breath and a deep breath were considered [8], [9]. The RCS was evaluated in a frequency range between 1 and 9 GHz with 1 GHz step, taking into account the frequency behavior of the tissues' dielectric parameters and the variations of the lung geometry and dielectric parameters with the respiration.

II. METHODS AND MODELS

A. FDTD method

The RCS was computed by using a parallel self-developed code based on the FDTD method and implemented in the MPI environment [10]. Figure 1 shows the simulated geometry: a plane wave with sinusoidal time dependence propagating along the y-axis impinges on the human body (front-back of the body model) with the electric field linearly polarized along the z-axis (height of the body model). To excite the plane wave, the code divides the whole volume under study in a total-field and a scattered-field region by means of a Huygens' surface [11], [12]. The scattered-field region is closed by applying a uniaxial perfectly matched layer (UPML) absorbing boundary condition made by a 5-cell layer with parabolic profile and a 0.01% nominal reflection coefficient. At steady state, the scattered electric field values obtained on a surface surrounding the human body were stored and used to evaluate the RCS of the considered body model by way of a near-far field transformation.

Submitted On: January 28, 2015
Accepted On: November 8, 2015

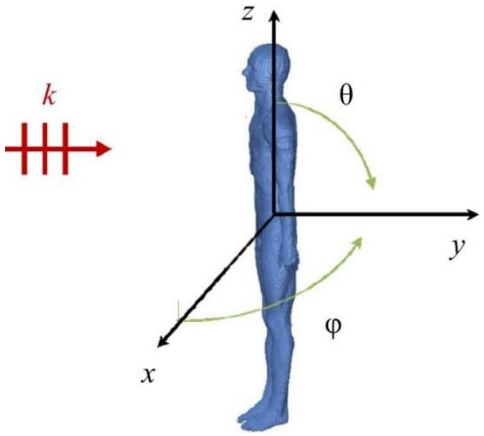

Fig. 1. Simulated geometry: the human body anatomical model faces the plane wave propagating towards the positive y-axis with a linear vertical polarization (i.e., the electric field is aligned with the z-axis).

B. Human anatomical models

Two different anatomical models were considered: the Visible Human [13] (VH) and Duke of the Virtual Family [14]. In particular, the VH was used for validation purposes, while the Duke, representing a model closer to the standard man than the VH, was used to study the RCS as a function of the breathing activity. To this end, it is worth mentioning that the body models usually considered in dosimetry studies represent resting state bodies (RS); i.e., a body at the end of the respiration phase, when little air is present into the lungs.

To take into account the breathing activity, in [8] two models were developed considering the respiration physiology and the pulmonary mechanics [15]. In brief, starting from the RS Duke model, constituted by a three-dimensional matrix of integer numbers representing 77 different tissues, lung cells were added simulating both a diaphragm displacement and an enlargement of the rib cage.

Changing the entity of the diaphragm displacement and of the rib cage enlargement, two respiration phases were obtained: the tidal breath (TB), corresponding to a state of normal inspiration with an inhaled volume of air equal to about 500 cm^3 [15], and the deep breath (DB), corresponding to a state in which a high volume of air, approximately 860 cm^3, is inhaled into the lungs [15].

Figure 2 (a) shows the Duke thorax model, with the lungs highlighted, while Fig. 2 (b) illustrates the number of lung cells in each horizontal section of the human body, as a function of the height from the feet. In particular, the figure reports the number of lung cells in the model representing the resting state (RS); i.e., the original model, and in the two realized models, the tidal breath (TB) and the deep breath (DB), respectively.

From the figure, an overall view of the levels where the lung expansion occurred is obtained. In particular, it can be noted that the rib cage expansion in the TB and DB models follows the behavior of the RS model in the higher sections (from 140 cm to 150 cm in Fig. 2 (b)). Then the expansion becomes more irregular; this is due to the drop in the diaphragm of 2 cm and 4 cm for the TB model and DB model, respectively.

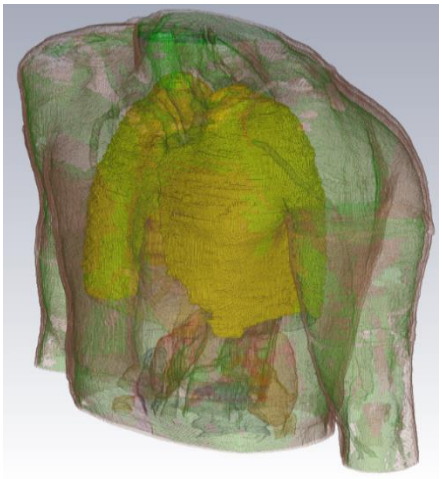

(a)

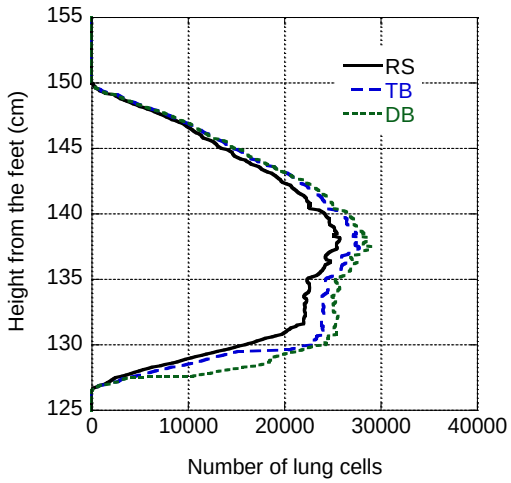

(b)

Fig. 2. (a) Thorax model of the Duke with lungs highligthed, and (b) number of lung cells in the transversal plane, for the RS, TB and DB models, as a function of the height from the feet.

The two new lung models have a final volume of 4262.171 cm^3 and 4530.206 cm^3, for TB and DB respectively, obtained from an initial volume of 3849.216 cm^3 (RS). Each model is made by 77 different tissues whose dielectric properties' values were obtained as a function of the frequency from the database available online at http://www.itis.ethz.ch/itis-for-health/tissueproperties/database/database-summary and based on data of Gabriel et al. [16].

In particular, the dielectric properties of the lung were assumed equal to that of inflated lung for the TB and DB models, and equal to the deflated lung for the RS model.

Moreover, the lung mass density was assumed equal to that of inflated lung (ρ_{LI} = 394 kg/m^3) in both TB and DB models, while for the RS model (man at the end of the expiration phase) an average value between the inflated lung (ρ_{LI}) and deflated lung mass density (ρ_{LD} = 1050 kg/m^3) was used, in order to take into account that the lung is never totally deflated; i.e., there is always a certain percentage of air within it.

To insert the VH into the FDTD code, a spatial resolution of 2 mm was chosen between 1 GHz and 5 GHz, that was reduced to 1 mm between 6 GHz and 9 GHz. On the other hand, for the Duke models, a 1 mm resolution was used at all frequencies. At the highest frequency of interest (9 GHz), the 1 mm resolution corresponds to less than 1/5 of the wavelength for all body tissues and is almost equal to 1/10 of the penetration depth of the electromagnetic field, thus allowing a good approximation of the spatial variations of the electromagnetic field [17].

III. RESULTS

A. Validation

Table 1 reports the RCS of the human body obtained from literature data, both experimental [2], [4]-[5] and numerical [1], [6]-[7]. In particular, in [6] and [7] the human body model considered is the Visible Human, while in [1] a scaled version (i.e., a thinner version) of the Visible Human was studied. The reported data indicates that, in the considered frequency range, RCS absolute values show large fluctuations with frequency and with the anatomical model considered, with values between 0.01 m^2 and 6.3 m^2. In particular, these variations can be attributed to the positioning and shape of the various sub-scatterers on which each considered subject can be divided [6].

In order to validate the numerical procedure, the RCS of the VH was studied between 1 and 9 GHz and compared with the data reported in [6]. In these simulations, the dielectric properties of tissues were varied with the frequency according to [16].

Figure 3 shows the backward RCS; i.e., the RCS obtained for $\theta = 90°$ and $\varphi = 270°$ (see Fig. 1).

From the figure a good agreement with [6] is obtained, with differences within 20% up to 7 GHz. At 8 GHz a very high value is obtained in [6], which seems to be out-side the trend of the other data.

It must be noted here that, in [6] a cell resolution of 2 mm was used for all the considered frequencies, even if, at the highest frequencies considered, such values are higher than the standard used criteria for FDTD stability and accuracy.

Furthermore, it is worth noting that similar discrepancies in the RCS results were also obtained in [7], where the RCS was computed, for the same human body model, by using two different numerical codes; i.e., FDTD and Xpatch.

Table 1: Literature data

	RCS (m^2) Experimental Results			RCS (m^2) Numerical Results		
f (GHz)	Shultz [2]	Bernardi [4]	Piuzzi [5]	Dogaru [6]	Dogaru [7]	Pisa [1]
0.40	1.12					
0.50						1.00
1.00		0.45	0.46	0.01	1.58	0.60
1.10	0.88					
1.50			0.11			0.90
2.00		0.26	0.03	0.19	0.32	1.00
2.40						
2.50			0.03			
2.80	0.49					
3.00		0.25	0.05	0.79	3.16	
3.50						
4.00		0.27	0.02	0.39	1.00	
4.50			0.15			
4.80	1.74					
5.00		0.29	0.18	1.00	1.00	
5.50			0.07			
6.00		0.24	0.06	0.10	6.31	
6.50						
7.00		0.2	0.03	0.25		
7.50			0.04			
8.00		0.23	0.06	1.26		
8.50			0.03			
9.00		0.25	0.01	0.10		
9.40	1.00					
9.50			0.02			
10.0		0.4	0.03			

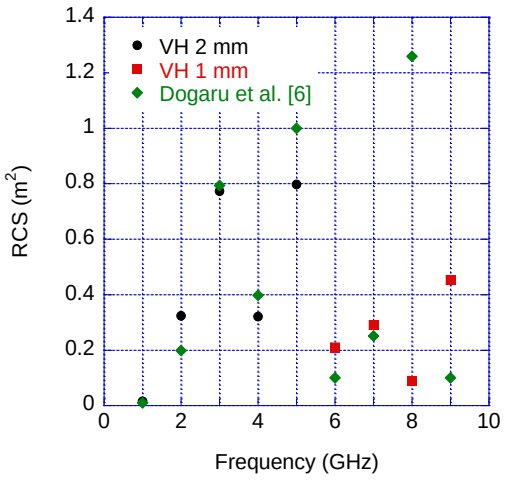

Fig. 3. Comparison between the Visible Human results and RCS values reported in [6].

B. Duke RS model

The Duke anatomical model in the resting state condition was then considered. The Duke RCS was evaluated with 1-degree resolution. Figure 4 shows the RCS at the frequency of 3 GHz as a function of the azimuth (φ). A persistent feature of the RCS is the strong value from the back of the body (φ = 90°), while lower values are obtained along the other directions.

Figure 5 shows the RCS for the Duke RS model as a function of the frequency in the xy plane along the propagation direction; i.e., for θ = 90° and φ = 270°. In the figure, the RCS values previously obtained from the Visible Human (Fig. 3) are also reported for comparison purposes. From the figure, the great variability of the RCS is evident (see also Table 1): it shows an oscillating behavior with peaks and valleys depending both on the frequency and on body models. In particular, with reference to the body models it can be noted that the VH is 1.80 m tall and weighs 105 kg, while the Duke is 1.77 m tall and weighs 72.4 kg.

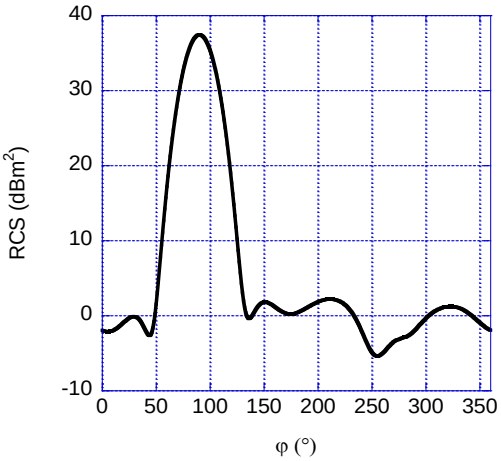

Fig. 4. RCS in the xy plane (θ = 90°) as a function of φ.

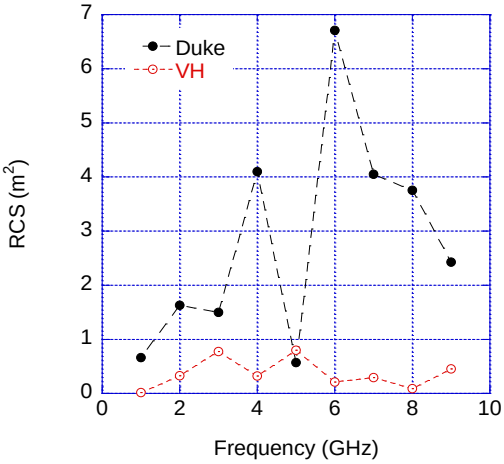

Fig. 5. RCS as a function of the frequency in the xy plane at φ = 270°.

C. Breath anatomical model results

Exploiting the TB and DB models described in Section II.B, simulations were conducted sweeping the frequency in the 1 GHz - 9 GHz range, with 1 GHz step.

Figure 6 shows the RCS obtained for the three developed models in the direction of the incident plane wave (θ =90°; φ = 270°). Observing the data, the RCS values are different for the three models, suggesting that the RCS changes during respiration and that this change varies with the frequency.

To interpret the obtained results, it can be noted that the three models have a different geometry both of the lungs and of the external surface, due to the rib cage enlargement and to the drop of the position of the diaphragm during respiration. Moreover, also the lung tissue characteristics change among the three models, both with reference to the dielectric properties and to the lung mass density, as previously detailed. It is worth mentioning that a similar result, i.e., an oscillating behavior of the RCS values, was also obtained experimentally in [5], for the end-inspiration and end-expiration breathing phases.

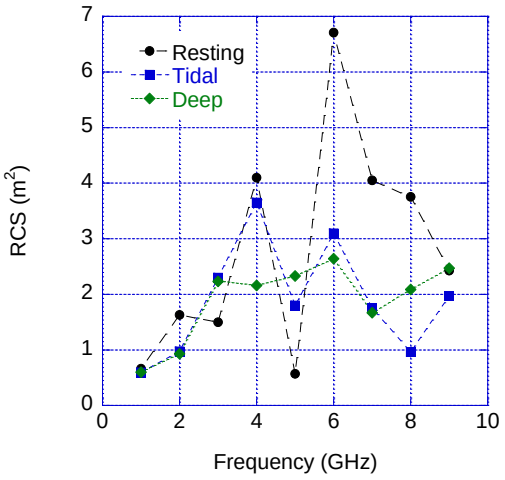

Fig. 6. RCS for the resting state, tidal breath, and deep breath models for theta = 90° and φ = 270°.

D. Homogeneous model

To understand if the results of the previous section are conditioned by the geometry rather than by the dielectric parameter differences, a homogeneous man model was considered.

In particular, the TB model was simulated substituting all the 77 tissues with the skin dielectric parameters at each computed frequency. Obtained RCS results for the homogeneous tidal breath (HTB) model are shown in Fig. 7 compared with those of the non-homogeneous TB model.

Results show differences between the HTB and the TB models, less evident at high frequencies where, due to superficial absorption of the field, the homogeneous skin

model behaves like the inhomogeneous one. Moreover, it is interesting to note that low differences between TB and HTB are obtained at low frequencies also, where probably the different dimensions of the thorax due to the different lung geometries influence most the electromagnetic reflection process.

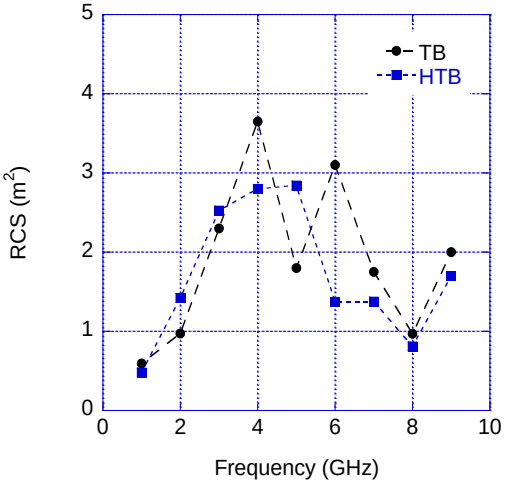

Fig. 7. Comparison between the tidal breath Duke model and the homogeneous tidal break Duke model.

IV. CONCLUSION

The knowledge of the RCS of the human body is of vital importance in the development of UWB radar for the remote detection of the respiratory activity. In fact, these radars rely on the electromagnetic field scattered by the human body towards the receiving antenna. Several studies were devoted to the evaluation of the human body RCS, finding very different results, so that it is very difficult to obtain a general rule to be used in UWB radar design. Moreover, the published studies considered resting state human body; i.e., bodies at the end of the respiration, when the lungs are almost empty.

In this paper, the RCS values of breathing subjects as a function of frequency were evaluated in the 1-9 GHz frequency band using a self-developed numerical code. In particular, three phases of the respiration activity were considered: resting state, tidal breath and deep breath. The three human body models had different geometries, both of the lungs and of the surrounding thorax, as well as different dielectric properties values to represent the different states of the lungs; i.e., empty (RS), partially filled with air (TB), almost completely filled with air (DB).

Obtained RCS absolute values for the resting model showed large fluctuations with the frequency, with values between 0.5 m^2 and 6.7 m^2 in agreement with the literature. With reference to breathing subjects, it was shown that the RCS changes between the three considered models, and that the entity of this change depends on the frequency.

In order to understand if the computed results were more influenced by the different geometries of the thorax or by the dielectric parameters, a homogeneous tidal breath model was considered. Results showed that RCS changes are due both to the different anatomy between the two models and to the differences in tissues dielectric parameters; in particular, the dielectric properties values seem responsible for most of the differences obtained in the frequency range between 4 and 6 GHz.

It is worth noting that the obtained behavior of the RCS with the frequency can be understood observing that the RCS of the human body is influenced by resonances of the various body segments. Therefore, small variations of the body geometry and of the tissue dielectric properties have a strong influence on the RCS values.

REFERENCES

[1] S. Pisa, P. Bernardi, M. Cavagnaro, E. Pittella, and E. Piuzzi, "A circuit model of an ultra wideband impulse radar system for breath-activity monitoring," *Int. J. Num. Model.*, vol. 25, no. 1, pp. 46-63, 2012.

[2] F. V. Schultz, R. C. Burgener, and S. King, "Measurement of the radar cross section of a man," *Proc. IRE*, vol. 46, no. 2, pp. 476-481, Feb. 1958.

[3] J. E. Kiriazi, O. Boric-Lubecke, and V. M. Lubecke, "Dual-frequency technique for assessment of cardiopulmonary effective RCS and displacement," *IEEE Sensors J.*, vol. 12, no. 3, pp. 574,582, Mar. 2012.

[4] P. Bernardi, R. Cicchetti, S. Pisa, E. Pittella, E. Piuzzi, and O. Testa, "Design, realization, and test of a UWB radar sensor for breath activity monitoring," *IEEE Sensors J.*, vol. 14, no. 2, pp. 584-596, Feb. 2014.

[5] E. Piuzzi, P. D'Atanasio, S. Pisa, E. Pittella, and A. Zambotti, "Complex radar cross section measurements of the human body for breath activity monitoring applications," *IEEE Trans. Instrum. Meas.*, vol. 64, no. 8, pp. 2247-2258, Aug. 2015.

[6] T. Dogaru, L. Nguyen, and C. Le, "Computer models of the human body signature for sensing through the wall radar applications," *ARL-TR-4290*, Adelphi, MD: U.S. Army Research Laboratory, 2007.

[7] T. Dogaru and C. Le, "Validation of Xpatch computer models for human body radar signature," *ARL-TR-4403*, Mar. 2008.

[8] M. Cavagnaro, S. Pisa, and E. Pittella, "Anatomical models of breathing subjects for absorption and scattering analysis," *EMC Europe 2013*, Sept. 2013.

[9] M. Cavagnaro, E. Pittella, and S. Pisa, "Evaluation of the electromagnetic power absorption in humans exposed to plane waves: the effect of breathing activity," *Int. J. Ant. Prop.*, vol. 2013, Article ID 854901, 7 pages, 2013.

[10] K. S. Nikita, M. Cavagnaro, P. Bernardi, N. K.

Uzunoglu, S. Pisa, E. Piuzzi, J. N. Sahalos, G. I. Krikelas, J. A. Vaul, P. S. Excell, G. Cerri, S. Chiarandini, R. De Leo, and P. Russo, "A study of uncertainties in modeling antenna performance and power absorption in the head of a cellular phone user," *IEEE Trans. Microw. Theory Techn.*, vol. 48, no. 12, pp. 2676-2685, 2000.

[11] K. S. Kunz and R. J. Luebbers, *The Finite Difference Time Domain Method for Electromagnetics*, CRC Press, Boca Raton, FL, USA, 1993.

[12] A. Taflove, *Computational Electrodynamics: The Finite-Difference Time-Domain Method*, Artech House, Norwood, MA, USA, 1995.

[13] M. J. Ackerman, "The visible human project," *Proceedings of the IEEE*, vol. 86, no. 3, pp. 504, 511, Mar. 1998.

[14] A. Christ, W. Kainz, E. G. Hahn, et al., "The virtual family—development of surface-based anatomical models of two adults and two children for dosimetric simulations," *Phys. Med. Biol.*, vol. 55, no. 2, pp. N23-N38, 2010.

[15] E. N. Marieb and K. Hoehn, *Human Anatomy & Physiology*, Pearson International Edition, 2007.

[16] S. Gabriel, R. W. Lau, and C. Gabriel, "The dielectric properties of biological tissues: III. parametric models for the dielectric spectrum of tissues," *Phys. Med. Biol.*, vol. 41, pp. 2271-2293, 1996.

[17] P. Bernardi, M. Cavagnaro, S. Pisa, and E. Piuzzi, "SAR distribution and temperature increase in an anatomical model of the human eye exposed to the field radiated by the user antenna in a wireless LAN," *IEEE Trans. Microw. Theory Techn.*, vol. 46, no. 12, pp. 2074-2082, Dec. 1998.

Marta Cavagnaro received the Electronic Engineering degree (cum laude) and the Ph.D. degrees from Sapienza University of Rome, Rome, Italy, in 1993 and 1997, respectively. From 2000 to 2012, she was Assistant Professor at the Dept. of Electronic Engineering, Sapienza University of Rome. Presently she is Associate Professor at the Department of Information Engineering, Electronics and Telecommunications of the same university. Her research interests are related to dosimetric aspects of the interaction between EM fields and biological systems, medical applications of EM fields, environmental impact of mobile communication systems, and numerical techniques in electromagnetics. She is author or co-author of more than 120 scientific papers, and serves as Reviewer for several scientific journals.

Erika Pittella received the M.S. (cum laude) and Ph.D. degrees in Electronic Engineering from Sapienza University of Rome, Rome, Italy, in 2006 and 2011, respectively. She is currently a Research Associate with the Dept. of Information Engineering, Electronics and Telecommunications, Sapienza University of Rome. Her main research activities are related to the modeling of UWB radars for the remote monitoring of cardio-respiratory activity and to the design of sources, antennas, and receivers of such systems. Her research interests also include dosimetric aspects of the interaction between electromagnetic fields radiated by UWB radar systems and exposed subjects.

Stefano Pisa (M'91) received the Electronic Engineering and Ph.D. degrees from Sapienza University of Rome, Italy, in 1985 and 1988, respectively. In 1989, he joined the Dept. of Information Engineering, Electronics and Telecommunications as a Researcher. Since 2001, he has been an Associate Professor with the same university. His research interests are the interaction between EM fields and biological systems, therapeutic and diagnostic applications of EM fields, and the modeling and design of MW circuits. He has authored over 150 scientific papers and numerous invited presentations. He serves as a Reviewer for different international journals. He is currently "Consulting Member" of the "Scientific Committee on Physics and Engineering" of the ICNIRP and a Member of the Advisory Group of the Dutch project "Electromagnetic Fields and Health".

Bandwidth Enhancement of Small Square Monopole Antenna Using Self-Complementary Structure for Microwave Imaging System Applications

Mohammad Ojaroudi and Ozlem Aydin Civi

Department of Electrical and Electronics Engineering
Middle East Technical University, Ankara, Turkey
ojaroudi@metu.edu.tr, ozlem@metu.edu.tr

Abstract ─ A novel printed monopole antenna for ultra-wideband (UWB) applications is designed based on self-complementary structure as a matching network. The proposed antenna consists of a square radiating patch and a self-complementary structure located next to feed line, which provides a wide usable fractional bandwidth of more than 100% (3.04-11.43 GHz). Self-complementary matching network is created, by cutting two rectangular ring slots on the ground plane and by inserting two rectangular rings coupled elements in the top layer; hence, additional resonances are excited and much wider impedance bandwidth can be produced. The designed antenna has a small size of 14×22 mm^2, about 0.15λ×0.25λ at 4.3 GHz. It is shown that simulated and measured results agree well with each other and demonstrate the usefulness of the proposed antenna for UWB applications. The proposed antenna exhibits almost omni-directional radiation patterns with low cross-polarization levels and provides an acceptable gain over whole band.

Index Terms ─ Babinet's equivalence principle, microwave imaging system, self-complementary structure, square monopole antenna.

I. INTRODUCTION

One of key issues in ultra-wideband (UWB) imaging systems is the design of a compact antenna while providing wideband radiation characteristics over the whole operating band. Consequently, a number of printed microstrip antennas with different geometries have been experimentally characterized [1]-[2]. These types of UWB antennas are also suitable for the short-range indoor and outdoor communications [3]. However, for radar systems, such as an UWB microwave imaging system for detection of breast tumor, a moderate gain directional antenna is advantageous. In addition to an UWB impedance bandwidth, as defined by the minimum return loss of 10 dB, the UWB antenna is required to support a very short pulse transmission with negligible distortion. This is necessary to achieve precision imaging without ghost targets. Several UWB antenna designs with compact size and low distortion have been proposed for the use in the medical imaging systems [4-6]. Each has its own merits and drawbacks. Some of the proposed antennas have no planar structure, whereas others have low-gain and/or low radiation efficiency. The unipolar and antipodal Vivaldi antennas presented in the literature [7, 8] satisfy the requirements for imaging systems in terms of bandwidth, gain, and impulse response. However, the achieved performance is at the expense of significant size, which has a length of several wavelengths.

In this paper, a simple method for designing a novel and compact microstrip-fed monopole antenna with multi resonance performance based on self-complementary structure for UWB applications has been presented and discussed. The proposed self-complementary structure is designed using the Babinet's equivalence principle to achieve impedance matching throughout a wide frequency range, such that Z_{in} has constant value for all frequencies [9]. To the authors' knowledge, it is the first time that a self-complementary matching network consisting of two rectangular ring slots on the ground plane and two rectangular ring coupled elements in the top layer is used to increase the bandwidth of an ordinary square patch monopole antenna. The size of the designed antenna is smaller than the UWB antennas reported recently [2]-[8]. Good return loss and radiation pattern characteristics are obtained in the frequency band of interest, 3.04-11.43 GHz.

II. ANTENNA CONFIGURATION

The square monopole antenna fed by a 50 Ω microstrip line is shown in Fig. 1, which is printed on an FR4 substrate with the thickness of 0.8 mm, dielectric constant of 4.4, and the loss tangent of 0.018. The basic antenna structure consists of a square patch, a feed line, and a ground plane. All dimensions of the antenna are given in Table 1. To increase the bandwidth of the antenna, we propose to insert a self-complementary structure as shown in Fig. 1. Self-complementary structure includes two rectangular rings on the patch side and two rectangular ring slots in the ground plane. The

Submitted On: June 12, 2015
Accepted On: November 8, 2015

resonant behavior of the self-complementary structures used here introduces new resonance frequencies and consequently improves the bandwidth of the antenna. Opening two rectangular ring slots of suitable dimensions on the ground plane results in a much enhanced impedance bandwidth. Regarding defected ground structures (DGS), creating slots in the ground plane provides an additional current path. Moreover, this structure changes the inductance and capacitance of the input impedance, which in turn leads to a change in the bandwidth. The DGS applied to a microstrip line causes a resonant character of the structure transmission with a resonant frequency controllable by changing the shape and size of the slot [10]. Therefore, by cutting two rectangular ring shaped slots at the ground plane and carefully adjusting its parameters, much enhanced impedance bandwidth can be achieved.

In addition, the complementary coupled rings on the top layer are playing an important role in the broadband characteristics of this antenna, because it can adjust the electromagnetic coupling effects between the patch and the ground plane, and improves its impedance bandwidth without any cost of size or expense. This phenomenon occurs because, with the use of a complementary coupled structure in transmission line distance, additional coupling is introduced between the bottom edge of the square patch and the ground plane [8].

The first step in the design of the antenna is to determine the initial dimensions of the structure. These parameters, including the substrate are $W_{Sub} \times L_{Sub} = 14 \times 22$ or about $0.15\lambda \times 0.25\lambda$ at 4.3 GHz (the first resonance frequency). There is flexibility in choosing the width of the radiating patch. This parameter mostly affects the antenna bandwidth. As W decreases, so does the antenna bandwidth, and vice versa. The length of the radiating patch is approximately $\frac{\lambda_{lower}}{4}$, where λ_{lower} is the wavelength of the lower frequency of the bandwidth. λ_{lower} frequency of lower edge of the usable band depends on a number of parameters such as the width of the radiating patch as well as the thickness and dielectric constant of the substrate on which the antenna is fabricated [8]. The important step in the design is to choose L_r (the length of the new resonators). L_r is set to resonate at $0.25\lambda_g$, where $L_{r3} = 2L_P + 1.75W_P$, and $L_{r4} = 2L_P + 0.75W_P$, λ_g corresponds to wavelength of resonance frequencies (10.5 GHz is the third resonance frequency and 11.4 GHz is the fourth resonance frequency) [8]. The parameters of this antenna are studied by changing one parameter at a time while others are kept fixed. Ansys HFSS simulations are used to optimize the design and agreement between the simulation and measurement is obtained [11].

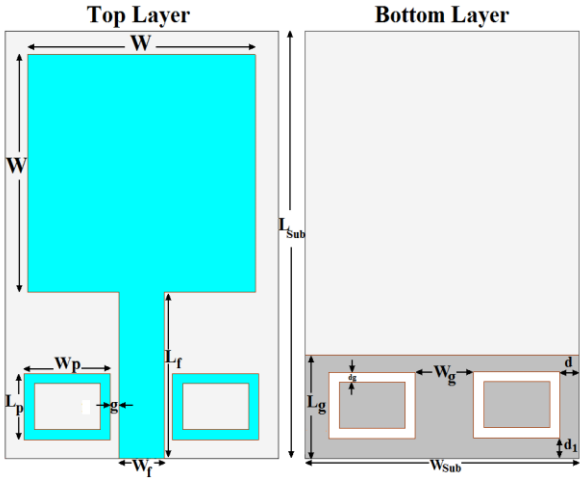

Fig. 1. Geometry of the proposed square monopole antenna with self-complementary matching network.

Table 1: The proposed monopole antenna dimensions

Parameter	Value (mm)	Parameter	Value (mm)
W_{Sub}	14	L_{Sub}	22
W_f	1.5	L_f	8
W	12	L_g	5
W_p	5	L_p	3
W_g	2	d	1
d_1	2	g	0.25

III. RESULTS AND DISCUSSION

The designed square monopole antenna is fabricated on FR4 substrate by fast PCB prototyping machine. The simulated and experimental results of the input impedance and radiation characteristics are presented and discussed in this section.

Figure 2 shows the return loss characteristics for an ordinary printed square monopole antenna, a monopole antenna with two modified rectangular ring slots on the ground plane, and a monopole antenna with a pair of rectangular ring self-complementary structures. As shown in Fig. 2, in the proposed antenna configuration, the ordinary square monopole can provide the fundamental and next higher resonant radiation band at 4.3 and 8.1 GHz, respectively, in the absence of the self-complementary structure. The upper frequency bandwidth is significantly affected by using the rectangular ring slots on the ground plane. This behavior is mainly due to the fact that creating slots in the ground plane provides an additional current path. In addition, by inserting two rectangular ring coupled elements on the top of these slots, the impedance bandwidth is effectively improved at the upper frequency [10]. It is observed that by using this modified self-complementary structure, additional third (10.5 GHz) and fourth

(11.4 GHz) resonances are excited respectively, and hence, the bandwidth is increased. It is also noticed that the resonance frequencies introduced by self-complementary structure are different and smaller than the ones due to having only slot rings in the ground and ones due to having only metallic rings on the upper plane.

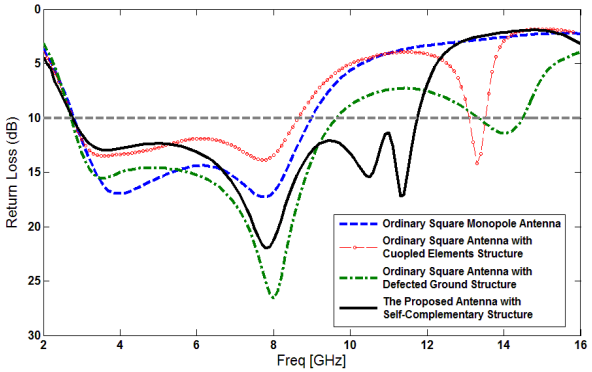

Fig. 2. Comparison of simulated return loss characteristics for ordinary square monopole antenna, monopole with two modified rectangular ring slots on the ground plane, and monopole with a pair of rectangular ring self-complementary structures.

The simulated current distributions on the radiating patch and the ground plane for the proposed antenna at 10.5 GHz (third resonance) and at 11.4 GHz (fourth resonance) are plotted in Figs. 3 and 4, respectively. As shown in Figs. 3 and 4, the current is concentrated on the edges of the interior and exterior of the rectangular ring slots and coupled elements at these resonance frequencies.

In order to understand the phenomenon behind the self-complementary structure effects on decreasing resonance frequency and generation of new additional resonances frequencies, the electrical lengths of the corresponding resonating parts due to electromagnetic coupling between self-complementary structures are plotted on Fig. 5. Regarding coupling between the elements of self-complementary structure, since the polarization of the two antennas are reversed, the surface current direction is changed on the other side of the structure [12]. Therefore, we can claim that the resonator lengths shown in Fig. 5 are longer than the ones of the isolated rings and slots so that new resonance frequencies are appeared in the lower frequencies as shown in Fig. 2. In addition, by inserting coupled elements on the other side of substrate, the electromagnetic coupling is effectively improved. The rectangular rings coupled elements can be regarded as parasitic resonators electrically coupled to the rectangular ring slots. As shown in Fig. 5, the electrical current for the new generated resonances frequency does continue its direction along the bottom or top side of substrate.

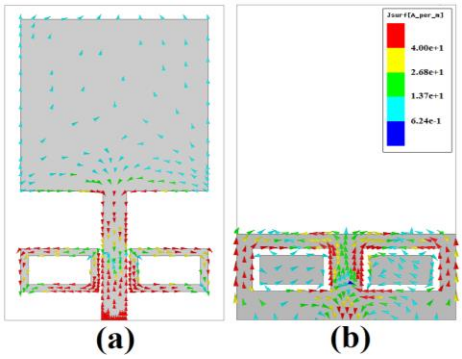

Fig. 3. Simulated surface current distributions for the proposed monopole antenna at third resonance frequency (10.5 GHz): (a) on the radiating patch, and (b) on the ground plane.

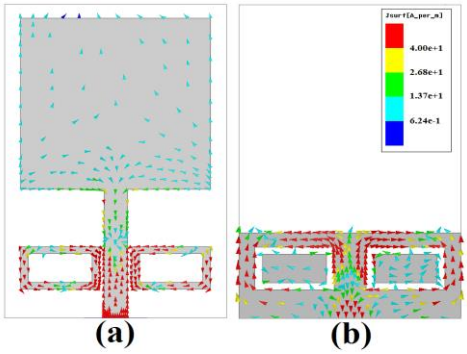

Fig. 4. Simulated surface current distributions for the proposed monopole antenna at fourth resonance frequency (11.4 GHz): (a) on the radiating patch, and (b) on the ground plane.

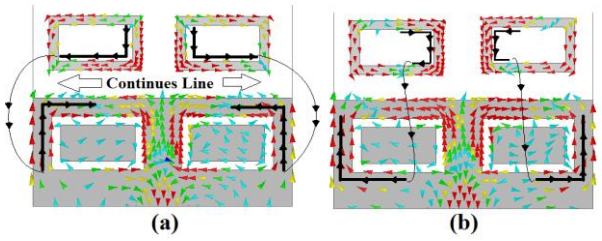

Fig. 5. Simulated surface current distributions show the new resonator electrical lengths due to electromagnetic coupling between self-complementary structures: (a) at the third resonance frequency (10.5 GHz), and (b) at the fourth resonance frequency (11.4 GHz).

In order to investigate the effects of the separation distance between self-complementary matching network and microstrip feed-line on the proposed antenna, the return loss characteristics for various gap distance lengths are analyzed and results are illustrated in Fig. 6. It is observed that the impedance bandwidth is effectively improved at the upper frequency band as

separation distance is changed. It is seen that the frequency of the lower edge of bandwidth is improved with decreasing the gap, but the matching becomes poor for lower frequencies. By adjusting this separation distance, the electromagnetic coupling between the lower edge of the square patch and the ground plane can be properly controlled [10].

Another important parameter of this structure is the rectangular ring length (W_P). By adjusting W_P, the upper edge of the frequency bandwidth can be properly controlled. The simulated return loss characteristics for various rectangular ring lengths are illustrated in Fig. 7. It is seen that the upper-edge frequency of the impedance bandwidth is increased with decreasing W_P, but the matching becomes poor for lower band.

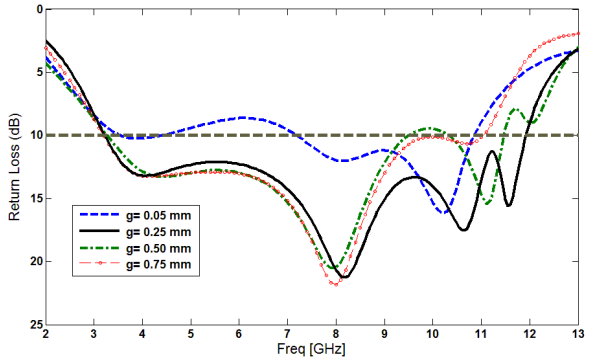

Fig. 6. Simulated return loss characteristics of the proposed antenna with different values of separation distance between self-complementary matching network and microstrip feed-line.

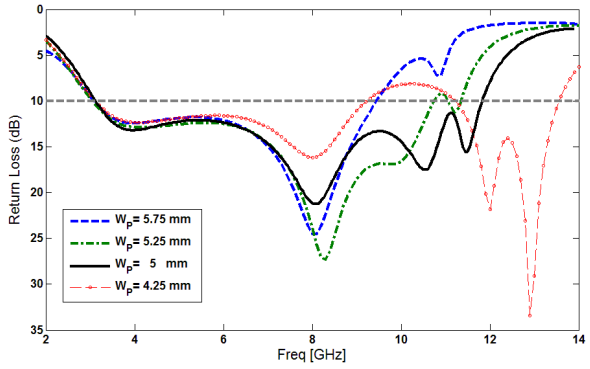

Fig. 7. Simulated return loss characteristics of the proposed antenna with different values of W_P.

Figure 8 shows the effects of the self-complementary structure on the maximum gain in comparison to the same antenna without them. As shown in Fig. 8, the ordinary square antenna has a gain that is low at 3 GHz and increases with frequency. However, the gain of the ordinary square antenna is decreased in the higher frequency band with the use of the self-complementary structure; the proposed antenna gain has a flat property which is advantageous for microwave imaging applications.

In UWB microstrip antennas analysis, the transfer function is transformed to time domain by performing the inverse Fourier transform. Fourth derivative of a Gaussian function is selected as the transmitted pulse. Therefore, the output waveform at the receiving antenna terminal can be expressed by convoluting the input signal and the transfer function. The input and received wave forms for the face-to face and side-by-side orientations of the antenna are shown in Fig. 9. The results of the calculations using the CST software [13] indicated that the shape of the pulse is preserved in most cases, especially in the first configuration. Using the reference and received signals, it becomes possible to quantify the level of similarity between signals [3].

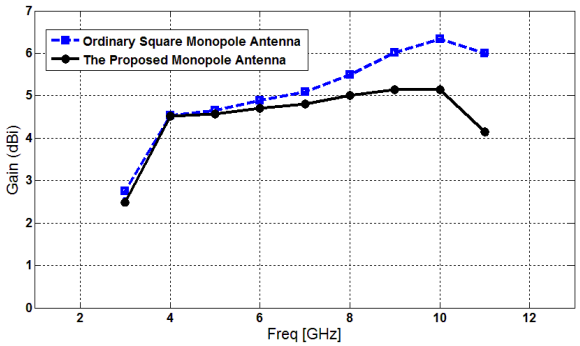

Fig. 8. Simulated maximum gain comparisons for the ordinary square antenna and the proposed antenna.

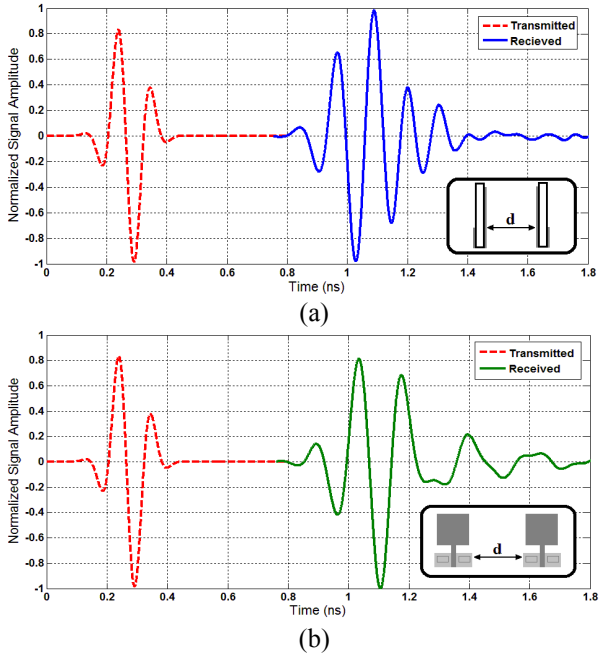

Fig. 9. Transmitted and received pulses: (a) side by side, and (b) face to face.

The proposed antenna with optimal design is fabricated as shown in Fig. 10 and measured. Figure 11 compares the measured and simulated VSWR characteristics of the proposed antenna. The fabricated antenna has the frequency band of 3.04 to over 11.43 GHz. The slight discrepancy between simulated and measured results is mostly due to a number of parameters such as possible errors in fabricated antenna dimensions as well as nonuniformity of the thickness and the dielectric constant of the low cost FR4 substrate over the wide range of simulation frequencies.

Figure 12 and Fig. 13 depict the measured and simulated radiation patterns, the co-polarization and cross-polarization in the *H*-plane (*x*-*z* plane) and *E*-plane (*y*-*z* plane), at different frequencies in the operation band. These patterns demonstrate that the antenna actually radiates over a wide frequency band. It can be seen that the radiation patterns in *x*-*z* plane are nearly omni-directional even at higher frequencies, and also the cross-polarization levels are low. These radiation characteristics show that the proposed antenna is a promising candidate for UWB microwave imaging applications.

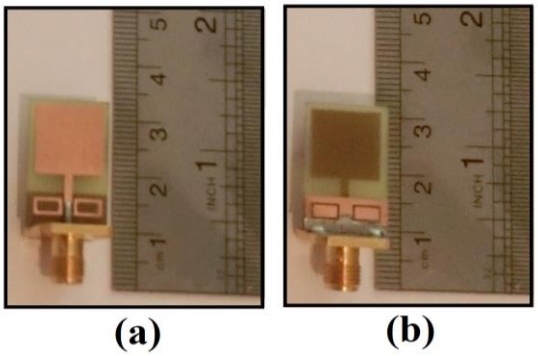

Fig. 10. Photograph of the realized printed square monopole antenna: (a) top view, and (b) bottom view.

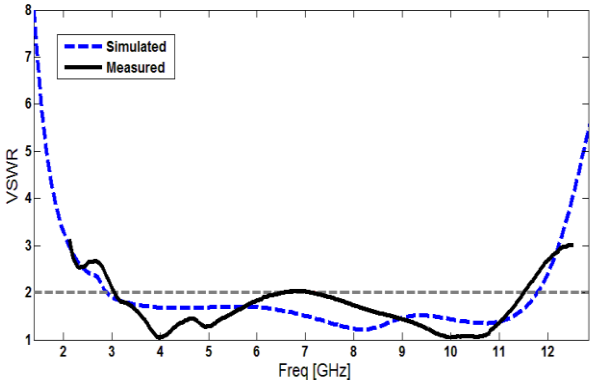

Fig. 11. Measured and simulated VSWR for the proposed antenna.

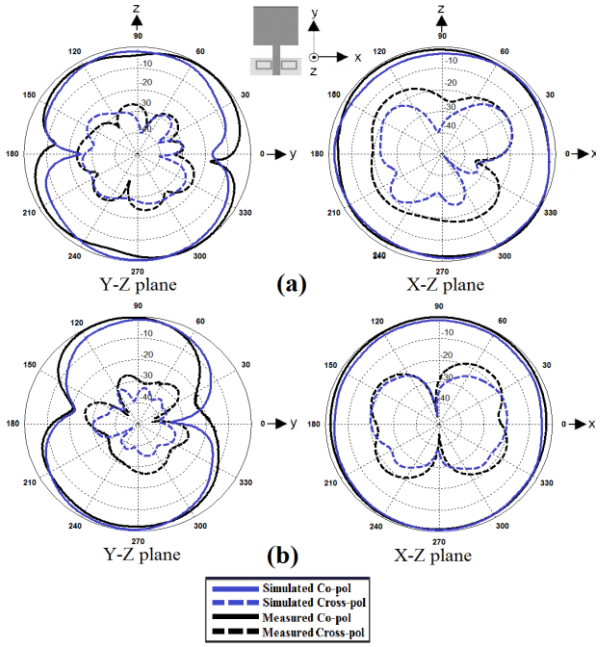

Fig. 12. Measured and simulated radiation patterns of the proposed antenna: (a) first resonance frequency (4.3 GHz), and (b) second resonance frequency (8.1 GHz).

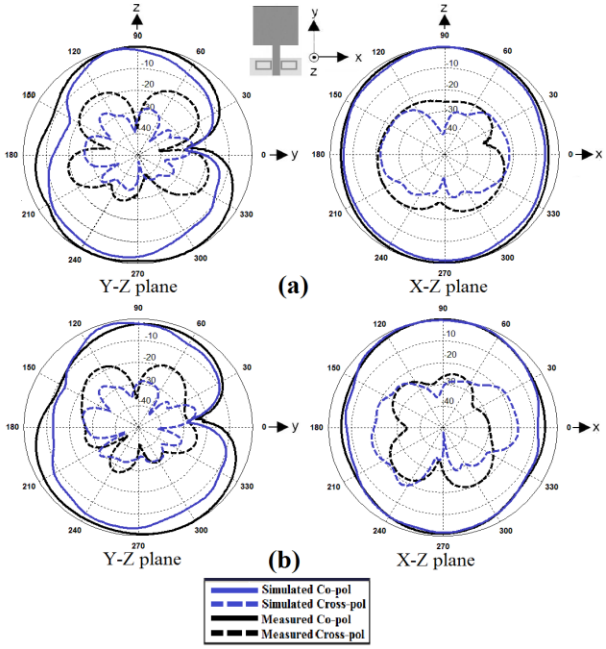

Fig. 13. Measured and simulated radiation patterns of the proposed antenna: (a) third resonance frequency (10.5 GHz), and (b) fourth resonance frequency (11.4 GHz).

IV. CONCLUSION

In this paper, a compact printed monopole antenna with multi resonance characteristics with a novel

matching network based on self-complementary structure has been proposed for UWB applications. In this structure, by cutting two rectangular ring slots on the ground plane and by inserting two rectangular ring coupled elements in the top layer, the self-complementary structure is created; hence, additional resonances are excited and much wider impedance bandwidth is achieved. The fabricated antenna has an impedance bandwidth of 3.04 to 11.43 GHz which covers the frequency range of UWB systems. Furthermore, in this band gain level is satisfactory varying between 3 to 5 dBi. The proposed antenna is small, low cost and can be easily fabricated.

REFERENCES

[1] M. Ojaroudi and N. Ojaroudi, "Ultra-wideband small rectangular slot antenna with variable band-stop function," *IEEE Transactions on Antenna and Propagation*, vol. 62, no. 1, pp. 490-494, Jan. 2014.

[2] M. C. Tang, S. Xiao, T. Deng, D. Wang, J. Guan, B. Wang, and G. D. Ge, "Compact UWB antenna with multiple band notches for WiMAX and WLAN," *IEEE Trans. Antennas Propag*., vol. 59, no. 4, pp. 1372-1376, Apr. 2011.

[3] E. J. Bond, X. Li, S. C. Hagness, and B. D. Van Veen, "Microwave imaging via space-time beamforming for early detection of breast cancer," *IEEE Trans. Antennas Propag*., vol. 51, no. 8, pp. 1690-1705, Aug. 2003.

[4] M. Chiappe and G. L. Gragnani, "Vivaldi antennas for microwave imaging: theoretical analysis and design considerations," *IEEE Trans. Instrum. Meas*., vol. 55, no. 6, pp. 1885-1891, Dec. 2006.

[5] X. Yun, E. C. Fear, and R. Johnston, "Broadband cross polarized bowtie antenna for breast cancer detection," in *Proc. IEEE Antennas Propag. Soc. Int. Symp*., Columbus, OH, vol. 3, pp. 1091-1094, June 2003.

[6] L. Guo, S. Wang, X. Chen, and C. G. Parini, "A small printed quasi-self-complementary antenna for ultrawideband systems," *IEEE Antennas and Wireless Propagation Letters*, vol. 8, pp. 554-557, 2009.

[7] L. Guo, S. Wang, Y. Gao, Z. Wang, X. Chen, and C. G. Parini, "Study of a printed quasi-self-complementary antenna for ultra wideband systems," *IET Electronic Letters*, vol. 44, no. 8, pp. 511-512, Apr. 10, 2008.

[8] C. J. Shannon, E. C. Fear, and M. Okoniewski, "Dielectric filled slot line bowtie antenna for breast cancer detection," *Electron. Lett*., vol. 41, no. 7, pp. 388-390, 2005.

[9] J. A. Kong, *Electromagnetic Wave Theory*, EMW Publishing, Cambridge, 2000.

[10] M. Ojaroudi, Sh. Yzdanifard, N. Ojaroudi, and M. Nasser-Moghaddasi, "Small square monopole antenna with enhanced by using inverted T-shaped slot and conductor-backed plane," *IEEE Transactions on Antenna and Propagation*, vol. 59, no. 2, pp. 670-674, Feb. 2011.

[11] Ansoft High Frequency Structure Simulation (HFSS), ver. 13, Ansoft Corporation, 2011.

[12] J. Zou, L. Liu, and S. W. Cheung, "Compact quasi-self-complementary antenna for portable UWB applications," *Microwave and Optical Technology Letters*, vol. 56, no. 6, pp. 1317-1323, June 2014.

[13] CST Microwave Studio, ver. 2014, CST, Framingham, MA, USA, 2014.